

# First principles study of point defects in diamond

**Chloe Victoria Peaker**

Supervisory Team:

Dr. Jonathan Goss, Prof. Patrick Briddon and Dr. Alton Horsfall

A Thesis submitted to the  
Faculty of Science, Agriculture and Engineering  
in partial fulfilment for the degree of  
Doctor of Philosophy.



**Newcastle**  
University

**D E B E E R S**  
GROUP OF COMPANIES

School of Engineering  
April, 2018





Dedicated to my family and friends that helped me through this.

## Abstract

Diamond is well known for its superlative properties and, with the advent of improved growing techniques, electronic and optical grade synthetic diamond can be realised. Although this is a major step forward for the use of diamond in technological applications, the production of high quality synthetics brings new challenges to the gem trade: it is crucial to be able to confidently distinguish between natural, man-made and treated diamonds.

In both natural and synthetic diamond, nitrogen is commonly the dominant impurity, identified in experiment in different forms. Nitrogen substitutes for carbon, and building upon the isolated single nitrogen centre, a series of complexes in progressively aggregated forms, sometimes combined with a vacancy and hydrogen, have been identified. For example hydrogen has been found in both natural and synthetic diamonds in the form of the  $3107\text{ cm}^{-1}$ ,  $\text{N}_3\text{VH}$  centre.

This Thesis presents a systematic quantum-chemical study of point defects in diamond that incorporate a combination of nitrogen, hydrogen and a vacancy ( $V$ ). Focusing on the set  $\text{N}_n\text{VH}_m$  where  $n + m \leq 4$ , the work is broken down further into isoelectronic defects ( $n + m = 1, 2, \dots$ ). The hydrogen atom(s) saturate the carbon radical(s) that are produced when the vacancy is formed and the nitrogen(s) replace a carbon radical. *Ab initio* calculations are used to model the structure of the defects, the electrical properties, electronic structure, magnetic interactions, relative thermal stability and infrared vibrational properties.

As a key reference state of nitrogen, the hyperfine interactions of the simplest nitrogen containing defect, the single substitutional nitrogen defect labelled the P1

---

centre are also investigated further. The P1 centre is a paramagnetic centre and the unpaired electron spin interacts with nearby  $^{13}\text{C}$  nuclei; understanding this hyperfine coupling is important, it can be used to identify structure and is of technological importance, such as in the main decoherence mechanism for NV centres. It is found that the experimentally derived model for the  $^{13}\text{C}$  sites detected is mainly correct, but as a consequence of the detailed calculations one of the carbon sites is reassigned.

Some outcomes from reviewing the expanse of data associated with the  $\text{N}_n\text{VH}_m$ ,  $n + m \leq 4$  set are as follows.

Where radicals remain around the vacancy, different charges are possible, until the carbon radicals are converted to lone-pairs by negatively charging the defects, or removed in positively charged defects. The VH defect has three carbon radicals, and is found to be able to adopt multiple charge states.

$\text{VH}^0$ , which is isoelectronic to  $\text{NV}^0$ , is determined to have  $S = 3/2$  and  $S = 1/2$  states that are indistinguishable in energy. Indeed, low lying excited spin states are found for a number of the complexes that contain radicals. A specific consequence of the possibility of a  $S = 3/2$  ground state or experimentally accessible excited state for  $\text{VH}^0$  is that this would surprisingly render it without any internal electronic transitions, so might not be visible in experiments such as optical absorption.

There are also pronounced effects of charge upon the vibrational modes. For  $\text{N}_2\text{VH}$  the C–H stretch mode is predicted to shift from 3040 to 2630  $\text{cm}^{-1}$  when it becomes negatively charged. Such a change might represent a critical factor in its identification from experiment.

A potential assignment of vibrational modes, amongst others, to the  $\text{NVH}^+$  defect has also been identified. The calculated stretch mode is within 1% of a mode found in boron and nitrogen doped CVD diamond. A corresponding bend mode is also found to be within 5% of the calculated value.

Finally, the thermal stability of the defects were compared. The stability increased as radicals were removed from the carbons surrounding the vacancy. This is in line with the high thermal stability of the 3107  $\text{cm}^{-1}$  centre.

## Acknowledgements

I would like to thank Dr. Jonathan Goss for his guidance, patience and invaluable support throughout my years at Newcastle University. I am not sure I would have survived my PhD without him.

I would like to extend my thanks to my other supervisors to: Prof. Patrick Briddon, for his crucial input in the use of AIMPRO and Dr. Alton Horsfall for his blunt but true wise words.

Also thanks to the extended AIMPRO family: including Dr. Mark Rayson and Prof. Bob Jones, for sharing their knowledge and input to the next generation of 'AIMPROers' and Dr. Hugo Pinto for his support, encouragement and uplifting positive outlook.

A special thanks to the experimental diamond group past and present at Warwick, they were always so welcoming and happy to engage in prolonged discussions at various conferences.

Of course without the financial support from De Beers Technologies this project would not have happened. In particular I thank Dr. Philip Martineau and Dr. David Fisher for their technical guidance and support.

Finally, I would like to thank all my friends and family who have supported me through the ups and more importantly the downs associated with this Thesis.



## Declaration of authorship

I, Chloe Victoria Peaker, declare that all work presented in this Thesis is my own except where stated otherwise. The work was carried out at Newcastle University between September 2013 to April 2018, primarily under the supervision of Dr. Jonathan P. Goss. The research reported here has not been submitted, either wholly or in part, in this or any other academic institution for admission to a higher degree. Where work reported in this Thesis has been published it will be noted in the appropriate chapter. A full list of publications I am involved with are listed below.

C. V. Peaker  
April, 2018

## Publications, conferences and prizes

### List of Publications

1. **C. V. Peaker**, J. P. Goss, P. R. Briddon, A. B. Horsfall and M. J. Rayson, The vacancy-hydrogen defect in diamond: A computational study, *physica status solidi (a)* 212 (11), 2431-2436, (2015).
2. **C. V. Peaker**, J. P. Goss, P. R. Briddon, A. B. Horsfall and M. J. Rayson, Di-nitrogen-vacancy-hydrogen defects in diamond: a computational study, *physica status solidi (a)* 212 (11), 2616-2620, (2015).
3. **C. V. Peaker**, M. K. Atumi, J. P. Goss, P. R. Briddon, M. J. Rayson and R. Jones, Assignment of  $^{13}\text{C}$  hyperfine interactions in the P1-center in diamond, *Diamond and Related Materials* 70, 118-123, (2016).

- 
4. A. K. Tiwari, **C. V. Peaker**, J. P. Goss, P. R. Briddon, M. J. Rayson and N. G. Wright, Ultra-thin layers of Fe and Co on diamond, (in preparation).
  5. M. Al-Hadidi, **C. V. Peaker**, J. P. Goss, P. R. Briddon, M. J. Rayson. Modelling the impact of strain and pressure upon the migration of self-interstitials and vacancies in diamond, (in preparation).

### List of Conferences

1. **Annual Research Conference 2014**, 23<sup>rd</sup>–24<sup>th</sup> January 2014, School of Electrical & Electronic Engineering, Newcastle University, Newcastle upon Tyne, U.K., First principles study of diamond, (**poster presentation**).
2. **The 65<sup>th</sup> Diamond Conference 2014**, 8<sup>th</sup>–11<sup>th</sup> July 2014, University of Warwick, Warwick, U.K., Quantum chemical determination of charge- and spin-states of the vacancy-hydrogen defect complex in diamond, (**oral presentation**). Calculations of mono- and di-nitrogen-vacancy centers in diamond partially or fully saturated with hydrogen, (**poster presentation**). Magnetic order in sub-monolayer Fe and Co termination of (001) diamond, (**poster presentation**).
3. **Annual Research Conference 2015**, 21<sup>st</sup>–22<sup>nd</sup> January 2015, School of Electrical & Electronic Engineering, Newcastle University, Newcastle upon Tyne, U.K., An introduction to diamond and the vacancy-hydrogen defect, (**oral presentation**).
4. **Towards Reality in Nanoscale Materials VIII**, 9<sup>th</sup>–11<sup>th</sup> February 2015, Levi, Finland, Quantum chemical determination of charge- and spin-states of the vacancy-hydrogen defect complex in diamond, (**poster presentation**).
5. **Hasselt Diamond Workshop 2015**, 25<sup>th</sup>–27<sup>th</sup> February 2015, Quantum chemical determination of charge- and spin-states of the vacancy-hydrogen defect complex in diamond, (**poster presentation**),  $N_2VH_n$  ( $n = 1, 2$ ) centers in diamond: a quantum-chemical study, cultuurcentrum Hasselt (Cultural Centre), Hasselt, Belgium, (**poster presentation**).
6. **New Diamond and Nano Carbons (NDNC) 2015**, 24<sup>th</sup>–28<sup>th</sup> May 2015, Shizuoka GRANDSHIP, Japan, Nitrogen, vacancy and hydrogen point defects in diamond: a quantum-chemical study, (**oral presentation**).
7. **The 66<sup>th</sup> Diamond Conference 2015**, 6<sup>th</sup>–9<sup>th</sup> July 2015, University of Warwick, Warwick, U.K., Single vacancy, nitrogen and hydrogen aggregates: A computational study, (**oral presentation**).

- 
8. **Hasselt Diamond Workshop 2016**, 9–11 March 2016, cultuurcentrum Hasselt (Cultural Centre), Hasselt, Belgium, Single vacancy, nitrogen and hydrogen aggregates: A computational study, **(poster presentation)**, Ultra-thin layers of Fe and Co on diamond for magneto-tunnel junctions, **(poster presentation)**.
  9. **The 67<sup>th</sup> Diamond Conference 2016**, 11<sup>th</sup>–14<sup>th</sup> July 2016, University of Warwick, Warwick, U.K. Single vacancy, nitrogen and hydrogen aggregates: A computational study; Ultra-thin layers of Fe and Co on diamond, **(poster presentation)**, Modelling the impact of strain and pressure upon the migration of self-interstitials and vacancies in diamond, **(oral presentation)**.

### Prizes

1. **Annual Research Conference 2014**, 23<sup>th</sup>–24<sup>th</sup> January 2014, School of Electrical & Electronic Engineering, Newcastle University, Newcastle upon Tyne, U.K., First principles study of diamond, **(poster presentation)**. **Best Poster Award**.
2. **Annual Research Conference 2016**, 21<sup>st</sup>–22<sup>nd</sup> January 2016, School of Electrical & Electronic Engineering, Newcastle University, Newcastle upon Tyne, U.K., The vacancy-hydrogen defect in diamond: A computational study, **(oral presentation)**. **Third Best Paper Award**.

# Contents

<b>Dedication</b>	<b>i</b>
<b>Abstract</b>	<b>ii</b>
<b>Acknowledgements</b>	<b>iv</b>
<b>Declaration of authorship</b>	<b>vi</b>
<b>Publications, conferences and prizes</b>	<b>vi</b>
<b>Table of Contents</b>	<b>ix</b>
<b>Glossaries</b>	<b>xiv</b>
Glossary of mathematical notation . . . . .	xiv
Acronyms and abbreviations . . . . .	xvii
Defect notation . . . . .	xviii
<b>List of Figures</b>	<b>xxi</b>
<b>List of Tables</b>	<b>xxv</b>
<b>1 Introduction</b>	<b>1</b>
1.1 The history of diamond . . . . .	1
1.2 What is diamond? . . . . .	3
1.3 Why diamond? . . . . .	5
1.4 Defects in diamond . . . . .	5
1.5 Classification . . . . .	7
1.6 Synthesis . . . . .	9
1.6.1 High pressure high temperature . . . . .	10
1.6.2 Chemical vapour deposition . . . . .	11
1.7 Treatments . . . . .	12
1.7.1 Heat treatments . . . . .	12

## Contents

---

1.7.2	Irradiation treatments	13
1.8	Possible diamond applications	14
1.9	Motivation	15
1.10	Thesis outline	16
<b>I</b>	<b>Theory and method</b>	<b>18</b>
<b>2</b>	<b>Fundamental theory</b>	<b>19</b>
2.1	Introduction	19
2.2	The many-body problem	19
2.3	The Born-Oppenheimer approximation	21
2.4	Solution of the many-body wave function	22
2.4.1	Hartree-Fock approximation	22
2.4.2	Density functional theory	23
2.4.3	The theorems of Hohenberg and Kohn	24
2.4.4	Kohn-Sham equations	24
2.4.5	The exchange and correlation functional in DFT	26
2.5	Summary	27
<b>3</b>	<b>Method</b>	<b>29</b>
3.1	The AIMPRO software package	29
3.2	Self-consistency cycle	29
3.3	Pseudopotential approximation	30
3.4	Supercell	32
3.5	Brillouin zone sampling	33
3.6	Basis sets	35
3.7	Summary	38
<b>4</b>	<b>Derived quantities</b>	<b>40</b>
4.1	Modelling physical quantities	40
4.2	Lattice constant and bulk modulus	40
4.3	Structural optimisation	42
4.4	Electronic levels	42
4.5	Vibrational modes	46
4.6	Hyperfine parameters	48
4.7	Electrical levels	52
4.8	Binding energy	54
4.9	Diffusion barrier	58
4.10	Summary	60

<b>II Applications</b>	<b>61</b>
<b>5 Investigated defects</b>	<b>62</b>
5.1 Introduction . . . . .	62
5.2 Method . . . . .	64
<b>6 Assignment of <sup>13</sup>C hyperfine interactions in the P1-centre</b>	<b>66</b>
6.1 The P1 centre . . . . .	66
6.2 Computational method . . . . .	69
6.3 Results . . . . .	72
6.4 Summary and conclusions . . . . .	77
<b>7 N<sub>n</sub>VH<sub>m</sub>, where n + m = 1</b>	<b>79</b>
7.1 VH . . . . .	80
7.2 NV . . . . .	80
7.3 Results . . . . .	81
7.3.1 Structural analysis . . . . .	81
7.3.2 Electrical properties . . . . .	82
7.3.3 Electronic structure . . . . .	85
7.3.4 Vibrational properties . . . . .	89
7.3.5 Hyperfine interaction . . . . .	90
<b>8 N<sub>n</sub>VH<sub>m</sub>, where n + m = 2</b>	<b>96</b>
8.1 VH <sub>2</sub> . . . . .	97
8.2 NVH . . . . .	97
8.3 N <sub>2</sub> V . . . . .	97
8.4 Results . . . . .	98
8.4.1 Structural analysis . . . . .	98
8.4.2 Electrical properties . . . . .	100
8.4.3 Electronic structure . . . . .	101
8.4.4 Vibrational properties . . . . .	106
8.4.5 Hyperfine interaction . . . . .	108
<b>9 N<sub>n</sub>VH<sub>m</sub>, where n + m = 3</b>	<b>113</b>
9.1 VH <sub>3</sub> and NVH <sub>2</sub> . . . . .	114
9.2 N <sub>2</sub> VH . . . . .	114
9.3 N <sub>3</sub> V . . . . .	114
9.4 Results . . . . .	114
9.4.1 Structural analysis . . . . .	114
9.4.2 Electrical properties . . . . .	116
9.4.3 Electronic structure . . . . .	118

## Contents

---

9.4.4	Vibrational properties	123
9.4.5	Hyperfine interaction	124
<b>10</b>	<b><math>N_nVH_m</math>, where <math>n + m = 4</math></b>	<b>128</b>
10.1	$VH_4$ , $NVH_3$ and $N_2VH_2$	129
10.2	$N_3VH$	129
10.3	$N_4V$	129
10.4	Results	129
10.4.1	Structural analysis	129
10.4.2	Electrical properties	131
10.4.3	Vibrational properties	132
10.4.4	Hyperfine interaction	134
<b>11</b>	<b>Energetics</b>	<b>135</b>
11.1	Quantum tunnelling	135
11.2	Binding energies	138
11.3	$VH$	140
11.4	$NV$	142
11.5	$VH_2$	144
11.6	$NVH$	146
11.7	$N_2V$	147
11.8	$VH_3$	149
11.9	$NVH_2$	151
11.10	$N_2VH$	152
11.11	$N_3V$	156
11.12	$VH_4$	157
11.13	$NVH_3$	160
11.14	$N_2VH_2$	162
11.15	$N_3VH$	165
11.16	$N_4V$	168
<b>III</b>	<b>Summary and conclusions</b>	<b>170</b>
<b>12</b>	<b>Summary</b>	<b>171</b>
12.1	Conclusions	172
12.2	Further work	176

## Contents

---

<b>Bibliography</b>	<b>179</b>
<b>The Hohenberg and Kohn proof</b>	<b>195</b>

# Glossaries

## Glossary of mathematical notation

$a_{1,2,3}$	Unit vectors of reciprocal space.
$A$	Attempt frequency.
$\underline{A}_j$	Hyperfine tensor for the $j^{\text{th}}$ nucleus.
$A_p$	Anisotropic hyperfine coupling constant.
$A_{\parallel}$	Eigenvalue of the hyperfine tensor that aligns along the axis of the defect.
$A_{\perp}$	Eigenvalues of the hyperfine tensor that are perpendicular to the defect.
$A_{\text{RMS}}$	Calculated root-mean-square magnitude of the principal values.
$A_s$	Isotropic hyperfine coupling constant.
$A_{1,2,3}$	Principal values of the hyperfine matrices defined by $(\theta, \varphi)$ .
$B$	External magnetic field.
$B_R$	Resonant absorption occurs when the external magnetic field is at this point.
$B_0$	Variable external magnetic field.
$c$	Speed of light in a vacuum.
$c_0$	A constant for each plane wave function.
$d$	Distance from the centre point between the $G_1$ and the N site in units of $a_0$ .
$\underline{D}$	Zero field tensor.
$e$	Elementary charge.
$E$	Energy.
$E_a$	Activation energy.
$E_b$	Binding energy.
$E_c$	Conduction band minimum.

## Glossary of mathematical notation

---

$E_{\text{cut off}}$	Energy that defines the confinement of the reciprocal lattice vectors of the supercell.
$E_{\text{diff}}$	Energy difference calculated from the initial and 'new' charge density in the self consistency cycle.
$E_{\text{f}}$	Formation energy.
$E[n(\mathbf{r})]$	Ground state energy dependent on the electronic density.
$E_{\text{tot}}$	Calculated total energy of the system.
$E_{\text{v}}$	Valance band maximum.
$E_{\text{XC}}$	Exchange and correlation energy functional.
$E_{\text{XC}}^{\text{GGA}}[n(\mathbf{r})]$	Exchange and correlation energy functional due to the GGA approximation.
$E_{\text{XC}}^{\text{LDA}}[n(\mathbf{r})]$	Exchange and correlation energy functional due to the LDA approximation.
$E_0$	Equilibrium energy.
$\varepsilon_{\text{electron}}$	Total energy of the electrons.
$\varepsilon_j$	Total energy of the system $j^{\text{th}}$ state.
$\varepsilon_{\text{nucleus}}$	Total energy of the nuclei.
$\varepsilon_{\text{XC}}$	Exchange and correlation energy per particle of a homogeneous electron gas.
$f(\mathbf{k})$	A function of $\mathbf{k}$ across the first Brillouin zone.
$F[n(\mathbf{r})]$	Universal function that depends on the electronic density.
$\mathbf{g}$	Reciprocal lattice vectors of the supercell.
$\mathbf{g}_{\text{cut off}}$	Confined reciprocal lattice vectors of the supercell.
$g_{\text{e}}$	Zeeman splitting constant.
$g_{\text{N}_j}$	Is the nuclear $g$ value.
$\gamma$	A constant for each Gaussian function.
$h$	Plank constant.
$\hat{H}$	Hamiltonian operator.
$\hbar$	Reduced Planck constant.
$\mathcal{H}$	Effective spin-Hamiltonian.
$\mathcal{H}_{\text{p}}$	Anisotropic hyperfine Hamiltonian.
$I$	Nuclear spin.
$\hat{\mathbf{I}}_j$	Nuclear spin operator for the $j^{\text{th}}$ nucleus.
$I, J, K$	Integers used to define MP mesh.
$K_{\text{B}}$	Boltzmann's constant.
$K_0$	Bulk modulus.

## Glossary of mathematical notation

---

$K'_0$	Bulk modulus first derivative with respect to pressure.
$l$	Orbital angular momentum quantum number.
$m_e$	Rest mass of an electron.
$m_l$	Magnetic quantum number.
$m_p$	Rest mass of a proton.
$M_l$	Nuclei masses.
$M_{i,j}$	Masses of two different atoms.
$\mu_a$	Chemical potential of the atoms.
$\mu_B$	Bohr magneton.
$\mu_e$	Chemical potential of the electrons.
$\mu_N$	Nuclear magneton.
$\mu_0$	Magnetic permeability in a vacuum.
$n$	Number of equivalent sites.
$n_i$	Integer used to define the symmetry of the Gaussian type orbital.
$n(\mathbf{r})$	Ground state charge density as a function of electron position.
$n_0$	Energy density of a homogeneous electron gas.
$N$	A set of $N$ electron coordinates.
$\nu$	Frequency of electromagnetic radiation.
$\Omega_{\text{Brillouin zone}}$	Volume of the Brillouin zone.
$\Omega_{\text{supercell}}$	Volume of the real space supercell.
$P$	A set of $P$ nuclei coordinates.
$\underline{\mathbf{P}}_j$	Quadrupole interaction term for the $j^{\text{th}}$ nucleus.
$\phi_i$	Gaussian type orbital.
$\Psi$	Wave function.
$\Psi_i$	Wave function in the $i^{\text{th}}$ state.
$\Psi_{\text{electron}}$	Wave function as a consequence of the electrons.
$\Psi_{\text{HF}}$	Hartree-Fock wave function.
$\Psi_N(\mathbf{x}_N)$	Wave functions of a single-electrons, where $\mathbf{x}$ represents a single electron's spin state and position..
$\Psi_{\text{nucleus}}$	Wave function as a consequence of the nuclei.
$\Psi_{\text{pseudo}}$	Wave function of an atom when pseudopotentials are used.
$\Psi_{\text{total}}$	Total wave function of a system.
$\Psi^*$	Complex conjugate of the wave function.
$ \psi(0) ^2$	Spin density at the nucleus.

## Glossary of mathematical notation

---

$q$	Charge state of the modelled system.
$r$	Radius of an atom.
$r_c$	Cut-off radius.
$\mathbf{r}$	Positions of the electrons.
$R_{i,j}$	Position of two different atoms.
$\mathbf{R}$	Positions of the nuclei.
$\mathbf{R}_{\text{Bravis}}$	Bravis lattice vectors.
$S$	Electron spin.
$\hat{S}$	Effective electron spin operator.
$T$	Temperature.
$\hat{T}$	Kinetic energy of the particle operator.
$\hat{T}_{\text{electron}}$	Kinetic energy operator of the electrons.
$\hat{T}_{\text{nucleus}}$	Kinetic energy operator of the nuclei.
$\mathbf{T}$	Anisotropic hyperfine matrix.
$(\theta, \varphi)$	Direction taken as the principal value of the hyperfines matrices where $\theta$ is the angle with [001] and $\varphi$ the angle of the projection of the direction onto the (110) plane measured from [100] towards [010].
$u(\mathbf{r})$	A periodic function with the same periodicity as the lattice.
$V$	Potential.
$\hat{V}$	Potential energy of the particle operator.
$\hat{V}_{\text{electron—electron}}$	Potential energy operator associated with the electrons interacting with each other.
$\hat{V}_{\text{electron—nucleus}}$	Potential energy operator associated with the interacting electrons and nucleus.
$\hat{V}_{\text{ext}}$	Fixed external potential operator.
$\hat{V}_{\text{nucleus—nucleus}}$	Potential energy operator associated with the nuclei interacting with each other.
Vol	Total volume.
Vol <sub>0</sub>	Equilibrium volume.
$V_{\text{pseudo}}$	Potential of an atom when pseudopotentials are used.
$V(\mathbf{r}_{\text{Bravis}})$	Potential as a function of position within the Bravis lattice.
$\xi$	A correction for the periodic boundary condition.
$Y$	Modelled system.
$Z_l$	Nuclei numbers.

Symmetry of the defects are labelled using the Schoenflies notation.

**Acronyms and abbreviations**

AIMPRO	<i>Ab-Initio</i> Modelling PROgram.
ASEA	Allmänna Svenska Elektriska Aktiebolaget.
CVD	Chemical vapour deposition.
DFT	Density functional theory.
ENDOR	Electron double nuclear resonance.
EPR	Electron paramagnetic resonance.
FCC	Face-centred cubic.
FTIR	Fourier transform infrared.
GGA	Generalised gradient approximation.
GIA	Gemological Institute of America.
HF	Hartree-Fock.
HGH	Hartwigsen, Goedecker and Hutter.
HPHT	High pressure high temperature.
IR	Infrared.
LDA	Local density approximation.
LSDA	Local spin density approximation.
LVM	Local vibrational mode.
MP	Monkhorst-Pack.
NEB	Nudged elastic band.
PBE	Perdew, Burke and Ernzerhof.
PI	Photo-luminescence.
ppb	Parts per billion.
ppm	Parts per million.
Ref.	Reference.
RMS	Root-mean-square.
Sym.	Symmetry.
Trig.	Trigonal.
UV	Ultraviolet.
Vis.	Visible.
ZPL	Zero phonon line.

## Defect notation

A-centre	Two substitutional nitrogen nearest neighbours.
B-centre	Four substitutional nitrogen atoms surrounding a vacancy. $N_4V$ .
C-centre	Substitutional nitrogen defect, also known as the P1 centre in EPR.
Centre	Used interchangeably with defect, i.e. NVH centre.
Defect <sub>i</sub>	Interstitial defect.
Defect <sub>s</sub>	Substitutional defect.
GR1	Optical absorption peak labelled 'general radiation' defect. It is the $V^0$ defect.
H1	Proposed EPR label for $VH^0$ .
H2	Optical label for $N_2V^-$ .
H3	Optical label for $N_2V^0$ .
KUL2	Proposed EPR label for $V_2H^-$ .
KUL9	Proposed EPR label for $V_2H^0$ .
M2	EPR label for a di-nitrogen centre, where the second nitrogen in relation to the first is in the fourth shell of carbons.
M3	EPR label for a di-nitrogen centre, where the second nitrogen in relation to the first is in the sixth shell of carbons.
$N_nVH_m$	A set of defects containing nitrogen(s) and hydrogen(s) surrounding a single vacancy where $m$ and $n$ are positive integers and $m + n \leq 4$ .
N1	EPR label for the di-nitrogen centre in diamond (N-C-N+), similar to the P1 in structure with an additional nitrogen replacing a carbon bonded to the carbon radical. (Also termed second-shell pairs).
N2	Optical label associated with $N_3V$ .
N3	Optical label for $N_3V$ , the 'N' refers to natural line.
N4	Optical label associated with $N_3V$ .
N4	EPR label for a di-nitrogen centre, where the second nitrogen in relation to the first is in the fifth shell of carbons.
ND1	Optical absorption peak. It is the $V^-$ defect.
P1	EPR label for substitutional nitrogen also known as a C-centre.

## Defect notation

---

P2	EPR label for $N_3V^0$ , $S = 1/2$ .
V	An atom in a crystal that has been removed leaving a vacancy.
W15	Proposed EPR label for $NV^-$ .
W24	EPR label for the ionised A-centre.
W26	EPR label for $N_2V^0$ .
W7	EPR label for a di-nitrogen centre, where the second nitrogen in relation to the first is in the third shell of carbons.
WAR13	EPR label for $N_2VH^0$ .

## List of Figures

1.1	Conventional unit cell of diamond. . . . .	4
1.2	The phase diagram for carbon for varying temperatures and pressures. (Image after [12, p. 12]). . . . .	4
1.3	Atomic illustrations of the A- and B-centre, and the $N_s$ . . . . .	8
1.4	A phase diagram of carbon, highlighting areas of HPHT and CVD growth. . . . .	10
1.5	A schematic of HPHT apparatus. (Image after [31, p. 9]). . . . .	11
1.6	Hot filament CVD apparatus setup. (Image after [37]). . . . .	12
2.1	Illustration of the effect of the Kohn-Sham equations on a system of interacting electrons. . . . .	25
2.2	Summary of the theory used in AIMPRO. . . . .	28
3.1	Flow chart describing the self-consistency cycle. . . . .	30
3.2	Schematic of the Coulombic potential of an atom and the comparative pseudopotential. . . . .	31
3.3	Demonstration of periodic boundary conditions in an eight and 64 atom unit cell. . . . .	33
3.4	Fractional deviation from the lattice constant ( $a_0$ ) and time (s) as a function of the number of $k$ -points. . . . .	35
3.5	Lattice constant as a function of the number of Gaussians used to describe carbon in diamond. . . . .	37
3.6	Summary of approximations and methodologies used in AIMPRO. . . . .	39
4.1	Total energy (eV) as a function of unit cell volume ( $\text{\AA}^3$ ), with the Birch-Murnaghan equation of state fitted to the data. . . . .	41
4.2	Band structure of bulk diamond reproduced using a two atom unit cell. . . . .	43
4.3	Band structure comparison between a 54 atom cell and a 1000 atom cell. . . . .	45
4.4	Simplistic image of the process of EPR splitting. . . . .	49
4.5	Schematic of the formation energy as a function of the electron chemical potential. . . . .	54
4.6	Schematic of the binding energy of $N_2$ VH, formed by the addition of $N_2$ V to $H_i$ as a function of the electron chemical potential. . . . .	56

## List of Figures

---

4.7	Diagram of a reaction process under kinetic or thermodynamic control.	57
4.8	A minimum energy reaction pathway for a hydrogen hopping between two carbon radicals. . . . .	59
5.1	A schematic introducing the set of defects investigated, along with an atomic diagram describing their structure. . . . .	64
6.1	Atomistic model of the P1 centre. . . . .	67
6.2	A schematic to show the carbon sites in the vicinity of the P1 centre. . .	70
6.3	The RMS principal values of the hyperfine tensors for $^{14}\text{N}$ and $^{13}\text{C}$ as a function of the distance from the carbon radical. . . . .	76
7.1	Illustrations of the VH and NV defects. . . . .	79
7.2	C–H bond length as a function of charge for the VH defect. . . . .	83
7.3	Donor and acceptor levels associated with the VH and NV defects. . .	84
7.4	Band structures of the high and low spin of the $\text{VH}^0$ defect. . . . .	86
7.5	The band structures for the $\text{VH}^{-1}$ and $\text{NV}^{-1}$ defects. . . . .	87
7.6	Isosurfaces of the $a_{1\uparrow}$ states of the $\text{VH}^{-1}$ and $\text{NV}^{-1}$ , $S = 1$ defects. . .	88
7.7	$\text{VH}^+$ and the $\text{NV}^+$ defect's corresponding band structures. . . . .	89
8.1	Images of the defects where $n + m = 2$ . . . . .	96
8.2	C–H bond length as a function of charge for the $\text{VH}_2$ and the NVH defect.	99
8.3	Available donor and acceptor levels for the $\text{VH}_2$ , NVH and $\text{N}_2\text{V}$ defects.	100
8.4	Band structures for high and low spin states of the neutral defects in the $n + m = 2$ set. . . . .	103
8.5	Band structures for the negatively and positively charged defects, where $n + m = 2$ . . . . .	104
9.1	Illustration of defects, where $n + m = 3$ . . . . .	113
9.2	The $\text{VH}_3$ , NVH <sub>2</sub> and $\text{N}_2\text{VH}$ C–H bond length(s) as a function of charge.	115
9.3	The donor and acceptor levels for the $\text{VH}_3$ , NVH <sub>2</sub> , $\text{N}_2\text{VH}$ and $\text{N}_3\text{V}$ . . .	117
9.4	Band structures of the $\text{VH}_3$ and $\text{N}_3\text{V}$ defect in the neutral and negative charge states. . . . .	119
9.5	Band structures associated with the NVH <sub>2</sub> and $\text{N}_2\text{VH}$ defect in their neutral and negative charge states. . . . .	120
9.6	Band structures of the NVH <sub>2</sub> <sup>+</sup> and $\text{N}_3\text{V}^+$ defects. . . . .	121
10.1	Illustrations of the defects where $n + m = 4$ . . . . .	128
10.2	The band structures of the $\text{VH}_4^0$ and the $\text{N}_4\text{V}^0$ , $S = 0$ defects. . . . .	131
11.1	The defects highlighted have the potential for the hydrogen(s) to tunnel between carbon radical sites. . . . .	135

## List of Figures

---

11.2	The defects highlighted have been uncontentionally identified in diamond, the VH defect however has been researched but the identification is uncertain. . . . .	138
11.3	Difference in binding energies as nitrogen and hydrogen are added to the defects in the full set. . . . .	139
11.4	The binding energy ( $E_b$ ) as a function of electron chemical potential $\mu_e$ through the theoretical band gap range (valance band maximum $E_V$ to conduction band minimum $E_C$ ) for the reaction between a V and $H_i$ to form the VH centre. . . . .	141
11.5	The reaction between a V and $N_s$ to form the NV centre, further details are listed in Figure 11.4. . . . .	143
11.6	The reaction between a V and $H_2^*$ defect to form the $VH_2$ centre, further details are listed in Figure 11.4. . . . .	144
11.7	The reaction between VH and $H_i$ defect to form the $VH_2$ centre, further details are listed in Figure 11.4. . . . .	145
11.8	The reaction between a NV and $H_i$ defect to form the NVH centre, further details are listed in Figure 11.4. . . . .	146
11.9	The reaction between a VH and $N_s$ defect to form the NVH centre, further details are listed in Figure 11.4. . . . .	147
11.10	The reaction between a V and $N_2$ defect to form the $N_2V$ centre, further details are listed in Figure 11.4. . . . .	148
11.11	The reaction between a NV and $N_s$ defect to form the $N_2V$ centre, further details are listed in Figure 11.4. . . . .	149
11.12	a) The reaction between a $VH_2$ and $H_i$ defect and b) the reaction between a VH and $H_2^*$ defect, both form the $VH_3$ centre, further details are listed in Figure 11.4. . . . .	150
11.13	The reaction between a NV and $H_2^*$ defect to form the $NVH_2$ centre, further details are listed in Figure 11.4. . . . .	151
11.14	The reaction between a $VH_2$ and $N_s$ defect to form the $NVH_2$ centre, further details are listed in Figure 11.4. . . . .	152
11.15	a) The reaction between a $N_2V$ and $H_i$ defect and b) the reaction between a NVH and $N_s$ defect, both form the $N_2VH$ centre, further details are listed in Figure 11.4. . . . .	154
11.16	The reaction between a VH and $N_2$ defect to form the $N_2VH$ centre, further details are listed in Figure 11.4. . . . .	155
11.17	The reaction between a $N_2V$ and $N_s$ defect to form the $N_3V$ centre, further details are listed in Figure 11.4. . . . .	156
11.18	The reaction between a NV and $N_2$ defect to form the $N_3V$ centre, further details are listed in Figure 11.4. . . . .	157

## List of Figures

---

11.19	a) The reaction between a $VH_2$ and $H_2^*$ defect and b) the reaction between a $VH_3$ and $H_i$ defect, both form the $VH_4$ centre, further details are listed in Figure 11.4. . . . .	158
11.20	The reaction between a $VH_3$ and $N_s$ defect to form the $NVH_3$ centre, further details are listed in Figure 11.4. . . . .	160
11.21	a) The reaction between a $NVH_2$ and $H_i$ defect and b) the reaction between a $NVH$ and $H_2^*$ defect, both form the $NVH_3$ centre, further details are listed in Figure 11.4. . . . .	161
11.22	a) The reaction between a $N_2V$ and $H_2^*$ defect and b) the reaction between a $N_2VH$ and $H_i$ defect, both form the $N_2VH_2$ centre, further details are listed in Figure 11.4. . . . .	163
11.23	a) The reaction between a $NVH_2$ and $N_s$ defect and b) the reaction between a $VH_2$ and $N_2$ defect, both form the $N_2VH_2$ centre, further details are listed in Figure 11.4. . . . .	164
11.24	a) The reaction between a $N_2VH$ and $N_s$ defect and b) between a $N_3V$ and $H_i$ defect to form the $N_3VH$ defect, further details are listed in Figure 11.4. . . . .	166
11.25	The reaction between a $NVH$ and $N_2$ defect to form the $N_3VH$ centre, further details are listed in Figure 11.4. . . . .	167
11.26	a) The reaction between a $N_2V$ and $N_2$ defect and b) the reaction between a $N_3V$ and $N_s$ defect, both form the $N_4V$ centre, further details are listed in Figure 11.4. . . . .	169

## List of Tables

1.1	Select diamond properties compared to other semiconductors (adapted from [14, 15]) with an explanation of the properties included. . . . .	5
2.1	Comparison of LDA and GGA calculations of the lattice constant (Å) and the band gap energy (eV) (taken from the conduction band minimum to the valance band maximum). . . . .	27
4.1	Comparison of both the calculated bulk modulus and lattice constant with experiment, using a GGA functional. . . . .	41
6.1	Hyperfine interactions assigned to seven <sup>13</sup> C sites that are associated with the P1 centre. . . . .	68
6.2	A comparison of calculated hyperfine tensors for the <sup>14</sup> N and C <sub>1</sub> –C <sub>4</sub> systems in P1 centre. . . . .	73
6.3	Hyperfine tensors for sites that have no site-symmetry in the P1-centre. . . . .	74
6.4	Remaining calculated hyperfine tensors for carbon sites in the vicinity of the P1 centre. . . . .	75
7.1	A comparison of bond lengths and C–H stretch modes as the charge and spin state of VH varies. . . . .	90
7.2	A comparison of calculated hydrogen ( <sup>1</sup> H) and nitrogen ( <sup>14</sup> N) hyperfine tensors for the VH, V <sub>2</sub> H and NV centres where applicable. Including an image describing the site positions . . . . .	92
7.3	A comparison of calculated carbon ( <sup>13</sup> C) hyperfine tensors for the VH and NV centres. . . . .	95
8.1	A comparison of bond lengths and C–H stretch modes as the charge and spin state varies for defects in the $n + m = 2$ set. . . . .	107
8.2	<sup>1</sup> H hyperfine tensors for the VH <sub>2</sub> and NVH centres. . . . .	109
8.3	<sup>14</sup> N hyperfine tensors for the NVH and N <sub>2</sub> V centres. . . . .	111
8.4	<sup>13</sup> C hyperfine tensors for the VH <sub>2</sub> , NVH and N <sub>2</sub> V centres. . . . .	112

## List of Tables

---

9.1	A comparison of bond lengths and C–H vibrational modes as the charge and spin state varies for defects in the $n + m = 3$ set. . . . .	123
9.2	A comparison of calculated hydrogen ( $^1\text{H}$ ) and nitrogen ( $^{14}\text{N}$ ) hyperfine tensors for the $\text{VH}_3$ , $\text{NVH}_2$ , $\text{N}_2\text{VH}$ and $\text{N}_3\text{V}$ centres where applicable. .	125
9.3	A comparison of calculated carbon ( $^{13}\text{C}$ ) hyperfine tensors for the $\text{VH}_3$ , $\text{NVH}_2$ , $\text{N}_2\text{VH}$ and $\text{N}_3\text{V}$ centres. . . . .	127
10.1	The C–H bond length associated with the $m + n = 4$ set of defects. All defects are in their neutral charge state. . . . .	130
10.2	A comparison of bond lengths and C–H stretch modes for the defects in the $n + m = 4$ set. . . . .	133
11.1	A description of the energy profile associated with defects within the set that contain a single H and radical sites. . . . .	136
12.1	A summary of the donor and acceptor levels associated with defects studied in the set. . . . .	173
12.2	Summary of electronic transitions between defect states, the magnitudes are included in eV and nm for ease of comparison with experimental results that are included. . . . .	174

# Chapter 1. Introduction

*'Diamond is the most valuable, not only of precious stones, but of all things  
in this world.'*

— Roman naturalist Pliny, first century AD [1].

Diamond is certainly of value to this Thesis.

## 1.1 The history of diamond

Diamond's etymology is from the Greek word *adamas*, which translates directly as 'invincible' [2]. This is testament to our enduring attraction to the gemstone: it is considered to be beautiful, durable and indestructible [3].

First found in India in alluvial deposits around the fourth century BC, the limited supply were destined for only the wealthiest of Indian classes [1]. They were adorned by males to provide them with courage and used in religious icons [3]. But supply soon grew and trade spread this exotic rarity to Western Europe, whereby the 1400s, cutting and polishing had been developed and diamonds became fashionable jewels for the European elite [1]. The first recorded use of an engagement ring was in 1477, in the marriage of Maximillian I to Mary of Burgundy [4].

As Indian supplies began to dwindle in the early 18<sup>th</sup> century, fresh sources of diamonds emerged from the jungles of Brazil, an accidental find, discovered by gold miners as they sifted through river deposits [1]. Despite this continuous supply, political upheavals in the late 1700s lead to a decline in the market of luxury items as the distribution of wealth shifted [1].

This changed in the 1800s, affluence returned to Western Europe and the United States of America, demand broadened, and the first diamond deposits were discovered in Kimberley, South Africa in 1866 [1]. 22 years later De Beers Consolidated Mines Limited were established by Cecil Rhodes and due to the majority control of the mines in South Africa, De Beers became the world leading diamond consortium [1].

As diamond deposits became harder to extract, developments came in mining techniques, cutting and polishing, and marketing strategies [1]. All to increase efficiency in the diamond industry. De Beers success arose as it controlled demand, through orchestrated advertising campaigns, as well as supply, by controlling the majority of the market. This left the general public an insatiable desire to own a piece of luxury: a diamond.

De Beers's successful advertising campaign famously coined the saying 'a diamond is forever' [5], creating a luxurious idea that a lasting diamond engagement ring is synonymous with a loving and eternal relationship. Making diamonds once again a coveted status symbol. Emphasising the idea that the bigger the better and therefore more loving. This renowned marketing campaign successfully added to the \$62 billion a year gemstone industry [6, 7] and by 1951, eight out of ten brides in the America received a diamond engagement ring [5].

With the advent of smaller diamonds flooding the market from Russia it had the possibility of undermining the persistent marketing campaign De Beers had launched [1]. To tackle this, the campaign shifted to promote the idea of perfection regardless of size. Capitalising on the 'four Cs': cut, clarity, colour and carat, a grading system established by the Gemological Institute of America (GIA) to set the standard for evaluating diamond quality [8]. A diamond suitable for any budget could therefore be found using a combination of these attributes.

Another development in the diamond industry came when the Argyle mine in Australia was discovered in the 1980s as a source of rare pink diamonds [9]. They were marketed as *fancy* coloured diamonds, a term used to describe any diamond that was not graded as colourless and due to their rarity and desirability they fetched a

considerably higher price [9]. The mine was also a source for previously unfashionable brown diamonds destined for industrial uses but they were successfully promoted as Champagne and Cognac gemstones, adding to their value [9].

Historically, diamond's hardness was also noted since its discovery and this has been exploited in the mining industry but the material has lesser known more technologically attractive properties that have come to light more recently and since the ability to grow synthetic diamond has become available these properties are now more accessible. But this creates a new challenge in the diamond gemstone market: naturally formed diamonds need to be distinguished from synthetically grown and treated diamonds.

## 1.2 What is diamond?

Diamond is composed of carbon, the sixth element in the periodic table; it therefore has the ground state electronic configuration of  $1s^2 2s^2 2p^2$ . In the case of diamond, the valence electrons in the second 'shell' ( $2s^2 2p^2$ ) hybridise to form  $sp^3$  orbitals, creating four strong bonds tetrahedrally arranged, with a length of 1.54 Å and angle of 109.47°.

The resultant diamond structure has a face-centred cubic (FCC) crystal structure, with a basis of two atoms Figure 1.1 [11].

Although diamond is a very hard material it is less stable than graphite at room temperature and pressure. Graphite is an  $sp^2$  hybridised form of carbon and it is the most common allotrope. Under atmospheric conditions diamond is a kinetically stable form of carbon, and graphite is a thermodynamically stable form [13]. Despite this, diamonds are still found naturally as they are created under suitable conditions in the Earth's mantle and once they are brought to the surface the conversion barrier at standard conditions is very high so carbon is locked in this form [13]. Figure 1.2 indicates when diamond can form under equilibrium, for varying pressures and temperatures.

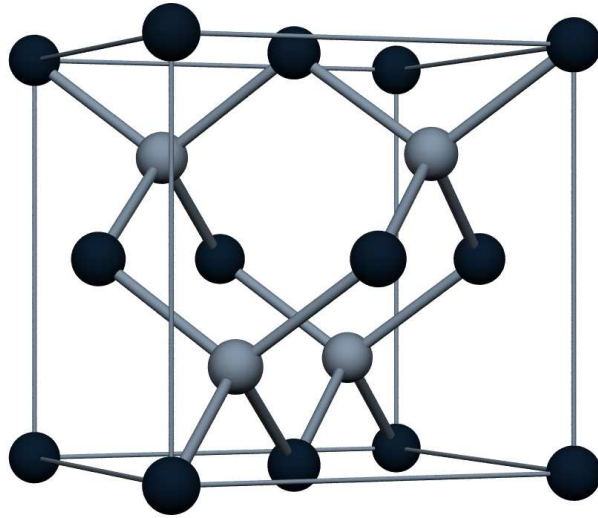


Figure 1.1: The crystal structure of diamond's conventional unit cell, where  $a_0 = 3.567 \text{ \AA}$  at 300 K [10] is the length of the cubic cell. The shaded carbon atoms represent one carbon atom in the basis, the lighter carbons represent the other carbon in the basis that is offset by  $\frac{a_0}{4}[1, 1, 1]$ . (Image after [11]).

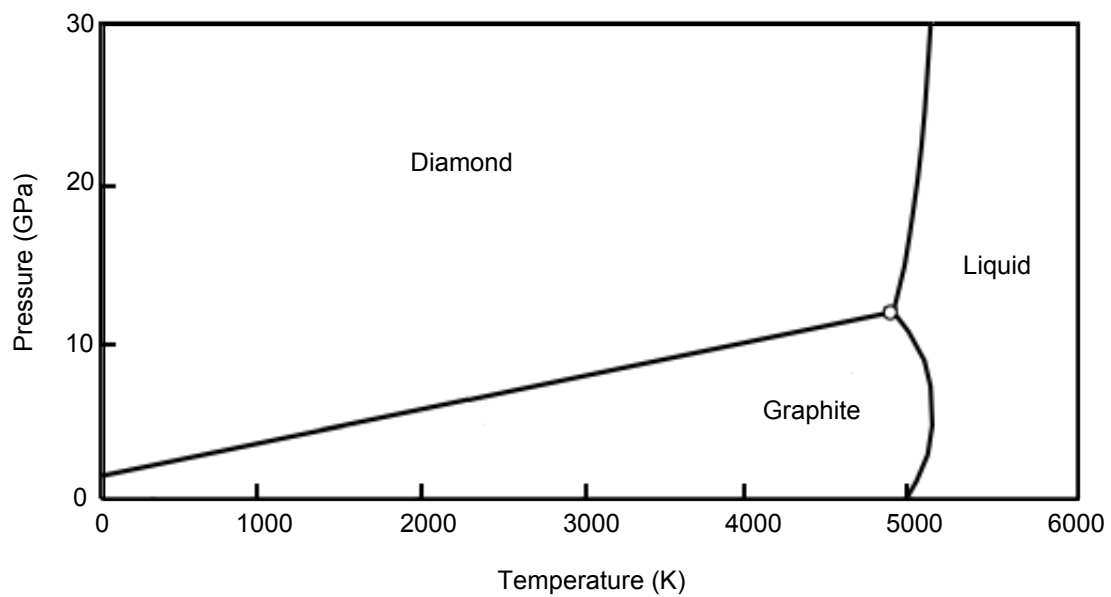


Figure 1.2: The phase diagram for carbon for varying temperatures and pressures. (Image after [12, p. 12]).

### 1.3 Why diamond?

The assembly of the atoms in perfect diamond are responsible for its superlative properties, some of which are summarised in Table 1.1.

Table 1.1: Select diamond properties compared to other semiconductors (adapted from [14, 15]) with an explanation of the properties included.

Property	Diamond	Si	4H-SiC	GaN	Notes
Hardness (Mohs scale)	10	6–7	9–9.5	6	Diamond was used to define the Mohs scale as the highest on the scale. Its hardness is a direct consequence of the strong covalent bonds.
Band-gap (eV)	5.45	1.12	3.26	3.45	There is a large separation between the bonding and anti-bonding orbitals and a very high phonon propagation frequency.
Electron mobility ( $\text{cm}^2\text{V}^{-1}\text{s}^{-1}$ )	2200	1500	1000	1250	As a result of weak phonon scattering the carrier mobilities are high.
Hole mobility ( $\text{cm}^2\text{V}^{-1}\text{s}^{-1}$ )	850	600	115	850	
Thermal conductivity ( $\text{Wcm}^{-1}\text{K}^{-1}$ )	22	1.5	4.9	1.3	It is very high as a consequence of strong covalent bonds and low phonon scattering. In diamond heat is propagated by phonons as opposed to electrons (in metals) and it is a very efficient process.

Because of the strong covalent bonding, diamond is also radiation hard and chemically inert. Diamond is also biologically stable.

These superlative properties can be modified with the addition of defects into the diamond structure as they alter the local symmetry. The addition can be beneficial but can also be detrimental to some properties.

### 1.4 Defects in diamond

Defects incorporated into the bulk of a crystal are categorised as either extended or point defects and come from *extrinsic* or *intrinsic* sources. Extended defects are classified as a defect that is dimensional (i.e. extended through the lattice). They

include dislocations: a linear defect where a lattice mismatch is created, voids: an area where several atoms are removed leaving an three dimensional gap in the crystal, and grain boundaries: seen in polycrystalline material where each grain is a single crystal and each one is orientated differently to its neighbour. If the misorientation between two grains is small then the boundary can be described as an edge dislocation. Point defects describe defects that do not extend throughout the crystal. Point defects are of interest to this Thesis and in this case they are on the scale of the unit cell described in Figure 1.1. They can be the result of the following three components:

1. Substitutional defect: A different impurity atom at a host atom site.
2. Interstitial: An impurity atom *not* at an atom site.
3. Vacancy: Removal of a host atom from an atom site.

Defects in diamond may be introduced into the lattice during growth of the diamond they may be intentionally doped during synthetic growth or they can also be accidentally introduced through the process. Both natural and synthetic diamonds may also undergo radiation and heat treatments or a combination post-growth to alter the form of the defects in the material.

Point defects with concentrations as low as parts per billion (ppb) may significantly affect the properties of diamonds. Some properties like the colour can be visibly detected by incorporation of point defects even at low concentrations and some colours are more sought after in the gemstone market than others. Specific elements or defects are linked to specific colourations. For example the inclusion of nitrogen can result in *fancy* coloured canary yellow diamonds. Rare natural blue diamonds are the result of the inclusion of boron. And vacancy clusters and plastic deformation can lead to a less desirable brown colour [16].

Nitrogen, the seventh element in the periodic table, is the most common defect in diamond due to its comparable size to carbon, natural abundance and accessibility

during growth; it therefore forms the basis of the diamond classification discussed in the next Section [17, 18].

## 1.5 Classification

As well as classifying the types of defects in diamond, diamond itself is classified into categories based on the impurities or lack thereof. By examining infrared (IR) absorption spectra Robertson *et. al.* in 1934 realised that diamonds can be separated into two groups [17]. Those that include a set of IR absorption peaks, labelled Type I and those that do not, labelled Type II. It was later realised that these peaks were associated with the incorporation of nitrogen within the diamond with Type I diamonds containing  $>1$ – $2$  parts per million (ppm) of nitrogen and Type II containing less than that. The labels are still in use today but further subcategories have been added and a breakdown of the labels are given below [18].

1. **Type I diamond:** These make up approximately 98% of natural diamonds. They contain relatively large amounts of nitrogen ( $>1$ – $2$  ppm and up to  $\sim 1000$  ppm). Varying gradients of yellow colouring are produced depending on the concentration of the nitrogen.
  - **Type Ia diamond:** Contains nitrogen in an aggregated or clustered form; depending on the form of aggregation leads to further specification.
    - **Type IaA diamond:** Contains nitrogen in A-centre form (Figure 1.3a) [18].
    - **Type IaB diamond:** Contains nitrogen in B-centre form (Figure 1.3b) [19,20].
    - **Type IaAB diamond:** Some diamonds contain a mixture of both A- and B-centres and their label reflects this.
  - **Type Ib diamond:** Contains nitrogen as isolated impurities which are sometimes labelled as C-centres or the P1 centre. (Figure 1.3c). Natural diamonds contains less than 0.1% of this type.

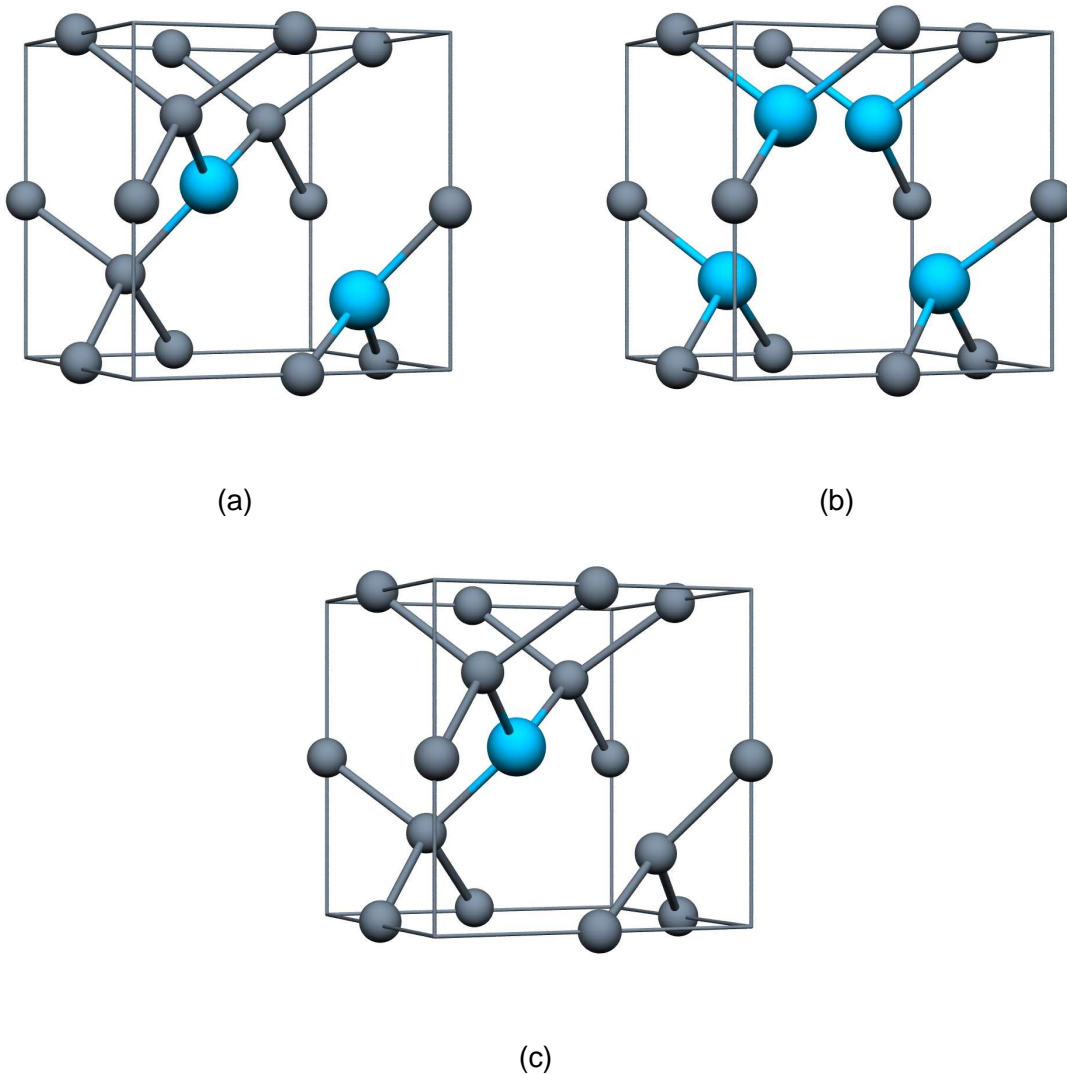


Figure 1.3: The nitrogen atoms are light blue and slightly larger, the carbon atoms are smaller grey atoms. (a) is the A-centre which is two substitutional nitrogen nearest neighbours, (b) is the B-centre which is four substitutional nitrogen atoms surrounding a vacancy and (c) is a single substitutional nitrogen.

Nitrogen can also aggregate in the form of a three atoms adjacent to a vacancy, this is an optical centre labelled N3; although it is not part of the classification system it does affect the colour of the diamond [21].

2. **Type II diamond:** Contains nitrogen below detectable concentrations by IR

absorption (<1–2 ppm) [22].

- **Type IIa diamond:** Contains neither nitrogen nor boron defects. They have enhanced thermal and optical properties as they are relatively free from defects; they are generally colourless.
- **Type IIb diamond:** Contains only single substitutional boron [23]. As boron is the fifth element in the periodic table it has one fewer electron than carbon. It therefore can act as an acceptor in diamond to produce p-type conductors, with a defect state in the 0.37 eV above the valence band top [24]. The addition of boron to the diamond gives the diamond a blue/grey colouring. Depending on the doping concentration of the boron diamond can become metallic [25].

Different growth conditions of diamond and/or treatments leads to a different ‘fingerprint’ of defects; understanding the processes and environments of growth or treatments is essential to the analysis of the formation of defects.

## 1.6 Synthesis

Natural diamonds are considered to be the most valuable to the gemstone industry so it is therefore important to be able to distinguish between different them and synthetically grown and/or treated diamonds.

Natural diamonds are formed in the Earth’s upper mantle at depths greater than 150 km over a period of millions of years [26]. The high temperature and pressure forms diamond which is the most stable form of carbon under these conditions. The environment slowly crystallises carbonaceous deposits into single crystal diamonds which are eventually brought to the surface in volcanic eruptions.

Contrary to the media, high quality synthetic diamonds can be realised and because of their commercial value as gemstones attempts to grow diamonds started in the 1800s. Currently there are two main procedures that are used; high pressure and high temperature (HPHT) synthesis and chemical vapour deposition (CVD). They are

discussed in the following Sections and both methods of growth are indicated on the phase diagram in Figure 1.4.

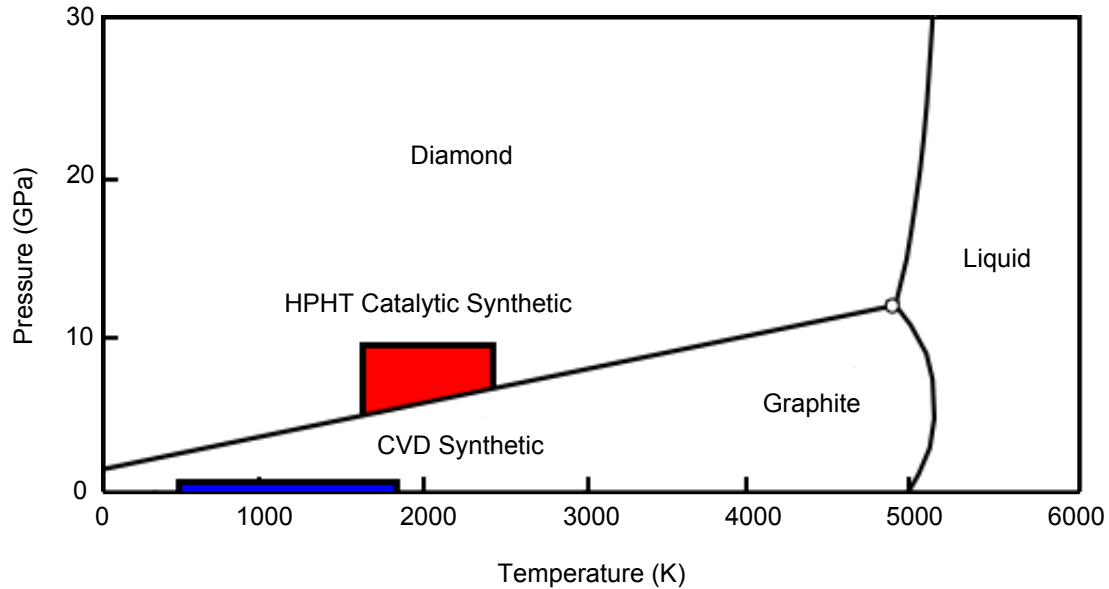


Figure 1.4: A phase diagram of carbon indicating the areas where HPHT catalytic synthesis occurs (red block near the centre) and CVD occurs (blue rectangle at low pressure). Note that the CVD is a non-equilibrium process. (Image after [12, p. 12]).

### 1.6.1 High pressure high temperature

HPHT method was pioneered by General Electric [27] in 1955 and ASEA (Allmänna Svenska Elektriska Aktiebolaget) [28] and Diamond Research Laboratory [29] in 1958. The process attempts to mimic the conditions in the Earth's mantle. It uses pressures of  $\sim 5$  GPa, a temperature of  $\sim 2000^\circ\text{C}$  and a metal solvent catalyst generally nickel or cobalt to convert graphite into diamond [30]. The choice of temperature, pressure and catalyst may be varied. The metal solvent acts to lower the temperature needed [30] and it stabilises the molten carbon as the mix rains down through a decreasing temperature gradient onto a diamond seed, where the carbon can condense and grow more diamond around the seed [10]. Figure 1.5 is an illustration of a typical setup used.

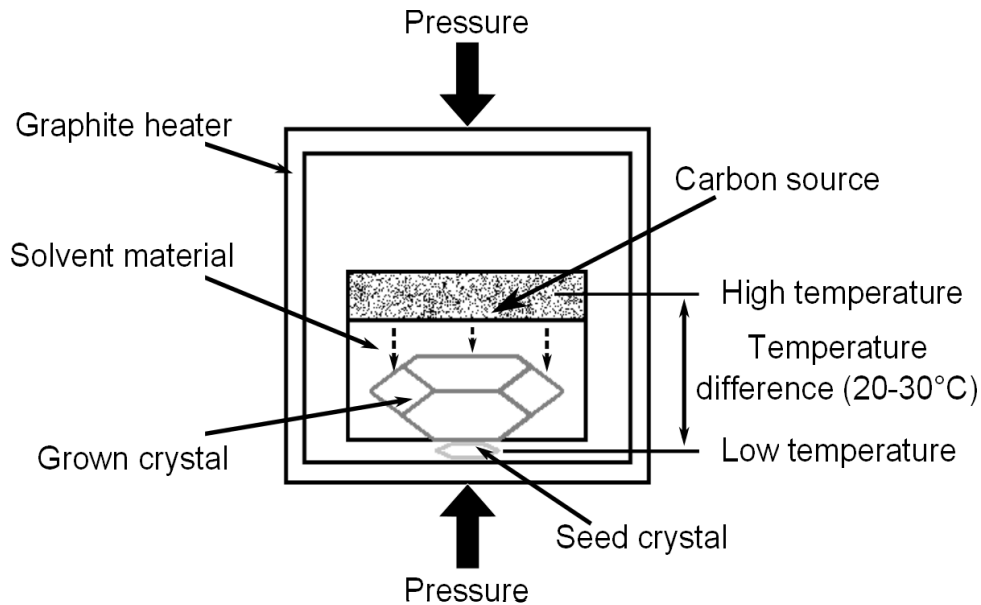


Figure 1.5: A schematic of HPHT apparatus. (Image after [31, p. 9]).

### 1.6.2 Chemical vapour deposition

Eversole and Kenmore first filed for a patent for this growth method in 1958 [32, 33]. CVD differs from HPHT as it is a non-equilibrium growth process from an activated gas-phase that is grown at low temperatures (800–1000°C at the substrate). Under these conditions the kinetic product is formed as opposed to the thermodynamical product in HPHT [34]. The source gas usually contains hydrogen ( $H_2$ ) and methane ( $CH_4$ ). The methane is the source of carbon and the hydrogen is used to prevent non- $sp^3$  bonded carbon forming around the substrate [34]. Microwaves [35] or a hot filament can be used to create a plasma that decomposes the source gases and creates the correct environment for diamond to be formed, a hot filament though is prone to incorporate defects [36]. Figure 1.6 is a schematic of a typical experimental setup of hot filament CVD.

CVD can produce very pure diamond but by controlling the growth temperature and source gases, tailored defects may be incorporated. A choice of substrate can also control the type of crystal produced, from single crystal, when diamond is the

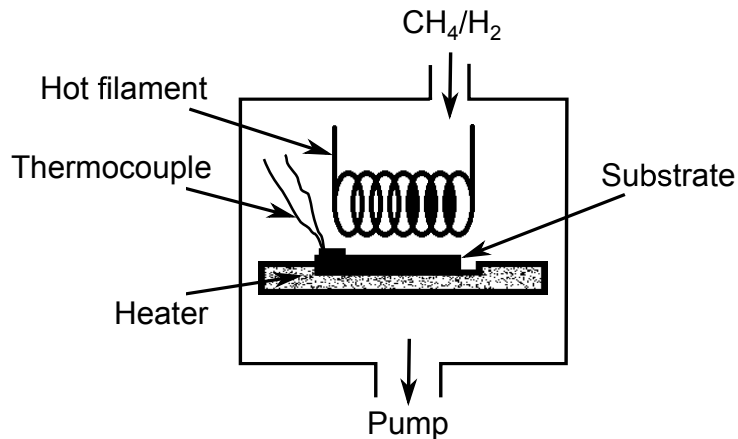


Figure 1.6: Hot filament CVD apparatus setup. (Image after [37]).

substrate to polycrystalline when the substrate is made from an alternative like silicon or tungsten.

Other defects can be introduced such as nitrogen, which is found to increase growth rates [38, 39], however this produces a brown colouration due to the increased incorporation of vacancies [40]. Silicon which is from the silica windows used in the growth environment may also be incorporated [38, 41]. CVD can produce both bulk and thin-film diamond.

## 1.7 Treatments

A combination of both or either heat and irradiation treatments can have a dramatic impact on the defects in diamond, consequently changing the colour of the diamonds and therefore their value.

### 1.7.1 Heat treatments

The process of applying heat to a diamond provides energy to defect structures; if this is sufficiently high it can cause defects to migrate through the lattice, aggregate into more stable products or dissociate. Aggregation is seen in natural diamonds as over time heat and pressure from the surrounding environment results in forming diamonds

with predominantly aggregated forms of nitrogen.

This process can be replicated and during the process of HPHT annealing it was found to turn natural brown diamonds that are less desirable in the gemstone market into near-colourless diamonds [42]. Although to the naked eye they look deceptively indistinguishable from naturally colourless diamonds it is possible to distinguish between them [43].

Heat treatments can also be applied to synthetic CVD diamonds and this results in a colour change from brown to near-colourless [44] although the origin of the brown colour is thought not to be the same in natural diamonds [45].

If the temperature applied is lower than annealing temperatures, charge transfer between defects may occur. Charge transfer processes may be temporary and reversible but may result in a defect changing from being visible in electron paramagnetic spectroscopy (Section 4.6) to not and vice versa. Thermochromism may also occur when low temperatures ( $\sim 150^{\circ}\text{C}$ ) are applied [46]. This property of a colour change with the application of heat is seen in chameleon diamonds which are amongst the rarest of gem diamonds [46]. The colour change is due to a defect containing hydrogen and nitrogen [46]; a possible defect that has been attributed to this colour change is the a hydrogenated substitutional nitrogen pair [47]. This defect in its metastable neutral charge state absorbs in the 600 nm–near-IR range, therefore contributing to the colour. But when it becomes negatively charged, the structure changes and it absorbs at a higher energy, therefore lending the diamond a different colour [47].

### **1.7.2 Irradiation treatments**

By bombarding diamond with radiation of enough energy it has the potential to displace the carbon atoms from a regular lattice site; this in turn creates vacancies and interstitials. Irradiating diamonds creates the GR1 (general radiation) defect. This is the  $V^0$  defect and it is responsible for a blue/green colour seen in diamonds as it adsorbs at 741 and 744 nm [48].

By using a combination of treatments heat can aggregate defects and newly created vacancies and impurities can act as a catalyst to speed the process of aggregation further once heat is applied again. Pink diamonds can be produced via a process of HPHT annealing, subsequent electron irradiation and then further annealing [49]. A tell-tale sign of heat treatments that have 'gone too far' are vivid *fancy* colours that are too bright and look unnatural.

### 1.8 Possible diamond applications

Now that high quality synthetic diamond can be realised with the potential to control impurities, the superlative properties of diamond can be exploited beyond the gemstone market and diamond can be used in technical applications, some of which are listed below:

- **Coatings and abrasives:** Historically diamond was used to cut and polish other hard materials as mentioned above (Section 1.1) and we still take advantage of diamonds hardness and wear resistance to this day, using diamond as an abrasive and also as coatings for drill bits and cutting tools.
- **Optical windows:** Due to its wide band gap and high refractive index of 2.417, diamond can be used as an optical window [50] as it remains transparent over a broad range (227 nm–2.5  $\mu\text{m}$  [48]).
- **Biological applications:** As diamond is chemically and biologically inert it has the potential to be used in medical applications such as drug transport, long lasting contact lenses and also as artificial joints.
- **Radiation detector:** Due to its rigid structure diamond is radiation hard. Making it suitable for harsh environments like outer space and also in the large hadron collider at CERN [51].
- **Magnetometry and nanoscale nuclear magnetic resonance:** Can be made

possible by taking advantage of the properties produced by the nitrogen-vacancy centre [52, 53].

- **Semiconductor:** As seen in Table 1.1, it out ranks common semiconductor materials like silicon making it a promising candidate for high power and frequency applications. But this is problematic as n-type diamond is difficult to manufacture.

Although boron acts as an acceptor in diamond creating p-type diamond and nitrogen acts as a donor because they have one less and one more electron than carbon respectively. The donor level produced by the introduction of nitrogen is too deep (1.7 eV below the bottom of the conduction band [54]) to be useful in technological applications. Possible donors such as those containing phosphorus do produce n-type diamond but the donor level at 0.6 eV is still relatively deep.

### 1.9 Motivation

The principal aim is to help identify defects by comparing density functional theory calculations with experimental evidence. To use this combined information to predict defects available in different starting materials and see how they could aggregate and change due to the applications of subsequent treatments.

The motivation of this work can be separated in to three sections:

1. It is necessary to track changes and identify the starting material to protect consumer confidence in the natural diamond gemstone market and to therefore accurately determine the value of the diamond.
2. Modelling the defects in diamond may also identify new defects that could be taken advantage of in technical applications like the famed nitrogen-vacancy centre.
3. If diamond is to be used in extreme environments, understanding how defects in diamond change under radiation exposure and heat is imperative to understand

how this affects defects within the diamond.

### 1.10 Thesis outline

A glossary of mathematical notation and a list of acronyms and abbreviations are included in the preamble to aid clarification of terms used. A description of defect notation is also included as notation is not universally used in the diamond community and the labels are not always intuitive or meaningful.

- **Chapter 1:** An introduction into diamond, starting with its history, properties, growth, treatments and applications.

**Part I:** Is broken down into three Chapters. Comprising of the fundamental theory, method and derived quantities.

- **Chapter 2:** The fundamental theory Chapter introduces the quantum mechanical problem that needs to be solved and the approximations used to do so.
- **Chapter 3:** Introduces the AIMPRO software package and the approximations and methods used.
- **Chapter 4:** The methods used to calculate specific properties.

**Part II:** Applications.

- **Chapter 5:** An introduction into the defects investigated, explaining the notation used and justifying how the following Chapters within the applications part are broken down. The method used for the following Chapters is described. In the case of Chapter 6 an alternative method was used which is discussed in the relevant Chapter. For the  $N_nVH_m$  set, the following were analysed: the structure, the electronic levels, the electrical levels, the hyperfine interactions and the vibrational modes.
- **Chapter 6:** A detailed look at the hyperfine interaction of the simplest nitrogen containing defect: the substitutional nitrogen.

- **Chapter 7:**  $N_n V H_m$ , where  $n + m = 1$ .
- **Chapter 8:**  $N_n V H_m$ , where  $n + m = 2$ .
- **Chapter 9:**  $N_n V H_m$ , where  $n + m = 3$ .
- **Chapter 10:**  $N_n V H_m$ , where  $n + m = 4$ .
- **Chapter 11:** A Chapter comparing the thermal stability of the defects previously mentioned, as well as additional defects.

**Part III:** Conclusions.

- **Chapter 12:** A summary of results presented in this Thesis and a comparison between defect sets as well as suggestions for possible extensions to this work.
- **References**
- **Appendix 12.2:** The Hohenberg and Kohn proof.

# **Part I**

## **Theory and method**

## Chapter 2. Fundamental theory

*'If you think you understand quantum mechanics, you don't understand quantum mechanics.'*

— Commonly attributed to Richard Feynman.

### 2.1 Introduction

To investigate complex atomic interactions and to determine the structure of an assembly of atoms density functional theory (DFT) is used. DFT uses a quantum mechanical approach as opposed to a classical method as the experimental observables that this Thesis models depend on the movement of the atoms and electrons: the problem is therefore a quantum mechanical one. These particles obey quantum mechanics and can not be modelled accurately using simplified methods that only consider classical interactions. This Chapter discusses the underpinning theory used in DFT.

### 2.2 The many-body problem

In quantum mechanics, the solution to time-independent Schrödinger equation [55] describes a system of interacting nuclei and electrons. It is the fundamental task behind DFT to solve this equation (Equation 2.1).

In general, the time-independent Schrödinger equation can be expressed as an

Eigenvalue problem,

$$\hat{H}\Psi_i = \varepsilon_i\Psi_i, \quad (2.1)$$

where  $\hat{H}$  is the Hamiltonian operator,  $\Psi_i$  is the wave function and  $\varepsilon_i$  is the total energy of the system in the  $i^{\text{th}}$  state.

The Hamiltonian operator for a single particle can be expressed as

$$\hat{H} = \hat{T} + \hat{V}, \quad (2.2)$$

where  $\hat{T}$  is the kinetic energy of the particle and  $\hat{V}$  is the potential energy of the particle.

More complex systems that are of interest to this Thesis contain numerous interacting particles and is therefore a *many-body problem*. In a many-body system the wave function ( $\Psi$ ) will depend on the position of the electrons ( $\mathbf{r}$ ) and nuclei ( $\mathbf{R}$ ); the many-body Hamiltonian operator is the kinetic energy ( $\hat{T}$ ) and the potential energy ( $\hat{V}$ ) of the interacting electrons and the nuclei which can be described below,

$$\hat{H} = \hat{T}_{\text{electron}} + \hat{T}_{\text{nucleus}} + \hat{V}_{\text{electron-nucleus}} + \hat{V}_{\text{nucleus-nucleus}} + \hat{V}_{\text{electron-electron}}. \quad (2.3)$$

By expanding Equation 2.3, it becomes:

$$\hat{H} = \underbrace{-\sum_{i=1}^N \frac{\hbar^2}{2m_e} \nabla_i^2}_{\hat{T}_{\text{electron}}} - \underbrace{\sum_{l=1}^P \frac{\hbar^2}{2M_l} \nabla_l^2}_{\hat{T}_{\text{nucleus}}} - \underbrace{e^2 \sum_{i=1}^N \sum_{l=1}^P \frac{Z_l}{|\mathbf{R}_l - \mathbf{r}_i|}}_{\hat{V}_{\text{electron-nucleus}}} + \underbrace{\frac{e^2}{2} \sum_{l=1}^P \sum_{j \neq l}^P \frac{Z_l Z_j}{|\mathbf{R}_l - \mathbf{R}_j|}}_{\hat{V}_{\text{nucleus-nucleus}}} + \underbrace{\frac{e^2}{2} \sum_{i=1}^N \sum_{j \neq i}^N \frac{1}{|\mathbf{r}_i - \mathbf{r}_j|}}_{\hat{V}_{\text{electron-electron}}}. \quad (2.4)$$

$\mathbf{r} = \{\mathbf{r}_i, i = 1, \dots, N\}$  is a set of  $N$  electronic coordinates, and  $\mathbf{R} = \{\mathbf{R}_l, l = 1, \dots, P\}$  is a set of  $P$  nuclei coordinates.  $\hbar$  is the reduced Planck constant,  $m_e$  and  $e$  is the rest mass and charge of an electron, respectively and  $M_l$  and  $Z_l$  are the nuclei masses and numbers respectively.

The many-body Schrödinger equation described above is complicated, it is completely parameter free but it does not have an analytical solution when  $N + P > 3$ . This necessitates a series of approximations to make progress.

### 2.3 The Born-Oppenheimer approximation

An approximation to tackle the complexity of the many-body Schrödinger equation is the Born-Oppenheimer approximation [56]. The approximation effectively simplifies the motion of a many-body system by separating the wave function ( $\Psi_{\text{total}}$ ) into the nuclear ( $\Psi_{\text{nucleus}}$ ) and electronic ( $\Psi_{\text{electron}}$ ) contributions. The total wave function can therefore be described as,

$$\Psi_{\text{total}} = \Psi_{\text{nucleus}} \Psi_{\text{electron}}. \quad (2.5)$$

This is possible to do as the mass of the nucleus is *much* greater than the mass of an electron and the motion of the nucleus and electron can be decoupled.

The many-body Schrödinger equation (Equation 2.1) can therefore be split accordingly, into its electronic and nuclear parts:

$$[\hat{T}_{\text{electron}} + \hat{V}_{\text{ext}} + \hat{V}_{\text{electron-electron}}] \Psi_{\text{electron}} = \epsilon_{\text{electron}} \Psi_{\text{electron}}, \quad (2.6)$$

and

$$\hat{H}_{\text{nucleus}} \Psi_{\text{nuclear}} = \epsilon_{\text{nucleus}} \Psi_{\text{nuclear}}, \quad (2.7)$$

where the Coulomb potential ( $\hat{V}_{\text{electron-nucleus}}$ ) is treated as a *fixed external potential* of the nuclei ( $\hat{V}_{\text{ext}}(R_i)$ ). These simplified Schrödinger equations that include the many-body Hamiltonian and wave function still cannot be solved exactly because of the electron–electron Coulombic interaction term ( $\hat{V}_{\text{electron-electron}}$ ): The Schrödinger equation can not be split further into one-electron equations as their movement is not independent of each other.

Additionally it is worth noting that the Born-Oppenheimer approximation (Equation 2.5), fails for systems that are subject to the Jahn-Teller effect, (a geometrical

distortion to break the degeneracy of the electronic ground state to lower the overall energy of the system), this occurs when degenerate electronic modes couple with degenerate nuclear states. Such systems are described as non-adiabatic as there is correlation between the electron and nucleus, and therefore the motion can no longer be separated.

## 2.4 Solution of the many-body wave function

It is not advisable to neglect  $\hat{V}_{\text{electron-electron}}$  in its entirety but to include it requires further understanding of the term. The electron-electron interaction can be described in two parts:

1. **Exchange interaction:** a quantum mechanical term that reflects the anti-symmetry of the wave function with respect to the exchange of two electrons, i.e. the wave function changes sign when two electrons are exchanged.
2. **Correlation interaction:** an affect of one electron's electrostatic potential on the other electron's position.

In order to continue, two principal methods have attempted to account for this interaction: Hartree-Fock (HF) and density functional theory (DFT). These methods are discussed in the following Sections.

### 2.4.1 Hartree-Fock approximation

The many-body wave function in the case of the HF method is replaced with a simpler wave function that enables the Schrödinger equation to be solved numerically.

The fundamental variable of the HF approximation is an anti-symmetrised many-electron wave function ( $\Psi_{\text{HF}}$ ). This is a requirement of the Pauli exclusion principle that states that two fermions (for example electrons) can not occupy the same quantum

state. The anti-symmetrised many-electron wave function is:

$$\Psi_{\text{HF}}(\mathbf{x}_1, \mathbf{x}_2, \dots, \mathbf{x}_N) = \frac{1}{\sqrt{N!}} \begin{vmatrix} \Psi_1(\mathbf{x}_1) & \dots & \Psi_1(\mathbf{x}_N) \\ \vdots & \ddots & \vdots \\ \Psi_N(\mathbf{x}_1) & \dots & \Psi_N(\mathbf{x}_N) \end{vmatrix}. \quad (2.8)$$

This is a Slater determinant of single-electron wave functions  $\Psi_N(\mathbf{x}_N)$ , where  $\mathbf{x}$  represents a single electron's spin state and position, i.e. an *orbital*. A consequence of the Slater determinant is that the electrons are indistinguishable from each other: every electron is associated with every orbital. This is consistent with the rules of quantum mechanics [57].

The HF approximation is a type of Mean Field Approximation as the effects of the other electrons on the wave function are taken into account as an average (i.e. the mean). Each electron feels an effective potential caused by the attraction to the nucleus and the other electrons; the electrons are considered to be 'smeared out' and 'static': the correlation interaction is an average effect [58]. To solve this numerically an iterative process is commonly used.

HF provides a reasonable model of atoms and simple molecules, it includes exchange exactly but correlation is included as an averaging effect. HF is computationally demanding and in practice this method has been superseded by DFT.

#### **2.4.2 Density functional theory**

DFT is a quantum mechanical method used to successfully describe the ground state properties of many-body systems. DFT is a versatile approach and in principle can be used to study a variety of materials of any level of dimensionality. DFT avoids the use of the all-electron wave function and instead uses the electronic charge density as the fundamental variable.

### 2.4.3 The theorems of Hohenberg and Kohn

The theorems of Hohenberg and Kohn form the mathematical basis of DFT [59].

The first Hohenberg-Kohn theorem attempts to solve the Hamiltonian and it states that:

*The ground state electron density uniquely determines the external potential.*

This means that two systems with the same ground state charge density  $n(\mathbf{r})$ , will have the same external potential unless they differ by a trivial additive constant. This can be proved by *reductio ad absurdum* (Appendix 12.2).

The second Hohenberg-Kohn theorem states that:

*The functional ( $F[n(\mathbf{r})]$ ) that determines the ground state energy ( $E[n(\mathbf{r})]$ ) is the same for all electronic structure problems which does not depend explicitly on the external potential only on the electronic density.*

$$E[n(\mathbf{r})] = F[n(\mathbf{r})] + \int n(\mathbf{r}) \hat{V}_{\text{ext}}(\mathbf{r}) d^3\mathbf{r}, \quad (2.9)$$

where  $F[n(\mathbf{r})]$  is a universal functional. It is a so called universal function as it does not depend on the external potential explicitly but on the electronic density, which has the formula:

$$F[n(\mathbf{r})] = \int \Psi^* (\hat{T} + \hat{V}) \Psi d^3\mathbf{r}. \quad (2.10)$$

A problem arises though, as the functional  $F[n(\mathbf{r})]$  is unknown, and for any practical system, its solution is a significant challenge; Kohn and Sham [60] resolved this.

### 2.4.4 Kohn-Sham equations

The explicit form of  $F[n(\mathbf{r})]$  in Equation 2.9 and the correct ground state density are unknown. The Kohn-Sham method [60] attempts to find an approximation to  $F[n(\mathbf{r})]$ . The approximation is a sum of component energies that reproduces  $F[n(\mathbf{r})]$ . Each component energy has a physical origin but approximations are needed for some components that are difficult to evaluate.

The Kohn-Sham approach states that:

A system of interacting particles is replaced with non-interacting electrons that sum to the same charge density ( $n(\mathbf{r})$ ).

This is illustrated in Figure 2.1.

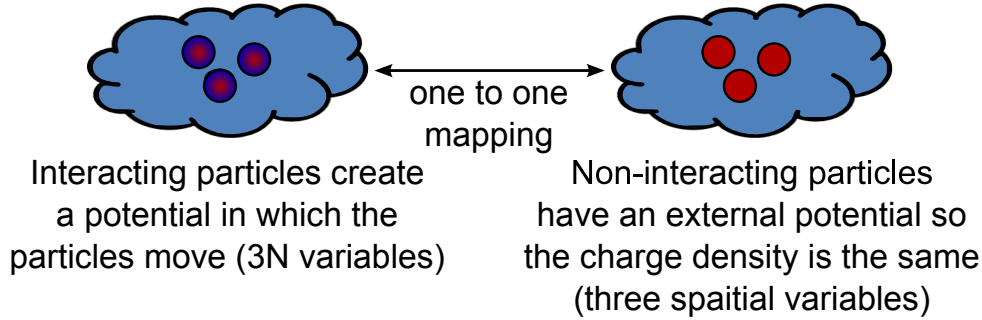


Figure 2.1: Illustration of the effect of the Kohn-Sham equations on a system of interacting electrons.

For a given system, when the energy is minimised and the number of electrons remains constant, using the approach above results in a set of one-electron Kohn-Sham equations,

$$\left[ \frac{-1}{2} \nabla^2 - \sum_{\alpha} \frac{Z_{\alpha}}{|\mathbf{r} - \mathbf{R}_{\alpha}|} + \int \frac{n(\mathbf{r}_2)}{|\mathbf{r}_1 - \mathbf{r}_2|} d\mathbf{r}_2 + \frac{\partial E_{xc}[n(\mathbf{r})]}{\partial n(\mathbf{r})} \right] \psi_{KS}(\mathbf{r}) = \epsilon_{KS} \psi_{KS}(\mathbf{r}) \quad (2.11)$$

and the electronic density is found by summing the density over all the occupied states:

$$n(\mathbf{r}) = \sum_{KS=1}^N |\psi_{KS}(\mathbf{r})|^2. \quad (2.12)$$

The Eigenvalues and Eigenfunctions of Equation 2.11 which are the Kohn-Sham states are often quoted as one-electron energies and wave functions [61]. To calculate the Kohn-Sham states which can be interpreted as a band structure, an iterative process (Section 3.2) is needed as both Equations 2.11 and 2.12 are dependent on the unknown charge density.

The Kohn-Sham Hamiltonian described in square brackets in Equation 2.11 includes the sum of the kinetic energy of the electrons, the external potential, the

Hartree energy due to the electrostatic electron–electron interaction and the exchange and correlation term. The final term is the only unknown that combines the remaining quantum effects. If the exchange and correlation functional was known, the Kohn-Sham Equations would be exact. Approximate forms of the exchange and correlation functional are described in Section 2.4.5.

### 2.4.5 The exchange and correlation functional in DFT

The exchange and correlation energy functional ( $E_{XC}$ ) has many approximation forms:

1. Non-empirical approximations are defined from results of first principles calculations.
2. Empirical and semi-empirical approximations use some experimental results as a basis.

The simplest approximation used in DFT is called the local density approximation (LDA). Essentially LDA replaces the exact  $E_{XC}$  with the energy density of a homogeneous electron gas that has the same electron density,  $n_0 = n(\mathbf{r})$ . For a spin-unpolarised system  $E_{XC}^{LDA}$  is as follows:

$$E_{XC}^{LDA}[n(\mathbf{r})] = \int n(\mathbf{r})\epsilon_{XC}[n(\mathbf{r})]d\mathbf{r}, \quad (2.13)$$

where  $n(\mathbf{r})$  is the electron density and  $\epsilon_{XC}$  is the exchange and correlation energy per particle of a homogeneous electron gas of charge density  $n(\mathbf{r})$ . LDA can be modified to include the effects of spin in an approximation called local spin density approximation (LSDA), or to account for the magnitude and gradient of the charge density in an approximation termed generalised gradient approximation (GGA). Mathematically GGA can be written as,

$$E_{XC}^{GGA}[n(\mathbf{r})] = \int n(\mathbf{r})\epsilon_{XC}[n(\mathbf{r})]\nabla n(\mathbf{r})d\mathbf{r}. \quad (2.14)$$

LDA and GGA approximations produce similar results for observables in diamond; LDA is known to underestimate bond lengths and GGA is known to overestimate them. A further summary of some diamond parameters are provided in Table 2.1.

Table 2.1: Comparison of LDA and GGA calculations of the lattice constant ( $\text{\AA}$ ) and the band gap energy (eV) (taken from the conduction band minimum to the valence band maximum).

Method	Lattice constant ( $\text{\AA}$ )	Band gap energy (eV)
LDA	3.53	4.22
GGA	3.57	4.15

The results presented in this Thesis use the Perdew, Burke and Ernzerhof (PBE) formulation [62] of the GGA approximation.

## 2.5 Summary

The theoretical framework that attempts to solve the Schrödinger equation has been discussed above and is summarised in Figure 2.2. Converting these mathematical principles into a usable computer program requires further approximations which are implemented in the AIMPRO code. The details of which are discussed in the following Chapter.

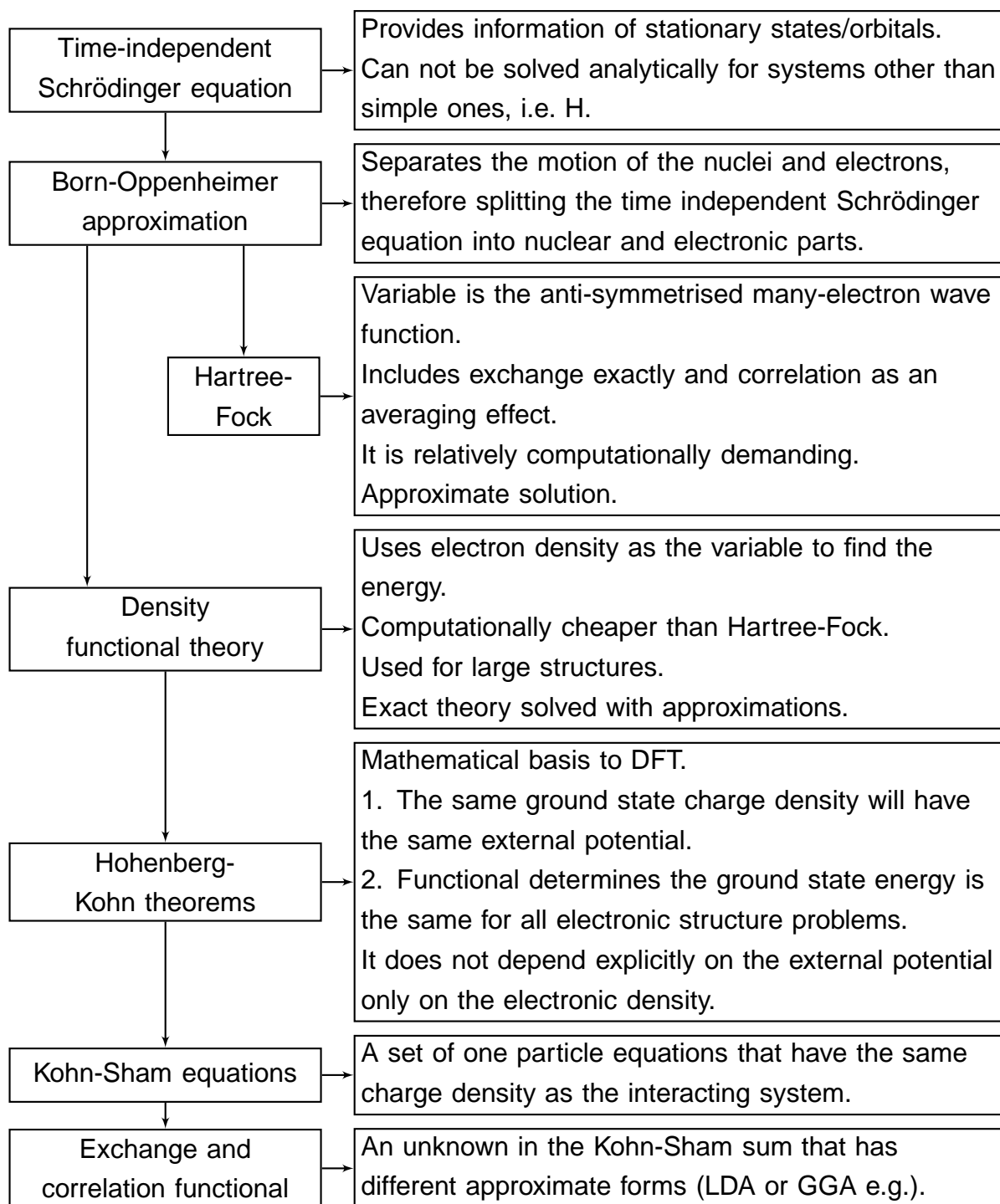


Figure 2.2: Summary of the theory used in AIMPRO.

## Chapter 3. Method

### 3.1 The AIMPRO software package

The fundamental methodologies that underpin DFT have previously been discussed but more approximations and methodologies are needed to create a usable code. In this case, DFT is implemented in AIMPRO: a software package that was developed by Briddon and Jones [63, 64]. AIMPRO stands for *Ab Initio* Modelling PROgram and the choices of parameters and algorithms used in the package although not specific to it are described in this Chapter.

### 3.2 Self-consistency cycle

In a system of non-interacting particles, the particles experience a potential; this potential can be determined if the charge density is known. The charge density can also be expressed as a sum of the squares of the Kohn-Sham functions, summed over the filled bands.

AIMPRO needs to solve the Kohn-Sham Equations described in Section 2.4.4; to do so it uses a self-consistency cycle (Figure 3.1) which is an iterative procedure that constructs an effective external potential. The process starts from an initial value of the charge density, (a value taken from the density of a previously optimised structure or from the density of a neutral atom) and this creates a potential. Using this preliminary potential a ‘new’ charge density is obtained from the squares of the wave functions which is generated by solving the Kohn-Sham equations. The initial and ‘new’ charge density generally differ but the process repeats itself until they are

considered self-consistent. Self-consistency is taken to have been achieved when the energy difference ( $E_{\text{diff}}$ ) calculated from the initial and 'new' charge density is less than  $10^{-5}$  au.

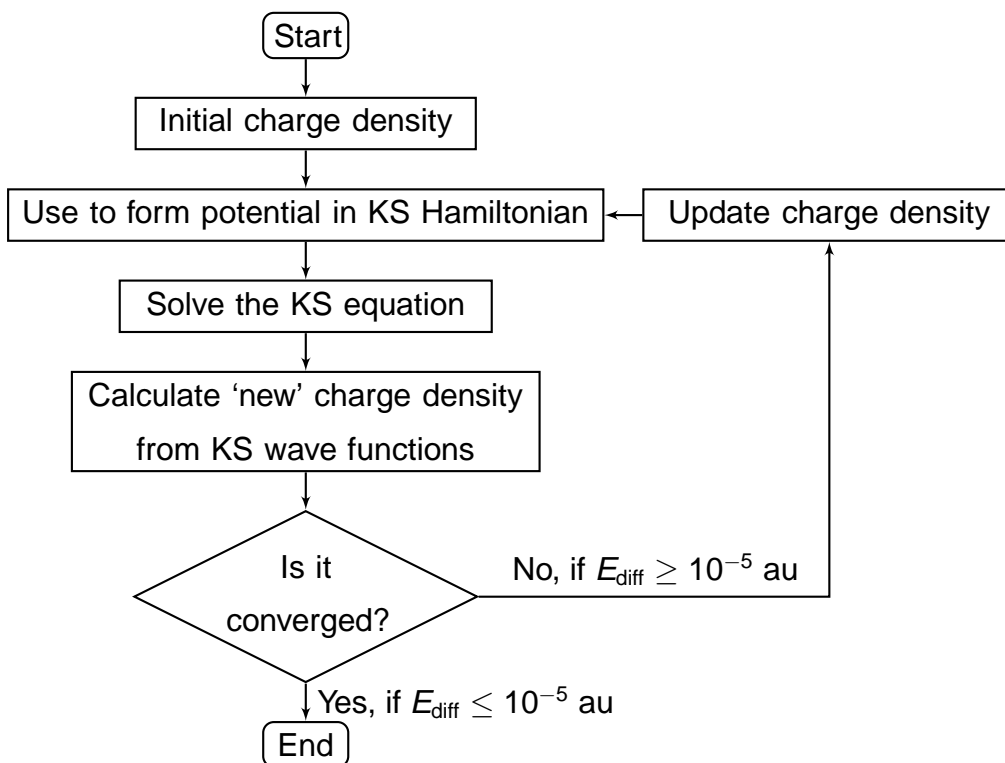


Figure 3.1: Flow chart describing the self-consistency cycle.

### 3.3 Pseudopotential approximation

Electrons are localised on the atom, for example the carbon has the electronic structure of  $1s^2 2s^2 2p^2$ . The core electrons in this case are the  $1s^2$  electrons, these are highly localised around the nucleus and are therefore considered not to take part in bonding, the remaining electrons are valence electrons ( $2s^2 2p^2$ ), they predominantly contribute to bonding. The treatment of the core states has its disadvantages and advantages. Core states are difficult to describe as they vary rapidly, require relativistic treatment and contribute a lot to final energies due to the fact they are tightly bound to the nucleus, inclusion is also computationally demanding

so including them may be more detrimental than helpful. Pseudopotentials are therefore used to describe the electron–nuclear interaction term so the Kohn–Sham equation can be solved. A pseudopotential simplifies the wave function of the core electrons making it much weaker and mimics the wave function produced by the valence electrons if the core and nucleus were there, this effective Coulombic potential is illustrated in Figure 3.2. Pseudopotentials of Hartwigsen, Goedecker and Hutter (HGH) [65] were implemented in this Thesis.

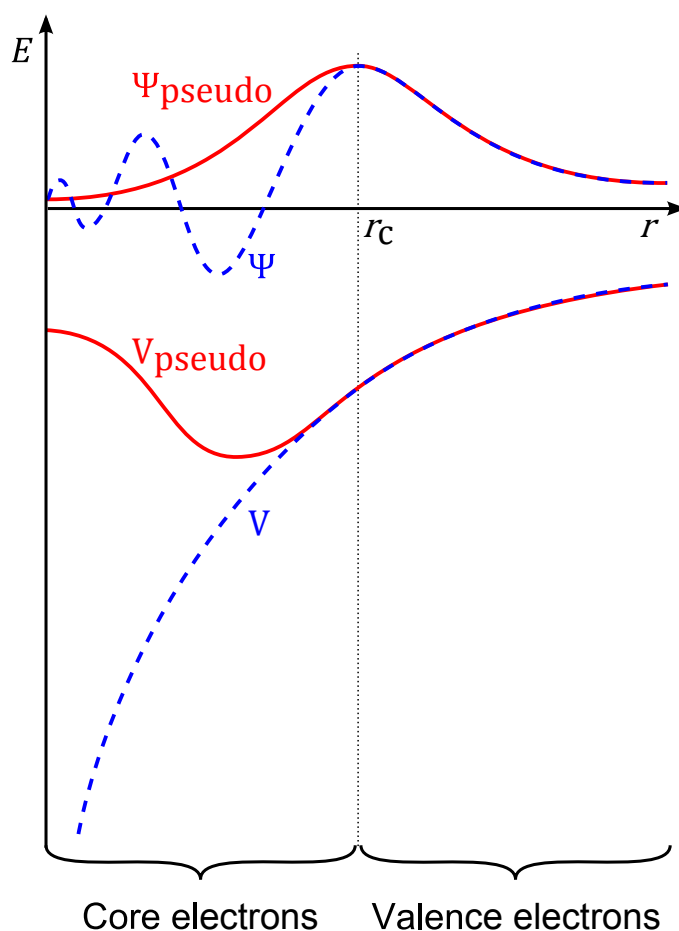


Figure 3.2: Schematic illustration of the Coulombic potential ( $V$ ) and wave function ( $\Psi$ ) of an atom (dashed line) and the comparative pseudopotential ( $V_{\text{pseudo}}$ ) and pseudo-wave function ( $\Psi_{\text{pseudo}}$ ) (solid line), where  $r_c$  indicates the cut-off radius where the potentials must match. Image after [66, p. 28].

Although core states are strictly not involved in bonding they do have a role in hyperfine interactions for example, and the negligence of this must be treated with care. In these cases the core electron wave functions are reconstructed.

### 3.4 Supercell

As discussed earlier in Chapter 1, this Thesis focuses on the properties of point defects in diamond which could have the concentration as low as parts per billion. It is unrealistic to model a billion atoms to reproduce the effects on the properties of diamond so the supercell method is used to circumvent this.

The supercell method exploits periodic boundary conditions that satisfy Bloch's theorem of electrons. In an ideal crystal of pure diamond, carbon atoms are arranged periodically according to a face-centred cubic Bravis lattice, defined by Bravis lattice vectors  $\mathbf{R}_{\text{Bravis}}$ , the system is infinite and each repeated Bravis lattice is identical. It follows that the potential as a function of position  $V(\mathbf{r}_{\text{Bravis}})$  is also periodic with respect to the Bravis lattice vectors  $\mathbf{R}$  so

$$V(\mathbf{r}_{\text{Bravis}}) = V(\mathbf{r}_{\text{Bravis}} + \mathbf{R}_{\text{Bravis}}). \quad (3.1)$$

Bloch's theorem states that the solutions to the Schrödinger equation in a periodic potential have the form:

$$\psi(\mathbf{r}_{\text{Bravis}}) = e^{i\mathbf{k}\cdot\mathbf{r}_{\text{Bravis}}} u(\mathbf{r}_{\text{Bravis}}), \quad (3.2)$$

where  $\psi(\mathbf{r}_{\text{Bravis}})$  is the wave function,  $i$  is the imaginary unit,  $\mathbf{k}$  is the wave vectors and  $u(\mathbf{r}_{\text{Bravis}})$  is a periodic function with the same periodicity of the diamond lattice in this case, i.e.

$$u(\mathbf{r}_{\text{Bravis}}) = u(\mathbf{r}_{\text{Bravis}} + \mathbf{R}_{\text{Bravis}}). \quad (3.3)$$

The supercell is effectively an *infinitely* repeated unit cell to give an artificial periodic crystal, the cell is effectively surrounded by and bonded to identical cells. The calculations are performed in a single unit cell although with infinite possible values of

**k.** Periodic boundary conditions are imposed on the wave function that restricts the values of  $\mathbf{k}$  and makes the calculation manageable. Under these circumstances the unit cell can be represented in reciprocal space. Which is discussed further in the next Section.

When a defect is introduced in to the supercell, the cell must be chosen so that it continuously fills the space and is large enough so it does not introduce defect–defect interactions, whereby the defect of interest in each cell detrimentally interacts with its repeated image in adjacent cells, an artefact of repeated cell calculations. Figure 3.3 compares a small unit cell with a larger cell.

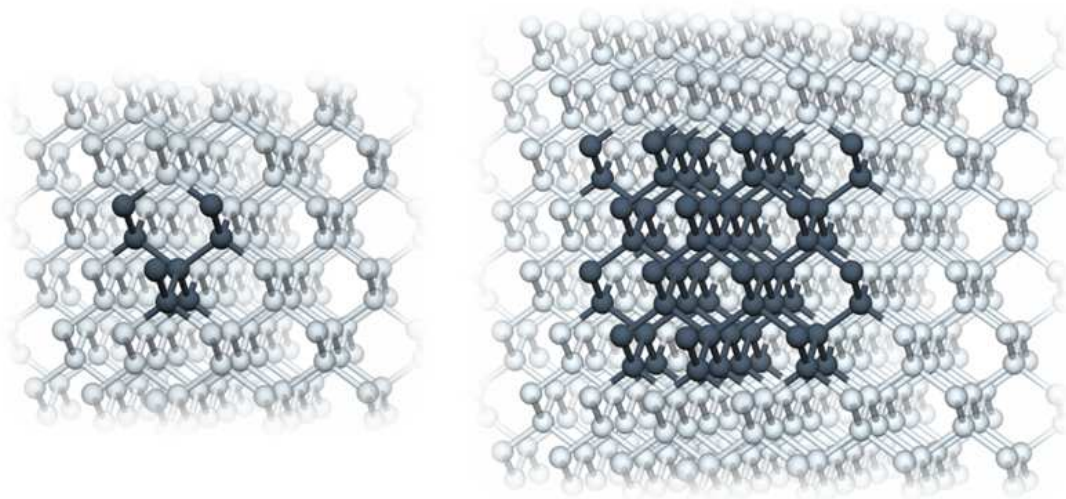


Figure 3.3: An eight atom unit cell (left) and 64 atom unit cell (right) represented by darkened carbon atoms in which the calculations are performed. They are surrounded by repeated cells represented by lighter carbon atoms, these repeat infinitely but only some are shown.

### 3.5 Brillouin zone sampling

Using a supercell with boundary conditions imposed means that all the properties of an electron have the periodicity of the reciprocal lattice. Therefore it is only necessary to do calculations in a primitive unit cell in reciprocal space.

The reciprocal space is related to real space by Fourier transforms. In reciprocal space the Wigner-Seitz primitive unit cell is called the Brillouin zone. The first Brillouin zone therefore contains all unique information about the wavefunction and as per in real space.

In order to calculate physical quantities such as the total energy of the system AIMPRO integrates for each allowed  $f(\mathbf{k})$  across the first Brillouin zone. This function does not have a known analytical form so a numerical approximation is made, similar to the ‘trapezium rule’. These AIMPRO calculations use a Monkhorst-Pack (MP) [67, 68] sampling mesh to approximate this integration.

The MP mesh of  $k$ -points is defined by  $I$ ,  $J$  and  $K$ ; three integers that are each more than or equal to 1. They define a grid of  $I \times J \times K$  (equally spaced) points in reciprocal space as follows,

$$\mathbf{k}(i, j, k) = \frac{2i - I - 1}{2I} \mathbf{a}_1 + \frac{2j - J - 1}{2J} \mathbf{a}_2 + \frac{2k - K - 1}{2K} \mathbf{a}_3, \quad (3.4)$$

where

$$i = 1, \dots, I, j = 1, \dots, J, k = 1, \dots, K, \quad (3.5)$$

and  $\mathbf{a}_1$ ,  $\mathbf{a}_2$  and  $\mathbf{a}_3$  are unit vectors of reciprocal space. If  $I$ ,  $J$  and  $K$  are equal the sampling scheme is labelled as MP- $I^3$ .

The more  $k$ -points defined in the MP mesh the more accurate the numerical integral will be but as the number of  $k$ -points increase so does computational time. This effect is demonstrated in Figure 3.4. It is imperative to find a balance between accuracy and time to choose the density of the mesh accordingly. The sampling was chosen to be sufficiently dense to converge the total energy to 10 meV.

As the volume of the real space supercell  $\Omega_{\text{supercell}}$  is related to the volume of the reciprocal space Brillouin zone  $\Omega_{\text{Brillouin zone}}$  via the relation,

$$\Omega_{\text{Brillouin zone}} = \frac{(2\pi)^3}{\Omega_{\text{supercell}}}. \quad (3.6)$$

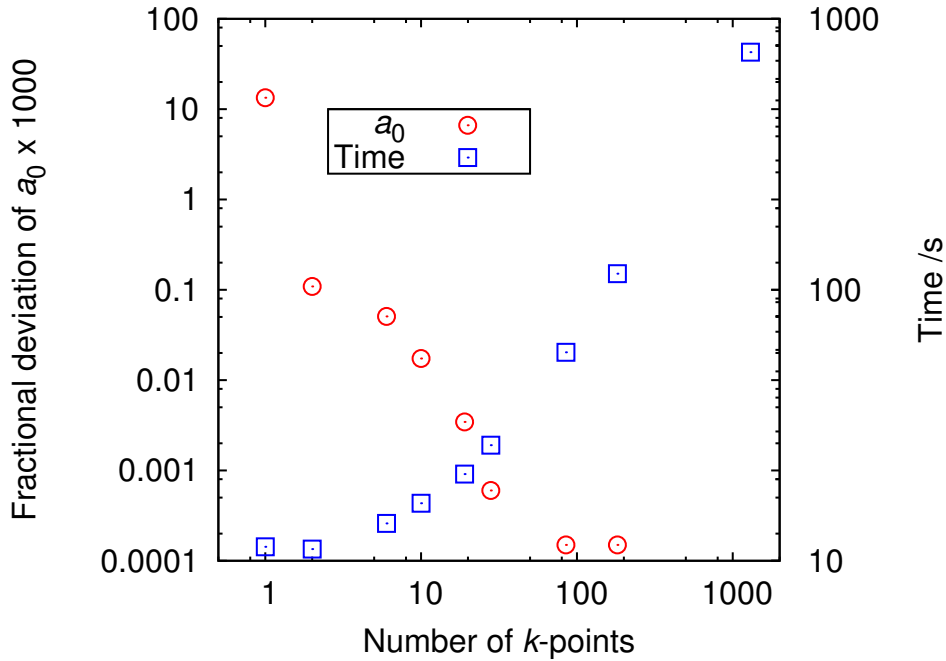


Figure 3.4: Fractional deviation (defined as the difference between the most converged result divided by the least converged result) from the lattice constant ( $a_0$ ) (circles) and time (s) (squares) as a function of the number of  $k$ -points.

The larger the supercell the smaller the Brillouin zone so less  $k$ -points are needed to describe the Brillouin zone accurately.

### 3.6 Basis sets

As described previously in Section 3.3, the pseudopotential is used to ‘smoothe’ the potential of the core electrons, a consequence of this is the valence states that feel this weaker potential do not need to be orthogonal to the core states. Therefore, rather than using an all-electron state, they can be represented accurately using a much smaller set of basis functions.

A basis function is a set of functions which do have an analytical form and is used to represent the wave function that does not have an analytical form. A Taylor expansion of the sine function can be viewed as an example of using a basis set of polynomials

to describe the function. To solve the Eigenvalue problem and proceed, a mathematical representation for the one-electron wavefunction is still required. The wavefunction is expanded mathematically and is labelled a basis set.

There are two popular choices when it comes to basis sets for electron structure calculations: plane waves (periodic) and Gaussian. Gaussian orbitals are a compact basis requiring a small number of functions. It produces integrals that are analytical.

Each Gaussian orbital is centred on an atomic site,  $R_i$  and it has the form

$$\phi_i(r - R_i) = (x - R_{i,x})^{n_1} (y - R_{i,y})^{n_2} (z - R_{i,z})^{n_3} e^{-\gamma(r-R_i)^2}, \quad (3.7)$$

where  $\gamma$  is a real parameter and  $n_1 + n_2 + n_3 = n_i$  where  $\sum n_i \geq 0 \forall i$ . As they are centered on the atom and decay rapidly away they represent localised orbitals very well. Different orbital symmetries can be constructed using the values of  $n_i$ . The more Gaussians used the more accurate the result, this is demonstrated in Figure 3.5.

The labels of the basis sets used in Figure 3.5, refer to the material it was optimised for: either diamond, graphite or beryllium carbide ( $\text{Be}_2\text{C}$ ). In the case of  $\text{Be}_2\text{C}$  and graphite, although not optimised to model diamond the associated basis sets provide reasonable results. The letters following the material refer to the number of exponents, the first being the smallest increasing in size to the largest. 'ddpp' for example means that the first exponent d has 10  $s/p/d$  functions, the next d exponent also has 10 and the following p exponents has four  $s/p$  functions each. 'graphie-ddpp' and 'diamond-ddpp' have the same number of basis functions but they are optimised for different materials therefore they produce different results. The letter 'C' after the material means contracted. This is where the number of functions are reduced to maintain accuracy, it is done by combining  $s$ -functions into a single combination and the  $p$ -functions into another. This combines to give four ('4') contracted Gaussian ('G') orbitals, i.e 'C4G'. 'C44G' includes two different  $s/p$  combinations so they have eight functions per atom and 'C44G\*' includes  $d$ -type functions so there are 13 functions per atom. 'a0.exp' refers to a basis that has been optimised to the experimental value

of the lattice constant of diamond in this case and ‘a0.44g\*’ optimised to the theoretical value of the lattice constant produced by using ‘44g\*’ basis.

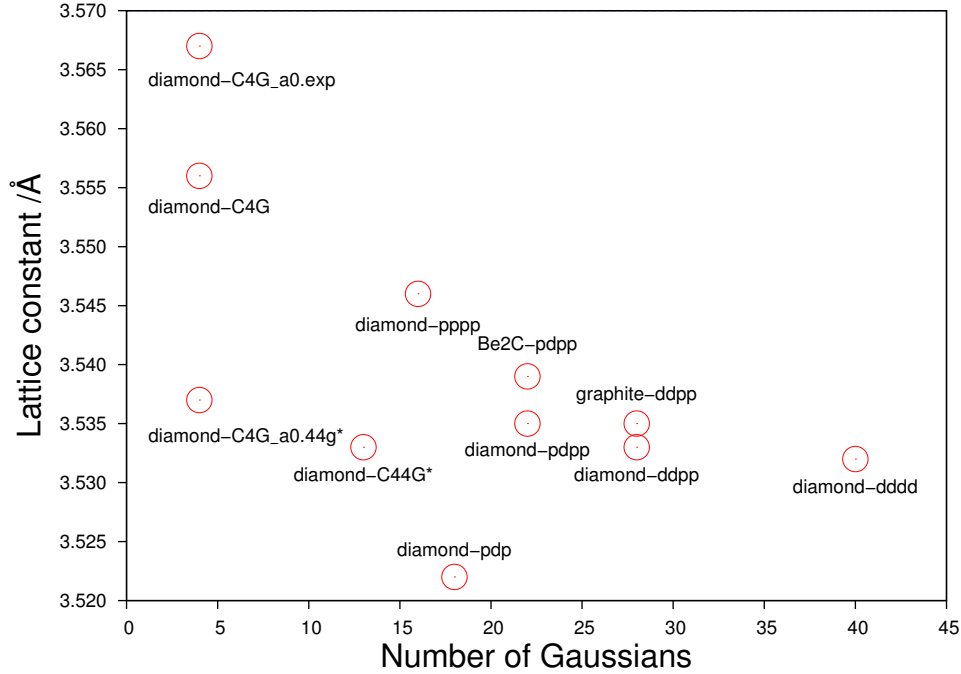


Figure 3.5: Lattice constant as a function of the number of Gaussians used to describe carbon in diamond.

An alternative are plane wave basis sets, which is a Fourier Series expansion of the wave function. This choice requires a huge number of basis coefficients, it has difficulties when the wave function varies rapidly and the treatment of a vacuum in a cell is just as computationally expensive as it is for atoms. Plane waves are used in crystalline systems as they are the solution to Bloch’s theorem. We recall from Section 3.4 that Bloch’s theorem states that:

$$\psi(\mathbf{r}_{\text{Bravais}}) = \underbrace{e^{i\mathbf{k}\cdot\mathbf{r}_{\text{Bravais}}}}_{\text{wave-like}} \underbrace{u(\mathbf{r}_{\text{Bravais}})}_{\text{periodic lattice}}, \quad (3.8)$$

where  $\psi(\mathbf{r}_{\text{Bravais}})$  is the wave function,  $i$  is the imaginary unit,  $\mathbf{k}$  is the wave vectors and  $u(\mathbf{r}_{\text{Bravais}})$  is a periodic function with the same periodicity of the real diamond lattice in

this case, i.e.

$$u(\mathbf{r}_{\text{Bravis}}) = u(\mathbf{r}_{\text{Bravis}} + \mathbf{R}_{\text{Bravis}}). \quad (3.9)$$

Because of this periodicity  $u(\mathbf{r}_{\text{Bravis}})$  can be expanded in terms of plane waves.

$$u(\mathbf{r}_{\text{Bravis}}) = \sum_{\mathbf{k}} c_0 e^{i\mathbf{k} \cdot \mathbf{r}_{\text{Bravis}}}. \quad (3.10)$$

Where  $c_0$  is a complex constant. Therefore Bloch's theorem can be written as:

$$\psi(\mathbf{r}_{\text{Bravis}}) = \sum_{\mathbf{g}} e^{i(\mathbf{k}+\mathbf{g}) \cdot \mathbf{r}_{\text{Bravis}}} c_{\mathbf{g}}, \quad (3.11)$$

where  $\mathbf{g}$  is the reciprocal lattice vectors of the supercell. In Equation 3.11  $\mathbf{g}$  must be infinite. However it is confined and the  $\mathbf{g}_{\text{cut off}}$  value is represented as a cut off energy ( $E_{\text{cut off}}$ ) (Equation 3.12),  $\mathbf{k}$  on the other hand covers the entire reciprocal space.

$$E_{\text{cut off}} = \frac{\hbar^2 \mathbf{g}_{\text{cut off}}^2}{2m_e}, \quad (3.12)$$

where  $\hbar$  is the reduced Planck's constant and  $m_e$  is the mass of an electron.

### 3.7 Summary

This Chapter describes the technical terms applied in computational methods such as in the AIMPRO software package. The terms are summarised in Figure 3.6.

The only information necessary as input for AIMPRO are:

1. the positions of the atoms in cell choice;
2. the identities of the atoms which are to be relaxed;
3. the basis to be used for the wave function and charge density;
4. the electronic configuration.

With this information AIMPRO can provide the energy of the system, the electronic levels, and the equilibrium positions of the atoms. More specialised output is available and the methods associated with these are discussed in the next Chapter.

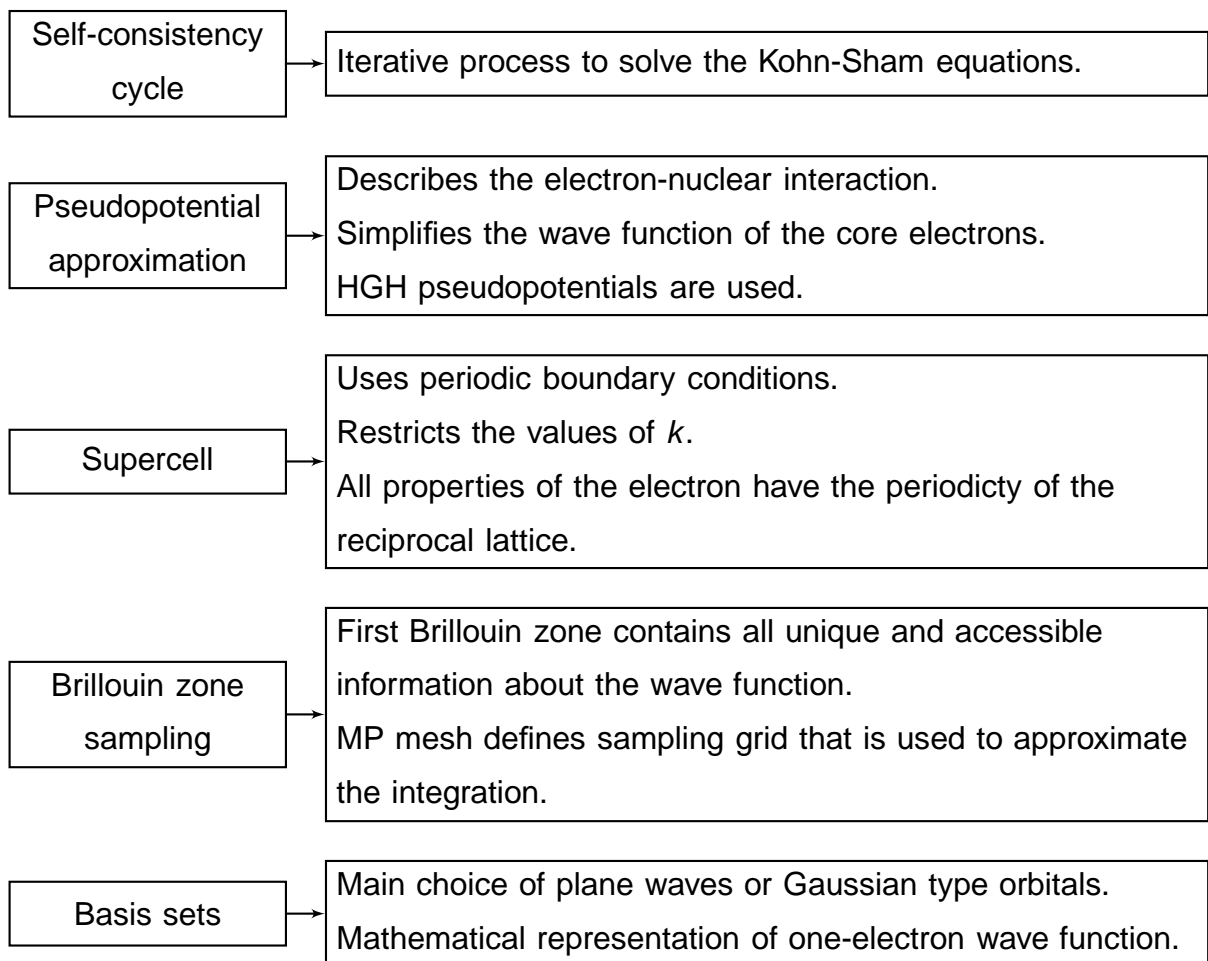


Figure 3.6: Summary of approximations and methodologies used in AIMPRO.

## Chapter 4. Derived quantities

### 4.1 Modelling physical quantities

DFT is a powerful tool as it has the capability to model a wide range of experimental observables. But before AIMPRO can calculate specific properties of the diamond structure it first needs to find the minimum energy of the system. The methods associated with this process are discussed below, with further derived experimental observables that can be calculated to a reasonable accuracy to follow: these include the electronic levels [69], vibrational modes [70,71], hyperfine parameters [72] electrical levels [73,74] and energetic processes [75,76,77].

### 4.2 Lattice constant and bulk modulus

Lattice parameters are fundamental properties of any crystal structure; they define the dimensions of a unit cell in a crystal lattice. In order to optimise a crystal structure the dimensions of the lattice must be known. Lattice parameters are found theoretically by optimising atomic positions for a sample of  $a_0$  values that are in the range of  $\pm 5\%$  of an approximate equilibrium value. The resultant energies are fitted to the Birch-Murnaghan equation (Equation 4.1). The equilibrium lattice parameters and also the bulk modulus are determined from the fit. The Birch-Murnaghan equation of state is:

$$E(\text{Vol}) = E_0 + \left[ \frac{(\frac{\text{Vol}_0}{\text{Vol}})^{K'_0}}{K'_0 - 1} + 1 \right] \frac{K_0 \text{Vol}}{K'_0} - \frac{K_0 \text{Vol}_0}{K'_0 - 1}, \quad (4.1)$$

where  $E$  is the total energy and  $Vol$  the the total volume and  $E_0$  and  $Vol_0$  is the equilibrium energy and volume.  $K_0$  and  $K'_0$  is the bulk modulus and its first derivative with pressure.

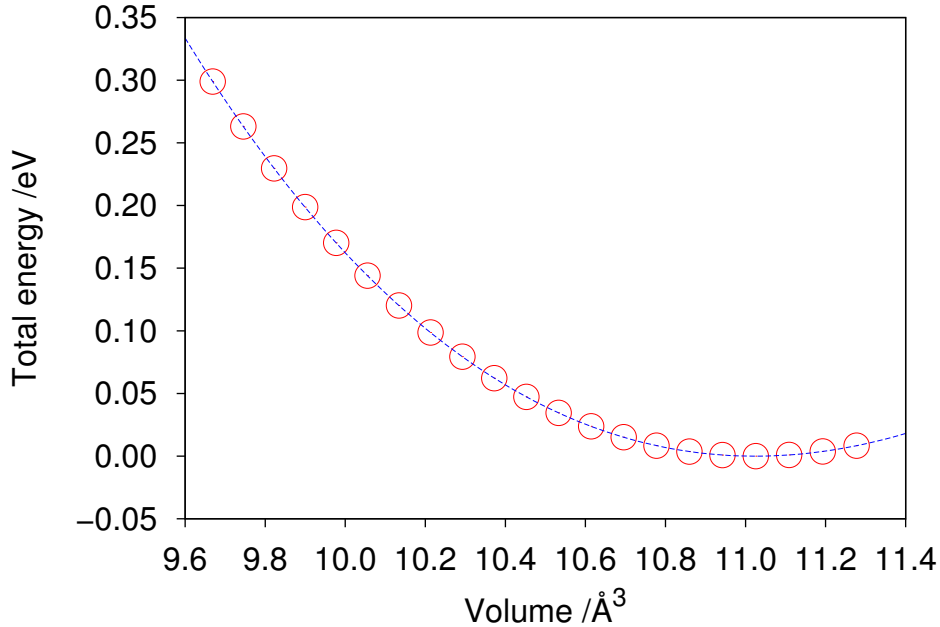


Figure 4.1: Total energy (eV) as a function of unit cell volume ( $\text{\AA}^3$ ), with the Birch-Murnaghan equation of state fitted to the data.

In GGA calculations  $a_0$  is typically overestimated and the bulk modulus is underestimated, whereas the reverse is true for LDA calculations. Despite this, agreement with experiment in both cases is acceptable, a comparison of results are listed in Table 4.1.

Table 4.1: Comparison of both the calculated bulk modulus and lattice constant with experiment, using a GGA functional.

	Theory	Experiment
Lattice constant ( $\text{\AA}$ )	3.57	3.567 [78]
Bulk modules (GPa)	440	442 [79]

### 4.3 Structural optimisation

Once the lattice constant is known the system can be optimised to find its equilibrium structure. This is the system that corresponds to the minimum free energy of the structure and this is generally a necessary starting point for further analysis.

Structural optimisation in AIMPRO is calculated using the conjugate gradient algorithm. To reduce the total energy, the conjugate gradient method defines the direction the atoms should be moved based on the forces within a conjugate gradients scheme. The minimum energy in this search direction is found in AIMPRO by calculating total energies and gradients in this direction and a cubic polynomial fitted, to interpolate the minimum. The structure is normally taken to be optimised when the forces on the atoms is  $< 10^{-3}$  au, if this is not the case, in the next step, the atoms are moved in a direction conjugate to all previous search directions and a minimum is found again. Apart from the first step, the direction moved is not the direction of the forces.

It is worth heeding that this may not be the ground state energy and rather a local minimum energy of the system. To ascertain the plausibility of the global minimum for the system, different chemically feasible initial structures are considered; if the initial structure possess any symmetry operations AIMPRO will apply these as constraints during the optimisation.

LDA functionals tend to underestimate bond lengths because it overestimates the bond strength. GGA functionals however tend to underestimate the bond strength and thus overestimate bond lengths. However, DFT (as an exact theory) would give you the correct answer if you did not have to use an approximate functional.

The optimised structure can then be used in deriving further quantities, as well as providing information about the bond lengths and angles.

### 4.4 Electronic levels

The band structure of a crystal provides information about its electronic properties. The Kohn-Sham Eigenvalues as a function of the wave vector ( $\mathbf{k}$ ) are plotted to create the

band structure; the band gap is taken as the energy difference between the conduction band minimum and the valence band maximum.

In standard DFT, it is a well known short coming that theoretical values of the band gap do not agree well with that of experiment [80,81]. An example of a band structure

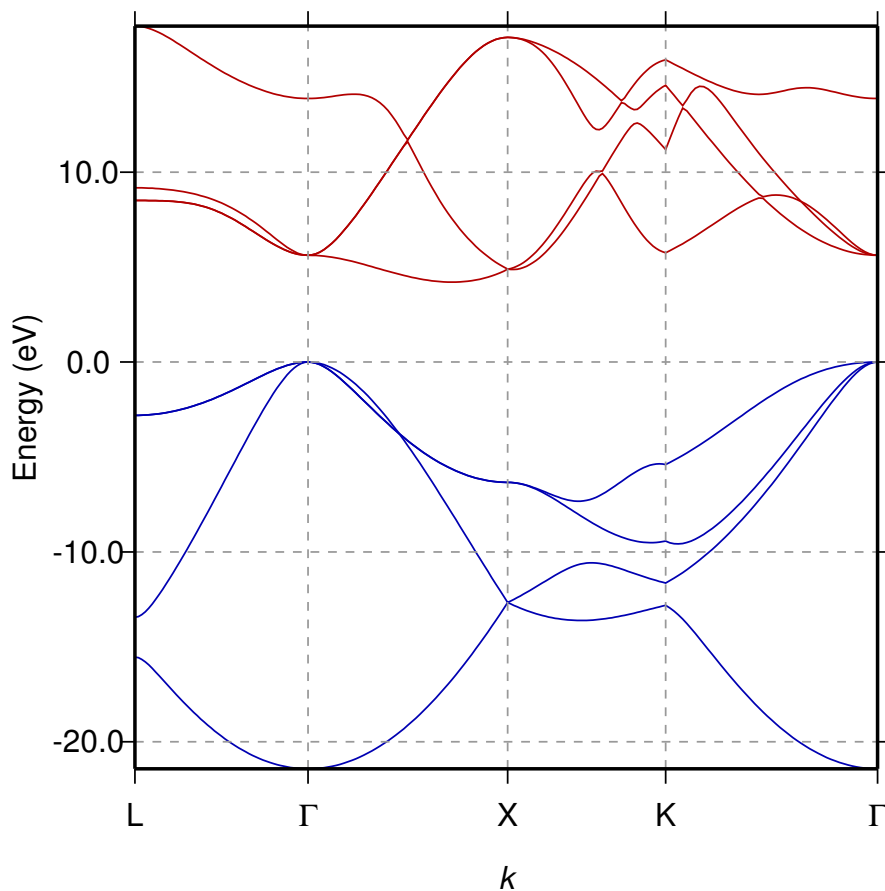


Figure 4.2: Band structure of bulk diamond reproduced using a two atom unit cell, calculated along high symmetry directions in the cubic Brillouin zone in the vicinity of the band gap. The red Kohn-Sham levels indicate unoccupied bands and the blue bands represent levels occupied by two electrons in each.

of diamond is represented in Figure 4.2. The band gap of diamond is indirect and

the experimental value at room temperature is 5.47 eV [82]. The theoretical values given by GGA and LDA calculations underestimate the band gap due to an error in the calculation of the excited states. The calculated band gap for GGA and LDA calculations is 4.98 eV and 5.01 eV respectively for an indirect band gap for a two atom cell.

Defects introduced in to diamond alter and add states, and a direct comparison can be made between a bulk diamond's band structure and that which includes a defect (Figure 4.3a). The electronic levels due to the defect can give an indication of possible spin or charge states available and if optical transitions between levels can be accessible.

An optical transition is where an electron is excited (absorption of a photon equal or larger than the transition) from an occupied state to an unoccupied state; when an electron de-excites and drops down to an equilibrium state a photon corresponding to the energy transition may be emitted. For an electron to be excited, selection rules apply: spin needs to be conserved, the orbital angular momentum quantum number  $l$  must change (i.e. s-orbital–s-orbital transitions are forbidden) and the magnetic quantum number  $m_l$  can only differ by one unit (i.e.  $\Delta m_l = 0, \pm 1$ ). These electronic transitions between states due to the defect and surrounding bulk or another defect can be detected in optical absorption/emission experiments. When the electronic transition due to a defect involves no change in  $\mathbf{k}$ , it is commonly referred to as a zero phonon line (ZPL). ZPLs are narrow and often easier to detect in experiment when compared to defect to band-edge transitions, they tend to be broad and more difficult to detect. ZPL are used to characterise defects but transitions may be obscured by others.

When a larger supercell (Section 3.4) is used the defect-defect interaction reduces, consequently reducing the dispersion of the states. Defect-defect interactions are an artifact of supercell calculations, it is where the defect detrimentally interacts with its infinitely repeated images of itself. The dispersion of the states refers to change in energy as  $k$  changes, there is more dispersion of the defect states in smaller cells as there is overlap between the defect state wave functions and the 'image's' wave

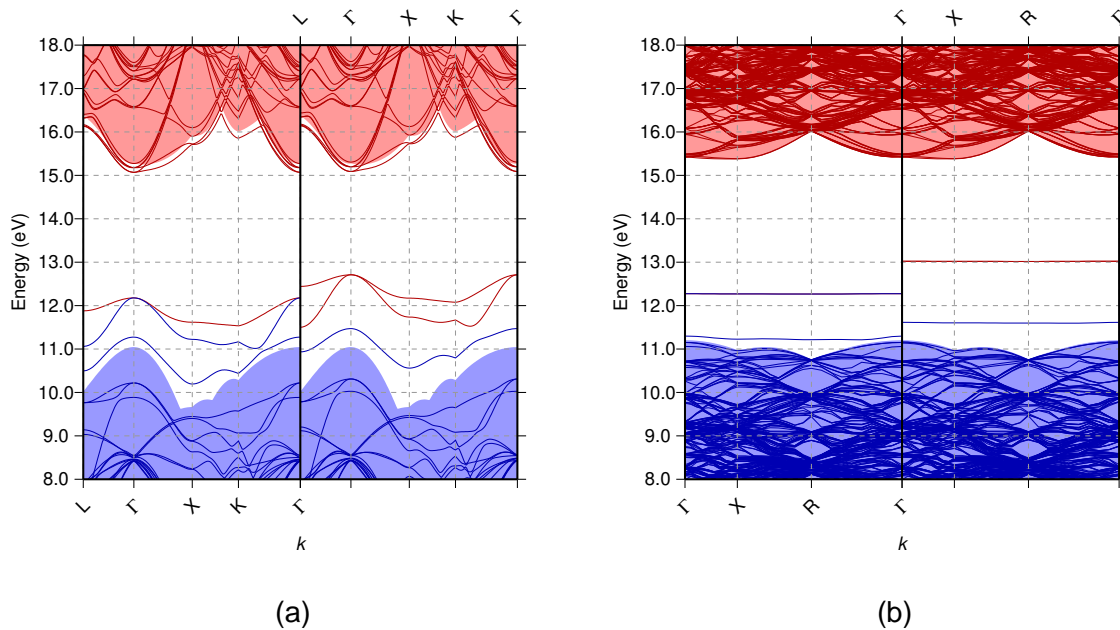


Figure 4.3: An example of defect states introduced into the band gap, calculations were done in a 54 atom cell: (a). And 1000 atom cell: (b), calculated along high symmetry directions in the cubic Brillouin zone in the vicinity of the band gap. Again the red levels are unoccupied and the blue occupied. The shaded red and blue areas represent defect-free bulk 54 or 1000 atom calculations overlaid for comparison respectively. The band structure is split in half, the left representing spin up for example and the right spin down, each band contains one electron. Note that the degeneracy of the levels obscures the occupation in the 1000 atom cell when compared with the 54 atom cell. The top left band of the defect state is two bands, one occupied and one empty. Both band structures are of the vacancy hydrogen neutral defect with  $S = 1/2$ .

functions. Figure 4.3b is the same defect in Figure 4.3a but is modelled in a cell of a 1000 atoms as opposed to a 54 atom cell. The states introduced into the gap due to the defect in Figure 4.3b have very little dispersion (i.e. the energy is constant when  $k$  changes) therefore transitions between states can be assessed more reliably. The defect in the larger cell also has very little effect on the bulk surrounding it, the underlying bulk calculation used for comparison lies directly on top of the defect calculation unlike the smaller cell where the bulk states do not directly correspond to

bulk bands in the defect calculation.

Optical spectroscopy includes techniques like Fourier transform infrared absorption (FTIR) and UV-Vis absorption, they can be used as a tool to ‘track defect concentrations’ through different treatments by measuring the absorption of different wavelengths at different stages of the process.

Absorption of a photon from IR or UV ranges of light can excite an electron into a higher energy state if the electric field part of the light can interact with the electric dipole of the system. The band structure provides information about possible transitions between different electronic states. Absorption of a photon, can also cause vibronic transitions and can be seen experimentally as side-bands to optical transitions. Vibrational modes are discussed in Section 4.5.

Photo-luminescence (PL) is typically more sensitive than optical absorption (i.e. smaller concentrations of luminescing centres may be detectable than is usually the case for optical absorption), but because emission is a competitive process (the fastest recombination routes dominate), PL is not quantitative (i.e. it is not routinely possible to determine the concentration of emitting defects). PL involves the detection of emitted, as opposed to absorbed, photons; the experiment typically involves the illumination of the sample with above band gap laser light, which generates electron-hole pairs, that recombine via a combination of radiative and non-radiative mechanisms. It is the detection of the former that allows for the PL characterisation of point defects in diamond, as the emitted photon energy is highly characteristic of the localised states introduced to the band gap when defects are formed.

### **4.5 Vibrational modes**

Vibrational modes can be obtained using AIMPRO and compared with Raman scattering and infrared absorption spectroscopy. A mode is Raman active if there is a change in the polarisability and it is infrared active if there is a change in the electronic dipole.

Localised vibrational modes are localised around the defect and have a higher

frequency than the surrounding diamond. The maximum phonon frequency permissible in diamond is the Raman frequency at  $1332\text{ cm}^{-1}$  [83].

The vibrational modes are found by AIMPRO using a simple harmonic approximation. The dynamical matrix is derived from the second derivative of the total energy  $E$  with respect to the displacements of pairs of atoms  $R_i$  and  $R_j$  with the masses  $M_i$  and  $M_j$  respectively. The dynamical matrix of the terms is given as:

$$\frac{\frac{d^2 E}{dR_i dR_j}}{\sqrt{M_i M_j}} \quad (4.2)$$

The Eigenvalues of the dynamical matrix are the squares of the oscillator frequencies. Some terms generated using this method produce anharmonic terms (negative Eigenvalues/imaginary oscillator frequencies) due to the finite displacement of the atoms. An anharmonic frequency is where the overtone frequencies are not multiples of the fundamental frequency. Others are termed quasi-harmonic as the harmonic approximation breaks down the further the bond is stretched away from equilibrium.

As the amplitude of hydrogen oscillations that are of particular interest to this Thesis are often large, the contribution from anharmonicity can be of the order of tens of  $\text{cm}^{-1}$ . As bond lengths calculated using GGA functionals within DFT tend to be overestimated, a 3% error in a carbon–hydrogen bond length can give rise to a 10% error in hydrogen stretch mode, therefore it is feasible to expect calculated vibrational modes to be underestimated.

The oscillator strength, which is the probability of an electromagnetic transition associated with the calculated frequencies is unknown. The time the transition takes is called the lifetime and is also unknown, electronic transitions generally have a much shorter lifetime typically around nano seconds compared to a vibrational mode that could last seconds. The lifetime of the mode determines the line width in the spectra. The longer the lifetime the sharper the spectral line. To increase the lifetime of a vibrational mode experimentally, the temperature of the material can be reduced

effectively slowing the modes.

Despite the fact that the frequencies can be obtained through AIMPRO, they might be difficult to see experimentally as it is unclear what the oscillator strength and the lifetime of the state is. They may also be enveloped by other peaks. It can be investigated further by looking at isotopic shifts, the effects of stress and strain on the mode, comparing different crystals that may have different effective charges and performing the experiment at lower temperatures to increase the lifetime of the mode.

#### 4.6 Hyperfine parameters

Hyperfine interaction is a measure of the interaction between an electron spin and a nuclear spin. This interaction is therefore only seen in defects with a non-zero nuclear and electron spin. For example  $^{13}\text{C}$  has a nuclear spin of  $I = 1/2$  and any defect with an unpaired electron will possess a non-zero spin, as each electron is  $S = \pm 1/2$ .

This interaction can be probed using electron paramagnetic resonance (EPR): a major spectroscopic technique used to identify defects in diamond but is inactive in the case of  $S = 0$ , for example in pure diamond where all electrons are involved in chemical bonding. EPR is non-destructive, very sensitive (can detect defects with concentrations less than parts per billion (ppb)) and can provide information about chemical composition and symmetry of the defect, providing that the hyperfine interaction is large enough.

In explaining the calculation of the hyperfine parameters, it is important to first outline the theory of EPR. In its simplest form, when a magnetic field is applied to a sample with an unpaired electron, the unpaired electron's spin may align with the direction of the external field or in the opposite direction of it. The applied magnetic field removes the degeneracy of the  $\pm 1/2$  electron spins and splits them into two different discrete energies (Figure 4.4). The electron energy levels created by this splitting means that absorption of quantised electromagnetic radiation is possible, stimulating a magnetic dipole transition between the states. The energy difference between the states is given

by

$$E = h\nu = \mu_B g_e B, \quad (4.3)$$

where  $E$  is the energy of the transition,  $h$  is the Plank constant,  $\nu$  is the frequency of the electromagnetic radiation,  $\mu_B$  is the Bohr magneton,  $g_e$  is the Zeeman splitting constant [84] and  $B$  is the external magnetic field.

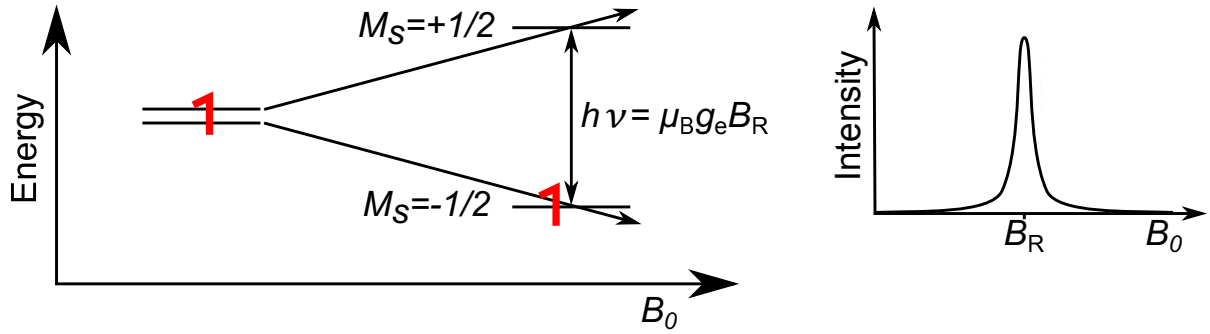


Figure 4.4: An example of a variable external magnetic field ( $B_0$ ) applied to a system with one unpaired electron ( $S = 1/2$ ), shown as a red half arrow. When the applied constant frequency microwave beam matches the energy of the splitting ( $h\nu = \mu_B g_e B_R$ ) absorption occurs.

In EPR experiments the sample is placed in a microwave cavity with a variable applied magnetic field orthogonal to applied electromagnetic radiation. When resonant (R) absorption occurs at  $B_R$ , an EPR signal is observed (Figure 4.4).

In addition to the energy term in Equation 4.3. The interactions between spins can be described by the effective spin-Hamiltonian ( $\mathcal{H}$ ) [84]:

$$\mathcal{H} = \underbrace{\mu_B \hat{\mathbf{S}} \cdot \mathbf{g}}_1 \cdot \mathbf{B} + \underbrace{\hat{\mathbf{S}} \cdot \mathbf{D} \cdot \hat{\mathbf{S}}}_2 + \sum_j \left[ \underbrace{\hat{\mathbf{S}} \cdot \mathbf{A}_j \cdot \hat{\mathbf{I}}_j}_3 - \underbrace{\mu_N g_{N_j} \hat{\mathbf{I}}_j \cdot \mathbf{B}}_4 + \underbrace{\hat{\mathbf{I}}_j \cdot \mathbf{P}_j \cdot \hat{\mathbf{I}}_j}_5 \right] + \text{higher order terms.} \quad (4.4)$$

$\hat{\mathbf{S}}$  is the effective electron spin operator,  $\hat{\mathbf{I}}_j$  is the nuclear spin operator for the  $j^{\text{th}}$  nucleus.  $g_{N_j}$  is the nuclear  $g$  value and  $\mu_N$  is the nuclear magneton defined by  $\mu_N = \frac{e\hbar}{2m_p c}$ , where  $e$  is the elementary charge,  $\hbar$  is the reduced Planck constant,  $m_p$  is the proton rest mass and  $c$  is the speed of light.  $\mathbf{P}_j$  is the quadrupole interaction term.  $\mathbf{D}$  is the zero field tensor and  $\mathbf{A}_j$  is the hyperfine tensor.

The effective spin-Hamiltonian is split in to the following and are labelled 1–5 in Equation 4.4, plus higher order terms that are not considered here:

1. The electronic Zeeman interaction.
2. The zero-field interaction (when  $S \geq 1$ ).
3. The hyperfine interaction.
4. The nuclear Zeeman interaction.
5. Nuclear quadrupole interaction (when  $I \geq 1$ ).

Hyperfine interactions are calculated by AIMPRO. The hyperfine interaction occurs for every non-zero nuclear spin that interacts with the effective spin of the electrons, so the hyperfine interaction of bulk material is:

$$\mathcal{H} = \sum_j \hat{\mathbf{S}}^T \cdot \mathbf{A}_j \cdot \hat{\mathbf{I}}_j \quad (4.5)$$

The hyperfine parameter can further be thought of as being comprised of an isotropic and anisotropic part.

The isotropic interaction is also known as the contact or Fermi interaction and as the name suggests it originates from *s*-state electrons interacting with the nuclei. I.e. states that are spherical and node-less. The isotropic hyperfine coupling constant is described by:

$$A_s = \frac{2}{3} \mu_0 g_e \mu_B g_N \mu_N |\psi(0)|^2, \quad (4.6)$$

$\mu_0$  is the value of magnetic permeability in a vacuum and  $|\psi(0)|^2$  is the spin density at the nucleus.

The anisotropic hyperfine interaction is also known as the dipolar interaction because it depends on the relative orientation of the magnetic moments. It takes into account the interaction between the nuclei and electrons that have zero spin density at the nucleus, i.e. *p*, *d*, *f*...-orbitals. These orbitals do not contribute to the isotropic hyperfine

interaction as  $|\psi(0)|^2$  in Equation 4.6 is equal to zero. The anisotropic hyperfine interaction can be described as:

$$\mathcal{H}_p = \hat{\mathbf{S}}^T \cdot \underline{\mathbf{T}} \cdot \hat{\mathbf{I}}, \quad (4.7)$$

where  $\underline{\mathbf{T}}$  is the anisotropic hyperfine matrix which is a traceless  $3 \times 3$  term.

The hyperfine parameter  $\underline{\mathbf{A}}$  is a  $3 \times 3$  matrix and can be expressed in full as:

$$\underline{\mathbf{A}} = \underline{\mathbf{T}} + A_s \mathbf{1}, \quad (4.8)$$

where  $A_s$  is the trace of  $\underline{\mathbf{A}}/3$  and  $\mathbf{1}$  is a unit matrix.

Calculated hyperfine parameters are the Eigenvalues of  $\underline{\mathbf{A}}$ . An Eigenvalue that aligns along the axis of a defect that is axially symmetric is labelled as  $A_{\parallel}$ , and two Eigenvalues that are perpendicular to the defect are labelled  $A_{\perp}$ ; these have the same value as one another. These are related to isotropic and anisotropic coupling constant  $A_s$  and  $A_p$  respectively via,

$$A_s = \frac{A_{\parallel} + 2A_{\perp}}{3} \quad (4.9)$$

and

$$A_p = \frac{A_{\parallel} - A_{\perp}}{3}. \quad (4.10)$$

These are labelled as such, as  $A_s$  originates from the  $s$ -states and  $A_p$  depends on  $p$ -states (as well as states where  $l > 1$ ).

As the hyperfine interaction involves spin density close to the nucleus, pseudopotential wave functions are not suitable and instead a true wave function should be used. As most calculations are performed with the use of pseudopotentials, an all-electron wave function is then *reconstructed* [85, 86], in the case of hydrogen there are no core electrons so core reconstruction is not necessary.

GGA has a tendency to overestimate bond lengths. A large change of +10% in C–H bond length, leads to a difference of 13 MHz in calculated  $A_s$  hyperfine constant and 1 MHz in  $A_p$  for the hydrogen in the NVH<sub>0</sub>,  $S = 1$  defect for example. For the nitrogen,

the  $A_p$  differs by 0.4 MHz but the  $A_s$  term differs by  $\sim 3$  MHz.

#### 4.7 Electrical levels

States that are introduced into the band gap (Section 4.4) when defects are placed into the crystal can give an indication of which charge state the defect can adopt and whether acceptor (become more negative) or donor (become more positive) levels can be found.

Donor and acceptor levels may be found using the formation energy ( $E_f$ ) method. It compares the energy of the optimised systems in different charge states and the levels are derived using Equation 4.11. The formation method is also used to determine the heats of formation associated with the formation of a defects. The formation energy is determined as follows:

$$E_f(\mu_e(Y, q)) = E_{\text{tot}}(Y, q) - \sum \mu_a + q(E_v(Y, q) + \mu_e) + \xi(Y, q), \quad (4.11)$$

where  $E_{\text{tot}}$  is the calculated total energy of the system  $Y$  in a charge state  $q$ .  $\mu_a$  and  $\mu_e$  are the chemical potential of the atoms and electrons, respectively.  $\mu_a$  may be calculated from a reference state for each element in  $Y$ , it is typically taken from their most common structure in diamond, or a range of values may also be taken. The number of types of atoms is constant for electrical level calculations so  $\mu_a$  can be set to any value without loss of generality; when comparing the formation of defects, if the types of elements do not balance the choice of  $\mu_a$  is important. For example with a defect containing nitrogen, a reasonable reference state to take could be the P1 centre, a common nitrogen defect in diamond that would be available to aggregate further.  $E_v$  is the energy of the valance band top and  $\xi$  is a correction for the periodic boundary.  $\xi$  is dependent on the charge of the system, particularly the Madelung correction (charge–charge interaction) which scales as  $q^2$ , therefore there is a greater error in electrical levels that involve higher charge states [87]. The larger the cell the smaller  $\xi$  is. In a 1000 atom cell for the (+/0) transition, the correction is about 0.1 eV, and approximately

0.2 eV for the  $(-/-2)$  transition.

The electrical levels that correspond to the defect are found when the electron chemical potential corresponds to the same energy for two charge states of the defect, these are labelled as  $(+/0)$  (donor level) and  $(0/-)$  (acceptor level) in Figure 4.5. The donor levels will move towards the valence band, and acceptor levels toward the conduction band when  $\xi$  is included.

In Figure 4.5 for example, if the electron chemical potential of the diamond is midgap (or below the donor level at 3 eV) then the illustrated defect will be in its positive charge state when in equilibrium. If the electron chemical potential lies between the donor and acceptor level the defect will be neutral and above the acceptor level the defect in equilibrium will be negatively charged.

As previously mentioned in Section 4.4, electrons in defect states introduced into the band gap may be thermally or optically excited into the conduction band and this transition can be quantised in optical absorption experiments for example. The loss of the electron from the defect to the surrounding bulk means that the defect is now ionised, i.e the charge of the defect has changed. The added electron in the conduction band increases the conductivity of material and this change can be detected in photoconduction spectra, whereby light optically excites an occupied defect state into the conduction band inducing a current change. By comparing optical absorption and photoconduction spectra donor levels can be detected. Investigating the resistance of the diamond as temperature changes, quantifies the energy when the defect is thermally excited and this can be used to further confirm the donor level. The electron that is ionised from the defect into the conduction band may relax into another state associated with another defect. This is a charge transfer process and is generally driven by illuminating the sample with UV light. Conversely charge transfer may also occur via electrons excited into acceptor states creating holes that can move through the valence band and that can then be filled by an electron associated with another defect, this charge transfer process is generally driven by the application of heat (enough to excite electrons but not enough to breakdown the defect).

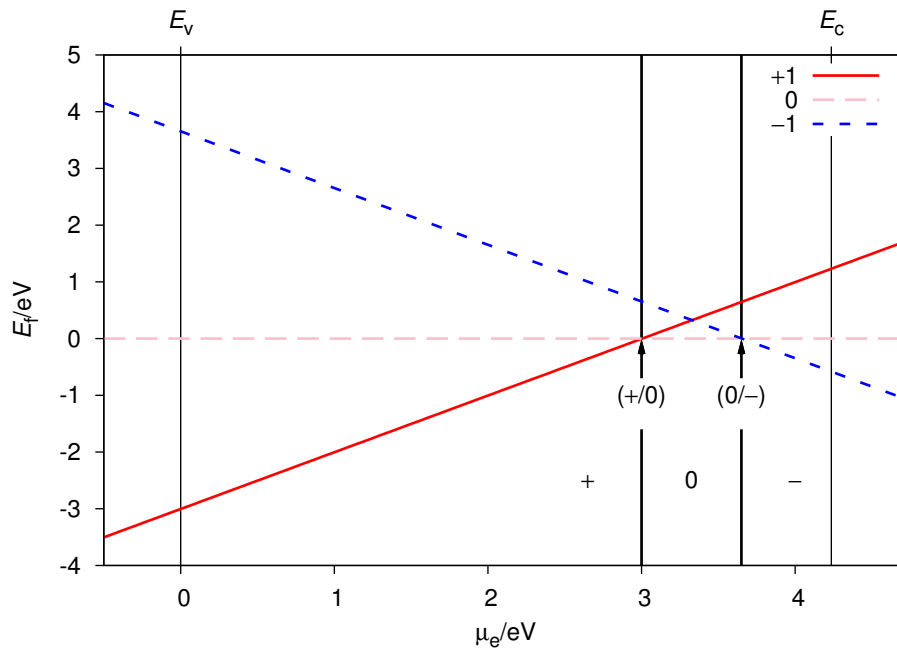


Figure 4.5: Schematic of the formation energy for each possible charge state for a defect as a function of the electron chemical potential, ranging from the valence band maximum  $E_v$  to conduction band minimum  $E_c$ . The donor level is labelled as  $(+/0)$  and an acceptor level labelled as  $(0/-)$ , they occur when the formation energy of the corresponding charges equal. In equilibrium the charge formed is that with the lowest formation energy, the equilibrium charge is labelled either side of the donor and acceptor levels.

Charge transfer is an important process as it changes the charge of the defect and not the composition of atoms in the defect. Consequently the defect that may be unobservable using one technique may become observable once the charge has changed, for example in EPR spectroscopy (Section 4.6) the defect may become paramagnetic and therefore it may be possible to detect.

#### 4.8 Binding energy

The binding energy ( $E_b$ ) of a defect refers to the energy difference between the defect (i.e. the product) and its possible constituents (i.e. the reactants). It is calculated as the difference in formation energies (Section 4.7) of the reactants and products and in

general is given by,

$$E_{b(\text{reactants})}(\mu_e) = \sum E_{f(\text{reactants})} - \sum E_{f(\text{products})}. \quad (4.12)$$

If charge and atomic composition is conserved in Equation 4.12 then the result is a constant. Nevertheless, all possible combinations of reactants whether the charge is conserved or not can be taken into account when the binding energy is plotted as a function of electron chemical potential. This results in something similar to Figure 4.5 seen in Section 4.7. But instead of the formation energy of each charge for a defect plotted as a function of electron chemical potential, the binding energy for each possible reaction is plotted as a function of electron chemical potential.

Figure 4.6 is an example of the reaction ' $N_2V + H_i = N_2VH$ ', in this example only three reactions of varying charge have been included for clarity. As previously discussed, the level of the electron chemical potential determines in which charge the relevant components of the reaction will be found, therefore as you move through the band gap the availability of the products and reactants changes. The reaction which corresponds to the minimum binding energy as the electron chemical potential varies will occur in equilibrium and it is this line that is plotted in further calculations. Each corresponding reaction is labelled in each section through the band gap in Figure 4.6 and each section range is determined by the donor or acceptor levels of the defects involved in the reaction. When charge is conserved in the reaction the binding energy remains a constant when the electron chemical potential changes (Eqn 2 in Figure 4.6). A change in gradient is determined by the change in charge in a reaction, for example Eqn 1 in Figure 4.6:  $N_2V^0 + H_i^+ = N_2VH^0$ , has an imbalance of one more electron in the product, therefore there is a positive gradient.

The binding energy provides some information about the relative stability of the defects involved, it can be used to infer the temperature dependence of the defects as it can give an indication when the defect would dissociate or remain stable during heat treatments or during growth.

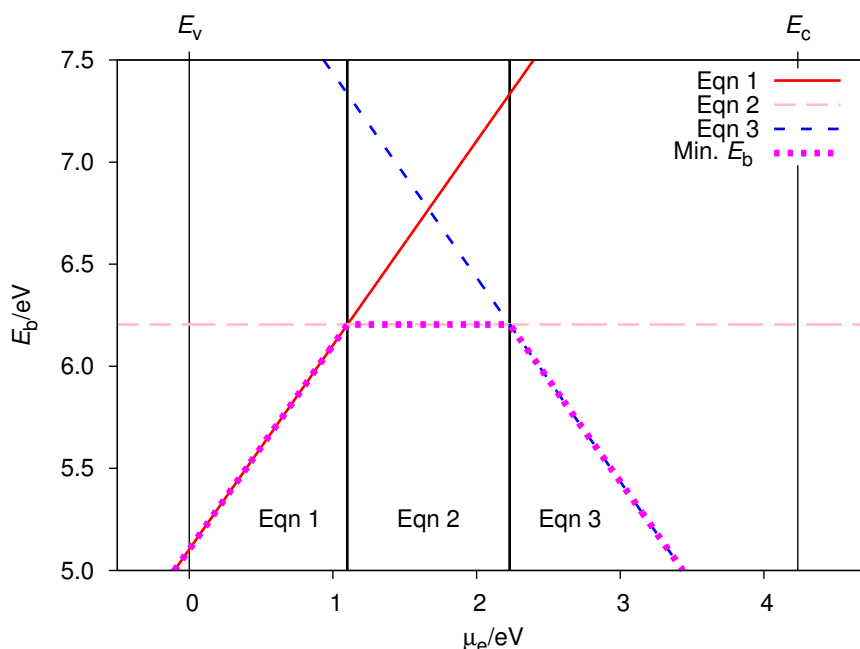


Figure 4.6: Schematic of the binding energy of  $N_2 VH^0$  formed by the addition of  $N_2 V$  to  $H_i$  in their corresponding equilibrium charge states as the electron chemical potential varies from the valence band maximum  $E_v$  to conduction band minimum  $E_c$ . The lowest binding energies as the electron chemical potential varies are highlighted and it is this line that is plotted in Section 11 (magenta dashed line), the corresponding Equation that will occur in equilibrium is also labelled. Eqn 1:  $N_2 V^0 + H_i^+ = N_2 VH^0$ , Eqn 2:  $N_2 V^0 + H_i^0 = N_2 VH^0$  and Eqn 3:  $N_2 V^- + H_i^0 = N_2 VH^0$ .

The binding energy quantifies the difference in energy between the products and reactants (Figure 4.7), it does not however give an indication about the reaction mechanism. This includes an energy barrier associated with the diffusion of the reactants and the binding mechanism of the reactants combining to form the products. Consequently it is unknown whether the products formed are the thermodynamic or kinetic products (Figure 4.7).

The thermodynamic products are formed when the reaction mechanism has a higher activation energy (this is the largest energy barrier in the reaction process, in Figure 4.7 the activation energy for both reactions under thermodynamic and kinetic control is shown to occur in the binding mechanism but it is not forced to be). The thermodynamic

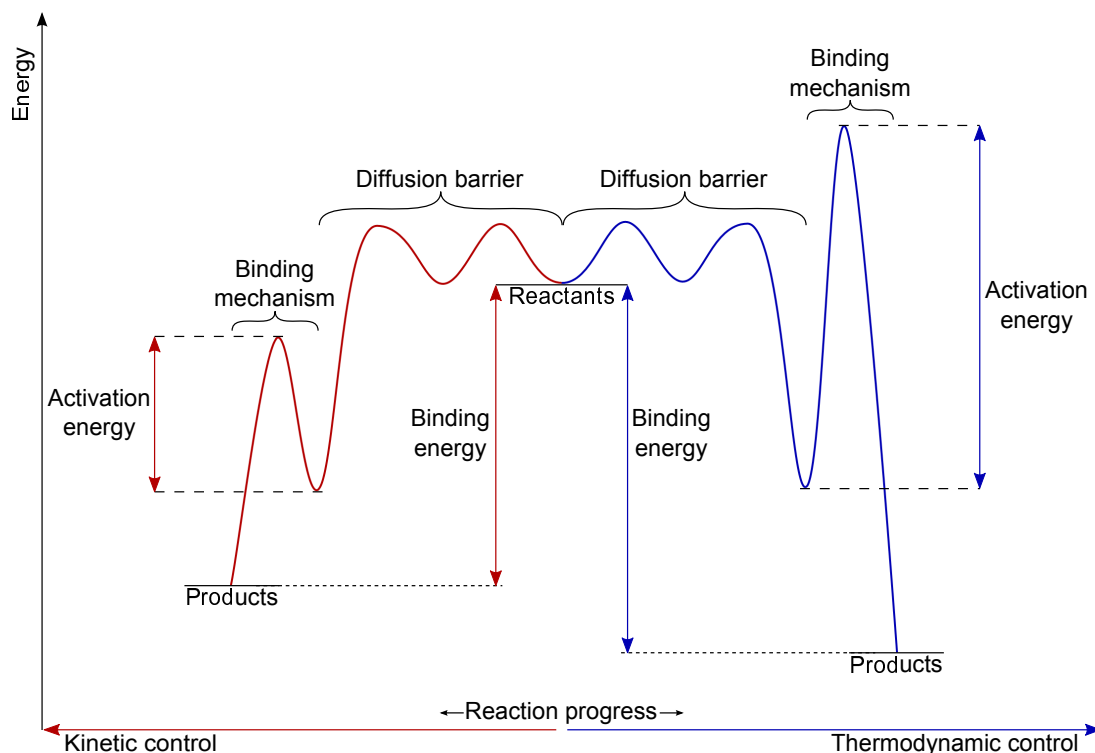


Figure 4.7: A reaction diagram depicting a reaction that can proceed under kinetic control (red and to the left of the centre) or under thermodynamic control (blue and to the right of the centre). The reaction process is broken down into a diffusion barrier and a binding mechanism. The activation energy and binding energy associated with each reaction process is labelled.

products also have the largest binding energy associated with them. Adversely the kinetic product has a smaller activation energy and smaller binding energy. Both reactions shown in Figure 4.7 are exothermic as the products are lower in energy than the reactants. The introduction of a catalysis (something that is not consumed during the reaction) lowers the activation energy in each reaction process.

In general a reaction may proceed to result in the kinetic products if enough time is available and if the energy provided is more or equal to the activation energy but less than then activation energy associated with the thermodynamic products. Even with the kinetic products formed, if enough energy is provided to exceed the activation energy associated with the thermodynamic products it is possible for a reaction to reverse and

proceed to ultimately form the thermodynamic products.

The rate the reaction proceeds is determined by the rate-limiting step. In general the rate can not be inferred from a chemical equation for the reaction but it is established experimentally. The concentrations of the reactants, the proximity to each other and the size of the activation energy may also contribute to rate-limiting step. An increase in temperature will generally increase the rate of the reaction. There is also an entropic contribution when considering the rate of the reaction which becomes larger as temperature is increased.

### 4.9 Diffusion barrier

To find minimum energy pathways between different orientations of defects or migration of a defect as a whole, the nudged elastic band (NEB) technique may be used [88, 89]. The minimum energy of the initial and final structures are first found. The saddle point is then the structure with the highest energy along the reaction path. The minimum energy path between each structure is found by linearly interpolating a number of structures called 'images' along a path and optimising each structure/image. The number of images is chosen to be odd to capture the saddle point. Each image is connected by spring forces to ensure equal spacing along the reaction path, hence the term NEB. A variant of the NEB process is where the saddle point can 'climb' during the optimisation; this can lead to a geometry that is closer to the transition state.

The resulting energy barrier (Figure 4.8) provides information about the likelihood of the reaction and it can give an indication as to whether the reaction occurs classically or as a result of quantum tunnelling.

The energy barrier in Figure 4.8 is considered symmetrical as the initial and final image are different orientations of the same defect structure. The barrier height can therefore be taken as the energy of the saddle point structure in Figure 4.8. The barrier width is difficult to quantify as all atoms move. In the case of a hydrogen orientating between equivalent carbon sites in examples seen in Chapter 11 a reasonable estimate taken is the difference between the position of the hydrogen in the initial and final structure

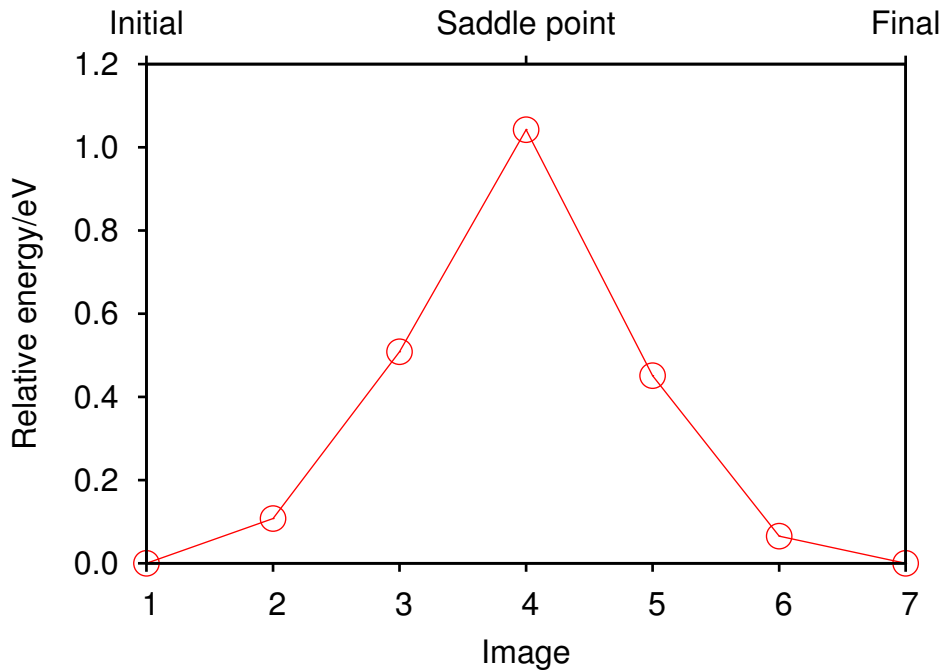


Figure 4.8: An illustration of a minimum reaction pathway from the initial structure to the transition point at the saddle point to the final structure. The energy of the initial and final structure in this are the same and chosen to be at zero.

as the surrounding carbons are not greatly influenced by the transition.

An estimation of the classical hopping rate can be calculated by:

$$\text{rate} = Ae^{-E_a/k_B T}, \quad (4.13)$$

where  $A$  is the attempt frequency (chosen as the phonon frequency of diamond in this case),  $E_a$  is the activation barrier, in this case it is the barrier height,  $k_B$  is Boltzman's constant and  $T$  is the temperature.

In the theoretical framework already discussed the motion of the atoms are taken to be classical. However hydrogen, as it is the lightest element in the periodic table has the potential to behave according to quantum mechanics. The zero-point motion of the proton ( $H^+$ ) is not included in these calculations but it has an effect on migration barriers. Although it is important to note the migration barriers are relatively small [61].

Quantum-mechanical interactions are important in cases like the nitrogen-vacancy-hydrogen defect, as the rate at which the hydrogen moves between the available symmetric carbon radicals can alter the perceived symmetry viewed in experiments like EPR (Section 4.6), from  $C_{1h}$  if it remains static to  $C_{3v}$  if an average of the hydrogen on each carbon is taken.

### 4.10 Summary

This Chapter discussed the methods that AIMPRO uses to calculate quantities that can be directly compared to experimental results. DFT, has proven high accuracy, in terms of comparison to the experimental observables and with the identification of defects but it is important to take into account all evidence both theoretical and experimental to exploit the full plethora of information prior to identifying the defect. The next Chapter applies these methods above to a series of point defects in diamond.

## **Part II**

# **Applications**

## Chapter 5. Investigated defects

### 5.1 Introduction

Defects introduced into the diamond may modify the material's properties either beneficially, for example in the case of the addition of boron to create p-type diamond, or deleteriously, for example in the case of donors in n-type material being compensated by impurity-vacancy complexes [90]. It is therefore necessary to know what defects are contained within a diamond and how they can affect the properties of the diamond.

The following Chapters focus on point defects that contain nitrogen, and those comprised from nitrogen combined with hydrogen and a vacancy. As previously mentioned, nitrogen is the most abundant defect found in diamond, so much so that its presence or lack of is used to classify them (Section 1.5).

Hydrogen is generally the most abundant element in the gas phase during CVD growth and it is thought to be generally found in external growth surfaces and grain boundaries [91, 92]. Under certain growth conditions hydrogen has also been found to be incorporated into the bulk [93]. Although it is present during growth of CVD diamonds, the concentration of hydrogen incorporated can vary from very low in high quality films [91] to 2000 ppm in polycrystalline diamond [92] which consequently has poor optical and electronic properties. Compared to nitrogen few defect centres involve hydrogen, although assignments have been made to centres that involve a lattice vacancy a hydrogen and another impurity like nitrogen [94, 95, 86] or silicon [96, 97].

The defects belonging to the group  $N_n V H_m$ , where  $n + m \leq 4$  (Figure 5.1a) have been

investigated and are referred to as a set of defects throughout this Thesis. A set may also refer to a group of the defects in the following Chapters, for example the set where  $n + m = 4$  is discussed in Chapter 10. Figure 5.1b is the NVH defect, an example of where  $n + m = 2$ . As a nitrogen is added in the set, it replaces a carbon surrounding the vacancy. As a hydrogen is added to the set it terminates a carbon's radical surrounding the vacancy. The set is limited to  $n + m \leq 4$  as additional nitrogens or hydrogens are relatively chemically unstable. As you move horizontally and vertically across in Figure 5.1a, the number of unstable radicals localised on the carbon around the vacancy decreases until no radicals remain and the defect is considered fully saturated ( $n + m = 4$ ). The shaded diagonals (from top right to bottom left) indicate defects that are isoelectronic with each other i.e.  $n + m = 1, 2, 3$  and 4. They are considered isoelectronic as they have the same number of radicals; the nitrogen has a stable lone pair which is similar to the saturated carbon radical via the addition of a hydrogen.

All of the top row of Figure 5.1a have been uncontentiously identified both experimentally and theoretically. The second row in Figure 5.1a have also been investigated. The more saturated the defect the more stable it is thought to be and consequently is formed at higher temperatures but although defects containing multiple nitrogens (column 3–5 in Figure 5.1a) have been found, multi-hydrogen containing defects (row 3–5 in Figure 5.1a) have avoided detection and only  $N_2 VH_2$  is thought to have been recently identified experimentally [12]. Experimental and theoretical details pertaining to each defect in the set are discussed further in the following Chapters.

Chapters 7–10 discusses the structural properties of the defects, electronic properties, potential electrical levels, hyperfine interactions and the vibrational modes. Chapter 6 focuses on the hyperfine interaction in detail for the P1 centre, the simplest nitrogen containing defect: the substitutional nitrogen in the neutral charge state.

Natural and synthetic HPHT diamonds have similar aggregation process where substitutional nitrogen anneals out to form A-centres. B-centres ( $N_4 V$ ) are then formed at higher temperatures and are considered fully saturated. CVD diamond generally has a higher concentration of hydrogen due to the growth environment and the role

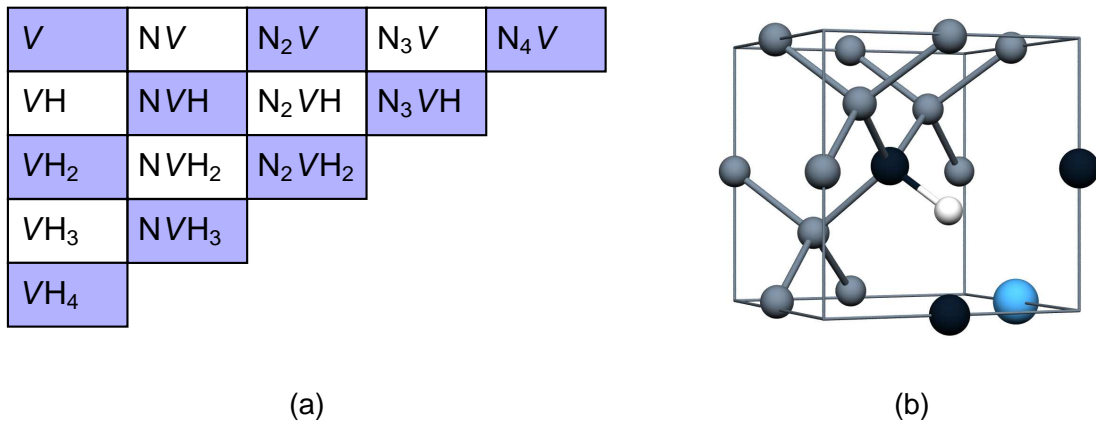


Figure 5.1: (a) A diagram of the set investigated, including the isolated vacancy. The highlighted diagonals going from top right to bottom left represent the combinations possible when  $m + n = 0, 1, 2, 3$  and  $4$  in  $N_n V H_m$ . (b) A schematic of the NVH defect. The nitrogen is the slightly larger blue atom, the hydrogen is white and remaining carbons surrounding the vacancy are dark grey and slightly larger than the surrounding carbons.

of hydrogen in the aggregation process is unknown. Energetic processes within and between the defects are discussed in Chapter 11 where additional defects to those in Figure 5.1a (including the vacancy) are taken into consideration. Also included are the A-centre, nitrogen and hydrogen interstitial ( $N_i$  and  $H_i$  respectively) and substitutional nitrogen and hydrogen ( $N_s$  and  $H_s$ ) respectively.

## 5.2 Method

The method used in the following Chapters unless otherwise stated is below. DFT was implemented within AIMPRO. The PBE formulation [62] of the GGA was used [64, 63]. HGH [65] norm-conserving separable pseudopotentials were used to model the atoms and the Kohn-Sham Eigen-functions were expanded using atom centred Gaussian basis sets [98]. The basis set for carbon consists of eight fixed linear combinations of  $s$  and  $p$ -orbitals and a set of five  $d$ -orbitals for polarisations. The hydrogen basis set has 12 functions in total constituting of three sets of independent  $s$

and  $p$  functions. The nitrogen basis sets constituted of four sets of  $s$ ,  $p$  and  $d$  functions. The computational parameters chosen underestimates the bulk modulus by 0.7% and overestimates the lattice constant by 0.2%. The band gap is also underestimated at 4.2 eV, an inherent underestimation corresponding to the underpinning methodology [99]. This is in agreement to previous similar calculations.

Exceptionally large cubic simulation supercells of 1000 host atoms before the defect was introduced were used (i.e. a simulation cell containing the NVH<sub>2</sub> defect will contain 1001 atoms in total). The large simulation cell allows for the reciprocal space to be sampled using only the gamma-point.

The conjugate gradient method was used to iteratively obtain the equilibrium structures. The structure is taken to be in equilibrium when the energy change between each step is less than 1 meV and the forces are less than  $10^{-3}$  au.

Electrical levels have been obtained using the standard formation energy method (Section 4.7), and vibrational frequencies are calculated in accordance to Section 4.5.

The hyperfine calculations were calculated in accordance to Section 4.6. The reconstructed atoms were limited to the first nearest neighbour carbon atoms, so for example in the VH<sub>3</sub> defect, the carbons surrounding the vacancy plus their first carbon neighbour and totalling 16 reconstructed carbon atoms and three hydrogen atoms. Reconstruction allows the hyperfine calculation to be calculated without the computational difficulties associated with a full all-electron calculation.

The calculation of the formation of the defects followed the method discussed in Section 4.7. As the choice of  $\mu_a$  and  $\mu_e$  determines the formation energy calculated the chemical potential of the atoms are taken from reasonable reference states. For example the chemical potential for a carbon atom was calculated from the bulk value, the nitrogen from the substitutional nitrogen (commonly found in diamond) and the  $\mu_H$  taken from the interstitial complex, so that  $E_i(H_i) = 0$  for example.

The binding energies were calculated using the method in Section 4.8 and diffusion processes were calculated in accordance to Section 4.9.

## Chapter 6. Assignment of $^{13}\text{C}$ hyperfine interactions in the P1-centre<sup>1</sup>

### 6.1 The P1 centre

Nitrogen is a dominant impurity in both natural and synthetic diamond and it forms the basis of the diamond classification system. The simplest nitrogen containing defect in diamond is the P1 centre (an EPR label), is also known as the C-centre which was introduced in Section 1.5. The P1 centre consists of a nitrogen atom substituting a carbon atom in a neutral charge state. The nitrogen bonds with three carbon neighbours, leaving the remaining nearest neighbour carbon with a localised unpaired electron (Figure 6.1). Consequently the neutral defect ( $\text{N}_s^0$ ) is EPR-active and is observed with  $C_{3v}$  symmetry with an effective spin of  $S = 1/2$  [101]. This extended bond between the nitrogen and carbon is due to the electronic repulsion of the nitrogen lone pair and radical localised on the unique carbon, this bond has been calculated to be 24–32% longer than a carbon-carbon bond in the host lattice [70, 102, 103, 104]. This repulsion also shortens the remaining three carbon-nitrogen bonds [105].

The electronic structure of the centre reflects this chemical description of the bonding. There is an energy level just above the valance band which is a consequence of the stable lone pair on the nitrogen and there is band in the upper half of the band gap occupied by one electron which can be attributed to the carbon's radical. This electronic structure creates a deep donor level at 1.7–2.2 eV below the conduction band minimum [54, 106].

---

<sup>1</sup>Results in this Chapter have also been published in [100].

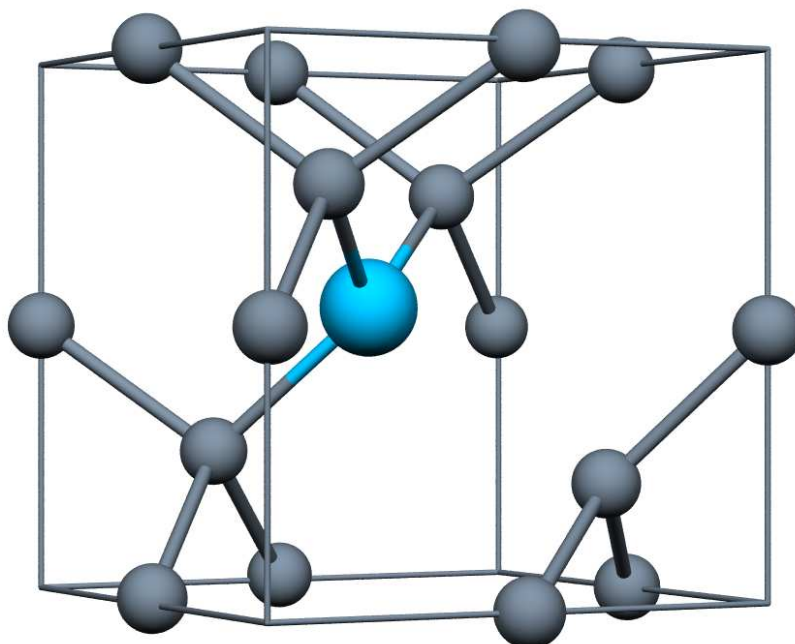


Figure 6.1: The P1 centre. The larger blue atom is the nitrogen and the smaller grey atoms are carbon.

With the removal of the carbon radical, creating a positive defect ( $\text{N}_s^+$ ). The repulsion seen in the neutral defect is lost and the defect has  $T_d$  symmetry. Although as the only unpaired electron is removed, it is no longer detectable in EPR. The negatively charged defect ( $\text{N}_s^-$ ) [107, 108, 109], also removes the unpaired electron rendering it EPR inactive but it increases the repulsion between the nitrogen and carbon resulting in a similar to structure to the neutral defect.

The P1 defect has also been detected in absorption spectroscopy.  $\text{N}_s^0$  gives rise to a yellow colouration in diamonds. Three broad bands at 376, 318 and 270 nm (3.3,

3.9 and 4.6 eV) [110] attributed to  $\text{N}_s^0$  are responsible for this.  $\text{N}_s$  is also observed via FTIR spectroscopy, with peaks at  $1130\text{ cm}^{-1}$  and a local mode at  $1344\text{ cm}^{-1}$  (sharp) [111, 112].  $\text{N}_s^+$  is responsible for peaks at  $1332\text{ cm}^{-1}$  [113] and weaker peaks at 1095, 1050 and  $950\text{ cm}^{-1}$  [114].

This Chapter focuses on the experimental details of the hyperfine interactions relating to the P1 defect, it has been examined experimentally via ENDOR [115, 116] and EPR [101, 117], details of which are discussed below.

Hyperfine interactions between electron and nuclear spins gives an indication of the defect structure but they also play an important technological role, for example in the main decoherence mechanism for NV centres: a closely related defect that has recently been the focus as a development of quantum computing. The defect has the potential to be used as a quantum bit, based on its long spin coherence times at room temperature [118]. The NV centre can be optically spin polarised [119] but the coherence time is limited by  $^{13}\text{C}$  nuclear spins. In order to control and exploit this mechanism it is imperative to understand the hyperfine interaction between the electron spin and the nearby  $^{13}\text{C}$  nuclei.

Table 6.1: Hyperfine interactions assigned to seven  $^{13}\text{C}$  sites that are associated with the P1 centre [117, 116]. Labels used previously are shown in parentheses to aid comparison. Site symmetries (sym.) and degeneracies ( $n$ ) inferred from experiment are also listed.

Hyperfine	Site assignment		$n$	Sym.
	Ref. [117]	Ref. [116]		
$\text{C}_1$	$\text{G}_1(\text{a})$	$\text{G}_1(\text{a})$	1	$\text{C}_{3v}$
$\text{C}_2$	$\text{G}_8(\text{d})$	$\text{G}_8(\text{d})$	3	$\text{C}_s$
$\text{C}_3$	$\text{G}_2(\text{c})$ or $\text{G}_3(\text{b})$	$\text{G}_2(\text{c})$	3	$\text{C}_s$
$\text{C}_4$	$\text{G}_2(\text{c})$ or $\text{G}_3(\text{b})$	$\text{G}_3(\text{b})$	3	$\text{C}_s$
$\text{C}_5$	$\text{G}_4(\text{e})$ or $\text{G}_5(\text{g})$	$\text{G}_4(\text{e})$ or $\text{G}_5(\text{g})$	$5.7 \pm 0.6$	$\text{C}_1$
$\text{C}_6$	$\text{G}_9(\text{f})$		$3.6 \pm 0.6$	-
$\text{C}_7$	$\text{G}_4(\text{e})$ or $\text{G}_5(\text{g})$		$8.4 \pm 1.8$	-

As previously mentioned the P1 centre has been experimentally identified via EPR

[101, 117] and ENDOR [115, 116]; Table 6.1 lists the assignments and labelling used from the experimental literature [117, 116] and Figure 6.2 is a visual aid showing sites that are in the vicinity of the defect. Sites were assigned based on the underlying geometry of the defect, proximity to the centre and degeneracy of the sites. More distant sites that have lower symmetries and uncertainties in the degeneracies means that these assignments should be viewed cautiously.

Seven carbon groups were assigned from experiment. Principal values and directions were determined for  $\text{C}_1$ – $\text{C}_5$ . More distant carbons:  $\text{C}_6$  and  $\text{C}_7$  were only assigned using an isotropic value and it is unclear whether the anisotropy has not been resolved or they are purely isotropic interactions. There is also an uncertainty in site degeneracies for sets  $\text{C}_5$ – $\text{C}_7$ , resultant from the small interactions making quantification difficult or possibly from the combination of two or more similar groups of  $^{13}\text{C}$  to produce the spectra.

This Chapter compares experimental data for  $^{14}\text{N}$  and  $^{13}\text{C}$  hyperfine interactions to density functional theory calculations. On the whole the theory agrees with the experimental site assignments but some sites need reconsidering. The P1 centre also follows the trend seen in other paramagnetic defects [120], whereby the magnitude of the hyperfine interaction is related to not only the distance from the defect but is also dependent on the chemical bonding connecting the site to the defect.

## 6.2 Computational method

The AIMPRO code [63, 64] was used to perform GGA calculations [62]. The Kohn-Sham Eigen-functions were expanded using a Gaussian basis [98]. The Kohn-Sham potential and density used a plain wave expansion [121] to calculate the matrix elements of the Hamiltonian. To achieve well converged total energies a cut off of 175 Ha was used. The atoms were modelled using norm-conserving, separable pseudopotentials [65]. 40 functions per atom made up of independent sets of  $s$ ,  $p$  and  $d$ -orbitals with four widths were used. The cell was optimised using the conjugate gradient method, with the forces on the atoms less than  $10^{-3}$  au in the optimised

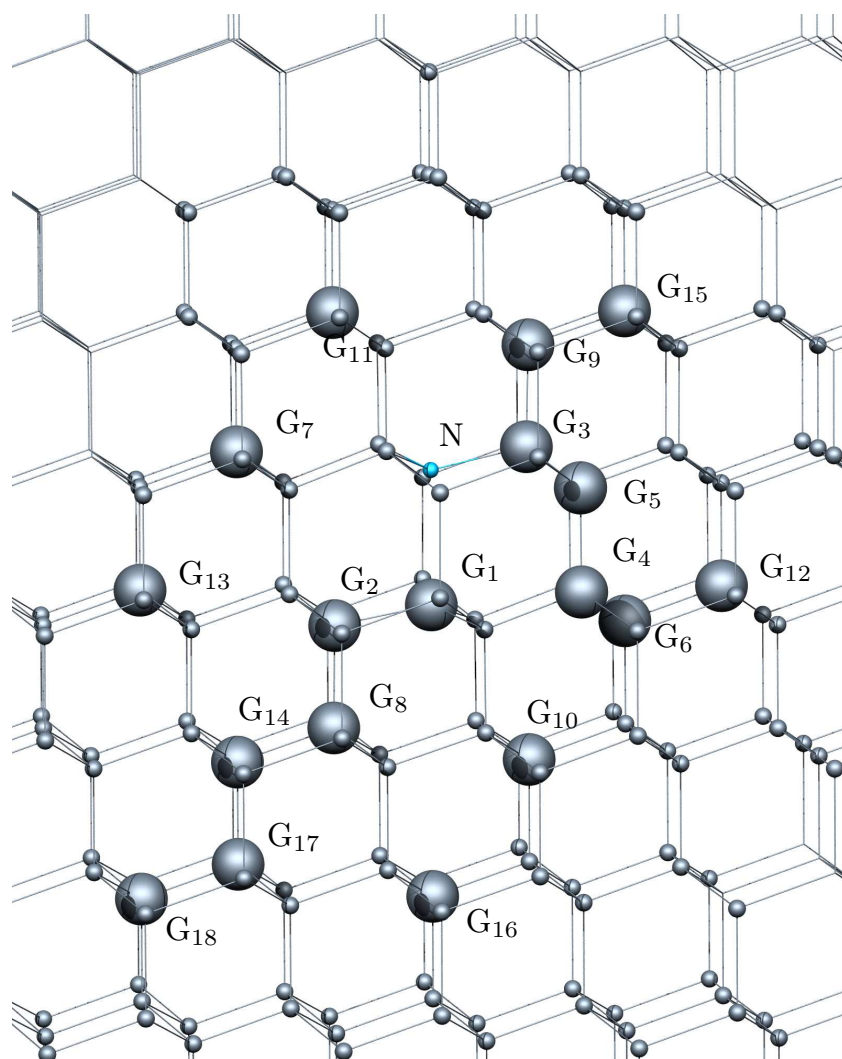


Figure 6.2: A schematic to show the carbon sites in the vicinity of the P1 centre. The carbon radical is labelled  $G_1$ , with  $G_2$ – $G_{18}$  labelling sites that are progressively more distant from the centre of the C–N broken bond. The labels show sites with a calculated RMS hyperfine value of  $> 1$  MHz. Other sites that are indicated with smaller spheres, have also had their hyperfine values calculated. The horizontal and vertical axes are  $[11\bar{2}]$  and  $[111]$ , respectively, with a slight tilt applied so all sites can be seen.

structure. The last step in optimisation the change in the total energy was less than  $10^{-5}$  Ha. In this case the calculated lattice constant and bulk modulus of pure diamond was 0.2% overestimated and 0.5% underestimated respectively. The band gap was

calculated to be 4.2 eV which is close to previous calculations [99]. Periodic boundary conditions were applied to a cell of 512 atoms. The Brillouin zone was sampled using an MP  $2^3$  grid [67], which results in a total energy converged to less than 1  $\mu\text{eV}/\text{atom}$ . A systematic polynomial basis [122] was used to model the hyperfine interactions of the  $^{14}\text{N}$  and  $^{13}\text{C}$ . This method has been shown to be quantitatively accurate for similar defects in diamond [123, 124, 125], including  $\text{N}_s$  pairs [104].

The hyperfine calculations combine pseudopotentials and reconstructed all-electron wave functions in the core region [85, 126]. This method removes the computational difficulties associated with a full all-electron calculation [86] whilst maintaining a rigorous approach as the reconstruction of the core allows the calculation of the hyperfine tensor element within a frozen-core all-electron wave function approximation. Nitrogen pairs are related to the P1 centre as they can be described as perturbed P1 defects. Nitrogen sites have been experimentally resolved for EPR centres: W24, N1, W7, M2, N4 and M3. For N1 the  $^{13}\text{C}$  hyperfine has also been experimentally resolved. Values calculated for the nitrogen sites and carbon sites in the case of N1 in reference [104] are in good agreement with experiment. In the case of N4, not only is it quantitatively accurate but the calculations predict the dynamical motion of the site. It is important to note that generally in EPR only *relative* signs of the hyperfine principal values are resolved not the *actual* sign. For the N1 defect, the sign was resolved experimentally using electron double nuclear resonance (ENDOR) [127]. The results matched theoretical calculations of hyperfine principal values in both sign and magnitude for the ionised nitrogen site in the N1 defect [104]. The ionised nitrogen in the N1 defect is equivalent to the G2 site in Figure 6.2.

Hyperfine calculations have several independent sources of error. For example in the choice of functional and core reconstruction [128]. However this approach yields similar levels of accuracy found in an all electron Green's function methodology [72] when used to model point defects in diamond [120]. All plane wave calculations [129] also achieve a similar level of accuracy for calculating  $^{13}\text{C}$  hyperfine values.

We conclude that our method adopted is of comparable accuracy to similar studies

on defects in diamond and it can successfully predict magnitude, sign and direction as shown in theoretical studies of nitrogen pair defects for  $^{13}\text{C}$  sites near by to the nitrogen.

### 6.3 Results

The optimised structure of  $\text{N}_s^0$  is trigonal with a single broken C–N bond (Figure 6.1). This bond is calculated to be 31% longer than surrounding C–C bonds. Hyperfine interactions were calculated at the  $^{14}\text{N}$  site and at  $^{13}\text{C}$  sites that are in the vicinity of approximately 10 Å from the defect centre. The results are broken down into sites that are progressively more distant from the centre.

Spin density is localised in orbitals in the lone pair on the nitrogen and an  $sp^3$  radical on  $G_1$  (Figure 6.2). In the neutral defect, this creates relatively large hyperfine interactions on the  $^{14}\text{N}$  and  $G_1$  atoms. For the  $^{14}\text{N}$  and  $G_1$  sites the calculated parameters (Table 6.2) are in reasonable agreement with experiment [115], observing that the principal directions are defined by symmetry of the defect so no nuisance can be picked out from this aspect. It is however noted that the the RMS value for  $^{14}\text{N}$  is underestimated by 7% and the value for  $G_1$  is overestimated by approximately 11%.

The  $C_2$  system has been assigned to the  $G_8$  sites. They have the correct mirror symmetry and the calculated principal values (Table 6.2) agree. The angle is not defined by symmetry and it is found to be within  $3^\circ$  of experiment. The calculations therefore confirm the assignment.

The analysis used above can be similarly applied to  $C_3$ , assigning it to the  $G_2$  site. Again the details are listed in Table 6.2. The calculated symmetry is correct, the magnitude of the principal values agree and the directions are within  $7^\circ$  of experiment. The sign difference seen in Table 6.2 is not problematic, as mentioned previously the signs of the principal values in experiment are not resolved. This is in poorer agreement when compared to previous sites but it is believed to be confidently assigned.

It is likely that the current assignment of  $C_4$  to  $G_3$ , which labels the three carbons adjacent to the nitrogen is incorrect. Although the symmetry is correct we are lead to believe this is so as the calculated results of the principal values are much smaller

Table 6.2: A comparison of calculated hyperfine tensors (MHz) for the P1 centre in diamond to experimental values taken from references [115, 117, 116]. Listed are the values for the  $^{14}\text{N}$  and  $\text{C}_1$ – $\text{C}_4$  systems in accordance to labelling in Figure 6.2. The direction taken as the principal value of the hyperfines matrices are given as  $(\theta, \varphi)$ .  $\theta$  is the angle with [001] and  $\varphi$  is the angle of the projection of the direction onto the (110) plane measure from [100] towards [010]. The relative intensity in experiment [117] and the number of equivalent sites is given by  $n$ .  $d$  is the distances from the centre point between the  $\text{G}_1$  and the N site in units of  $a_0$ .

		Experiment		Calculation						
$n$	Sym	$A$	$(\theta, \varphi)$	$n$	Sym.	$A$	$(\theta, \varphi)$	$d$		
$^{14}\text{N}$	1	$C_{3v}$	$A_{\parallel} = 114.032$ $A_{\perp} = 81.318$							
				$^{14}\text{N}$	1	$C_{3v}$	104 68	0.284		
$\text{C}_1$	1	$C_{3v}$	$A_{\parallel} = 340.8$ $A_{\perp} = 141.8$							
				$\text{G}_1$	1	$C_{3v}$	379 173	0.284		
$\text{C}_2$	3	$C_s$	$A_1 = 30.92$ $A_2 = 40.29$ $A_3 = 31.66$	(90, 315) (58.66, 45) (31.34, 225)	$\text{G}_8$	3	$C_s$	29 38 29	(90, 315) (56, 45) (34, 225)	0.899
$\text{C}_3$	3	$C_s$	$A_1 = 26.49$ $A_2 = 22.77$ $A_3 = 25.32$	(90, 315) (52.36, 45) (37.64, 225)	$\text{G}_2$	3	$C_s$	–23 –20 –22	(90, 315) (58, 45) (32, 225)	0.545
$\text{C}_4$	3	$C_s$	$A_1 = 10.64$ $A_2 = 14.5$ $A_3 = 10.62$	(90, 315) (59.19, 45) (30.81, 225)	$\text{G}_3$	3	$C_s$	–5 –2 –4	(90, 315) (77, 225) (13, 45)	0.553
$\text{C}_4$	3	$C_s$	$A_1 = 10.64$ $A_2 = 14.5$ $A_3 = 10.62$	(90, 315) (59.19, 45) (30.81, 225)	$\text{G}_{14}$	3	$C_s$	11 14 11	(90, 315) (58, 225) (32, 45)	1.246

(being  $-5$ ,  $-2$  and  $-5$  MHz) than the experimental results for  $\text{C}_4$  at 10.62, 10.64 and 14.5 MHz. The disagreement in assignment is again confirmed when looking at the principal directions: they deviate significantly from those of  $\text{C}_4$  (Table 6.2). An alternative site for the  $\text{C}_4$  group must therefore be sought.

It is proposed that  $\text{C}_4$  is instead assigned to  $\text{G}_{14}$ . As  $\text{G}_{14}$  has the correct magnitude and direction of the principal values (Table 6.2). It is noted that in the experimental literature

the calculated directions are not expressed definitively but instead are reflected in the (110)-plane. Therefore it is likely that the orientation of the  $C_4$  published is different to the core sites. The directions in the calculations listed in Table 6.2 are consistent with the orientation of the structure detailed in Figure 6.2.

Assigning  $C_4$  to  $G_{14}$  may seem surprising as  $G_{14}$  is comparatively further away from the defect.  $G_{14}$  is approximately 35% further away from the defect center and therefore the paramagnetic carbon radical (the main component of the interaction) than  $G_3$ . Nevertheless, the  $G_{14}$  site is considered to be more connected to the carbon radical than the  $G_3$  site, via the  $G_1$ – $G_2$ – $G_8$ – $G_{14}$  chain of bonded sites that all lie in the same mirror plane.

Table 6.3: Sites (with labelling shown in Figure 6.2) that have no site-symmetry in the P1-centre are listed with corresponding hyperfine tensors (MHz). The experimental data is taken from [116]. The symbols are defined in Table 6.2. The  $G_4^\dagger$  and  $G_5^\dagger$  directions relate to defect orientation which yields the best fit to the experimental data, being along  $[1\bar{1}1]$  and  $[\bar{1}10]$  respectively.

Site	$n$	$A_1$	$\theta_1$	$\varphi_1$	$A_2$	$\theta_2$	$\varphi_2$	$A_3$	$\theta_3$	$\varphi_3$	$d$
$C_5$	$5.7 \pm 0.6$	11.76	71.5	33.2	8.58	138.6	101.0	8.12	55.0	137.0	-
$G_4$	6	11	62	155	8	44	279	8	59	47	0.735
$G_4^\dagger$			68	30		133	98		51	139	
$G_5$	6	3	65	185	1	139	244	1	59	291	0.735
$G_5^\dagger$			85	25		126	111		37	120	

Site  $C_5$  has no symmetry in contrast to the sites  $C_1$ – $C_4$  previously discussed but it does have resolved directions.  $C_5$  has been assigned in reference [116] to either  $G_4$  or  $G_5$ . To decipher which assignment is correct Table 6.3 lists the experimental data for  $C_5$  alongside calculated values for all sites reviewed that have matching symmetry. It is clear that  $G_4$  is the best fit as it is the *only* site examined with  $C_1$  symmetry that has the correct order of magnitude for the principal values and the directions are also in good agreement. Therefore site  $C_5$  assigned to  $G_4$  is correct.

The remaining sites  $C_6$  and  $C_7$  only have the isotropic values reported. There are several possible candidates that are potential matches based on the RMS principal

Table 6.4: Remaining calculated hyperfine tensors (MHz) for carbon sites in the vicinity of the P1 centre that have not been previously assigned to  $\text{C}_1$ – $\text{C}_5$ , are listed in decreasing magnitude of hyperfine values. The labelling used is shown in Figure 6.2 and the symbols have the same meaning as in Table 6.2. Additionally to the symbols used previously  $A_{\text{RMS}}$  is the calculated root-mean-square magnitude of the principal values. These results are to be compared to the experimental values from [116] for sites  $\text{C}_6$  and  $\text{C}_7$  at 4.1 and 2.7 MHz, respectively.

Site	$n$	sym	$A_{\text{rms}}$	$A_1$	$\theta_1$	$\varphi_1$	$A_2$	$\theta_2$	$\varphi_2$	$A_3$	$\theta_3$	$\varphi_3$	$d$
$\text{G}_{15}$	3	$\text{C}_s$	4.8	4.3	90	135	4.3	29	45	5.6	61	225	1.252
$\text{G}_6$	3	$\text{C}_s$	4.5	3.7	90	315	3.9	59	45	5.8	31	225	0.894
$\text{G}_3$	3	$\text{C}_s$	4.0	-5.0	90	315	-4.4	13	45	-1.8	77	225	0.553
$\text{G}_9$	3	$\text{C}_s$	3.9	3.2	90	135	3.5	23	225	4.8	67	45	0.906
$\text{G}_{10}$	3	$\text{C}_s$	3.5	2.7	71	224	2.7	90	315	4.8	19	45	1.024
$\text{G}_7$	3	$\text{C}_s$	3.1	2.5	90	135	2.7	75	45	3.8	15	225	0.894
$\text{G}_{11}$	3	$\text{C}_s$	2.7	2.3	90	315	2.4	68	225	3.4	22	45	1.033
$\text{G}_{17}$	3	$\text{C}_s$	1.9	1.5	90	135	1.5	29	225	2.6	61	45	1.596
$\text{G}_5$	6	$\text{C}_1$	1.9	1.0	54	21	1.1	37	211	2.8	85	115	0.735
$\text{G}_{13}$	3	$\text{C}_s$	1.8	1.5	90	135	1.6	64	45	2.2	26	225	1.242
$\text{G}_{18}$	3	$\text{C}_s$	1.4	1.2	28	45	1.3	90	135	1.8	62	225	1.947
$\text{G}_{12}$	3	$\text{C}_s$	1.3	1.0	90	315	1.0	52	45	1.7	38	225	1.242
$\text{G}_{16}$	1	$\text{C}_{3v}$	1.0	0.8	35	225	0.8	90	315	1.4	55	45	1.514

values for these sites listed in Table 6.4. Figure 6.3 highlights the possibilities by plotting the RMS principal value as a function of distance from the point half-way between the nitrogen and  $\text{G}_1$  sites. As a comparison the experimental assignments for the  $^{13}\text{C}$  sites in [116] are shown to demonstrate the level of quantitative agreement in these cases.  $\text{G}_{15}$  down to  $\text{G}_{10}$  carbon sites shown in Table 6.4 are close in magnitude to site  $\text{C}_6$  that has an isotropic principal value of 4.1 MHz. These sites collectively amount to 15 carbon atoms. The relative intensity is  $3.6 \pm 0.6$  for the  $\text{C}_6$  system [117]. This may mean that a single site containing three carbons is responsible for the  $\text{C}_6$  system, consistent with the first five sites listed in Table 6.4, which includes the experimental proposal of  $\text{G}_9$ . Despite this agreement of hyperfine magnitude and the number of sites,  $\text{G}_{15}$ ,  $\text{G}_6$ ,  $\text{G}_3$  and  $\text{G}_{10}$  also remain plausible assignments.

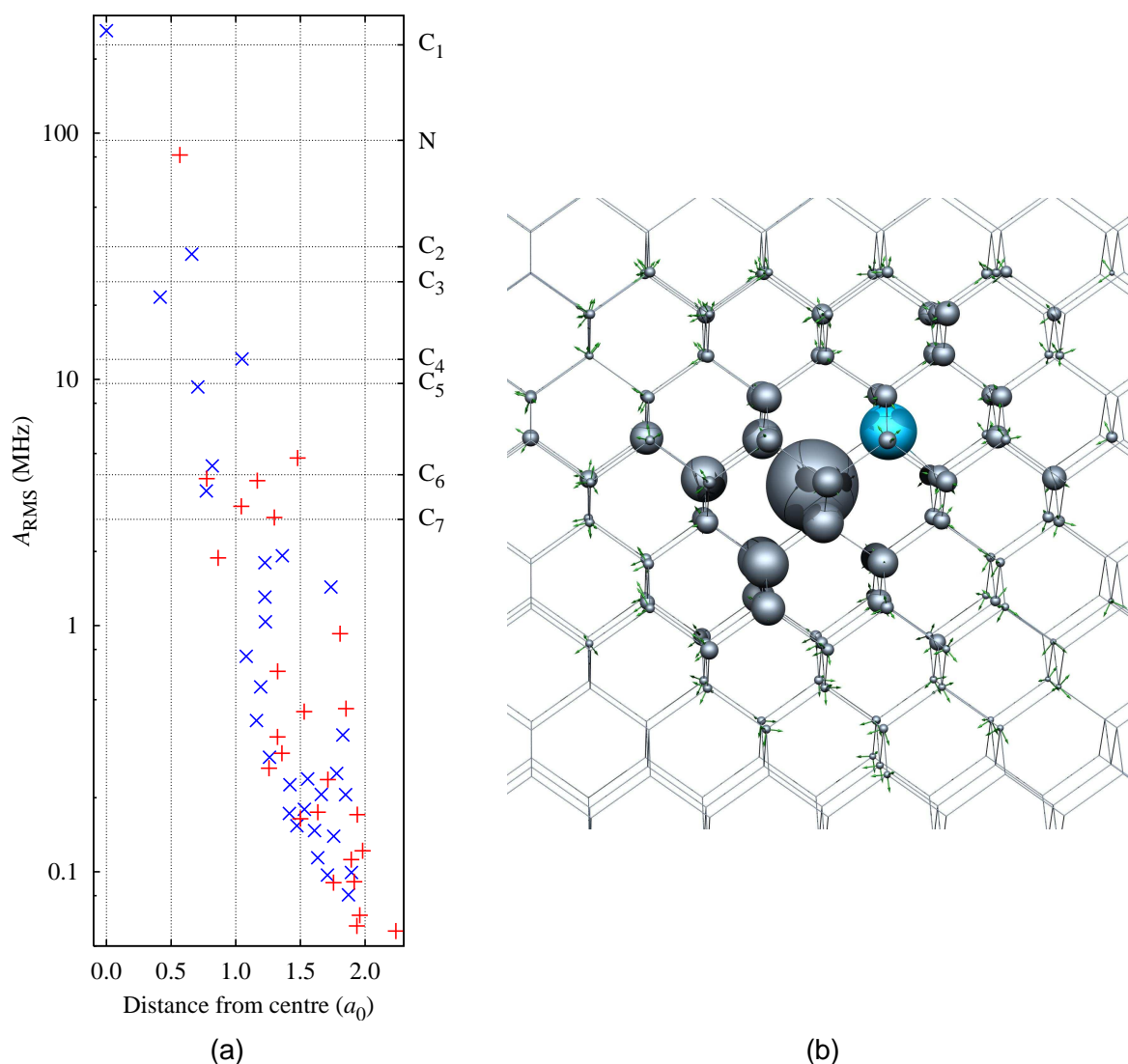


Figure 6.3: (a) The RMS principal values of the hyperfine tensors for  $^{14}\text{N}$  and  $^{13}\text{C}$  as a function of the distance from the carbon radical (Figure 6.2). The red plus symbols are sites above the (111) plane bisecting the N–C bond. The blues crosses are sites below the plane. The RMS values from experiment [116] for the nitrogen site and carbon systems from C<sub>1</sub>–C<sub>7</sub> are labelled as the horizontal grid lines. (b) Is the same data visualised on the structure where the volume of the spheres on the atoms are representative of the RMS hyperfine interaction.

Potential sites that match C<sub>7</sub> have also been assessed. Sites G<sub>10</sub> down to G<sub>5</sub> in Table 6.4 have RMS values within approximately 30% of experiment. It was suggested

[117] that  $G_5$  is a match to one of two sites for  $C_7$ , the other site proposed was  $G_4$  but this is believed to be  $C_5$ . Nonetheless, the relative intensity of  $C_7$  to  $C_1$  at  $8.4 \pm 1.8$  suggests that  $C_7$  is in fact a superposition of more than one group and a conclusive assignment would require experimental data, specifically the determination of principal directions and site degeneracy.

#### 6.4 Summary and conclusions

The hyperfine interactions for  $^{14}\text{N}$  and  $^{13}\text{C}$  at 438 sites in the vicinity of P1 centre in diamond have been calculated and compared to experimental results. The majority of assigned sites agree with experiment apart from three sites that require revision:

1. The  $C_4$  system arises from  $G_{14}$  (Figure 6.2) a more distant set from the carbon radical but with higher connectivity to it. As opposed to the three neighbours ( $G_3$ ) to the nitrogen atom previously suggested.
2. The  $C_5$  system had two sites proposed for the assignment: either  $G_4$  or  $G_5$ . It is ascertained that of the two,  $G_4$  is the correct assignment.
3. The  $C_6$  and  $C_7$  sites had only the isotropic component of the hyperfine interaction resolved experimentally therefore numerous sites could possibly assigned to them. It is proposed that experimental features arise from combinations of unresolved sites. This could explain the difficulties found in determining their anisotropic components and also the number of equivalent sites [117].

Of a more general significance, which is in line with previous observations, is that the hyperfine interaction does not follow a simple relationship with the distance from the centre of the defect [120]. Instead it is correlated with the connectivity to the carbon radical. Consequently this lead to site  $G_{14}$  assigned to  $C_4$  despite it being  $0.98 \text{ \AA}$  more distant from the carbon radical than site  $G_3$ . Nevertheless, it has greater connectivity to the carbon radical. This pattern determined by the bonding can be seen in Figure 6.3, where the size of the sphere indicates the RMS value.

Experimental sites have been redefined using the calculations presented, this consequently emphasises the vital contribution that computational analysis of hyperfine interactions can play and that the method used can quantitatively predict both the principal values and directions, this is particularly important to those centres that are being exploited for quantum information systems.

## Chapter 7. $N_n VH_m$ , where $n + m = 1$ <sup>1</sup>

The defects focused on in this Chapter are highlighted in Figure 7.1a and schematics of both are included in Figure 7.1b and 7.1c.

V	NV	$N_2V$	$N_3V$	$N_4V$
VH	NVH	$N_2VH$	$N_3VH$	
$VH_2$	$NVH_2$	$N_2VH_2$		
$VH_3$	$NVH_3$			
$VH_4$				

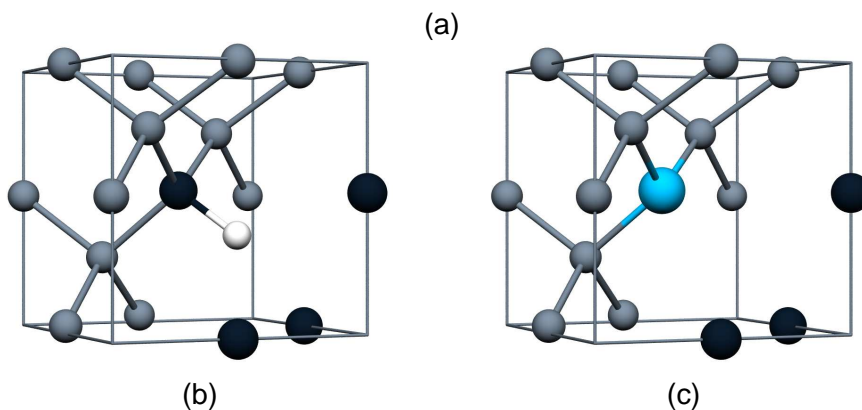


Figure 7.1: (a) Group of possible aggregates that involve nitrogen, a single vacancy and hydrogen. The highlighted defects are those studied in this Chapter. (b) The VH defect. (c) The NV defect. The structure of the defects are fully described in Figure 5.1b.

<sup>1</sup>Some results pertaining to the VH defect are similar to those published in reference [130].

## 7.1 VH

As hydrogen is the most abundant species in the gas phase during the CVD growth process and is found to play a key role in the gas-phase chemistry as it stabilises the growth surface. It therefore may be speculated that it can be included into the diamond in the forms of the investigated set.

Defects of a similar nature are found in silicon for example but unlike in silicon the VH defect in diamond does not undergo symmetry lowering reconstruction to form a  $C_{1h}$  defect, whereby due to Jahn-Teller distortions the neutral defect preferentially forms an extended Si–Si bond. This form of reconstruction is not seen in this case and it instead has been potentially identified by Glover *et al* [131] using EPR, to have trigonal symmetry. The VH defect is believed to be found in its negative charge state with  $S = 1$ , it has also been tentatively assigned to the  $3323\text{cm}^{-1}$  C–H stretch mode [132, 133]. Based on this it has also been suggested that  $VH^0$  may be present in diamond that is grown without nitrogen doping.

There is speculation around the assignment of the VH defect due to the unknown nature of the dynamics of the hydrogen involved in the centre, further analysis of the EPR assignment [131] is presented in Section 7.3.5.

## 7.2 NV

As discussed previously, nitrogen is readily incorporated in as-grown CVD as the P1 centre [134] and also as the NV centre [135]. Both of these defects can be seen simultaneously in the same sample in the neutral and negatively charged state.

Compared to the VH defect, NV has been extensively studied due to possible sensor and qubit applications for example that take advantage of its luminescence and optical spin polarisation properties. But the concentration in natural Type Ib and as-grown CVD is generally too low for application. The concentration however can be increased by irradiation to form vacancies which are consequently trapped by the P1 centre when heated, assuming a sufficient reservoir of P1 centres [136, 19].

Individual centers can be detected via photoluminescence and the  $NV^-$  is characterised by an energy difference between a  $^3A$  to  $^3E$  state of 1.945 eV (637 nm). The presence of  $NV^+$  has been inferred experimentally from photoconversion [137] and electrical biasing [138], whereby they see the  $NV^0$  defect become optically inactive. It has been suggested that by co-doping the diamond to include boron and nitrogen the electron chemical potential is such that the positive charge state becomes accessible due to the boron acting as an electron acceptor [139].

## 7.3 Results

### 7.3.1 Structural analysis

VH in all charge and spin states has  $C_{3v}$  ground state symmetry (Figure 7.1b), it has equivalent symmetry to the isoelectronic defect NV (Figure 7.1c). Whereby the trigonal axis of rotation lies along the C–H bond or from the nitrogen towards the vacancy respectively, perturbations from symmetry in either case do not result in lowering the energy.

The remaining carbon radicals surrounding the vacancy are therefore equivalent, allowing the hydrogen in the case of the VH defect to potentially quantum-mechanically tunnel between carbon radical sites. Tunnelling rates have been previously estimated of the order of a few picoseconds [86, 140]; depending on the process observed depends on the symmetry observed, from a static structure with  $C_{3v}$  symmetry or dynamic structure with perceived  $T_d$  symmetry. For example the rate of a C–H vibration has the order of  $10^{-14}$  s, therefore a vibrational mode is expected to happen many times before tunnelling occurs.

In the case of the VH defect the bond length of the C–H depends on charge and spin state of the defect (Figure 7.2). The C–H bond length ranges from 1.07–1.13 Å. Interestingly the  $VH^0$  neutral defect spin 1/2 and 3/2 are found to be indistinguishable in energy (difference of less than 0.08 eV) but the bond lengths associated with each define the range of bond lengths associated with the VH defect. In fact the spin 3/2

defect with the 1.13 Å bond length is the longest of all C–H bonds in the full set of defects investigated.

Barring the high-spin anomaly, as charge is added to the VH defect the C–H bond length increases in length (Figure 7.2). Explained simply, as the hydrogen when bonded to the more electronegative carbon becomes slightly positive, this in turn is attracted to the carbon radicals and this Coulombic attraction increases as charge is added.

The high-spin case sees a dramatic jump in corresponding bond length, this may be due to the energy of the orbitals introduced into the band gap, these are discussed further in Section 7.3.3. Like transition metal octahedral complexes that exist in high and low spin states, there can be a dramatic shift in structure due to spin preference. The change in spin changes the ionic radii (although from a quantum mechanical viewpoint the radius of an individual ion has no precise physical significance it is informative in understanding this difference in this instance), in high spin cases the ionic radii is larger, more proximal to the hydrogen and therefore much more attractive, this therefore increases the C–H bond length.

The C–C bonds directly surrounding the vacancy in each case, as well as the N–C bonds in the NV defects do not produce an obvious trend when the charge or spin of the defect is changed. There is however a slight difference of 0.04 Å in the average immediate three C–C bond lengths adjacent to the C–H bond in the VH defects investigated and the three N–C bond lengths surrounding the vacancy in the NV defects investigated. Insinuating that the nitrogen introduces more strain into the immediate lattice surrounding the nitrogen than the lattice surrounding the C–H bond. However, on average all C–C or N–C bonds surrounding the vacancy of each set of defects investigated only differ by 0.01 Å.

### **7.3.2 Electrical properties**

In the VH and NV defects there is the presence of empty gap states (Section 7.3.3) suggesting that multiple charge and spin states are possible depending on the location

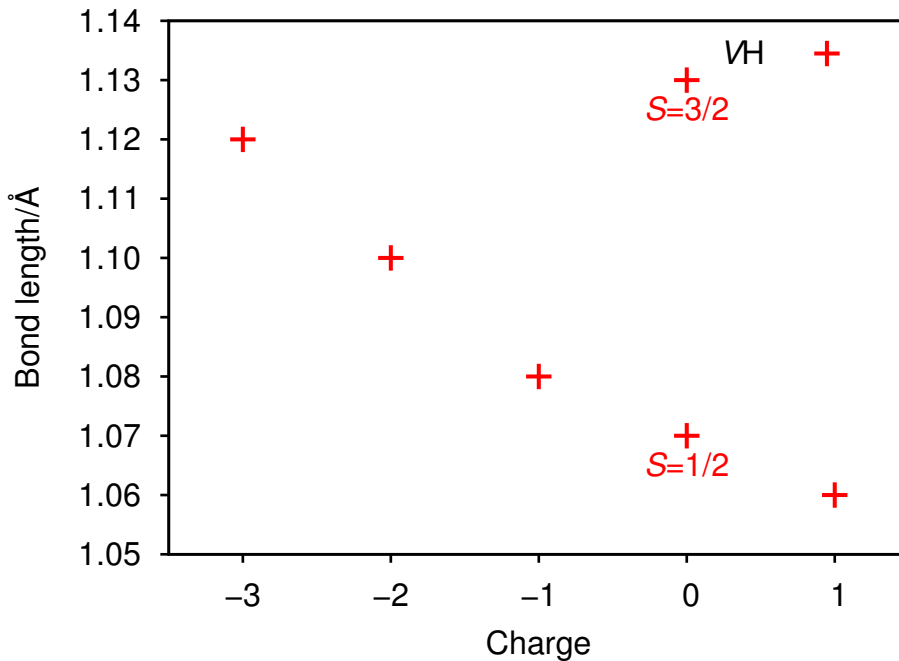


Figure 7.2: C–H bond length as a function of charge for the VH defect (red crosses). The bond lengths associated with different spins for the neutral defect are labelled.

of the electron chemical potential, which is defined by the presence of other donors or acceptors in the material.

Donor and acceptor levels of the VH and NV defect are compared in Figure 7.3. All levels associated with the nitrogen containing defect are higher in energy when compared to the VH defect. The experimental acceptor level ( $0/-$ ) of NV is situated mid-gap at  $E_C - 2.583$  eV [141, 142] and although this differs with the calculated values here, the trend is expected to hold.

Consistently lower levels associated with the VH defect means that they will preferentially trap electrons compared with the NV defect.

The results suggests that it is harder to add electrons to the NV centre when compared to the VH centre. This is primarily due to the inherent nature of the nitrogen lone pair: it is large, diffuse and extends into the vacancy much more than the comparably constrained C–H sigma bond. This wider distribution of charge introduces a larger

repulsive effect between charge as it is introduced to the defect.

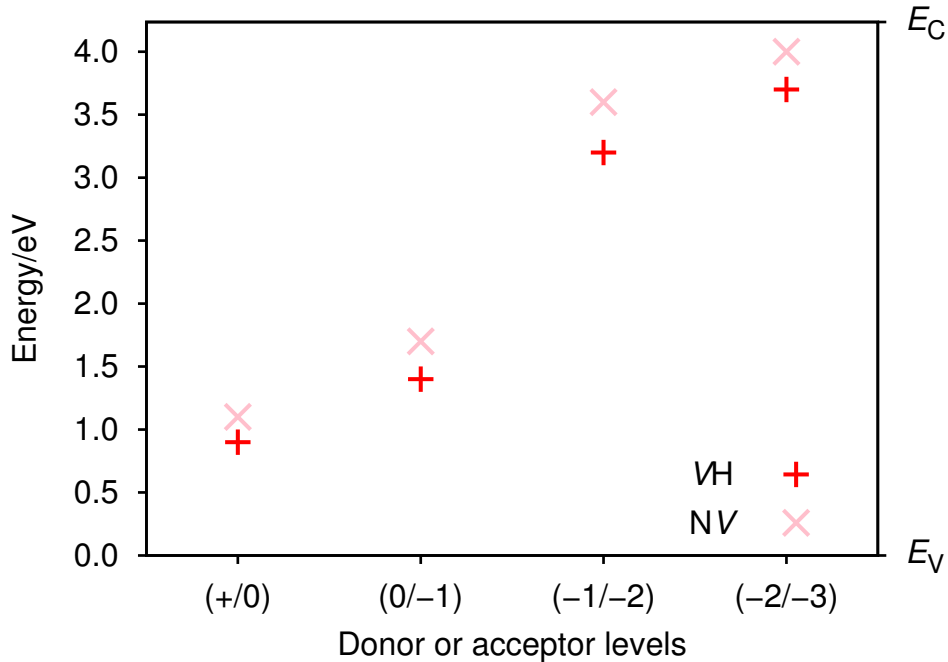


Figure 7.3: The donor level at (+/0) and acceptor levels between neutral and negatively charged states, for the VH (red crosses) and NV (and pink x's). The conduction band minimum  $E_C$  and valence band maximum  $E_V$  are labelled with  $E_V$  set to zero.

If the  $NV^+$  centre has been identified [139] there is potential for the VH defect to exist in the positive charge but the NV will preferentially lose its electron over the VH defect. The positive charge state in both the NV and VH defect most favoured spin is  $S = 0$  and therefore will not be detectable in EPR.

On the other hand, the  $NV^{-1}$  and  $VH^{-1}$  preferential spin state is  $S = 1$  as opposed to  $S = 0$ .

The higher charge states ( $-2$  and  $-3$ ) in both the VH and NV defect occur above the donor level of substitutional nitrogen at  $E_C - 1.7$  eV [54] and therefore would be difficult to access, as it is likely that this prominent defect would be present. Additionally  $NV^{-3}$  and  $VH^{-3}$  would be  $S = 0$  and therefore undetectable in EPR.

### 7.3.3 Electronic structure

The band structures of each possible charge and spin state have been calculated for the VH and the NV defect for comparison and key results presented in Figures 7.4 and 7.5. The states introduced into the band gap can be understood by reviewing the linear combinations of the three radicals in the neutral state and their corresponding orbitals labelled  $a$ ,  $b$  and  $c$ . The lowest energy state associated with the radicals will have no nodes and can therefore be described as  $a + b + c$ , this correlates with an  $a_1$  irreducible representation in the  $C_{3v}$  symmetry point group. A higher energy state is described by a linear combination of states with one node, i.e.  $a + b - c$  and  $a - b + c$ . This forms a degenerate  $e$  irreducible representation. The electrons predominately associated with the C–H sigma bond and the nitrogen lone pair are lower in energy than the carbon radicals and the levels are situated within the valance band. Assuming that no other orbitals are involved, like the corresponding C–H anti-bonding sigma orbital, it can be deduced that three electrons associated with the carbon radicals in the neutral charge state occupy the  $a_1$  and  $e$  levels.

In the case of VH neutral, there are two possible ground state spin configurations that are very close in energy, with the  $S = 1/2$  ( $a_1^2 e^1$ ) (Figure 7.4a) only lower than the  $S = 3/2$  ( $a_{1\uparrow}^1 e_{1\uparrow}^2 a_{1\downarrow}^0 e_{1\downarrow}^0$ , the relative spins are indicated by up and down arrows) (Figure 7.4b) by 0.08 eV. If it is similar to the NV defect the ground state is expected to have a  $S = 1/2$  ( $a_1^2 e^1$ ) ground state spin [143] but unlike NV the difference between the high and low spin states is acute enough that the high spin state should be visible during experiment.

In the  $S = 3/2$  ( $a_{1\uparrow}^1 e_{1\uparrow}^2 a_{1\downarrow}^0 e_{1\downarrow}^0$ ) defect, the electronic configuration satisfies Hund's rules as all electron spins are parallel. This occurs as the spin-down states are much higher in energy than the corresponding spin-up states, with the largest difference between  $e_{1\downarrow}$  and  $e_{1\uparrow}$  states around 2 eV. The electrons therefore preferentially fill the states parallel to each other.

Due to this electronic configuration only spin to conduction band electronic transitions are allowed, with spin-flip transitions forbidden, this is in contrast to the  $S = 1/2$  ( $a_1^2 e^1$ )

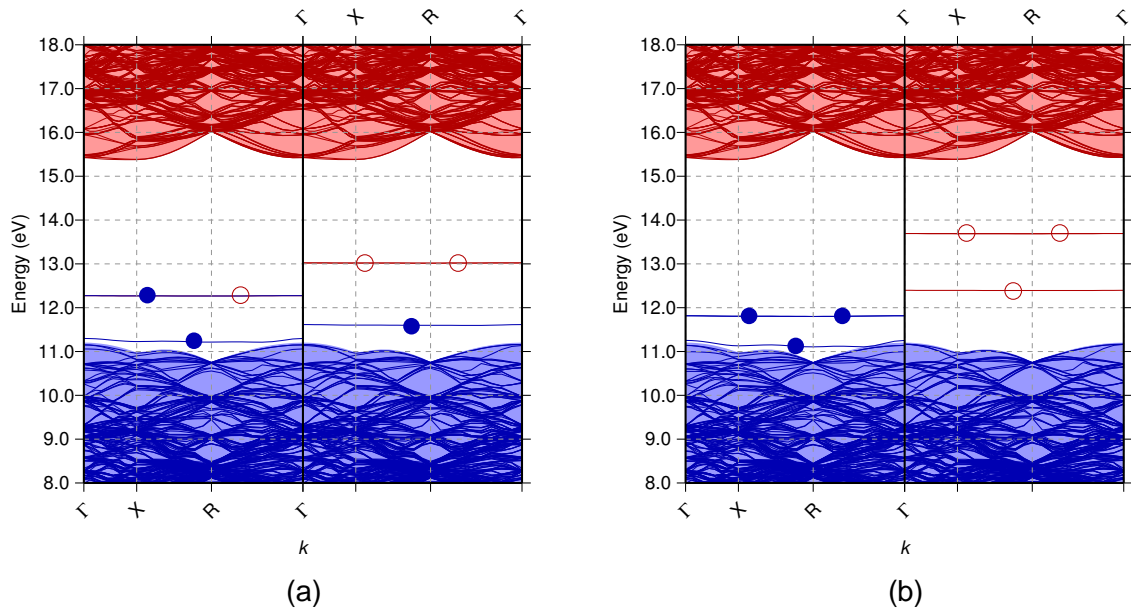


Figure 7.4: These band structures are calculated along high symmetry directions in the cubic Brillouin zone in the vicinity of the band gap. (a) Is the  $VH^0$ ,  $S = 1/2$  ( $a_{1\uparrow}^1 e_{1\uparrow}^1 a_{1\downarrow}^1 e_{1\downarrow}^0$ ) and (b)  $S = 3/2$  ( $a_{1\uparrow}^1 e_{1\uparrow}^2 a_{1\downarrow}^0 e_{1\downarrow}^0$ ). Again the red levels are unoccupied and the blue occupied. The shaded red and blue areas represent bulk 1000 atom calculations overlaid for comparison. The left represents spin up ( $\uparrow$ ) for example and the right spin down ( $\downarrow$ ), each band therefore contains one electron. The degeneracy of the gap levels obscures the occupation so occupation or emptiness is indicated by filled and empty circles respectively.

configuration where transitions between gap states are allowed due to the conservation of spin and therefore the  $S = 3/2$  is not expected to luminesce.

The optical transition available to the  $VH^0$ ,  $S = 1/2$  defect can be estimated by applying an empirical correction based on the known optical transition in the  $NV^{-1}$  defect, although there are several possible excited states the correction is based on the one electron picture from the  $a_{1\downarrow}^1 - e_{1\downarrow}^1$  states (Figure 7.5a). Therefore the transition energy can be estimated to occur at 1.4 eV.

When an electron is added to the  $VH$  defect it becomes negatively charged and now four electrons are available to fill the gap states. The corresponding band structure of the  $VH^{-1}$ ,  $S = 1$  defect is shown in Figure 7.5a and there are striking similarities

between that and the  $NV^{-1}$ ,  $S = 1$  band structure (Figure 7.5b) despite there being no lone pairs on the former; it is necessary to develop this comparison further by also viewing the wave function distribution in Figure 7.6.

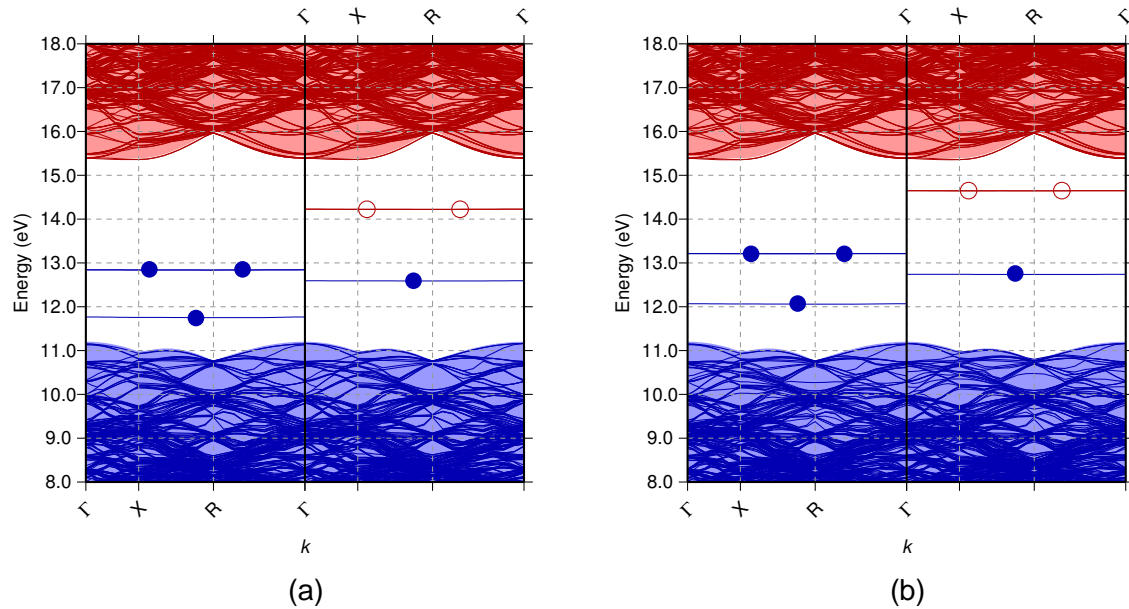


Figure 7.5: (a)  $VH^{-1}$  and (b)  $NV^{-1}$  band structures along high symmetry points in the cubic Brillouin zone, in the vicinity of the band gap. Notation is defined in Figure 7.4.

The band structure gap states were justified by referring to linear combinations of orbitals that belong to the three carbon radicals. They are the dominating contribution to these states but there is also a contribution from the electrons associated with the C–H sigma bond and the nitrogen lone pair where applicable. Despite the  $a_1$  gap state lying above the valence band in similar positions in the  $VH^{-1}$  and  $NV^{-1}$  defect band structures, the origin of this state is drastically different and this is highlighted in the wave function distribution in Figure 7.6. In the  $NV^{-1}$  defect the the  $a_1$  state has a contribution from the lone pair orbital on the nitrogen atom. The lone pair is inherently diffuse and extends into the vacancy, repelling the carbon radicals and hence reducing the component of the wave function associated with them. This is in contrast to the more contained sigma bond associated with the C–H bond that is also in anti-phase

with the radicals on the carbon atoms surrounding the vacancy. The  $NV^{-1}$ ,  $a_1$  gap state is slightly higher in energy than the  $VH^{-1}$ ,  $a_1$  gap state, this is highlighted in Figure 7.6 as there is an additional node between the nitrogen and the carbons directly behind it and away from the vacancy.

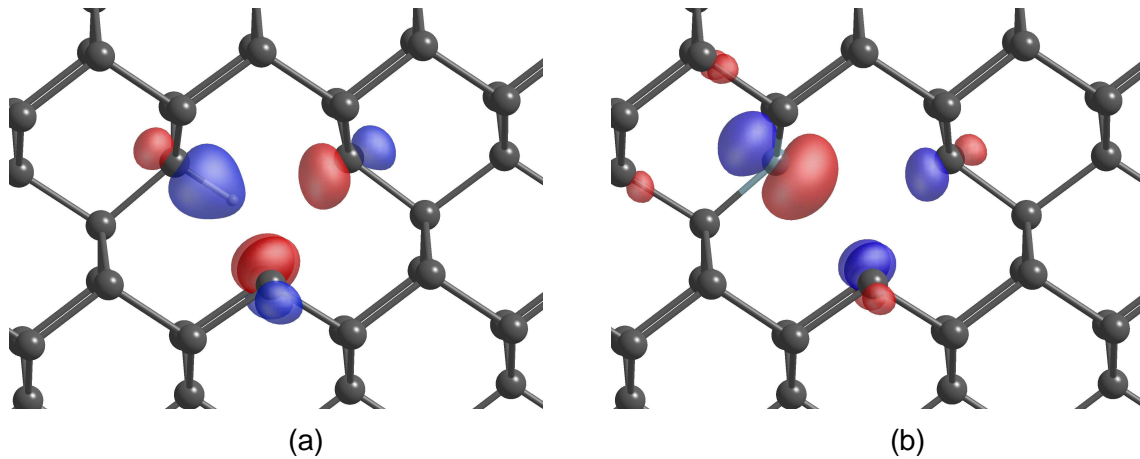


Figure 7.6: (a)  $VH^{-1}$  and (b)  $NV^{-1}$ ,  $S = 1$  isosurfaces of the  $a_{1\uparrow}$  states. Red and blue surfaces indicate the same amplitude but opposite phase. The  $[110]$  direction is perpendicular to the page.

Optical transitions between gap states are accessible in the  $VH^{-1}$ ,  $S = 1$  defect (Figure 7.5a) and can be estimated by comparing it to the known optical transition of the  $NV^{-1}$  defect at 1.945 eV ( ${}^3A-{}^3E$ ). Assuming that the errors are largely systematic and that the ground state band structure is sufficient to describe optical transitions an empirical correction can be applied. The transition in the  $NV^{-1}$  defect is scaled to match the experimental value, this is then in turn applied to the gap states in the  $VH^{-1}$  defect and the resultant  $a_1$  to  $e$  transition is 1.67 eV.

When an electron is removed from either defect making it positively charged, it leaves two remaining electrons to occupy the gap states. If the splitting between the  $a_1$  and  $e$  states is large the electronic configuration will be  $a_1^2e^0$  (Figure 7.7a) and therefore  $S = 0$  or conversely if it is small it will be  $a_1^1e^1$ , which has both spin singlet ( $S = 0$ ) and spin triplet ( $S = 1$ ) forms. The spin singlet state of the  $VH$  defect however is calculated

at 0.5 eV lower than the spin triplet configuration and in the case of the NV centre the spin singlet is 0.6 eV lower (Figure 7.7b). The electronic transition between the  $a_1$  and e state in the one electron picture of the  $NV^+$  defect is 0.81 eV, the  $VH^+$  defect is expected to have a transition of similar magnitude.

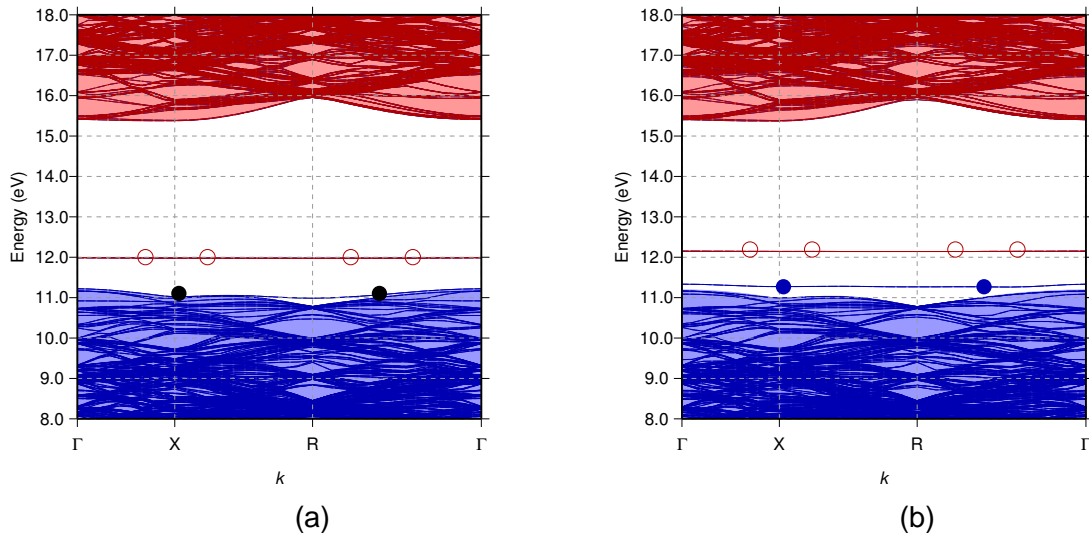


Figure 7.7: The band structures are calculated along high symmetry directions in the cubic Brillouin zone in the vicinity of the band gap, a full description of notation used is listed in Figure 7.4. (a) Is the  $VH^+$  defect and (b) is the  $NV^+$  defect. Both are  $S = 0$  ( $a_{1\uparrow\downarrow}^2 e_{1\downarrow}^0$ ). Black circles like the blue circles indicate occupation of one electron, they are darker for clarification as they sit close to the valance band top.

### 7.3.4 Vibrational properties

As discussed in Section 7.3.1, there is a strong correlation between charge of the system and associated C–H bond length: in general as charge increases so does the bond length. And in turn an increase in bond length leads to a decrease in vibrational frequency. The vibration of the C–H stretch mode associated with the possible variations of the VH defect are listed in Table 7.1; they all lie in the expected region, ranging from 2450 to 3100  $\text{cm}^{-1}$ . Bend modes below 1332  $\text{cm}^{-1}$  have been omitted as this is below the Raman frequency of diamond.

Table 7.1: A comparison of bond lengths and C–H stretch modes as the charge and spin state of VH varies.

Charge	1	0	-1	-2	-3	
Spin	0	3/2	1/2	1	1/2	0
Stretch mode ( $\text{cm}^{-1}$ )	3310	2450	3130	3010	2750	2470
Bend mode ( $\text{cm}^{-1}$ )	1370	-	-	1350	-	-
C–H bond length ( $\text{\AA}$ )	1.07	1.13	1.07	1.09	1.10	1.11

The NVH defect is known to tunnel [94] but the theoretical vibrational modes calculated using a similar approach adopted here are in close accord with experimental values [144], so it is expected that the methodology chosen here is sufficient to describe the VH defect.

The high spin neutral VH defect has a much larger bond length and the correlation remains between the C–H bond length and the stretch mode. As the bond length is much longer than expected when compared to the doublet with the same charge there is a corresponding jump in stretch modes from  $3130 \text{ cm}^{-1}$  for the quartet to  $2450 \text{ cm}^{-1}$  for the doublet. Depending on the ground state spin state there is also a measurable shift between the neutral and negative charge state of  $120 \text{ cm}^{-1}$  or  $560 \text{ cm}^{-1}$ .

### 7.3.5 Hyperfine interaction

Table 7.2 conveniently summarises the hydrogen and nitrogen hyperfine tensors for the VH and NV defects, the  $V_2H$  defect has also been included for comparison.

In the VH defect the hydrogen has the potential to tunnel between carbon radical sites, if the tunnelling rate is faster than the experimental timescale, then an average of the hydrogen is seen on each available carbon, this therefore changes the symmetry observed. The dynamic nature of the hydrogen is indicated in Table 7.2, along with the resulting symmetry and hyperfine tensors. The number of equivalent sites is apparent in the chemical formula of the defect listed in Table 7.2.

In an earlier publication [145] a hyperfine interaction was speculated to be single

Table 7.2: (Table overleaf). A comparison of calculated hydrogen ( $^1\text{H}$ ) and nitrogen ( $^{14}\text{N}$ ) hyperfine tensors for the  $V\text{H}$ ,  $V_2\text{H}$  and  $\text{NV}$  centres where applicable. They are compared to experimental values taken from references (ref.) listed in the Table. The principal values ( $A_{1-3}$ ) are measured in MHz and the direction taken as the principal value of the hyperfines matrices are given as  $(\theta, \varphi)$ , if the symmetry permits,  $A_{\perp}$  and  $A_{\parallel}$  along the  $\langle 111 \rangle$  direction is used as an alternate description.  $\theta$  is the angle with  $[001]$  and  $\varphi$  is the angle of the projection of the direction onto the  $(110)$  plane measured from  $[100]$  towards  $[010]$  measured in degrees.  $r_{\text{es}}$  measured in  $\text{\AA}$  is the distance between the hydrogen and carbon radical sites surrounding the vacancy. Calculated results may be listed with a greater number of significant figures to avoid ambiguity. Sites are described below.

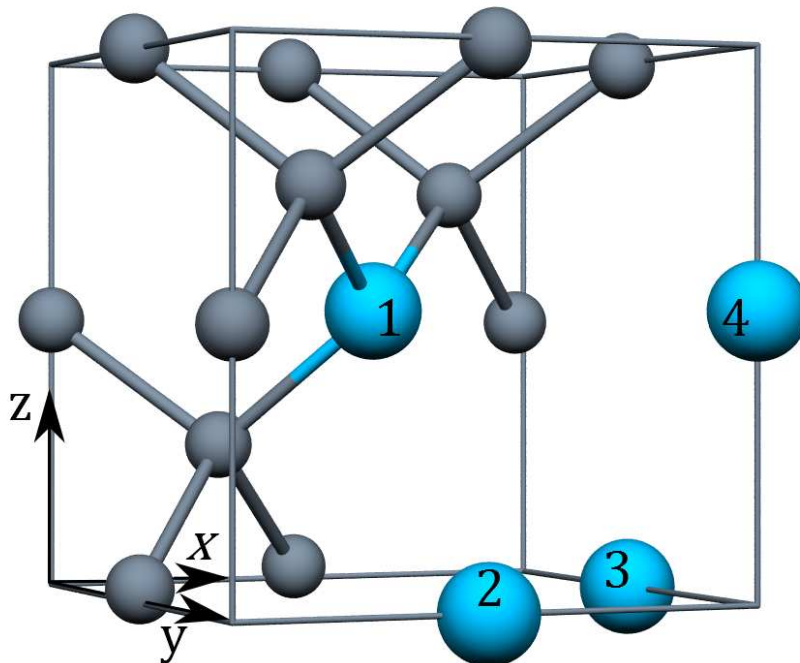


Table 7.2: Full caption on previous page.

Label	Assignment/ calculated	Site	Dynamic	Sym.	$A_1$	$(\theta_1, \varphi_1)$	$A_2/A_{\perp}$	$(\theta_2, \varphi_2)$	$A_3/A_{\parallel}$	$(\theta_{3 \text{ or } \parallel}, \varphi_{3 \text{ or } \parallel})$	$r_{es}$	Ref.	
-	VH <sup>0</sup> , S = 3/2	1	X	C <sub>3v</sub>	-	-	-4	-	17	(55,-135)	1.94		
-			✓	T <sub>d</sub>	3	(90,0)	3	(90,90)	3	(0,-)			
-	VH <sup>0</sup> , S = 1/2	1	X	C <sub>3v</sub>	-	-	1	-	0.4	(-55,45)	1.98		
-			✓	T <sub>d</sub>	0.8	(90,0)	0.8	(90,90)	0.8	(0,-)			
H1	H-V <sup>0</sup> , S = 1/2		-	axial	-	-	-6	-	27	(55,45)	1.7	[145]	
-	VH <sup>-</sup> , S = 1	1	X	C <sub>3v</sub>	-	-	0.3	-	-1	(-55,45)	1.94		
-			✓	T <sub>d</sub>	-0.2	(90,0)	-0.2	(90,90)	-0.2	(0,-)			
-			X	C <sub>3v</sub>	-	-	1.95(5)	-	1.10(5)	(55,45)		[131]	
-	V <sub>2</sub> H <sup>0</sup> , S = 1/2	3 (V at 4)	X	C <sub>1h</sub>	-6	(62,148)	6	(58,38)	2	(-45,90)	1.97/2.57/3.01		
-			✓	C <sub>3v</sub>	-	-	-2	-	5	(55,45)			
-			✓	D <sub>3d</sub>	-	-	-2	-	5	(55,45)			
KUL9			✓	trig.	-	-	-2.1	-	4.6	(55,45)		3.0	[147]
-	V <sub>2</sub> H <sup>-</sup> , S = 1	3 (V at 4)	X	C <sub>1h</sub>	1.6	(-45,90)	1.8	(45,95)	0.1	(88,2)	1.95/2.55/3.01		
-			✓	C <sub>3v</sub>	-	-	1.2	-	1.1	(55,45)			
-			✓	D <sub>3d</sub>	-	-	1.2	-	1.1	(55,45)			
KUL2			✓	trig.	-	-	2.8	-	1.1	(55,45)		3.2	[147]
-	NV <sup>0</sup> , S = 3/2	4	-	C <sub>3v</sub>	-	-	17	-	27	(55,45)	2.71		
-	NV <sup>0</sup> , S = 1/2	4	-	C <sub>3v</sub>	-	-	-2.1	-	-1.7	(55,45)	2.74		
-	NV <sup>-</sup> , S = 1	4	-	C <sub>3v</sub>	-	-	-2.2	-	-1.7	(55,45)	2.73		
W15			-	C <sub>3v</sub>	-	-	-2.70(7)	-	-2.14(7)	(55,45)		2.51	[148]
W15			-	C <sub>3v</sub>	-	-	2.10(10)	-	2.30(2)	(55,45)		2.5	[149]
W15			-	C <sub>3v</sub>	-	-	2.32	-	2.25	(55,45)		2.5	[150]

hydrogen atom entering a stretched bond at a grain boundary; due to the symmetry and the calculated distance between the hydrogen and the electron density, it was later asserted that this was the  $VH^0$  defect. However the model of  $VH^0$  for H1 was deemed incorrect in reference [146] due to its symmetry variation. We can confidently confirm that H1 is not the  $VH^0$ ,  $S = 1/2$  defect as the difference in calculated and experimental values is too large, therefore in Table 7.2 this defect is labelled as  $H-V^0$ .

Previous experimental results had identified an  $S = 1$  defect, with trigonal symmetry, that had similar zero field splitting to the  $NV^-$  centre. From the experimental evidence it was deduced from this that it was the  $VH^-$  defect [131]. If this was the case the hydrogen in the  $VH^-$  defect would be static, or appear to be static, as the rate of tunnelling would be slower than EPR timescales. As hydrogen is small, light, and averaged symmetry is seen in similar defects like the NVH centre, it might be expected that the VH defect would exhibit similar behaviour. Tunnelling rates, however, for the VH defect have been calculated to be larger than the NVH defect and on the upper limit of EPR timescales [86]. Based on this and further theoretical calculations [86] a reassignment was proposed, that the trigonal defect was in fact a  $V_2H^-$ ,  $S = 1$  defect. When static this defect has  $C_{1h}$  symmetry but when dynamic the symmetry changes to either  $C_{3v}$  or  $D_{3d}$  symmetry, the latter two are indistinguishable in experiment and theory. This reassignment however, was based on theoretical results that differ to those calculated in Table 7.2 by several orders of magnitude. The experimental results [131] are however closer in magnitude, direction and they have the same symmetry as a  $V_2H^-$  defect when the hydrogen is in motion. They are also comparable to the experimental results for the KUL2 centre which is assigned to the  $V_2H^-$  defect. This was assigned based partly on the point dipole approximation that calculates a distance that would only be feasible in a defect with two vacancies. Perhaps if this information was available for the defect in question an assignment may be more definitive. KUL2 and KUL9 were also recorded in the same sample so KUL9 may be identifiable in the samples used by Glover *et al.*

There is little difference between the nitrogen hyperfine low spin neutral case and the

negatively charged defect but the higher spin neutral case has a dramatic difference in magnitudes. This is a consequence of more unpaired electron density interacting with the nucleus. This is also seen in  $VH$  defect.

The signs have only been calculated experimentally in Reference [148]. All experimental results [148, 149, 150] however, regarding the  $NV^-$ ,  $S = 1$  case are in good agreement with the magnitude and direction calculated.

In Table 7.3 the carbon hyperfines are listed for the unique carbon bonded to the hydrogen and also the remaining group of three carbons surrounding the vacancy in both the  $VH$  and  $NV$  cases. If the hydrogen is in motion where feasible an average of the hyperfine parameters is taken, increasing the number of equivalent sites and altering the perceived symmetry.

The unique carbon involved in the  $C-H$  bond in a static view always has the lowest hyperfine parameter in Table 7.3, the largest hyperfine interaction occurs where there is more unpaired electron density on the remaining carbon radicals.

The calculated hyperfine values are in good agreement with both experiments listed in Table 7.3 for the  $NV^-$  defect. Although, only  $A_{\perp}$  and  $A_{\parallel}$  values are described in experiment the calculated values of  $A_1$  and  $A_2$  are within 1 MHz.

In general carbon hyperfine interactions are much larger than hydrogen and nitrogen hyperfine parameters due to the localisation of the unpaired electron density. The neutral and negative defects have similar hyperfine parameters for all types of hyperfine interactions in Tables 7.2 and 7.3, whereas in the higher spin neutral cases there is a dramatic decrease in carbon hyperfine values and an increase in corresponding hydrogen and nitrogen hyperfine parameters.

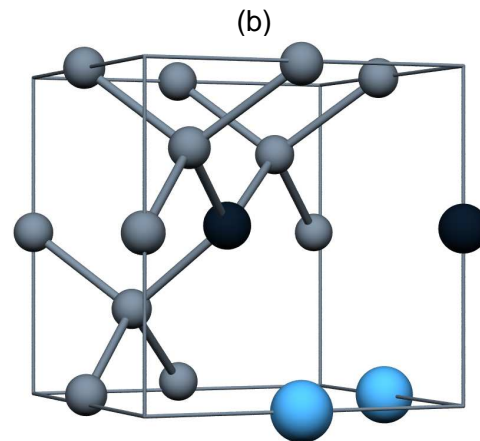
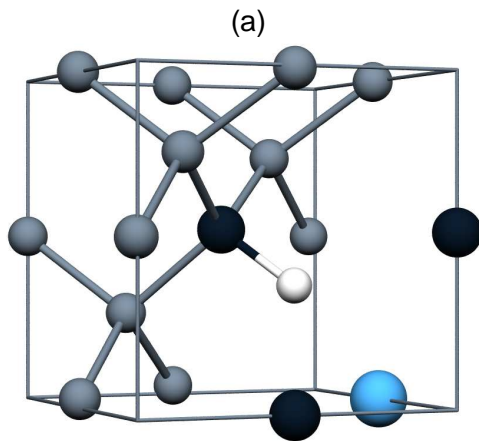
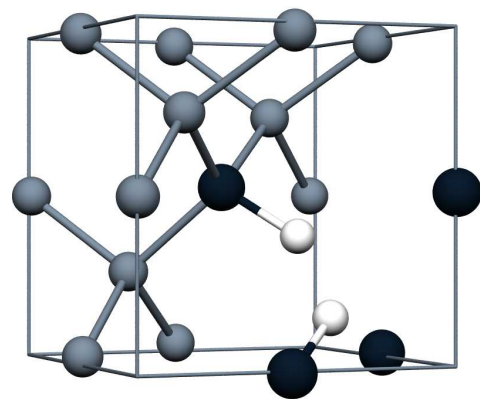
Table 7.3: A comparison of calculated carbon ( $^{13}\text{C}$ ) hyperfine tensors for the VH and NV centres, compared to experimental values taken from references (ref.) listed in the Table.  $n$  indicates the number of equivalent sites. A breakdown of terms is described in the previous Table.

Label	Assignment/ calculated	$n$	Site	Dynamic	Sym.	$A_1$	$(\theta_1, \varphi_1)$	$A_2/ A_{\perp}$	$(\theta_2, \varphi_2)$	$A_3/ A_{\parallel}$	$(\theta_{3 \text{ or } \parallel}, \varphi_{3 \text{ or } \parallel})$	Ref.
-		3	3	$\times$	$C_{1h}$	58.0	(-66,26)	58.1	(45,90)	134	(55,-45)	
-	VH $^0$ , $S = 3/2$	1	1	$\times$	$C_{3v}$	-	-	26	-	47	(55,-135)	
-		4		$\checkmark$	$C_{3v}$	-	-	50	-	112	(55,135)	
-		3	3	$\times$	$C_{1h}$	90.8	(-65,28)	91.1	(45,90)	182	(56,-43)	
-	VH $^0$ , $S = 1/2$	1	1	$\times$	$C_{3v}$	-	-	-8	-	-7	(-55,45)	
-		4		$\checkmark$	$C_{3v}$	-	-	75	-	148	(55,135)	
-		3	3	$\times$	$C_{1h}$	98	(-65,28)	98	(45,90)	182	(55,-43)	
-	VH $^-$ , $S = 1$	1	1	$\times$	$C_{3v}$	-	-	-7.3	-	-6.7	(-55,45)	
-		4		$\checkmark$	$C_{3v}$	-	-	71	-	135	(55,135)	
-	NV $^0$ , $S = 3/2$	3	1	-	$C_{1h}$	68.1	(35,45)	68.2	(90,-45)	145	(55,-135)	
-	NV $^0$ , $S = 1/2$	3	1	-	$C_{1h}$	112.7	(37,45)	113.0	(90,-45)	204	(53,-135)	
-		3	1	-	$C_{1h}$	116	(36,45)	117	(90,-45)	202	(54,-135)	
W15	NV $^-$ , $S = 1$	3		-	-	-	-	120.3(2)		199.7(2)	(125.2(3),45)	[148]
W15		3		-	-	-	-	123		205	(141.2,0)*	[151]

\*3.5° from  $\langle 1\bar{1}1 \rangle$ , directions described in [151].

## Chapter 8. $N_n V H_m$ , where $n + m = 2$

V	NV	$N_2 V$	$N_3 V$	$N_4 V$
VH	NVH	$N_2 VH$	$N_3 VH$	
$VH_2$	NVH <sub>2</sub>	$N_2 VH_2$		
VH <sub>3</sub>	NVH <sub>3</sub>			
VH <sub>4</sub>				



(c)

(d)

Figure 8.1: (a) Highlighted defects where  $n + m = 2$ . (b) The  $VH_2$  defect. (c) The  $NVH$  defect. (d) The  $N_2 V$  defect. Description of the structure remains the same as described in Figure 5.1b.

### 8.1 $VH_2$

It is well known that hydrogen readily forms complexes with vacancies in silicon; infrared absorption experiments [152] have shown that  $VH_n$ ,  $n = 1, 2, 3$  and 4, defects are present in ion-implanted samples. However multiple hydrogen containing defects have not been specifically identified in diamond, as hydrogen and carbon can form strong covalent C–H bonds it is surprising that more hydrogen related defects have not been recognised.

### 8.2 NVH

The NVH centre has been thought to have been grown in CVD diamond in the neutral charge state due to it being grown under a non-equilibrium environment. Once heated the electron distribution can equilibrate, resulting in  $NVH^-$ . The negative defect has been observed in EPR [153, 94] and in IR absorption experiments [154, 155].  $NVH^0$  is also thought to be associated with the optical band at 2.38 eV (520 nm).

The hydrogen in the NVH defect is known to tunnel, resulting in a perceived  $C_{3v}$  symmetry when the hydrogen reorientates between the equivalent carbon radicals in the defect. It is the motionally averaged dynamic mode that is seen in EPR. The static description of vibrational modes however successfully describes the centres properties [144].

### 8.3 $N_2V$

The  $N_2V^0$  has been assigned the H3 optical line (2.463 eV) and the H2 (1.26 eV) line is  $N_2V^-$  [156]. The neutral  $S = 1$  defect has been identified in EPR experiments and labelled W26 [157]. It has recently been suggested that as the H3 optical centre has a long photoluminescence lifetime (17.5 ns) and a quantum yield of 0.95, it has a possible application as a long-living quantum memory [158, 159]. The structure of  $N_2V$  has been confirmed by uniaxial stress measurements to conform to  $C_{2v}$  symmetry [156].

## 8.4 Results

### 8.4.1 Structural analysis

Both the  $VH_2$  and the  $N_2V$  have the same  $C_{2v}$  ground state symmetry (Figure 8.1b and Figure 8.1d respectively), the C–H bonds in  $VH_2$  are in the same plane and stretch towards the carbon radicals. The NVH defect on the other hand has  $C_{1h}$  ground state symmetry (Figure 8.1c), as although the nitrogen and associated lone pair and C–H bond may be considered to be isoelectric with each other they are not equivalent and therefore it reduces the symmetry in the defect accordingly.

The  $VH_2$  defect contains two equivalent carbon radicals when viewed statically, meaning that both hydrogens have the potential to quantum-mechanically tunnel between them. This is a more complex problem compared with the VH defect as there is another hydrogen involved in the process: one hydrogen will effect the other. If tunnelling is observable the symmetry will change from  $C_{2v}$  to  $T_d$ .

The NVH defect also has two remaining equivalent carbon radicals and quantum-mechanical tunnelling of the hydrogen has been observed at a rate which can alter the perceived symmetry in EPR.

C–H bond lengths associated with varying charges for the  $VH_2$  and NVH defect are illustrated in Figure 8.2. Similar to the VH defect discussed in Chapter 7 there are two spin states of indistinguishable energy ( $< 0.1$  eV) associated with the neutral  $VH_2$  and the NVH defect. Once again the different spin states correspond to different C–H bond lengths, although the difference is much more acute, between 1.07 Å in the high  $S = 1$  case and 1.05 Å in the low spin  $S = 0$   $VH_2$  defect. This is also seen in the NVH defect, the neutral  $S = 1$  and  $S = 0$  defects have a difference of 0.03 Å in the C–H bond length. In both cases the higher spin results in a longer C–H bond length. The longer C–H bond length in the  $VH_2$  and NVH neutral  $S = 1$  cases are second longest in each corresponding set only beaten by  $-2$  charged defect in each case. As these defects contain an additional hydrogen or an nitrogen when compared to VH, a combination of electronic interactions and sterical considerations will define the bond

length. The smaller difference in bond length due to spin when compared with the VH defect may be due to the increased steric hindrance within the defect caused by the additional hydrogen or nitrogen reducing the space available for extended bonds. When two electrons are added however the Coulombic attraction is strong and C–H bond does preferentially increases.

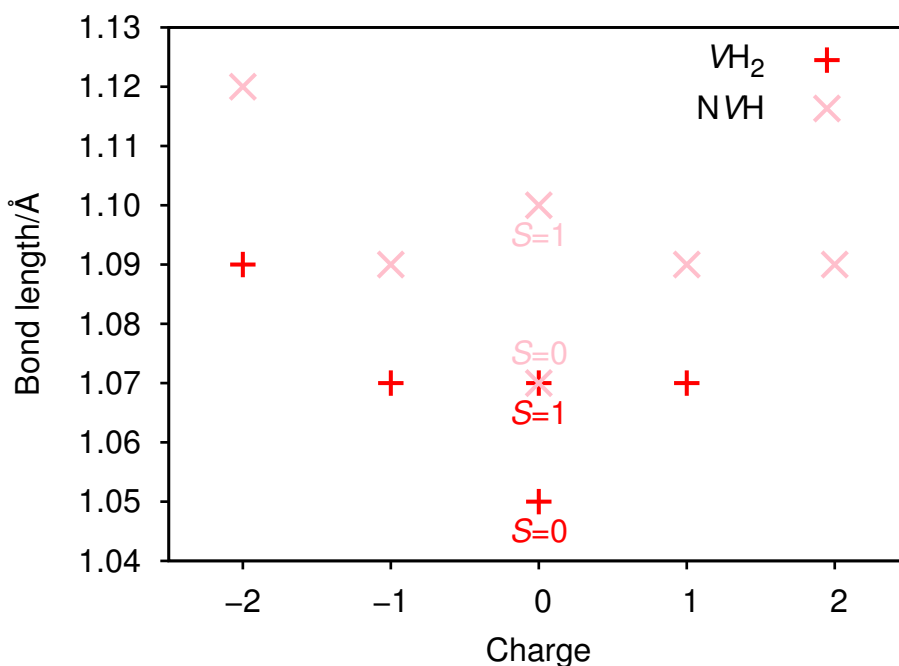


Figure 8.2: C–H bond length as a function of charge for the  $VH_2$  defect (red crosses) and the  $NVH$  defect (pink x's). The bond lengths associated with different spins for the neutral defect are labelled in their corresponding colour.

When comparing like spins and charges of the  $VH_2$  and  $NVH$  defects the corresponding  $VH_2$  C–H bonds are consistently shorter than the  $NVH$  C–H bonds. The C–H bonds in the  $VH_2$  defect range from 1.05–1.09 Å and from 1.07–1.12 Å in the  $NVH$  defects. The nitrogen lone pair and the C–H bond are attracted to each other due to the presence of intermolecular hydrogen bonding. Whereas the like C–H bonds repel each other as the H is slightly positively charged due to the fact they are bonded to a more electronegative atom.

In both defects the positive charge has the same C–H bond length as its corresponding negatively charged counterpart, suggesting that any further reduction in bond length is unfavourable.

With regards to the C–C bonds directly surrounding the  $VH_2$  defect, on average there is 0.02 Å difference with that of the shorter N–C/C–C bonds surrounding the  $N_2V$  defect. Similarly to Chapter 7, there is not an obvious trend between the surrounding bonds and the charge and spin of the defect.

#### 8.4.2 Electrical properties

All defects where  $m+n = 2$  have two carbon radicals available to be removed or ‘paired’ with two additional electrons. The removal of two electrons is not thermodynamically stable and is not considered further.

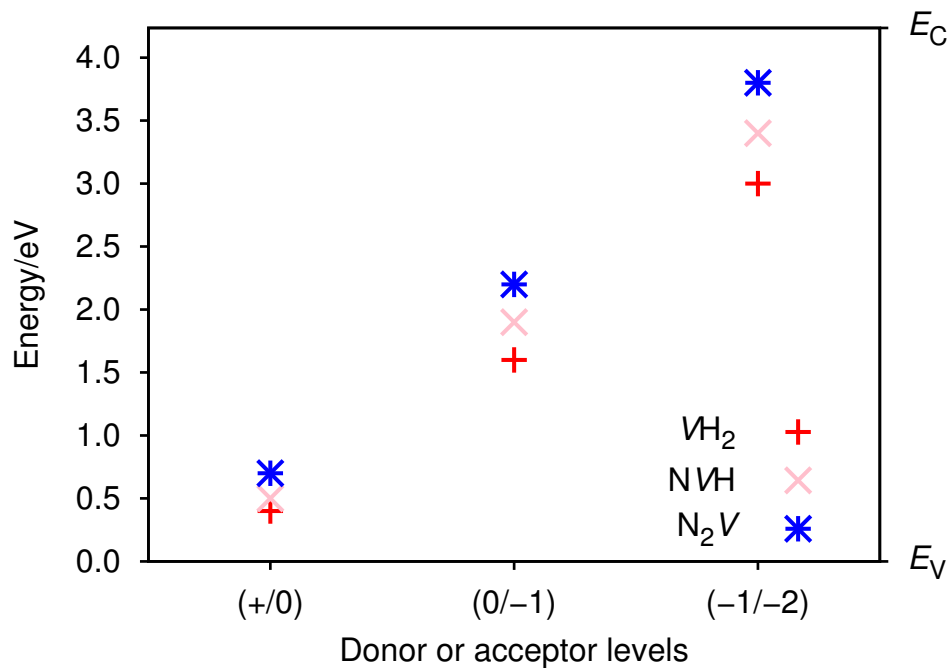


Figure 8.3: The donor level at (+/0) and acceptor levels between neutral and negatively charged states up to  $-2$ , for the  $VH_2$  (red crosses),  $NVH$  (pink x's) and  $N_2V$  (blue asterisks). The conduction band minimum  $E_C$  and valence band maximum  $E_V$  set to 0 eV are labelled.

Consistent with the VH and NV defects, nitrogen containing defects have donor and acceptor levels higher than hydrogen only containing defects. Following that, the  $N_2V$  defect contains the maximum number of nitrogens permitted in this set and therefore has the highest donor and acceptor levels of the three defects considered here.

When comparing these results with Chapter 7 the trends (or lack of) becomes more complicated, a brief discussion is presented below but all sets are reviewed in Chapter 12.

All three donor levels in Figure 8.3 are lower in energy than those corresponding to the VH and NV defects, suggesting it is easier to remove electrons from the latter rather than from this set.

On the other hand the  $(0/-)$  level of the  $VH_2$  sits in between the VH and NV defects corresponding  $(0/-)$  level, meaning it is easier to add an electron to the  $VH_2$  defect as opposed to the NV defect. Reinforcing the idea that nitrogen lone pairs are more repulsive to other electrons than C–H sigma bonds.

The NVH acceptor level lies at a higher energy than the NV defect, suggesting that the addition of hydrogen also has some effect on the ease of adding electrons.

Adding two electrons though is easier in the  $VH_2$  and NVH defect as their  $(-/-2)$  acceptor level resulting in a  $S = 0$  defect is lower in energy than the  $n + m = 1$  set where the spin of a  $-2$  defect is  $S = 1/2$ . But adding two electrons to the  $N_2V$  although making it  $S = 0$  defect the repulsion of the nitrogen lone pairs is too high.

It is speculated that the  $VH_2$  can exist in both the neutral if it is grown in and the negative once it has achieved thermal equilibrium similar to the NVH.

### **8.4.3 Electronic structure**

Once again the band structure, focusing on the states introduced into the gap, can be understood by looking at linear combinations of orbitals  $a$  and  $b$  as there are two carbon radicals.  $a+b$  is nodeless and relates to the  $a_1$  one-electron state.  $a - b$  introduces one node and corresponds to a  $b_1$  state. This describes the gap states due to the  $VH_2$  defect in Figures 8.4a and 8.4b.

Although  $N_2V$  has the same symmetry as the  $VH_2$  defect, a more comprehensive view is necessary to understand the band gap states, this includes all the electrons in the defect and can be derived from the neutral vacancy with  $T_d$  symmetry. By lowering it to the  $C_{2v}$  symmetry point group it splits the triply degenerate  $t_2$  state to introduce a  $b_2$  state and the previously mentioned  $a_1$  and  $b_1$  states which lie higher in energy. The singly degenerate  $a_1$  state can not split but is lowered in energy. This process is fully described in Lowther [160]. The  $VH_2$  defect has the same states but all are only visible in the gap when in its negative charge state (Figure 8.5a), the NVH on the other hand has  $C_{1h}$  symmetry and the gap levels are labelled  $a'$  and  $a''$ .

Confirming a previous study [161], our calculations predict that  $NVH^0$ ,  $S = 1$  defect is lower in energy than the  $S = 0$  defect. The difference is 0.02 eV, therefore we can not definitively say what the ground state spin state would be. The states are thought to be degenerate and both states should be accessible experimentally; the  $S = 1$  state could be visible in EPR whereas the  $S = 0$  state would not be. The  $S = 1$  state for the  $VH_2$  is the lowest in energy but as the energy difference is only 0.09 eV it is difficult to confirm, on the other hand the difference in energy for the  $N_2V$  defect is less than 0.1 eV but the lowest electronic configuration is the  $S = 0$  state. The previous study [161] suggests that they all have  $S = 0$  ground state but with the possibility to access higher spin states. Both associated band structures for each defect have been included in Figure 8.4.

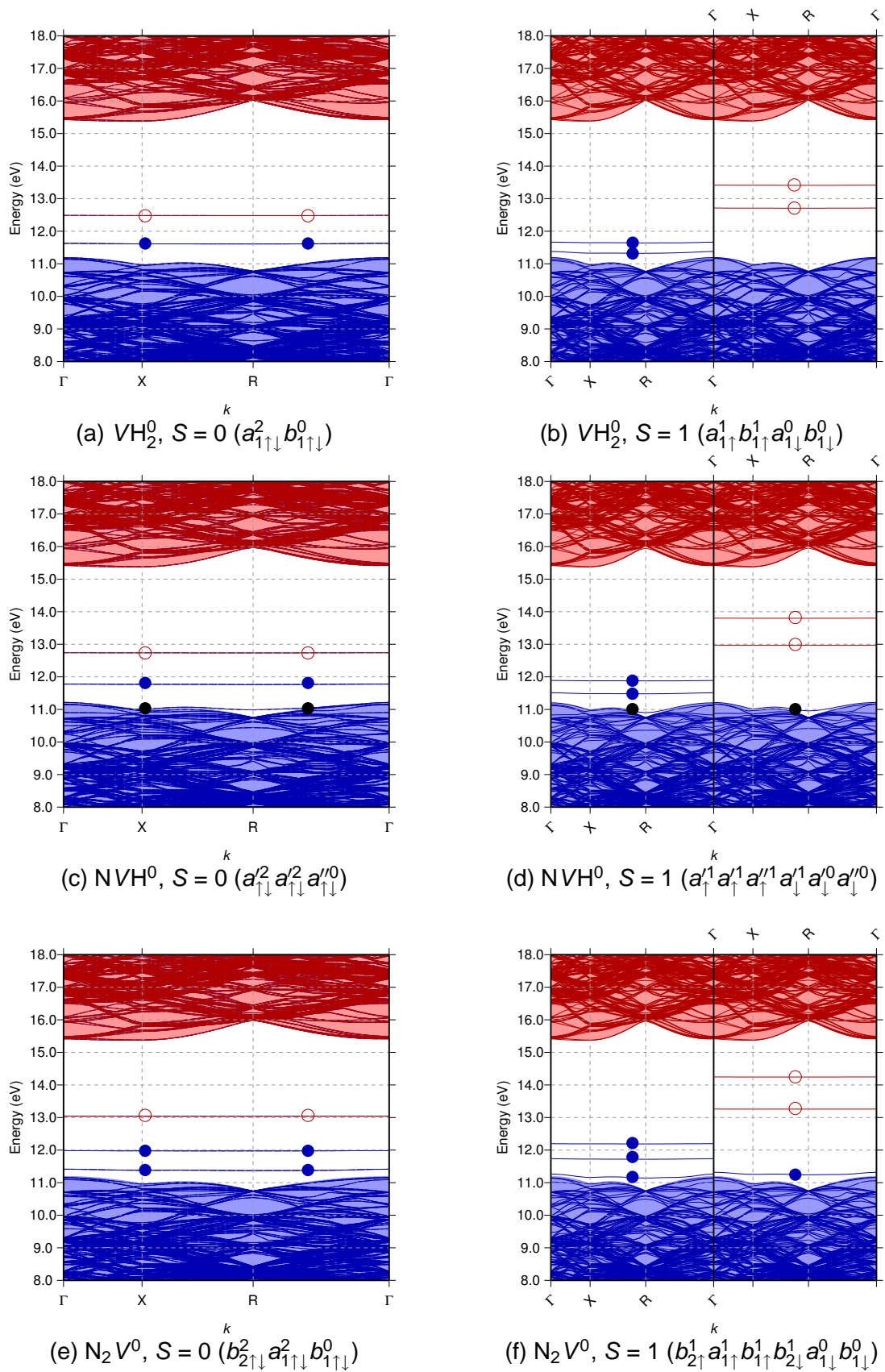


Figure 8.4: Band structures calculated along high symmetry directions in the cubic Brillouin zone in the vicinity of the band gap. The band structure notation is described fully in Figure 7.4. Black circles like the blue circles indicate occupation of one electron, they are darker for clarification as they sit close to the valance band top.

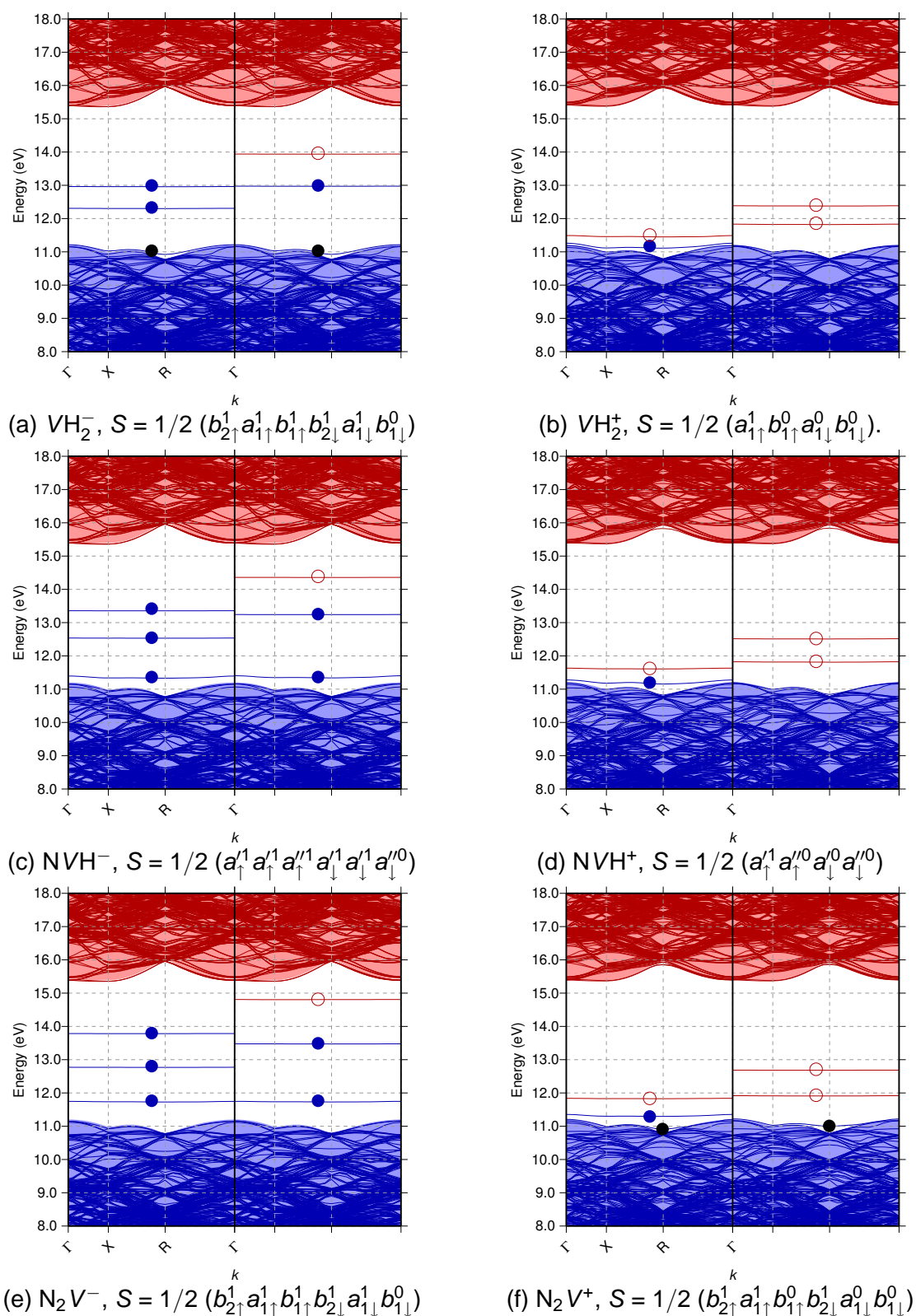


Figure 8.5: Band structures calculated along high symmetry directions in the cubic Brillouin zone in the vicinity of the band gap. The band structure notation is described fully in Figure 7.4, only visible band states are labelled. Black circles like the blue circles indicate occupation of one electron, they are darker for clarification as they sit close to the valence band top.

In all neutral  $S = 0$  defects, it is possible for an  $a_1-b_1$  optical transition (or  $a'-a''$  in the case of NVH). As hydrogen decreases and nitrogen increases in this set, both these levels increase in energy and the transition itself also slightly increases in energy, as seen down the left side of Figure 8.4. The  $a_1$  and  $b_1$  states are primarily due to bonding and anti-bonding orbitals respectively from the carbon radicals. The  $b_2$  state is primarily due to the C-H sigma bonds in  $VH_2$  and it is situated in the valence band, but as nitrogen is added and hydrogen removed the  $b_2/a'$  state rises out of the valence band as the state is now primarily as a consequence of the nitrogen(s) lone pair(s). The  $b_2-b_1$  internal transition is dipole forbidden but where  $b_2$  is above the valence band,  $b_2-E_c$  and  $b_1-E_c$  are possible.

In the higher spin state of the neutral defect (seen on the right of Figure 8.4), the states follow a similar pattern described above. Although internal transitions in  $VH_2$  are spin-flip forbidden. Only in the NVH and  $N_2V$  defect where the  $a'$  or  $b_2$  state is above the valence band have allowed internal transitions of around 2 eV. The  $NVH^0$ ,  $S = 1$  has an additional allowed transition between  $a'$  and  $a''$  states.

The band structures in Figure 8.5 illustrates the defects in this set in the negative and positive charge state. Like in the neutral  $S = 0$  case  $a_1-b_1$  (or  $a'-a''$  in the case of NVH) internal transitions are allowed and they increase in magnitude as hydrogen is removed in both charge states. The  $a_1-b_1$  transitions (or  $a'-a''$  transitions in the case of NVH) associated with the negative band structure all have a larger magnitudes when compared to their neutral  $S = 0$  and positive counterparts. Interestingly in the  $VH_2^-$  band structure (Figure 8.5a) the  $b_2$  state now becomes visible on top of the valence band.

1.26 eV is the optical H2 line and is associated with the  $N_2V^-$  defect, this in reasonable agreement with the calculated transition of 1.33 eV. It has been suggested that the 1.37 eV optical band is related to the  $NVH^-$  defect, this is surprising as although all  $a_1-b_1$  or  $a'-a''$  transitions in the negative charge states of this set are of similar magnitude, there is a clear and persistent trend that the transitions are reduced when hydrogen is added. One therefore might expect the optical transition of the  $NVH^-$  defect to be

smaller in magnitude than the  $N_2V^-$  defect, this trend becomes clearer when reviewing the optical peaks below.

The H3 optical line at 2.46 eV on the other hand is associated with the  $N_2V^0$  defect, although closer in magnitude to the transition associated with the  $S = 1$  defect (1.94 eV) it is associated with the  $S = 0$  defect that has a transition of 1.06 eV. The calculated ground state is the  $S = 0$  but the excited paramagnetic state has been detected in EPR; the calculated difference in energy between the  $S = 1$  and  $S = 0$  state is less than 0.1 eV. The difference in magnitude is down to a DFT implementation issue and a full many-body approach where the excited states are treated correctly, would yield a result in better agreement.

The broad 2.38 eV optical band is associated with the  $NVH^0$  defect, conversely to the  $N_2V^0$  defect, the  $S = 1$  is the calculated ground state spin but the difference in energy between this and  $S = 0$  is around 0.02 eV. Interestingly, the magnitude of this transition is 0.08 eV lower when compared to the  $N_2V^0$  defect (H3 optical line) and the calculated difference when comparing the  $S = 0$  defects in both cases is 0.1 eV. This transition is also described as broad which could imply that it is a transition between valence band states and the defect but the  $a'$  state is calculated to sit around the valence band top. The transition between the  $a'$  and  $a''$  is calculated as 1.76 eV which is within 0.62 eV of the experimental value of 2.38 eV.

#### **8.4.4 Vibrational properties**

The stretch and bend modes for feasible charge and spin states for the  $VH_2$  and  $NVH$  defects are listed in Table 8.1.

Once again there is a strong correlation between bond length and the stretch modes, there is however more variation in the bend modes. As the higher spin state for the neutral case in both defects has a larger bond length the corresponding frequencies are lower by a sizable difference of hundreds of wave numbers.

The peak at  $3123\text{ cm}^{-1}$  is seen experimentally, it was initially thought to be the  $NVH^-$  defect but then was reassigned to be the neutral defect [155]. This is in good agreement

Table 8.1: A comparison of bond lengths and C–H stretch modes as the charge and spin state varies for defects in the  $n + m = 2$  set.

Defect	$VH_2$					NVH				
	Charge	1	0	-1	-2	1	0	-1	-2	
Spin	1/2	0	1	1/2	0	1/2	0	1	1/2	0
Symmetric stretch ( $\text{cm}^{-1}$ )	3370	3520	3310	3330	3050	2950	3180	2850	2930	2550
Anti-symmetric stretch ( $\text{cm}^{-1}$ )	3100	3350	3040	3120	2770	-	-	-	-	-
Bend mode ( $\text{cm}^{-1}$ )	1520	1540/ 1350	1550	1590	1680	1330	1430	1310	1340	1400
C–H bond length ( $\text{Å}$ )	1.07	1.05	1.07	1.07	1.09	1.09	1.07	1.10	1.09	1.12

with the NVH defect but in the  $S = 0$  spin state, although not the calculated ground state, the spin states are within 0.02 eV.

It is also suggested that the  $VH_2$  is assigned to the  $1353 \text{ cm}^{-1}$  peak based on symmetry arguments [155]. The  $VH_2$ ,  $S = 0$  defect is within  $3 \text{ cm}^{-1}$  of this assignment, this is astonishingly close but  $S = 0$  is not the calculated ground state spin state. The lowest energy for the  $VH_2$  is  $S = 1$  but with a difference of 0.09 eV it is too small to ascertain the ground state. Despite this the  $VH_2$ ,  $S = 1$  defect also has a bend mode within  $90 \text{ cm}^{-1}$  calculated at  $1260 \text{ cm}^{-1}$ . If this assignment is correct this peak has been seen in as-grown material and is persistent at high temperature anneals [162].

Recent investigations into co-doped CVD diamonds with boron and nitrogen, reveal a stretch mode at  $2976 \text{ cm}^{-1}$  and a potentially related bend mode at  $1394 \text{ cm}^{-1}$  [163]. The NVH defect in the positive charge state is within 1% of the stretch mode and the bend mode is within 5%. As there is a high boron content if the NVH is formed during this particular growth process and the boron is also incorporated, the positive charge state may be accessible. If this is the case it gives extra rigour to the potential  $NV^+$

identification in similar material [139].

#### **8.4.5 Hyperfine interaction**

The hyperfine parameters corresponding to the defects in this Chapter are listed in Tables 8.2, 8.3 and 8.4.

Once again, for the hyperfine parameters due to the  $^1\text{H}$ , the magnitude of the principal hyperfine values are similar in both the negative and neutral charge state, when viewed statically. The positively charged  $VH_2$  and  $NVH$  defects have a much larger magnitude of hyperfine interaction than either the neutral or positively charged defect. When the hydrogen is in motion in the  $VH_2$  defect the treatment of the hydrogens becomes problematic as their interaction with each other is unknown. The hyperfine tensors for the dynamic view were taken, like before, as an average of the possible positions each hydrogen can occupy. The resulting symmetry is  $T_d$ .

For the positively charged defect the magnitude of the tensor is 11 MHz but in the neutral and negatively charged states the magnitude of the hyperfine tensor is much lower:  $-0.09$  and  $-0.06$  respectively. This small hyperfine interaction might be difficult to resolve from the mainline and hope of identifying this defect in EPR may be more likely if the defect is in the positive charge state.

The hydrogen hyperfine parameters for the  $NVH$  defect have been identified in EPR [94]. It was initially thought that due to the perceived symmetry of  $C_{3v}$ , the hydrogen had to be bonded to the nitrogen but it was later found that the hydrogen is in fact tunnelling between the carbon radicals, consequently changing the perceived symmetry viewed in EPR. The calculated results for the motionally averaged  $NVH^-$  defect are in reasonable agreement with the experimental results [94].

The hyperfine tensors due to  $^{14}\text{N}$  for the  $NVH$  and  $N_2V$  defects are listed in Table 8.3. There is a greater variation of hyperfine tensors between the charge states due to the  $^{14}\text{N}$  when compared to the results previously discussed results due to  $^1\text{H}$ .

The  $NVH^-$  is thought to be dynamic and attempts to make it static have failed. If it was possible however, the hyperfine parameters for the static  $NVH^-$  although relate

Table 8.2: A comparison of calculated hydrogen ( $^1\text{H}$ ) hyperfine tensors for the  $\text{VH}_2$  and  $\text{NVH}$  centres where applicable. A full breakdown of terms used are described in Table 7.2.

Label	Defect	Site	Dynamic	Sym.	$A_1$	$(\theta_1, \varphi_1)$	$A_2/A_\perp$	$(\theta_2, \varphi_2)$	$A_3/A_\parallel$	$(\theta_{3\text{ or } \parallel}, \varphi_{3\text{ or } \parallel})$	$r_{\text{es}}$	Ref.
-	$\text{VH}_2^+$ , $S = 1/2$	3	$\times$	$C_{1h}$	-5	(54,135)	7	(90,45)	32	(36,-45)	1.97	
-			$\checkmark$	$T_d$	11	(90,0)	11	(90,90)	11	(0,-)		
-	$\text{VH}_2^0$ , $S = 1$	3	$\times$	$C_{1h}$	-15	(55,135)	1	(90,45)	14	(-35,135)	1.95	
-			$\checkmark$	$T_d$	-0.09	(90,0)	-0.09	(90,90)	-0.09	(0,-)		
-	$\text{VH}_2^-$ , $S = 1/2$	3	$\times$	$C_{1h}$	-15	(57,135)	12	(90,45)	3	(1-33,45)	1.91	
-			$\checkmark$	$T_d$	-0.06	(90,0)	-0.06	(90,90)	-0.06	(0,-)		
-	$\text{NVH}^+$ , $S = 1/2$	3	$\times$	$C_{1h}$	5	(53,135)	12	(90,45)	37	(37,-45)	1.99	
-			$\checkmark$	$C_{3v}$	-	-	24	-	5	(-55,-45)		
-	$\text{NVH}^0$ , $S = 1$	3	$\times$	$C_{1h}$	-14	(57,135)	2	(90,45)	16	(33,-45)	1.95	
-			$\checkmark$	$C_{3v}$	-	-	9	-	-14	(55,135)		
-	$\text{NVH}^-$ , $S = 1/2$	3	$\times$	$C_{1h}$	-17	(67,135)	3	(-23,135)	11	(90,45)	1.91	
-			$\checkmark$	$C_{3v}$	-	-	6	-	-16	(-55,-45)		
-				$C_{3v}$	-	-	-9.05(20)	-	13.69(20)	(55,45)		

to  $C_{1h}$  symmetry the magnitudes are very similar so the symmetry may be difficult to resolve experimentally. For the dynamic view there is a greater variation of 0.6 MHz but this is still rather small. The calculated results are comparable with those found experimentally and reinforce the identification of a dynamic hydrogen at a rate that changes the perceived symmetry in EPR.

W26 has been identified experimentally as the  $N_2 V^0$ ,  $S = 1$  defect, and although only  $A_{\perp}$  and  $A_{\parallel}$  are listed, the difference in symmetry is down to the close magnitudes of the calculated  $A_1$  and  $A_2$  principal values. Despite this the results are in reasonable agreement with each other.

The experimental results are in good agreement with the calculated principal values and directions for the  $N_2 V^{-}$ ,  $S = 1/2$  defect.

Results pertaining to hyperfine parameters due to  $^{13}\text{C}$  are listed in Table 8.4.

Only the  $N_2 V^{-}$ ,  $S = 1/2$  defect's hyperfine parameters due to  $^{13}\text{C}$  have been identified experimentally and the calculated results are in reasonable agreement. There is a similar issue to the nitrogen hyperfine interaction mentioned above, as the difference in calculated magnitude of the principal values  $A_1$  and  $A_2$  is very small: only 0.5 MHz. So experimentally, this small difference was not resolved in this case.

Both the  $VH_2$  and  $NVH$  have smaller hyperfine principal values when compared to the  $N_2 V$  defect of like charges. There is also a marked difference between the hyperfine parameters when it is viewed as static and dynamic; it is much more prominent that the difference seen in the hyperfine parameters due to hydrogen or nitrogen. Therefore determining the effects of tunnelling may be easier if experimental evidence was available  $^{13}\text{C}$  material, especially in light of the small hyperfine interaction of the  $VH_2$  defect in either its negative or positive charge state.

Table 8.3: A comparison of calculated hydrogen ( $^{14}\text{N}$ ) hyperfine tensors for the NVH and  $\text{N}_2\text{V}$  centres. A full breakdown of terms used are described in Table 7.2.

Label	Defect	Site	Dynamic	Sym.	$A_1$	$(\theta_1, \varphi_1)$	$A_2/A_\perp$	$(\theta_2, \varphi_2)$	$A_3/A_\parallel$	$(\theta_{3\text{ or } \parallel}, \varphi_{3\text{ or } \parallel})$	$r_{\text{es}}$	Ref.
-	NVH <sup>+</sup> , $S = 1/2$	2	$\times$	$C_{1h}$	13.1	(90,45)	13.3	(-43,135)	26	(47,135)	2.77	
-			$\checkmark$	$C_{3v}$	-	-	19	-	14	(55,-45)		
-	NVH <sup>0</sup> , $S = 1$	2	$\times$	$C_{1h}$	5.7	(-43,135)	5.8	(90,45)	10	(47,135)	2.75	
-			$\checkmark$	$C_{3v}$	-	-	8	-	5.9	(55,-45)		
-	NVH <sup>-</sup> , $S = 1/2$	2	$\times$	$C_{1h}$	-2.4	(-54,135)	-2.0	(90,45)	-1.7	(-36,-45)	2.74	
-			$\checkmark$	$C_{3v}$	-	-	-1.8	-	-2.4	(55,-45)		
-				$C_{3v}$	-	-	$\pm 3.10(10)$	-	$\pm 2.94(10)$	(55,45)		
-	$\text{N}_2\text{V}^+$ , $S = 1/2$	1	-	$C_{1h}$	19.7	(90,-45)	19.9	(41,45)	37	(49,-135)	2.73	
-	W26 $\text{N}_2\text{V}^0$ , $S = 1$	1	-	$C_{1h}$	9.8	(-41,-135)	9.9	(90,-45)	16	(-49,45)	2.71	[157]
-			-	-	-	-	10.25	-	21.5(5)	$(90 \pm 25(3)^\circ, 45)^\circ$		
-	$\text{N}_2\text{V}^-$ , $S = 1/2$	1	-	$C_{1h}$	-2.9	(-51,-135)	-2.5	(90,135)	-2.0	(40,-135)	2.71	[164]
-			-	$C_{1h}$	3.47(2)	$(145,45)^\dagger$	4.51(2)	$(55,45)^\ddagger$	4.09(2)	(90,-45)		

\*Directions described further in [157].  $^\dagger$  Defined as  $-3.5(5)^\circ$  from  $[11\bar{2}]$ .  $^\ddagger$  Defined as  $-3.5(5)^\circ$  from  $[111]$ . Further description of directions is provided in reference [164].

Table 8.4: A comparison of calculated carbon ( $^{13}\text{C}$ ) hyperfine tensors for the  $\text{VH}_2$ ,  $\text{NVH}$  and  $\text{N}_2\text{V}$  centres. A full breakdown of notation used is described in Table 7.2. C–H indicates if the carbon is bonded to the hydrogen in a static view and  $n$  indicates the number of equivalent sites.

Label	Assignment/ calculated	$n$	Site	Dynamic	Sym.	$A_1$	$(\theta_1, \varphi_1)$	$A_2$	$(\theta_2, \varphi_2)$	$A_3$	$(\theta_3, \varphi_3)$	Ref.
-		2 (C–H)	3	$\times$	$C_{1h}$	15.7	(90,45)	16.2	(46,135)	38	(44,–45)	
-	$\text{VH}_2^+$ , $S = 1/2$	2	1	$\times$	$C_{1h}$	67.6	(90,–45)	68.2	(38,45)	192	(52,–135)	
-		4		$\checkmark$	$C_{1h}$	44	(–49,82)	44	(61,21)	106	(55,135)	
-		2 (C–H)	3	$\times$	$C_{1h}$	11.8	(–44,–45)	12.3	(90,45)	25	(–46,135)	
-	$\text{VH}_2^0$ , $S = 1$	2	1	$\times$	$C_{1h}$	76	(90,–45)	77	(36,45)	187	(55,–135)	
-		4		$\checkmark$	$C_{1h}$	44	(–49,92)	44	(61,21)	106	(55,135)	
-		2 (C–H)	3	$\times$	$C_{1h}$	–7.2	(19,–45)	–7.1	(90,–45)	–9	(–71,–45)	
-	$\text{VH}_2^-$ , $S = 1/2$	2	1	$\times$	$C_{1h}$	137	(33,45)	136	(90,–45)	261	(57,–135)	
-		4		$\checkmark$	$C_{1h}$	64	(90,45)	64	(35,–45)	127	(55,135)	
-		1 (C–H)	3	$\times$	$C_{1h}$	20.6	(90,45)	21.2	(45,135)	43	(45,–45)	
-	$\text{NVH}^+$ , $S = 1/2$	2	1	$\times$	$C_{1h}$	68.7	(89,–44)	69.2	(38,48)	182	(52,–135)	
-		3		$\checkmark$	$C_{1h}$	36	(65,–28)	41	(46,90)	86	(–55,43)	
-		1 (C–H)	3	$\times$	$C_{1h}$	19.1	(–42,–45)	19.5	(90,45)	34	(–48,135)	
-	$\text{NVH}^0$ , $S = 1$	2	1	$\times$	$C_{1h}$	89	(–88,–46)	90	(35,42)	203	(55,–135)	
-		3		$\checkmark$	$C_{1h}$	42	(66,–29)	45	(44,89)	89	(–56,43)	
-		1 (C–H)	3	$\times$	$C_{1h}$	–9	(62,135)	–8	(90,45)	–7	(–28,135)	
-	$\text{NVH}^-$ , $S = 1/2$	2	1	$\times$	$C_{1h}$	156.9	(34,59)	157.3	(84,–41)	282	(57,–135)	
-		3		$\checkmark$	$C_{1h}$	47.7	(66,–29)	47.0	(44,–89)	89	(–56,43)	
-	$\text{N}_2\text{V}^+$ , $S = 1/2$	2	3	-	$C_{1h}$	72	(90,45)	73	(39,135)	171	(51,–45)	
W26	$\text{N}_2\text{V}^0$ , $S = 1$	2	3	-	$C_{1h}$	105	(90,45)	106	(35,135)	221	(55,–45)	
-		2	3	-	$C_{1h}$	184.8	(–33,–45)	185.3	(90,45)	311	(–57,135)	
-	$\text{N}_2\text{V}^-$ , $S = 1/2$	2		-				202.3(5)		317.5(5) *		[164]

\*Defined as  $2.0(5)^\circ$  from  $[\bar{1}11]$ . Further description of directions is provided in reference [164].

## Chapter 9. $N_n VH_m$ , where $n + m = 3$ <sup>1</sup>

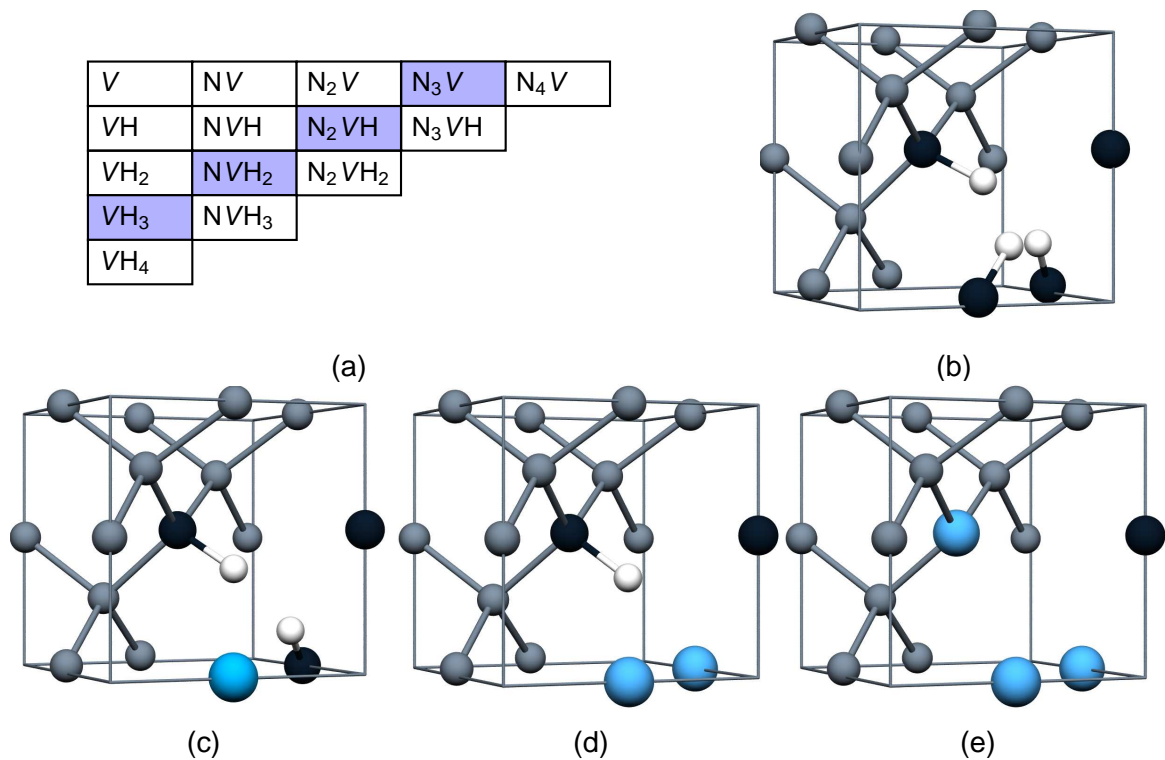


Figure 9.1: (a) Highlighted defects, where  $n + m = 3$ . (b) The  $VH_3$  defect. (c) The  $NVH_2$  defect. (d) The  $N_2VH$  defect. (e) The  $N_3V$  defect. The description of the atomic models are described in Figure 5.1b.

<sup>1</sup>Some results pertaining to the  $N_2VH$  defect have been published in reference [165].

### 9.1 $VH_3$ and $NVH_2$

Both  $VH_3$  and  $NVH_2$  have yet to be observed in diamond but other defects in this set have been and are discussed below.

### 9.2 $N_2VH$

$N_2VH$  was recently identified via EPR and labelled WAR13 [12]. When viewed in EPR the defect has  $C_{2v}$  symmetry as it reorientates quicker than Q-band EPR at 34 GHz [12], a similar effect is also seen in the  $NVH$  defect.

It is suggested that this defect correlates with a LVM (local vibrational mode) of 1375 and 1378  $\text{cm}^{-1}$  but a corresponding stretch mode has not been observed, suggesting that it is possibly obscured in a broad feature at 2750–2900  $\text{cm}^{-1}$  [12].

### 9.3 $N_3V$

The  $N_3V$  defect was briefly mentioned in the [Introduction](#) as an aggregated form of nitrogen seen in diamond but not used in the classification process, it is generally found in smaller concentrations than the A- and B-centre. The  $N_3V$  defect is responsible for the optical centre labelled N3 (natural line three), it is an  ${}^2A_1$  to  ${}^2E$  transition that occurs at 415 nm/2.985 eV [166, 167, 168, 169]. This gives the diamond a yellow colour characteristic of Cape Yellow diamond gemstones. It also has associated weak broad transitions labelled N2 at 2.596 eV [166, 167] and N4 at 3.603 eV. In EPR the  $S = 1/2$  neutral defect has been identified and labelled the P2 centre.

## 9.4 Results

### 9.4.1 Structural analysis

Both the  $VH_3$  and  $N_3V$  are trigonal defects with  $C_{3v}$  symmetry with the axis of rotation through the remaining carbon radical towards the centre of the vacancy. The  $NVH_2$  and  $N_2VH$  have  $C_{1h}$  ground state symmetry.

As all defects in this set have a free carbon radical and hydrogens where applicable there is a possibility of the hydrogens tunnelling between each of the carbons surrounding the vacancy.

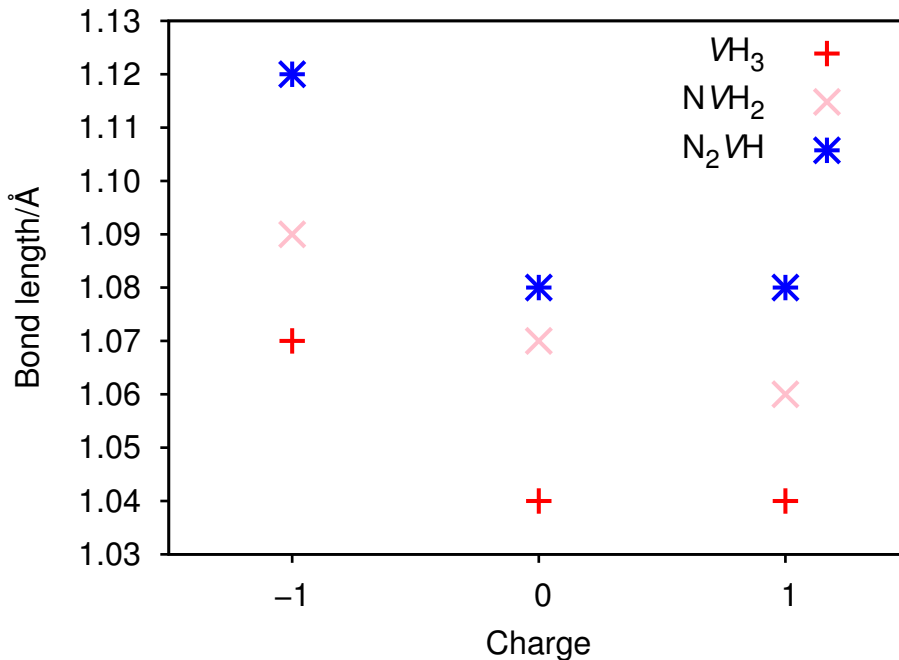


Figure 9.2: The  $VH_3$  (red crosses)  $NVH_2$  (pink x's) and  $N_2VH$  (blue asterisks) C–H bond length(s) as a function of charge.

Unlike the previous defects discussed in Chapter 7 and 8, as there is only one carbon radical only  $S = 1/2$  is accessible and it is considered the ground state spin of all neutral defects in this set.

The C–H bond lengths as a function of charge are displayed in Figure 9.2. The hydrogen bond lengths increase as the defect becomes negatively charged but the change in length due to the  $NVH_2$  is less so, for this defect the bond length decreases for the positively charge defect but for the  $VH_3$  and  $N_2VH$  they remain the same as the neutrally charged defect.

The C–H bonds are defined by a balance between the electronic and steric interaction with the defect components. Hydrogen bonds between the C–H bond and the nitrogen

extend the C–H bond but sterically when another hydrogen is included the extension is limited in  $NVH_2$ . When there are three hydrogens but no nitrogens, the steric interaction between the C–H bonds reduces the bond lengths making them the shortest studied in this set. However, when the  $VH_3$  is charged the Coulombic attraction overcomes the steric hindrance and extends the C–H bond.

The C–N bonds surrounding the  $N_3V$  defect are 1.48 Å, which is 0.03 Å shorter than the C–C bonds surrounding the  $VH_3$  at 1.51 Å. Suggesting that the nitrogen has a greater influence on the surrounding diamond than the introduction of hydrogen, despite more strain introduced within the defect when hydrogen is incorporated into a vacancy.

#### **9.4.2 Electrical properties**

Again the (+/0) and (0/–) lie in the expected region and the lowest–highest donor and acceptor levels respectively are ordered like previously discussed sets: from zero nitrogens to the max number of nitrogens permitted in this case. Consistent with the view that it is harder to add electrons to nitrogen containing defects but easier to remove them.

When comparing these levels to the  $n + m = 1$  and 2 sets it becomes more complicated and the order is no longer separated by sets. The data is summarised in the [Summary](#).

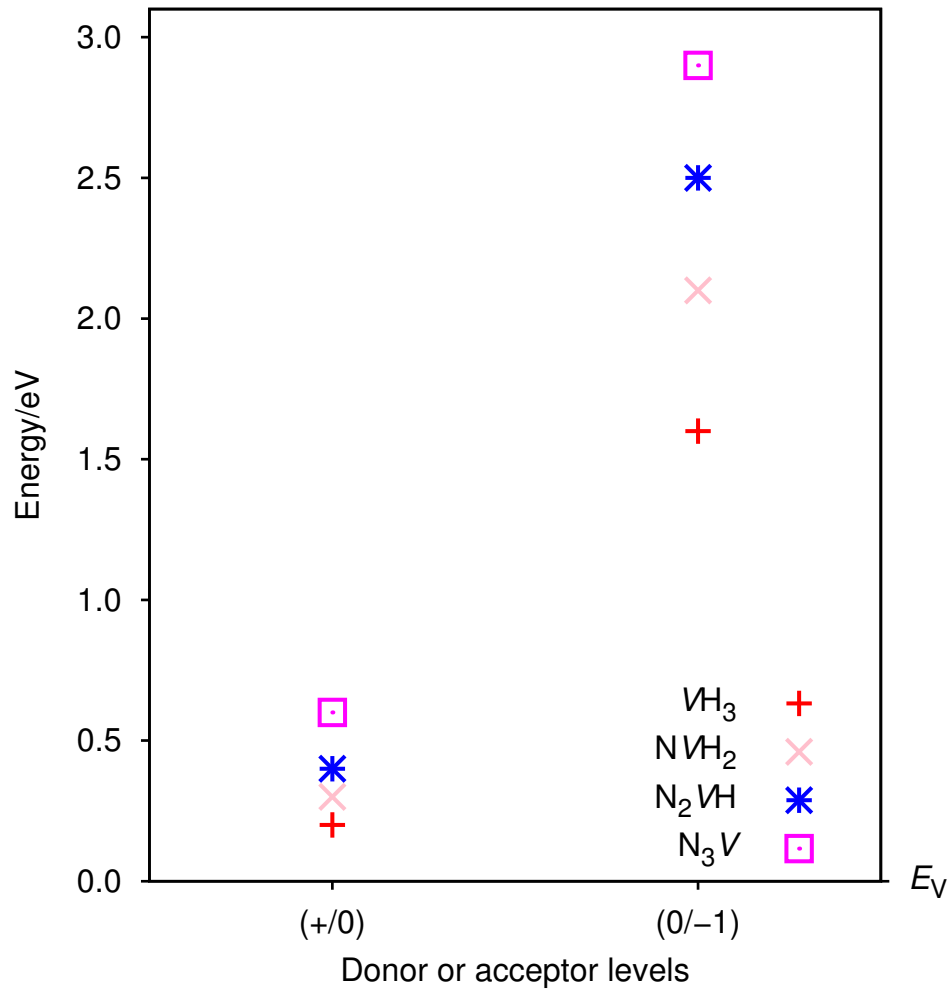


Figure 9.3: The donor and acceptor levels for the  $V H_3$  (red crosses),  $N V H_2$  (pink x's),  $N_2 V H$  (blue asterisk's) and  $N_3 V$  (magenta squares). The energy range has been reduced and extended to separate the data points when compared to Figure 7.3 and 8.3, the full band gap is therefore not visible, the valence band top ( $E_V$ ) is set to 0 eV.

### 9.4.3 Electronic structure

The  $VH_3$  and  $N_3V$  both have the same symmetry as the  $VH$  and  $NV$  defects. But the  $e$  states are not visible in the band gap in the neutral (Figure 9.4a) and positive (not pictured)  $VH_3$  defect and barely visible in the negative defect's band structure (Figure 9.4b), there are therefore no internal transitions in the  $VH_3$  defect, in either the neutral and negative or positive charge state.

The  $N_3V$  defect however in the neutral charge state has an internal transition as the  $e$  state is located in the band gap in Figure 9.4c. The transition between the  $e$  and the  $a_1$  state is 2.47 eV which is 0.5 eV within the experimental transition of 2.985 eV. There are no internal transitions in the negative charge state (Figure 9.4d) and only defect to band edge transitions.

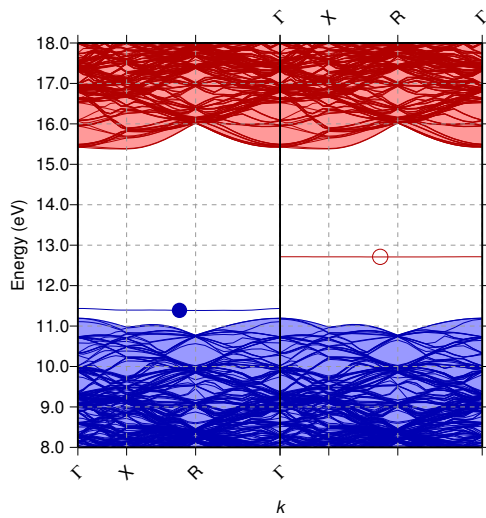
The band structures for the  $NVH_2$  and  $N_2VH$  are described by different states in the band gap when compared to the  $VH_3$  and  $N_3V$  defects; they are instead described by the states in the previous Chapter.

There are no internal transitions in the negatively charged defects in Figure 9.5b and 9.5d but the Figures are included as a comparison to highlight the hidden states seen in the neutral charge state that lie just above the valence band, they also demonstrate that the splitting between the  $a''-a'$  or  $a'-a'$  states increases as hydrogen is removed. In the neutral charge states of the  $NVH_2$  and  $N_2VH$  defects there is an allowed transition between the  $a_1$  and  $b_1$  states, this increases in magnitude from  $NVH_2$  and  $N_2VH$ .

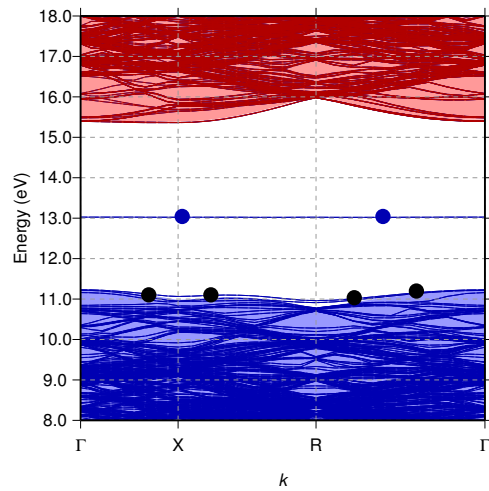
Interestingly there appears to be an anti-bonding orbital that appears on the edge of the conduction band minimum in the case of the  $NVH_2^0$  (Figure 9.5b).

Only the calculated donor levels of the  $N_3V$  and  $N_2VH$  defects in this set lie above the experimental acceptor level of boron doped diamond at  $E_V + 0.37$  eV (this level was previously attributed to aluminium acceptors [24]), therefore these may be the only defects with an accessible positive charge state. The band structures of  $N_3V^+$  and  $N_2VH^+$  are included in Figure 9.6.

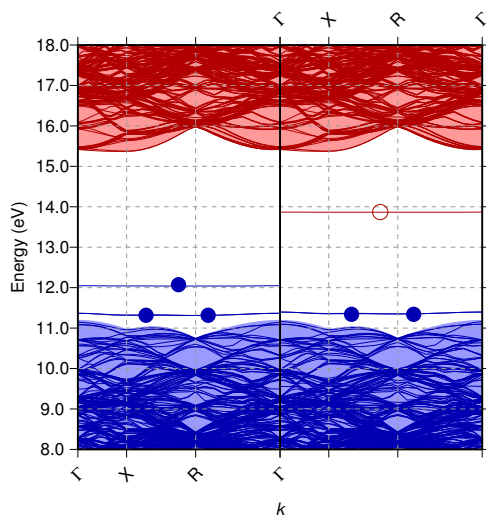
The  $N_2VH^+$  band structure (Figure 9.6a) appears to have an occupied band associated



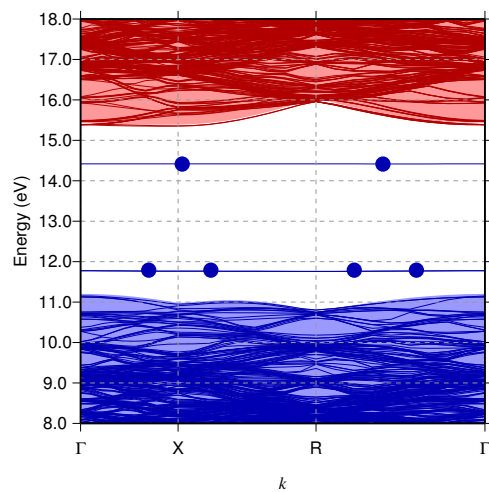
(a)  $VH_3^0$ ,  $S = 1/2$  ( $a_{1\uparrow}^1 a_{1\downarrow}^0$ )



(b)  $VH_3^{-1}$ ,  $S = 0$  ( $e_{\uparrow\downarrow}^4 a_{\uparrow\downarrow}^2$ )



(c)  $N_3V^0$ ,  $S = 1/2$  ( $e_{\uparrow}^2 a_{\uparrow}^1 e_{\downarrow}^1 a_{\downarrow}^0$ )



(d)  $N_3V^-$ ,  $S = 0$  ( $e_{\uparrow\downarrow}^4 a_{\uparrow\downarrow}^2$ )

Figure 9.4: Band structures calculated along high symmetry directions in the cubic Brillouin zone in the vicinity of the band gap. The band structure notation is described fully in Figure 7.4. Black circles like the blue circles indicate occupation of one electron, they are darker for clarification as they sit close to the valance band top.

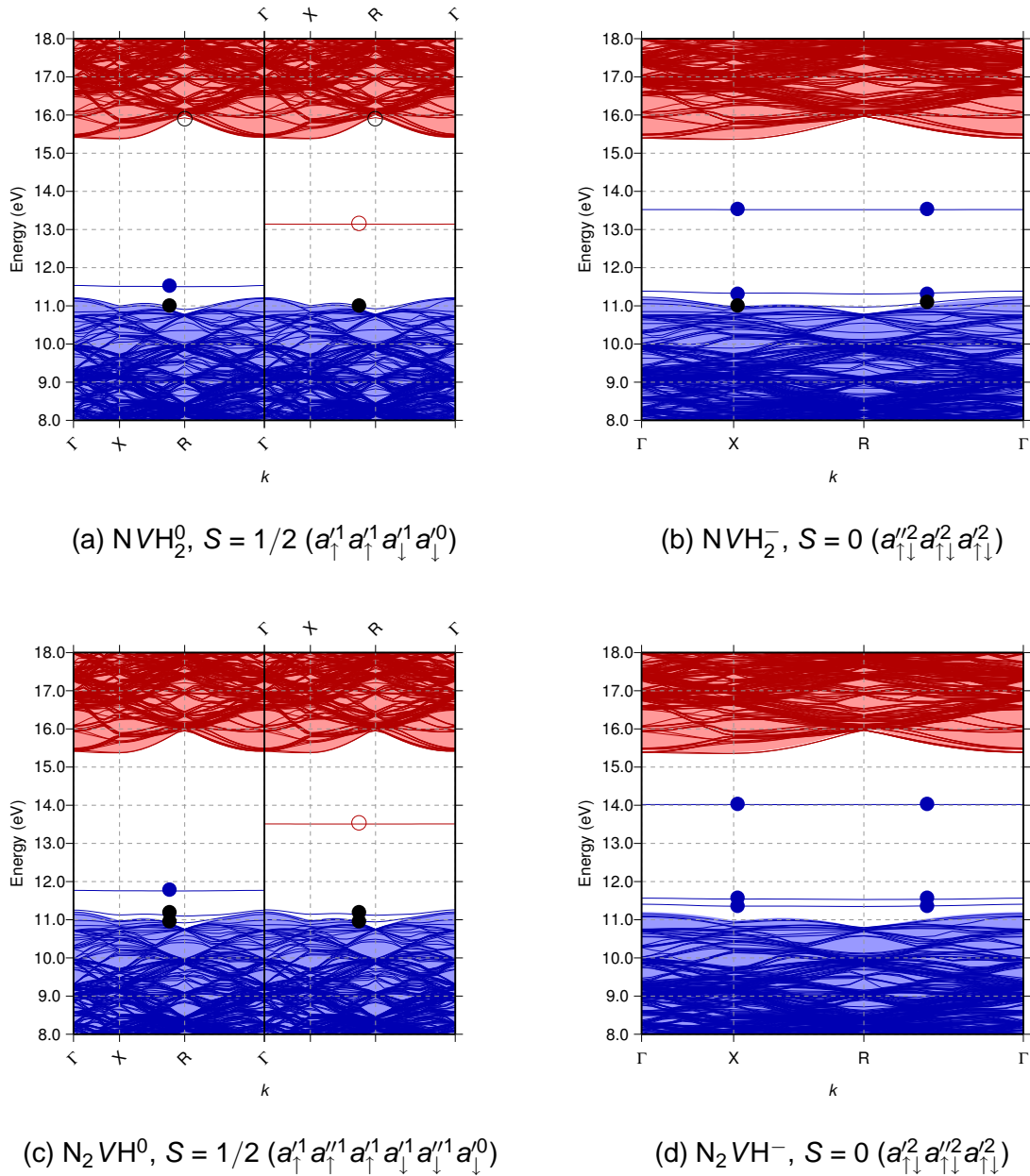


Figure 9.5: Band structures calculated along high symmetry directions in the cubic Brillouin zone in the vicinity of the band gap. The band structure notation is described fully in Figure 7.4. Black circles like the blue circles indicate occupation of one electron, they are darker for clarification as they sit close to the valance band top.

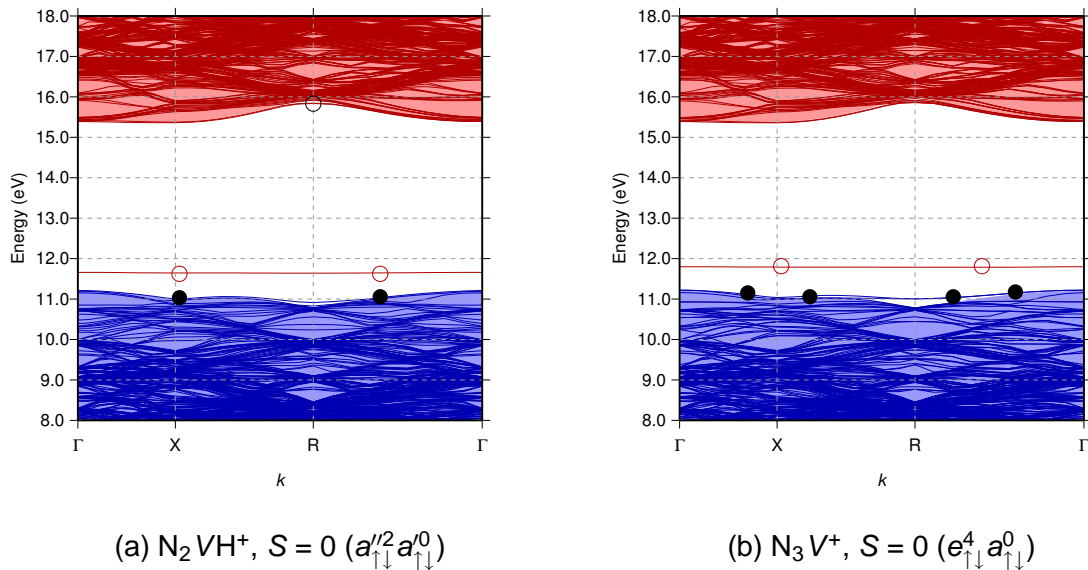


Figure 9.6: Band structures calculated along high symmetry directions in the cubic Brillouin zone in the vicinity of the band gap. The band structure notation is described fully in Figure 7.4. Black circles like the blue circles indicate occupation of one electron, they are darker for clarification as they sit close to the valence band top.

with the defect just above the valence band and an unoccupied band within and also just below the conduction band, using this information in Figure 9.6a it is difficult to assert this but as charge is removed in all cases in this set the defect bands reduce in energy.

In the  $N_3 V^+$  defect's band structure (Figure 9.6b) the evidence of a band above the valence band is clearer, although this is a doubly degenerate  $e$  band as opposed to the  $a''$  state in the  $N_2 V H^+$  band structure (Figure 9.6a).

There is  $e$  to  $a$  transition in the case of the  $N_3 V^+$  defect with a magnitude of around 0.6 eV, if the  $V H_3^+$  defect was accessible the  $e$  state is not visible in the band gap so only band edge to the  $a$  state transitions would be available with a smaller magnitude of around 0.3 eV.

In the  $N_2 V H^+$  band structure (Figure 9.6a) an  $a''$  to  $a'$  transition may be possible and

the magnitude will be less than the  $N_3 V^+$  transition discussed above. As these bands however lie along the valence band top the transition will likely be broad as the band takes a range of values. If the  $NVH_2^+$  is accessible it will have a similar transition to the  $N_2 VH^+$  defect but it will be smaller in magnitude.

**9.4.4 Vibrational properties**Table 9.1: A comparison of bond lengths and C–H vibrational modes as the charge and spin state varies for defects in the  $n + m = 3$  set.

Defect	$VH_3$			$NVH_2$			$N_2VH$		
Charge	1	0	-1	1	0	-1	1	0	-1
Spin	0	1/2	0	0	1/2	0	0	1/2	0
Symmetric stretch ( $cm^{-1}$ )	3700	3710	3430	3410	3420	3100	3050	3040	2630
Anti-symmetric stretch ( $cm^{-1}$ )	3450/ 3420	3460/ 3450	3120/ 3090	3200	3230	2850	-	-	-
Bend mode ( $cm^{-1}$ )	1440/ 1430/ 1400	1450/ 1410	1560/ 1520	1550	1580	1680/ 1330	1350/ 1310	1340/ 1330	1470
C–H bond length (Å)	1.04	1.04	1.07	1.06	1.07	1.09	1.08	1.08	1.12

A summary of vibrational modes are shown in Table 9.1, symmetric and anti-symmetric bend modes associated with this set are included where applicable. Bend modes close to the Raman frequency are also included.

As defects containing hydrogen correspond to shorter C–H bonds, generally the vibrational mode occurs at a higher wave number and therefore a higher frequency. The bend modes however are more variable due to the influence of their surroundings. There is no experimental evidence pointing to vibrational modes corresponding to the  $VH_3$  defect but they are expected to be larger than the corresponding  $NVH_2$  and  $N_2VH$  defects.

The  $3234\text{ cm}^{-1}$  peak has been observed in diamonds treated by hot transition metals and it becomes particularly strong after treatment in a hydrogen-containing atmosphere [83]. Previously it was tentatively attributed to C–H vibrations within graphite inclusions

[83] but as it correlates to a band at  $1617 \text{ cm}^{-1}$  a potential assignment could be to the  $NVH_2^0$  defect. The calculated anti-symmetric mode is within  $4 \text{ cm}^{-1}$  and the bend mode is within 2%.

The  $N_2VH^0$  defect is thought to have been recently identified via EPR [12] and a bend mode doublet at  $1375/1378 \text{ cm}^{-1}$  has been correlated with this find. This is within around 3% of the calculated bend modes at  $1340/1330 \text{ cm}^{-1}$ . It is suggested that the associated bend mode would be obscured by a broad feature from  $2750\text{--}2900 \text{ cm}^{-1}$ , the calculated bend mode is within 5% of this upper limit, making the signal difficult to isolate experimentally.

#### **9.4.5 Hyperfine interaction**

The calculated hyperfine parameters due to the hydrogen and nitrogen are listed in Table 9.2.

Once again multiple hydrogen defects when viewed dynamically are problematic as the interaction between the mobile hydrogens is unknown but an average of each possible orientation is taken.

There is a large difference between the hyperfine parameters when the  $VH_3$  is static when compared to when the hydrogens are treated as dynamic. The symmetry as a consequence also changes.

All the static hydrogen hyperfine parameters listed in Table 9.2 are of a similar magnitude. Whereas the magnitude of the hyperfine tensors when the hydrogen is dynamic is more variable.

The hyperfine parameters due to the nitrogen are of a similar magnitude in both static and dynamic views where possible.

In the case of the  $N_2VH$  defect that was recently identified [12], both the calculated hydrogen and nitrogen principal hyperfine values and directions are in reasonable agreement. The identification also confirms the dynamic nature of the hydrogen in this case.

The calculated hyperfine principal values associated with  $N_3V$  defect listed in Table 9.2

Table 9.2: A comparison of calculated hydrogen ( $^1\text{H}$ ) and nitrogen ( $^{14}\text{N}$ ) hyperfine tensors for the  $\text{VH}_3$ ,  $\text{NVH}_2$ ,  $\text{N}_2\text{VH}$  and  $\text{N}_3\text{V}$  centres where applicable. A full breakdown is given in Table 7.2.

Label	Assignment/ calculated	$^1\text{H}/^{14}\text{N}$ Site	Dynamic	Sym.	$A_1$	$(\theta_1, \varphi_1)$	$A_2/A_\perp$	$(\theta_2, \varphi_2)$	$A_3/A_\parallel$	$(\theta_{3\text{ or } \parallel}, \varphi_{3\text{ or } \parallel})$	$r_{\text{es}}$	Ref.
-	$\text{VH}_3^0, S = 1/2$	$^1\text{H}$	3	$\times$	$C_{1h}$	-19	(45,-179)	-16	(87,-86)	27	(45,-6)	1.93
-			$\checkmark$	$T_d$	-3	(90,0)	-3	(90,90)	-3	(0,-)		
-	$\text{NVH}_2^0, S = 1/2$	$^1\text{H}$	1	$\times$	$C_1$	-17	(-78,136)	-14	(14,165)	27	(-83,-133)	1.95
-			$\checkmark$	$C_{3v}$	-	-	6	-	-15	(55,135)		
-		$^{14}\text{N}$	2	$\times$	$C_{1h}$	2.47	(78,12)	2.48	(-45,90)	5	(47,113)	2.77
-		$\checkmark$	$C_{3v}$	-	-	3	-	5	(55,135)			
-	$\text{N}_2\text{VH}^0, S = 1/2$	$^1\text{H}$	2	$\times$	$C_{1h}$	-12	(-9,-45)	-16	(90,45)	29	(-81,135)	1.95
-			$\checkmark$	$C_{2v}$	-11	(0,90)	-16	(90,45)	28	(90,-45)		
WAR13		$\checkmark$	$C_{2v}$	-16.07(9)	(0,45)	-20.68(6)	(90,45)	27.41(4)	(90,135)		[12]	
-		$^{14}\text{N}$	1	$\times$	$C_1$	4.31	(48,25)	4.33	(-70,-46)	8	(49,-117)	2.75
-	$\text{N}_3\text{V}^0, S = 1/2$	$^{14}\text{N}$		$\checkmark$	$C_{1h}$	4	(43,45)	5	(90,-45)	8	(47,-135)	
WAR13			$\checkmark$	$C_{1h}$	3.91(2)	(43.2(1), 225)	4.24(2)	(90.0, 135)	6.51(2)	(47.2(1), 45)		[12]
-	$\text{N}_3\text{V}^0, S = 1/2$	$^{14}\text{N}$	1	-	$C_{1h}$	7.1795	(90,-45)	7.1815	(23,45)	12	(67,-135)	2.72
P2			-	$C_{1h}$	7.44(4)		7.46(4)		11.30(4)	157.8(2)*		[170]
-			-	$C_{1h}$	7.4(1)		7.4(1)		11.2(1)	158(1)*		[171]

\* $\varphi$  from [110] toward [001]

are within 0.8 MHz of the experimental results.

The carbon hyperfine parameters are listed in Table 9.3.

When hydrogen is removed in this set of defects, the magnitude of the principal value in each case, (either the carbon radicals or the carbon bonded to the hydrogen in the static view or the averaged dynamic view) increases.

As before, the hyperfine values associated with the carbon in the C–H bond has a much smaller value as there is little localisation of unpaired electron density, whereas, the unique radical in the static view has values that are much larger.

The experimental results associated with the P2 defect, although there is a difference of ten's of MHz, they are taken to be in good agreement of the calculated values.

Table 9.3: A comparison of calculated carbon ( $^{13}\text{C}$ ) hyperfine tensors for the  $\text{VH}_3$ ,  $\text{NVH}_2$ ,  $\text{N}_2\text{VH}$  and  $\text{N}_3\text{V}$  centres. A full breakdown of notation used is described in Table 7.2. C–H indicates if the carbon is bonded to the hydrogen in a static view and  $n$  indicates the number of equivalent sites.

Label Assignment/ calculated	$n$	Site	Dynamic	Sym.	$A_1$	$(\theta_1, \varphi_1)$	$A_2/ A_\perp$	$(\theta_2, \varphi_2)$	$A_3/ A_\parallel$	$(\theta_{3\text{ or}\parallel}, \varphi_{3\text{ or}\parallel})$	Ref.
$\text{VH}_3^0, S = 1/2$	3 (C–H)	1	$\times$	$C_{1h}$	7.090	(45,180)	7.095	(77,77)	19	(48,–25)	
	1	4	$\times$	$C_{3v}$	-	-	129	-	339	(55,45)	
	4		$\checkmark$	$C_{3v}$	-	-	38	-	98	(55,135)	
$\text{NVH}_2^0, S = 1/2$	2 (C–H)	1	$\times$	$C_{1h}$	10.53	(–88,–46)	10.58	(20,37)	22	(70,–135)	
	1	4	$\times$	$C_{1h}$	156.07	(–45,90)	156.09	(–66,–27)	378	(55,45)	
	3		$\checkmark$	$C_{1h}$	108	(45,91)	158	(88,–1)	208	(–45,87)	
$\text{N}_2\text{VH}^0, S = 1/2$	1 (C–H)	2	$\times$	$C_{1h}$	15.98	(90,45)	16.05	(–22,135)	29	(68,135)	
	1	3	$\times$	$C_{1h}$	184.45	(–35,–45)	184.50	(90,45)	413	(–55,135)	
	2		$\checkmark$	$C_{1h}$	100	(90,45)	101	(35,–45)	220	(–55,–45)	
P2 $\text{N}_3\text{V}^0, S = 1/2$	1	4	-	$C_{3v}$	-	-	220	-	451	(55,45)	
	1		-	$C_{3v}$	-	-	186(6)	-	432(6)	*	[171]

\*Directions described in reference [171].

## Chapter 10. $N_nVH_m$ , where $n + m = 4$

V	NV	$N_2V$	$N_3V$	$N_4V$
VH	NVH	$N_2VH$	$N_3VH$	
$VH_2$	$NVH_2$	$N_2VH_2$		
$VH_3$	$NVH_3$			
$VH_4$				

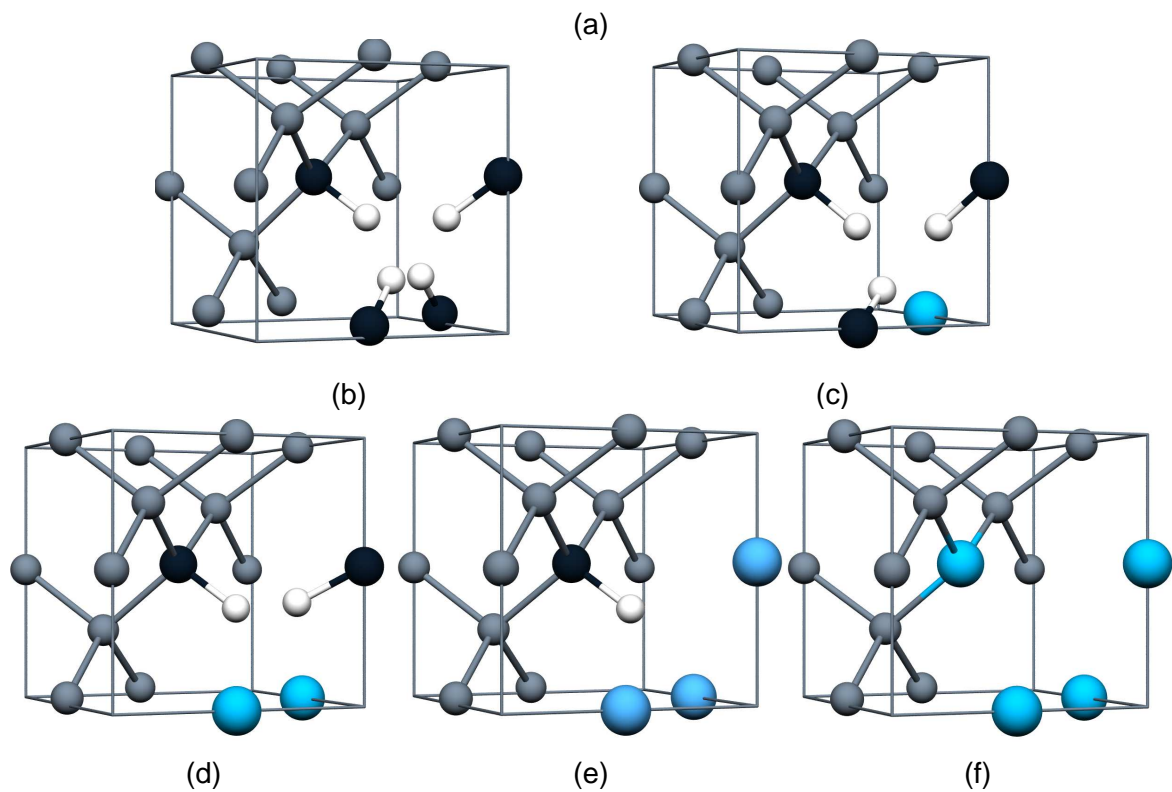


Figure 10.1: (a) Highlighted defects, where  $n + m = 4$ . (b) The  $VH_4$  defect. (c) The  $NVH_3$  defect. (d) The  $N_2VH_2$  defect. (e) The  $N_3VH$  defect. (f) The  $N_4V$  defect. The schematics of the defect structure are the same as those described in Figure 5.1b.

### 10.1 $VH_4$ , $NVH_3$ and $N_2VH_2$

Only two defects of the those highlighted in Figure 10.1a have been identified experimentally and are discussed below; any defects with multiple hydrogens ( $VH_4$ ,  $NVH_3$  and  $N_2VH_2$ ) have not been previously detected in diamond but multi-hydrogen defects have been identified in silicon.

### 10.2 $N_3VH$

$N_3VH$  C–H stretch mode has been recently confirmed by theory to belong to the  $3107\text{ cm}^{-1}$  peak seen in IR absorption [144]. This peak is also accompanied with a bend mode at  $1405\text{ cm}^{-1}$  which has also been attributed to the  $N_3VH$  defect. The  $3107\text{ cm}^{-1}$  is found in natural type-Ia diamond and can be introduced by in CVD diamonds when annealed above  $1700\text{ }^\circ\text{C}$  [44, 172, 173]. HPHT annealing of natural diamonds is also found to increase the concentration of  $N_3VH$ . The defect is found to be trigonal, with the C–H bond being the axis of rotation, Figure 10.1e is a schematic of the defect.

### 10.3 $N_4V$

The  $N_4V$  defect is also known as the B-centre, it was briefly discussed in Chapter 1 as it is used in the classification of diamonds. It is a tetrahedral defect (Figure 10.1f). They are formed in natural diamonds type IaB and can be formed in synthetics after extended annealing. The B-centre is responsible for the IR absorption bands at  $1332\text{ cm}^{-1}$  (sharp) and at  $1280\text{ cm}^{-1}$  (broad).

## 10.4 Results

### 10.4.1 Structural analysis

Both the  $VH_4$  and  $N_4V$  are tetrahedral defects with  $T_d$  symmetry (Figure 10.1b and 10.1f respectively), they therefore have the same symmetry as the surrounding bulk

diamond.  $NVH_3$  and  $N_3VH$  have  $C_{3v}$  symmetry and the axis of rotation goes through either the single nitrogen or hydrogen respectively towards the centre of the vacancy (Figure 10.1c and 10.1e respectively). The  $N_2VH_2$  has  $C_{2v}$  ground state symmetry (Figure 10.1d).

Varying charges apart from neutral are not accessible due to the absence of unstable carbon radicals. Effectively removing charge from either a C–H bond or from a nitrogen lone pair costs energy and adding charge to either a C–H bond or to a nitrogen lone pair is also unfavoured. All the defects in this set are therefore neutral and  $S = 0$ ; the C–H bond lengths where applicable vary according to Table 10.1.

The addition of a hydrogen (from one–four) or alternatively the removal of a nitrogen (from three–zero) in this set of defects reduces the C–H bond length by 0.02 Å each time. This suggests that intermolecular hydrogen bonding between the disperse nitrogen lone pair and the hydrogen(s), extends and weakens the C–H bond(s). Conversely, as the carbon is slightly negative when bonded to a hydrogen it makes the hydrogen slightly positive, as the hydrogens are equivalent in the defect the like slightly positive charges on the hydrogens repel each other, consequently shortening the C–H bonds. The  $VH_4$  has the smallest hydrogen bond length of 1.02 Å of all defects investigated.

Table 10.1: The C–H bond length associated with the  $m + n = 4$  set of defects. All defects are in their neutral charge state.

Defect	$VH_4$	$NVH_3$	$N_2VH_2$	$N_3VH$
C–H bond length (Å)	1.02	1.04	1.06	1.08

Although, where there are hydrogens available in this set, there are no radicals so therefore there is no possibility of tunnelling within this set of defects; the structure will therefore be the symmetry described above.

The C–N bonds surrounding the vacancy in the  $N_4V$  defect are around 1.48 Å compared to the C–C bonds extending out from the vacancy in the  $VH_4$  where they are

around 1.52 Å. Suggesting that nitrogen adds more strain around the defect compared to when hydrogen is introduced.

### 10.4.2 Electrical properties

As they are spin zero defects all gap states are occupied leaving no allowed transitions between them, so they are not expected to luminesce. Despite this the band structures reveal some interesting features (Figure 10.2).

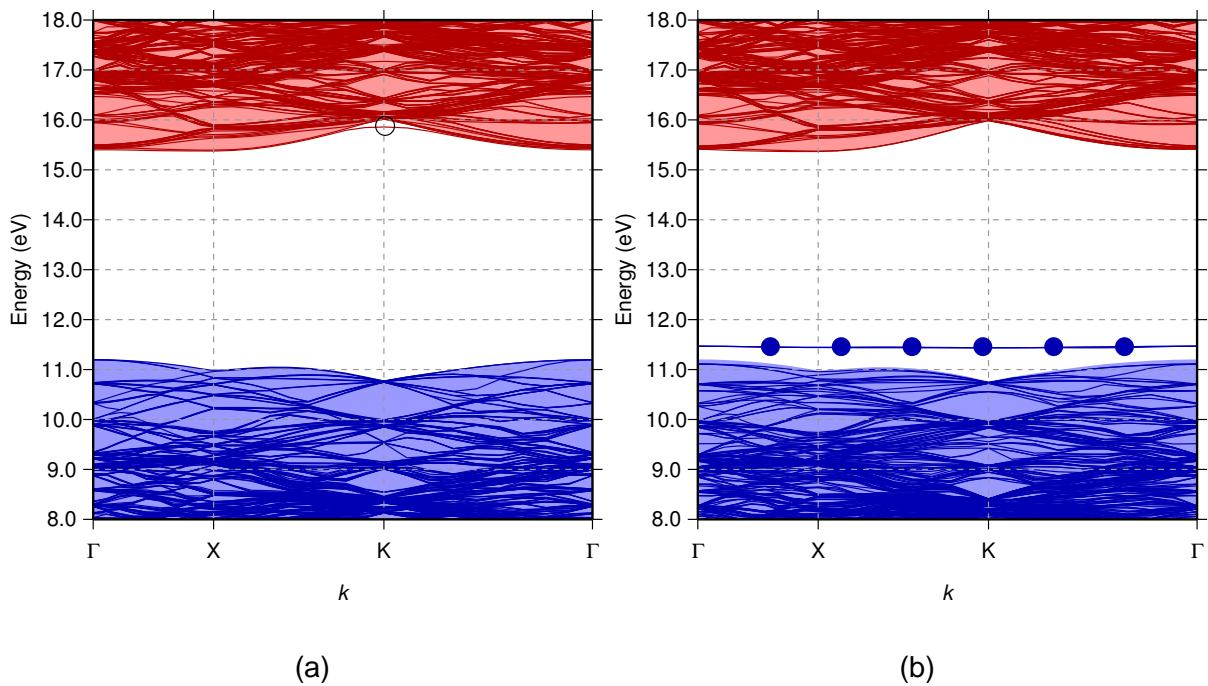


Figure 10.2: The band structures of (a) the  $VH_4$  and (b) the  $N_4V$  defects, follow the same nomenclature as briefed in Figure 7.4 Both are neutral,  $S = 0$  defects.

Both the  $VH_4$  and the  $N_4V$  defects have  $T_d$  symmetry. Following the logic before, this time including four orbitals:  $a$ ,  $b$ ,  $c$  and  $d$ . It leads to the lowest energy nodeless combination of  $a + b + c + d$ , which is an  $a_1$  irreducible set. The next highest energy

set will form one node and yields a triply degenerate  $t_2$  set consisting of:  $a - b - c + d$ ,  $a - b + c - d$  and  $a + b - c - d$ . This is also the symmetry of the neutral vacancy.

In Figure 10.2a all four occupied states introduced by the defect are occupied and lie within the valance band. Interestingly there is also a possible anti-bonding sigma orbital visible on the edge of the conduction band.

At the other end of the spectrum in the  $n + m = 4$  set, where there are four nitrogens, the band structure is visibly different as seen in Figure 10.2b. The triply degenerate  $t_2$  lies above the valance band top by approximately 0.3 eV and is fully occupied. The  $a_1$  state also occupied lies within the valance band. In this case here are no anti-bonding orbital visible.

The differences seen in the two band structures in Figure 10.2 suggests that the C–H bonds are lower in energy and more stable when compared to the nitrogen lone pair in this case.

The band structures of the remaining defects in this set are not included as they look similar to the band structures in Figure 10.2, they are however described below.

The  $NVH_3$  and  $N_3VH$  have  $C_{3v}$  symmetry like the  $VH$ ,  $NV$ ,  $VH_3$  and  $N_3V$  defects. The irreducible representation therefore corresponds to two  $a_1$  states and a doubly degenerate  $e$  state. In the case of  $N_3VH$ , the doubly degenerate  $e$  state lies around 0.1eV above the valance band top and one  $a_1$  state is just visible along the top of the valance band, the other lies within it. All states introduced by the defect are occupied. The  $NVH_3$  has a barely visible  $e$  state just above the valance band top and there is also a slightly visible anti-bonding sigma orbital on the edge of the conduction band.

$N_2VH_2$  has  $C_{2v}$  symmetry, the band structure has one  $a_1$  and one  $b_2$  state that in the valance band and one  $b_1$  and the remaining  $a_1$  state lie just above it.

### 10.4.3 *Vibrational properties*

The  $VH_4$ ,  $NVH_3$  and  $N_2VH_2$  defect will not be detectable in EPR as they have paired electrons so observations should be directed towards infrared absorption experiments. It is known that where hydrogen bonding is present in a defect the observed vibration

Table 10.2: A comparison of bond lengths and C–H stretch modes for the defects in the  $n + m = 4$  set.

Defect	$VH_4$	$NVH_3$	$N_2VH_2$	$N_3VH$
Symmetric stretch ( $\text{cm}^{-1}$ )	4120	3790	3490	3120
Anti-symmetric stretch ( $\text{cm}^{-1}$ )	3830	3570	3320	-
Bend mode ( $\text{cm}^{-1}$ )	1390/1380	1480/1460	1620	1360
C–H bond length ( $\text{\AA}$ )	1.02	1.04	1.06	1.08

occurs at a higher wave number [174, p. 273], as seen in Table 10.2 however the stretch modes are higher when less nitrogen is present. In fact the highest wave number found in the full set of defects occurs at  $4120 \text{ cm}^{-1}$  for the  $VH_4$  defect. This breathing mode however, would be IR inactive and it would be the second degenerate mode at around  $3830 \text{ cm}^{-1}$  that would be observed.

The  $3107 \text{ cm}^{-1}$  has been recently assigned to the  $N_3VH$  defect by using a similar method here, in this case our result is within 0.5% of the experimental value and is considered an excellent agreement, the associated bend mode assigned to  $1405 \text{ cm}^{-1}$  is within approximately 4% agreement.

Although there is a strong correlation between C–H bond lengths and the frequency of stretching vibration (and therefore an indication if nitrogen is involved), there seems to be little correlation between bond lengths and bend modes.

The  $1371 \text{ cm}^{-1}$  bend mode has been suggested based on symmetry grounds to belong the  $VH_4$  defect [155] and our results are within  $9\text{--}11 \text{ cm}^{-1}$  of this suggestion. No stretch mode has been associated with the bend mode as it has been suggested that it would be obscured by a broad band from  $2850\text{--}3000 \text{ cm}^{-1}$  but the calculated bend mode is outside this region at  $3830 \text{ cm}^{-1}$ . If this assignment is correct, according to reference [162] it is also found to be grown in and persists to  $1800 \text{ }^\circ\text{C}$ .

A peak at  $3310 \text{ cm}^{-1}$  has been observed previously as a weak broad feature in natural diamonds exhibiting type 1b character [175]. But information provided from De Beers [162] sees a strong peak at  $3310 \text{ cm}^{-1}$  annealing in at  $1500 \text{ }^\circ\text{C}$  that remains until  $1800$

°C in a nitrogen doped CVD diamond. The  $N_2VH_2$  anti-symmetric stretch is a potential for this stretch as it is within  $10\text{ cm}^{-1}$  of  $3310\text{ cm}^{-1}$ . But there is no mention of other potential experimental candidates for stretch or bend modes associated with  $N_2VH_2$  that correlate with those calculated in Table 10.2.

There is a strong correlation between the bond length and the frequency of the local vibrational stretch modes. The shortest C–H bond length modelled in the full set covered corresponds to the  $VH_4$  defect at  $1.02\text{ \AA}$  and this defect has the largest symmetric stretch at  $4120\text{ cm}^{-1}$ . According to reference [162], a peak at  $4677\text{ cm}^{-1}$  is found to anneal in at  $1500\text{ °C}$ . By extrapolating the correlation between the C–H bond length and stretch modes,  $4677\text{ cm}^{-1}$  would correspond to a bond length of around  $0.99\text{ \AA}$ . An  $sp^3$  bonded hydrocarbon is approximately  $1.9\text{ \AA}$  so a reduction of  $0.9\text{ \AA}$  would result in a highly strained defect. Therefore this mode in particular is more likely associated to an overtone of a stretch mode or possibly a combination of stretch and bend modes.

#### **10.4.4 Hyperfine interaction**

As there is no possibility for the defects in this set to adopt a non-zero spin there is no hyperfine interactions and therefore they will not be detectable in EPR.

## Chapter 11. Energetics

### 11.1 Quantum tunnelling

In the defects reviewed where there is at least one hydrogen and a carbon radical (listed in Figure 11.1), tunnelling of the hydrogen between radical sites is possible as hydrogen is a light element and the distance between sites is inherently small due to the size of the vacancy.

V	NV	N <sub>2</sub> V	N <sub>3</sub> V	N <sub>4</sub> V
VH	NVH	N <sub>2</sub> VH	N <sub>3</sub> VH	
VH <sub>2</sub>	NVH <sub>2</sub>	N <sub>2</sub> VH <sub>2</sub>		
VH <sub>3</sub>	NVH <sub>3</sub>			
VH <sub>4</sub>				

Figure 11.1: The defects highlighted have the potential for the hydrogen(s) to tunnel between carbon radical sites.

Tunnelling of hydrogen is also seen in silicon, where the  $VH^0$  defect, when stationary has  $C_{1h}$  symmetry: the hydrogen is bonded to one silicon atom and two silicons adjacent to vacancy form a bond perpendicular to a  $\{110\}$  mirror plane [176]. When tunnelling occurs above 100 K the geometry is averaged and the defect becomes  $C_{3v}$  symmetry as the bond Reconstruction and the Si–H bond occupy each possible position around the vacancy.

Tunnelling has also been seen in defects in diamond. The NVH and N<sub>2</sub>VH all show averaged symmetry when viewed in EPR due to the comparatively long timescales of

the experiment. The P1 centre is also known to tunnel [177].

The possibility of the hydrogen tunnelling depends on the barrier width and height of the energy profile of the hydrogen migrating between each carbon site. As the width and height increases the probability of tunnelling decreases. At higher temperatures, reorientation will be a thermally activated process but at lower temperatures if the barrier permits the rate will be determined by quantum effects.

There is little correlation between the width and height of the barrier for the defects discussed in Table 11.1 and little correlation between the contents or charge of the defect and the energy profile of the hopping.

Table 11.1: The barrier height (eV) and width (Å) associated with the migration of the hydrogen between available carbon sites in each charge and spin state listed.

Defect	Barrier width (Å)	Barrier height (eV)
$VH^+$ , $S = 0$	1.0	1.1
$VH^0$ , $S = 3/2$	0.8	0.3
$VH^0$ , $S = 1/2$	1.0	0.6
$VH^-$ , $S = 1$	0.9	0.8
$NVH^+$ , $S = 1/2$	0.9	0.6
$NVH^0$ , $S = 1$	0.9	0.5
$NVH^0$ , $S = 0$	1.0	1.1
$NVH^-$ , $S = 1/2$	0.9	0.5
$N_2VH^+$ , $S = 0$	0.9	0.5
$N_2VH^0$ , $S = 1/2$	0.6	0.9
$N_2VH^-$ , $S = 0$	0.7	0.1

There is a greater variation with the barrier height: this varies between 0.1–1.1 eV.  $N_2VH^0$ ,  $S = 1/2$  is observed in Q- (30–50 GHz) and X- (8–12 GHz) band EPR with an

averaged symmetry, therefore hydrogen is hopping between carbon sites faster than the rate of experiment at room temperature for this defect. An approximation of a classical rate, based on the energy barrier of 0.9 eV, the hydrogen hopping between carbon radicals at room temperature equates to the hydrogen associated with each carbon for around 300 s, this means at room temperature if the motion of the hydrogen was purely classical the symmetry seen in EPR would be static.

At higher temperatures the likelihood of hopping increases and the time the hydrogen is associated with each carbon is reduced. At an extremely high temperature of 2300 K, (at which point defects may migrate themselves) the calculated time the hydrogen is associated with a carbon is around  $\times 10^{-12}$  s, at this rate the symmetry seen in Q-band (30–50 GHz) EPR would now be the average view (if the defect remains intact). Therefore it is apparent that for this energy profile associated with the NVH<sub>2</sub> defect, quantum tunnelling rather than classical activation is occurring at room temperature and therefore the prominent determining property would be the barrier width.

The barrier widths show little variation between 0.6–1.0 Å due to the constrained structure around the vacancy (the width is difficult to define as all atoms move when the hydrogen hops, the width in this case is taken to be the distance between the hydrogen in its start and end position). The NVH<sup>-</sup>,  $S = 1/2$  has a barrier width of 0.9 Å which is close to the upper boundary of this range, at room temperature the barrier height corresponds to a classical residence time of approximately  $4 \times 10^{-5}$  s, long enough for a static structure to be seen in EPR. As this defect tunnels at room temperature the barrier must allow this to happen sufficiently fast enough, suggesting that even the larger width does not allow the hydrogen wave function to exponentially decay to zero as it penetrates through this classically forbidden zone, therefore tunnelling may occur for this associated energy profile.

The rates of quantum tunnelling, which will be the deciding factor in what symmetry is seen in EPR is not perused in the Thesis. It was however suggested in reference [86] and [140] that the tunnelling period for VH<sup>-</sup> is 50 ps an upper limit of EPR time resolution and the NVH a rate of 8.1 ps. Based on the information presented in

Table 11.1, the widths of both the  $VH^-$  and  $NVH^-$  defects are the same and the barrier height differs by 0.3 eV, it seems surprising that this difference in height only, changes the rate of tunnelling this dramatically.

Ultimately, due to no clear correlation between the contents of the defect and the barrier height and also the limited distance due to the constrained vacancy, it is suggested that all defects that contain hydrogen and an available radical in the sets previously discussed will tunnel.

## 11.2 Binding energies

The defects highlighted in Figure 11.2 have been unintentionally identified in diamond but binding energies associated with all the defects mentioned are discussed below.

V	NV	$N_2V$	$N_3V$	$N_4V$
VH	NVH	$N_2VH$	$N_3VH$	
$VH_2$	$NVH_2$	$N_2VH_2$		
$VH_3$	$NVH_3$			
$VH_4$				

Figure 11.2: The defects highlighted have been unintentionally identified in diamond, the VH defect however has been researched but the identification is uncertain.

The difference in the binding energies between each defect via the addition of a ( $N_s$ ) and ( $H_i$ ) are listed in Figure 11.3. In Figure 11.3 there is no dependence on the electron chemical potential as only neutral defects are being considered, there is also no dependence on the choice of atomic chemical potential as there is no imbalance of elements. The difference in binding energies between the defects either side of the number in Figure 11.3 is defined by:  $E(N_nVH_m) + E(N_s) - E(N_{n+1}VH_m) - E(\text{pure})$  for the addition of nitrogen and  $E(N_nVH_m) + E(H_i) - E(N_nVH_{m+1}) - E(\text{pure})$  for the addition of hydrogen.  $E(\text{pure})$  is the total energy of a defect free cell. Note that the V has not been corrected here or in the following calculations [178].

V	4.3	NV	4.6	N <sub>2</sub> V	4.5	N <sub>3</sub> V	4.5	N <sub>4</sub> V
5.8		6.1		6.2		6.3		
VH	4.7	NVH	4.7	N <sub>2</sub> VH	4.6	N <sub>3</sub> VH		
5.6		5.6		5.7				
VH <sub>2</sub>	4.7	NVH <sub>2</sub>	4.7	N <sub>2</sub> VH <sub>2</sub>				
5.1		5.1						
VH <sub>3</sub>	4.7	NVH <sub>3</sub>						
4.6								
VH <sub>4</sub>								

Figure 11.3: The defects are highlighted. Nitrogen (N<sub>s</sub>) is added as you move horizontally across the figure from left to right and hydrogen (H<sub>i</sub>) is added as you move down the defects. The number is the difference in binding energy between the defects either side.

In general, as the vacancy's radical sites become saturated, providing there is an excess of hydrogen and nitrogen the more thermodynamically stable the defect becomes; the addition of a H<sub>i</sub> or an N<sub>s</sub> is exothermic in all cases in Figure 11.3.

The addition of hydrogen to a hydrogen containing defect introduces an unfavorable sterical hindrance between the C–H bonds as well as a repulsive Coulombic interaction between the hydrogens as they both are slightly positive. Whereas the addition of hydrogen to a nitrogen containing defect introduces an attractive Coulombic force between the C–H bond and the nitrogen lone pair. This balance between the attractive and repulsive forces as the vacancy becomes saturated is highlighted below when viewing the trends seen in Figure 11.3.

There is less variation when nitrogen is added in each transition when compared to the addition of hydrogen.

As you move horizontally between defects in Figure 11.3 the energy released reduces but when you compare the energy released when nitrogen is added to a hydrogen containing defect there is more energy released the more hydrogen is in the defect.

As you move vertically in Figure 11.3 when hydrogen is added, less energy is released in each subsequent transition and the difference between transitions is larger when compared to the addition of nitrogen.

Adding hydrogen to a defect containing more nitrogen releases more energy when compared to the addition of a hydrogen to a defect saturated with solely hydrogen.

### 11.3 VH

The H1 defect, seen in polycrystalline CVD diamond, was thought to be a VH-like defect found in samples that have a low  $N^0$  content [145]. It was later suggested [146] that this was the VH defect, but the calculated EPR results presented in this Thesis are at odds with this assignment.

The VH defect was also thought to have been identified in CVD samples grown in a nitrogen rich atmosphere by Glover *et al.* [131]. Although the calculated hyperfine interactions are in broad agreement with experiment, a firm assignment can not be made based on the information in this Thesis. Indeed, based upon tunnelling rates and previous hyperfine calculations [86] a viable alternative explanation for the experimental observation is a  $V_2H$  centre.

Nevertheless, it seems reasonable to expect hydrogen to be found as the VH defect in as-grown CVD material: as the vacancy is a suitable trap for the hydrogen making it more thermodynamically stable as strong C–H bonds are formed in the process; the addition of hydrogen to a vacancy increases the migration energy when compared to an isolated vacancy so the defect may be stable at growth temperatures; similar defects like the NV and the NVH are found in as-grown material; there is hydrogen available in the source gases in the CVD growth process; hydrogen is readily incorporated in polycrystalline CVD diamond films in grain boundaries or in inter-granular material.

Alternatively, the defect might be created by ion implantation, as is the case in silicon [176]. Such an approach might be suitable for determining whether the grown in defects are mono- or di-vacancy based.

The calculated binding energy of a vacancy and a hydrogen interstitial to form VH as

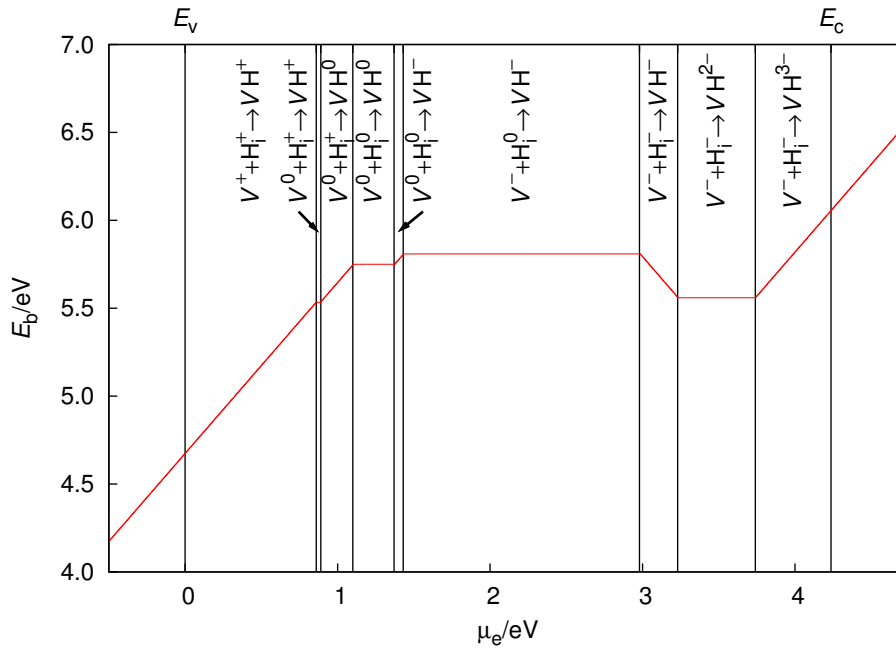


Figure 11.4: The binding energy ( $E_b$ ) as a function of electron chemical potential  $\mu_e$  through the theoretical band gap range (valance band maximum  $E_V$  to conduction band minimum  $E_C$ ) for the reaction between a  $V$  and  $H_i$  to form the  $VH$  centre.

a function of the electron chemical potential is pictured in Figure 11.4.

The binding energies shown in Figure 11.4 range from approximately 4.7–6.0 eV. As the binding energy is always above 4 eV, the calculated value of diffusion of the  $VH$  defect, the  $VH$  defect will diffuse before it dissociates. The  $VH$  defect therefore has the potential to diffuse through diamond and be involved in further aggregation processes before it breaks down.

The mechanism of binding will change as the reactants are mobile at different temperatures, therefore the properties of the vacancy and hydrogen need to be considered.

Irradiation of diamond introduces vacancies into the structure and after irradiation all vacancies are found to be in either their neutral or negative charge state [179]. The migration energy associated with  $V^0$  is 2.3 eV and the  $V^-$  is found to be immobile as they are first converted to neutral centres [179].

For the hydrogen interstitial defect, the bond centred defect is the lowest energy site [180] and the positively charged defect has a migration barrier around 0.1 eV and the neutral charge state a barrier of 1.9 eV [181]. So when the electron chemical potential is below around 3.0 eV above the valence band maximum, the hydrogen will migrate before the vacancy. Above this level the migration of reactants will also primarily be the hydrogen as the negatively charged vacancy is immobile but the barrier to migration of the hydrogen is higher at 2.5 eV [181].

### 11.4 NV

The NV defect is found in low concentrations in as-grown and natural diamonds, it is also readily incorporated in single crystal CVD. In fact when nitrogen is included in the source gases during CVD growth the growth rate increases [39, 182].

Only a small ( $< 0.5\%$ ) amount of nitrogen is typically incorporated as NV during CVD homoepitaxial diamond growth but both the neutral and negatively charged defects have been identified in the same samples. Studies show that the NV centre is grown in preferentially orientated along the [111] and  $\overline{[111]}$  direction rather than individual reactants migrating together to form the centre [183].

However the concentration of the NV centre may be increased as it is formed by the P1 centre trapping a mobile vacancy, via a process of irradiation to form vacancies followed by annealing with temperatures of more than 600 °C to make them migrate [184].

The binding energies associated with the reaction between a vacancy and a substitutional nitrogen to form the NV centre are illustrated in (Figure 11.5).

As previously mentioned the  $V^0$  defect has a migration energy of 2.3 eV and the  $V^-$  is thought to be immobile [179]. The barrier for migration of a substitutional nitrogen defect was previously calculated as 8 eV [185] but it has been suggested that assisted migration, either via a vacancy or an carbon interstitial, or with the addition of a transition metal catalyst, will lower the barrier, sufficiently.

At all possible values the electron chemical potential can take in diamond the NV centre is more thermodynamically stable than a separate vacancy and a  $N_s$  defect

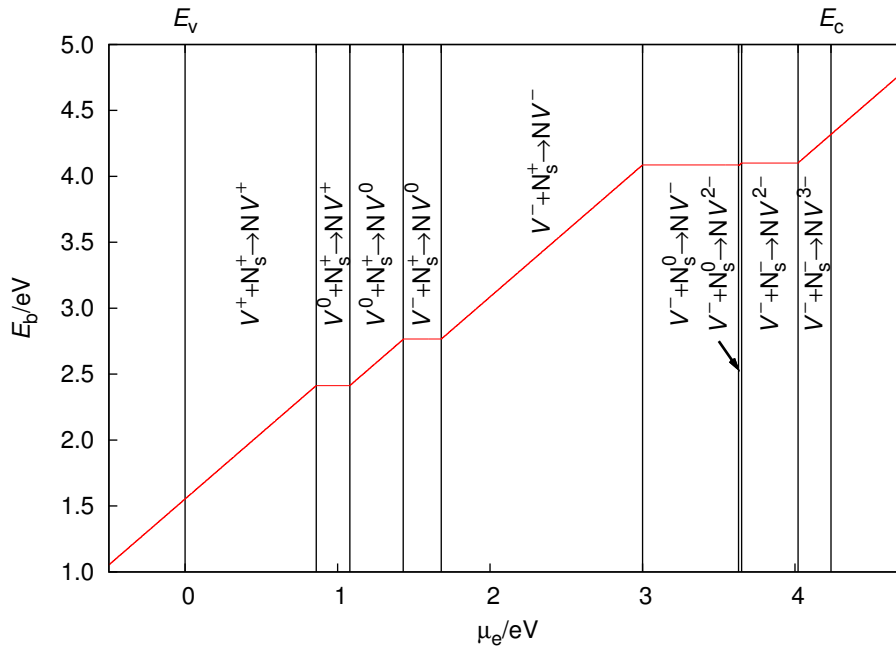


Figure 11.5: The reaction between a  $V$  and  $N_s$  to form the NV centre, further details are listed in Figure 11.4.

(Figure 11.5) with a  $E_b$  ranging from around 1.5–4.3 eV.

As the  $V^0$  is the defect that migrates to the  $N_s$  as opposed to the other available charge states the  $E_b$  for possible reactions involving the  $V^0$  defect ranges from 2.40–2.75 eV. It is suggested that the NV centre will remain immobile up to around 1700 °C, as the barrier for migration is calculated at 4.5 [186]–5 eV [187], unless self-interstitials which may assist diffusion are released from larger aggregates, this will lower the barrier for migration.

The dissociation barrier can be approximated as the binding energy plus the migration energy of the vacancy at 2.3 eV, therefore any reaction that results in a binding energy of more than approximately 2.2 eV will result in a defect that will remain stable before it dissociates.

As it is unlikely that higher charged states beyond  $-1$  are accessible for the NV defect, the  $E_b$  of a  $V^-$  and either a  $N_s^+$  or  $N_s^0$  defect ranges from 2.75–4.00 eV.

11.5  $VH_2$ 

The  $VH_2$  has not been identified in diamond and it was previously calculated that it is 2.7 eV less stable than the  $VH$  defect, justified by the rigidity of the diamond lattice and the Pauli repulsion between the C–H bonds [145].

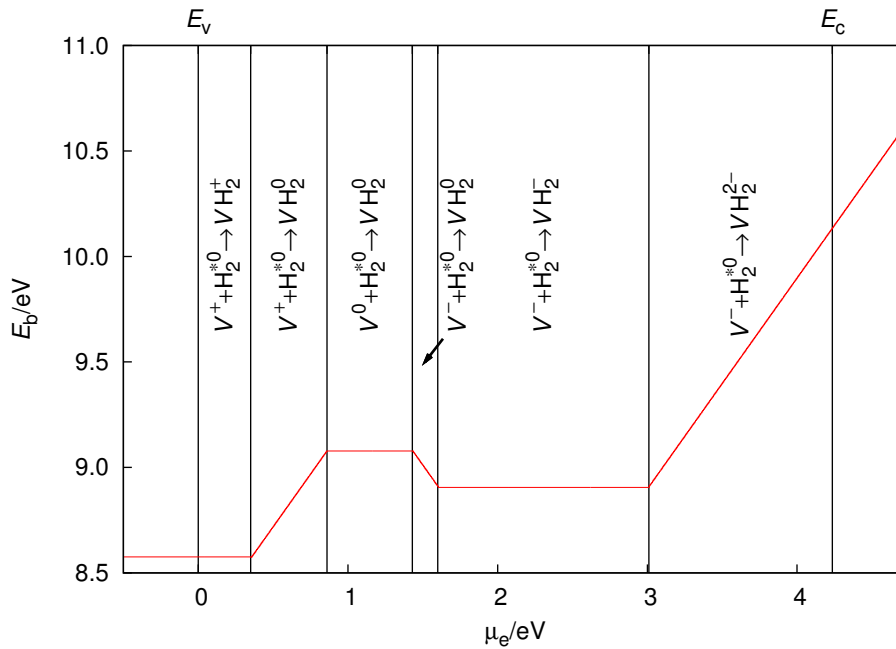


Figure 11.6: The reaction between a  $V$  and  $H_2^*$  defect to form the  $VH_2$  centre, further details are listed in Figure 11.4.

In the results presented here the addition of a hydrogen to a  $VH$  centre does in fact form a more thermodynamically stable defect. Also, a potential vibrational mode assignment previously alluded to in Chapter 8 means that the  $VH_2$  is seen in as-grown material and is persistent to at least 1800 °C [155, 162]. This does not seem entirely unreasonable as the  $NVH$  defect is also seen in as-grown CVD material.

The defect may also be formed via the addition of a vacancy to the  $H_2^*$  defect (Figure 11.6) or alternatively of a hydrogen combining to the  $VH$  defect (Figure 11.7). The  $H_2^*$  defect consists of a bond-centred hydrogen with a proximal anti-bonded hydrogen forming an axially symmetric defect [188]. The defect is fully saturated. It

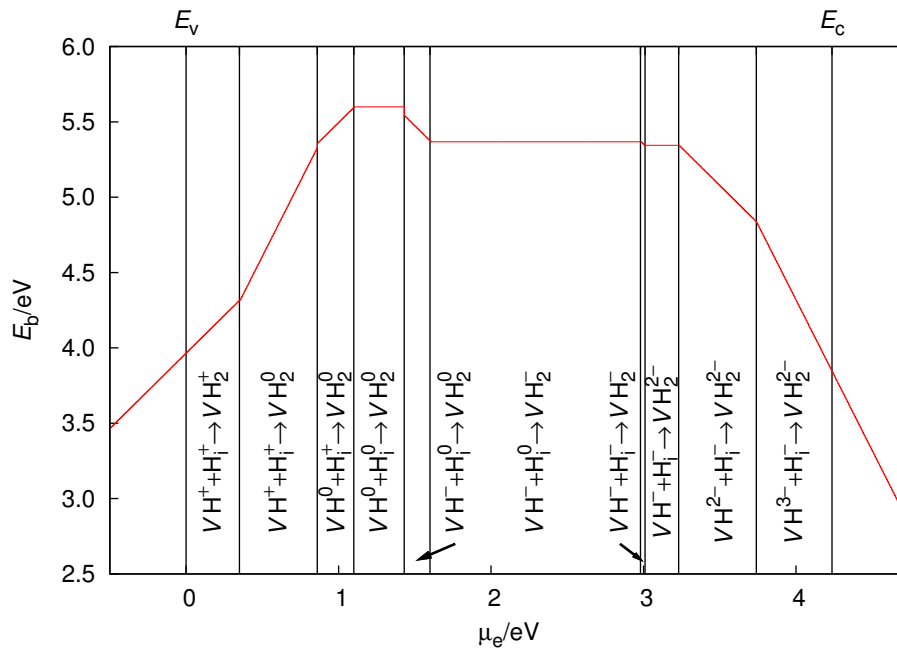


Figure 11.7: The reaction between  $VH$  and  $H_i$  defect to form the  $VH_2$  centre, further details are listed in Figure 11.4.

is considered here because it is a stable form of a hydrogen dimer when compared to a  $H_2$  molecule in diamond. This defect has been previously calculated to be 2.1–3.32 eV higher in energy than the  $H_2^*$  defect [180, 189]. The migration barrier for the  $H_2^*$  defect has been estimated to be 3.5 eV [180, 190], therefore the vacancy would preferentially migrate towards the more stable  $H_2^*$  defect.

In the full range of the band gap the ' $H_2^* + V = VH_2$ ' binding energy is much larger at 8.6–10.1 eV than the ' $H_i + VH = VH_2$ ' at 3.5–5.6 eV, this is due to the formation energy of the  $H_2^*$  defect being much higher than any of the other components of the reactants.

As the addition of hydrogen to a vacancy progressively reduces the mobility of the resulting defect, under the reaction of a  $VH$  and a hydrogen interstitial, it would be the hydrogen that migrates to the  $VH$  defect. The increased stability due to the addition of hydrogen means that the migration of the  $VH_2$  as a whole will be higher than either the vacancy (2.3 eV) or the  $VH$  defect (4 eV). Therefore, it may be possible for the  $VH_2$  to migrate before it dissociates.

## 11.6 NVH

Like the NV defect, the NVH is grown into CVD diamond with a preferential orientation [94], it is also thought that the  $NV^-$  can trap a mobile hydrogen to form the NVH defect [94]. The  $NVH^-$  although seen in CVD it has yet to be detected in natural or HPHT. Suggesting it either is not formed initially in the diamond or once formed it is not stable at the temperatures or pressures subjected in either natural or HPHT growth.

The NVH may be formed via the process of an NV capturing a  $H_i$ , this reaction has a calculated binding energy ranging from 4.4–6.1 eV (Figure 11.8).

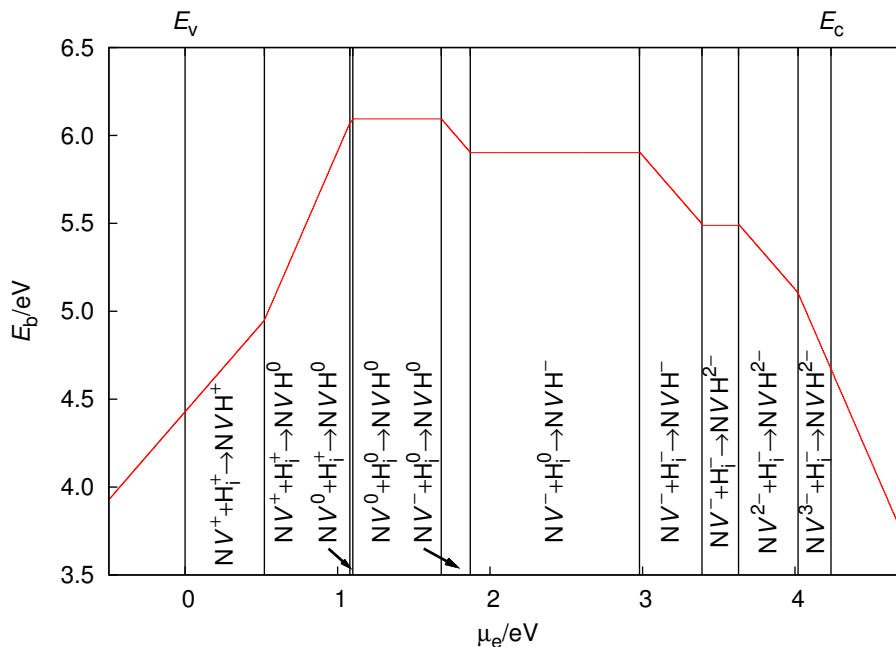


Figure 11.8: The reaction between a NV and  $H_i$  defect to form the NVH centre, further details are listed in Figure 11.4.

An alternative route is the VH defect binding with a substitutional nitrogen. The binding energy associated with this process ranges from 1.3–4.2 eV (Figure 11.9).

As the hydrogen is the most mobile species in the defects discussed in these reactions, it may be speculated that it is more likely for the NV centre to trap a hydrogen interstitial, when compared to a VH defect trapping a substitutional nitrogen.

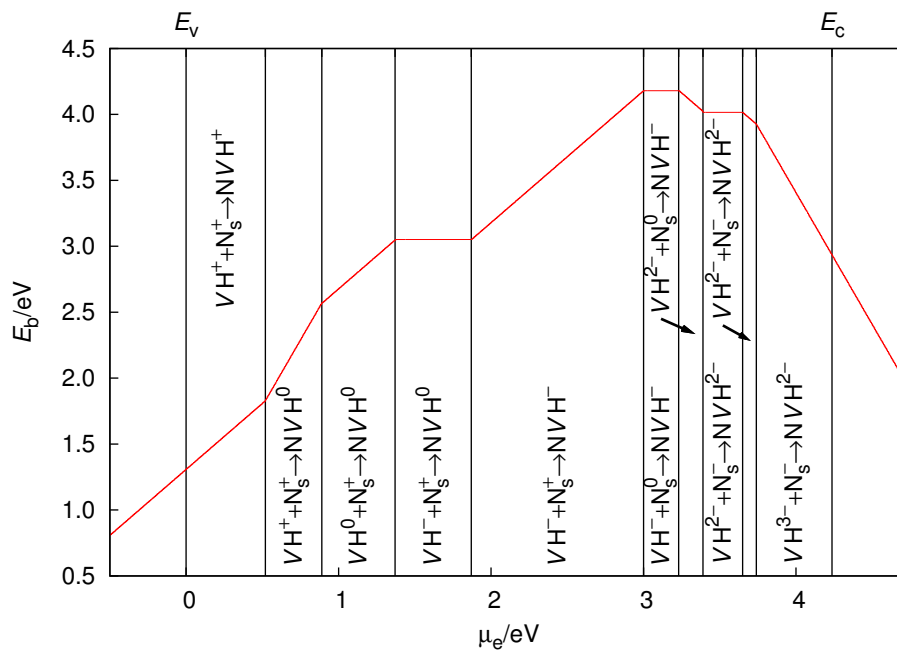


Figure 11.9: The reaction between a VH and  $N_s$  defect to form the NVH centre, further details are listed in Figure 11.4.

### 11.7 $N_2V$

The  $N_2V$  defect is thought to be formed via an A-centre trapping a mobile vacancy in HPHT diamonds. It is present in treated synthetics and is also commonly found in irradiated natural type IaA diamonds.

The defect is less thermodynamically stable than the  $N_3V$  defect but both are found in HPHT diamonds that have been treated above 1900 °C. Although when compared to the concentrations of A- and B- centres the concentrations are comparatively small. Due to this, it was suggested that either the  $N_2V$  or  $N_3V$  defect were not directly involved in the aggregation process to create B-centres or that the stages of aggregation were not long-lived under annealing conditions [12].

An A-centre is two neighbouring substitutional nitrogen defects and is considered to be more stable than two separate substitutional nitrogen defects. It is considered here in the formation of  $N_2V$  as the A-centre can trap a comparatively more mobile vacancy.

The binding energy for this reaction ranges from around 4.0–5.2 eV (Figure 11.10).

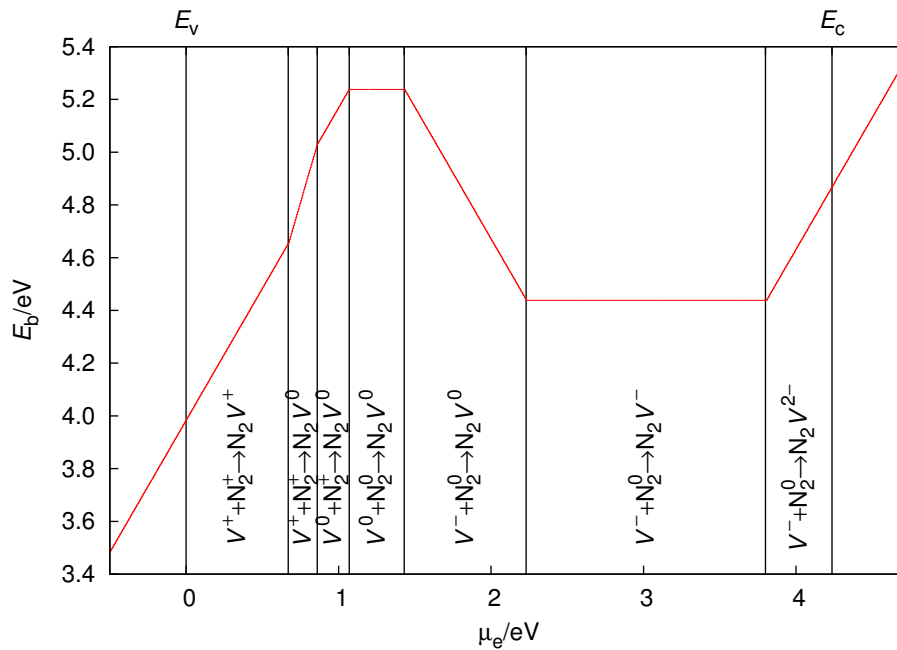


Figure 11.10: The reaction between a  $V$  and  $N_2$  defect to form the  $N_2 V$  centre, further details are listed in Figure 11.4.

An alternative reaction considered is a  $NV$  capturing an substitutional nitrogen. The binding energies corresponding to this reaction range from 1.3–4.0 eV (Figure 11.11).

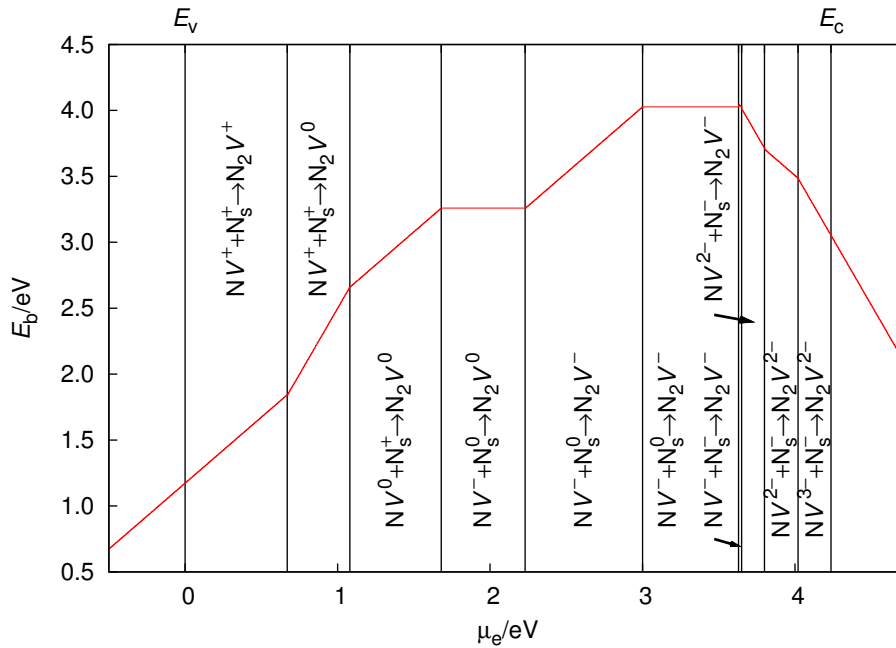


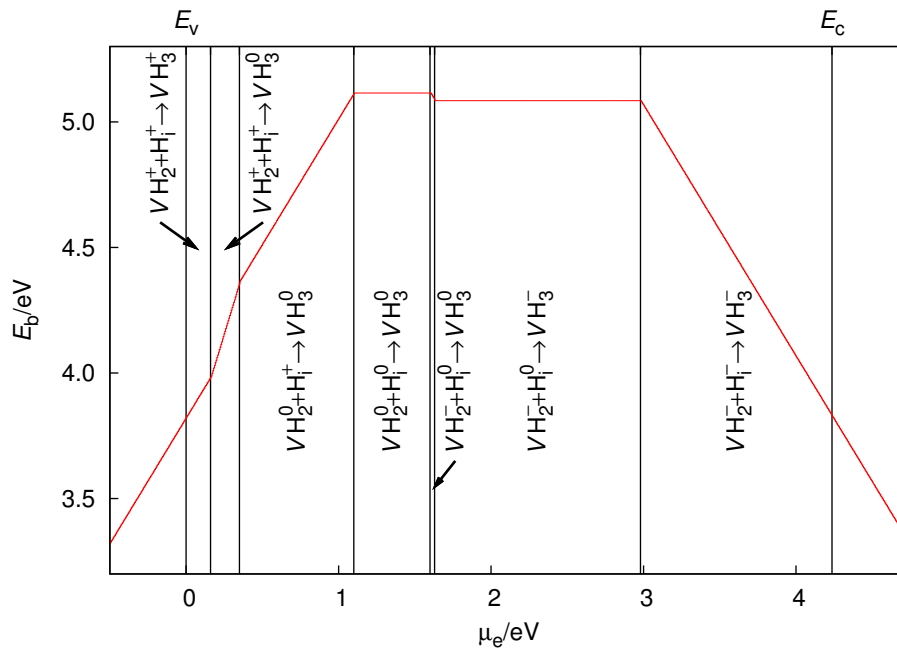
Figure 11.11: The reaction between a NV and  $N_s$  defect to form the  $N_2V$  centre, further details are listed in Figure 11.4.

### 11.8 $VH_3$

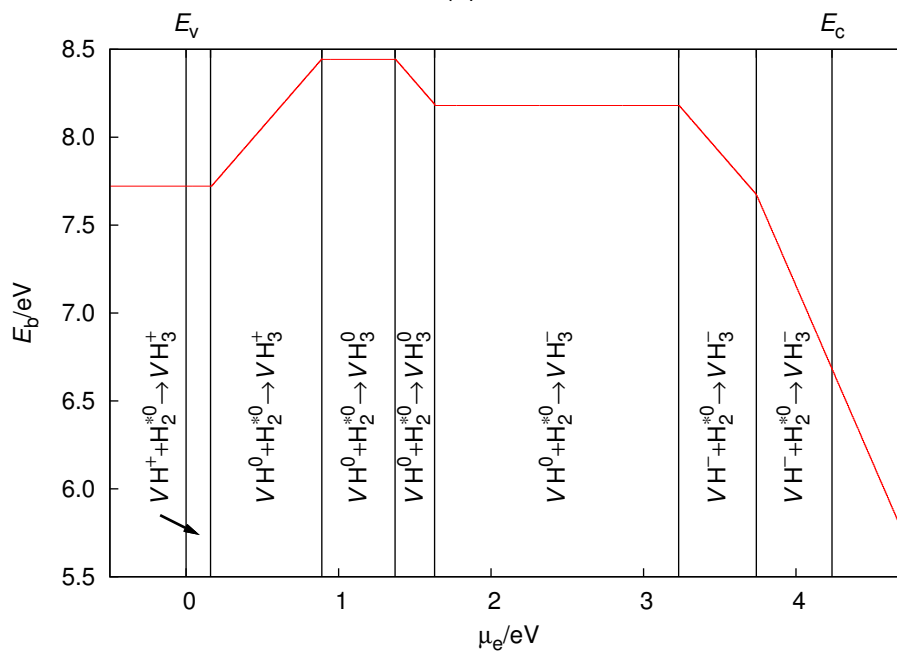
There is no experimental evidence that suggests that the  $VH_3$  defect has been identified in diamond as of yet.

Here two reactions have been considered as possible pathways to formation. The  $VH_2$  plus the hydrogen interstitial (Figure 11.12a) or alternatively the  $VH$  defect plus the  $H_2^*$  defect (Figure 11.12b).

The binding energy ranges from around 3.75 eV to 5.2 eV for the reaction between  $VH_2$  plus  $H_i$  (Figure 11.12a), whereas the associated binding energy when the  $H_2^*$  is involved is always much higher (Figure 11.12b).



(a)



(b)

Figure 11.12: a) The reaction between a  $VH_2$  and  $H_i$  defect and b) the reaction between a  $VH$  and  $H_2^*$  defect, both form the  $VH_3$  centre, further details are listed in Figure 11.4.

If the precursors are available and not used in competing reaction processes, in the case of the reaction between the  $VH_2$  defect and the  $H_i$  the interstitial hydrogen will more likely to be mobile first whereas the  $VH$  defect will become mobile before the more stable  $H_2^*$  defect.

### 11.9 $NVH_2$

The  $NVH_2$  defect is a multiple hydrogen containing defect that has not been identified in diamond as of yet. Possible routes to its formation include the addition of  $NV$  and  $H_2^*$  defect (Figure 11.13) or a reaction between  $VH_2$  and  $N_s$  defects (Figure 11.14). As this defect only has one remaining radical, it is unlikely that a defect this saturated is grown in to CVD diamond.

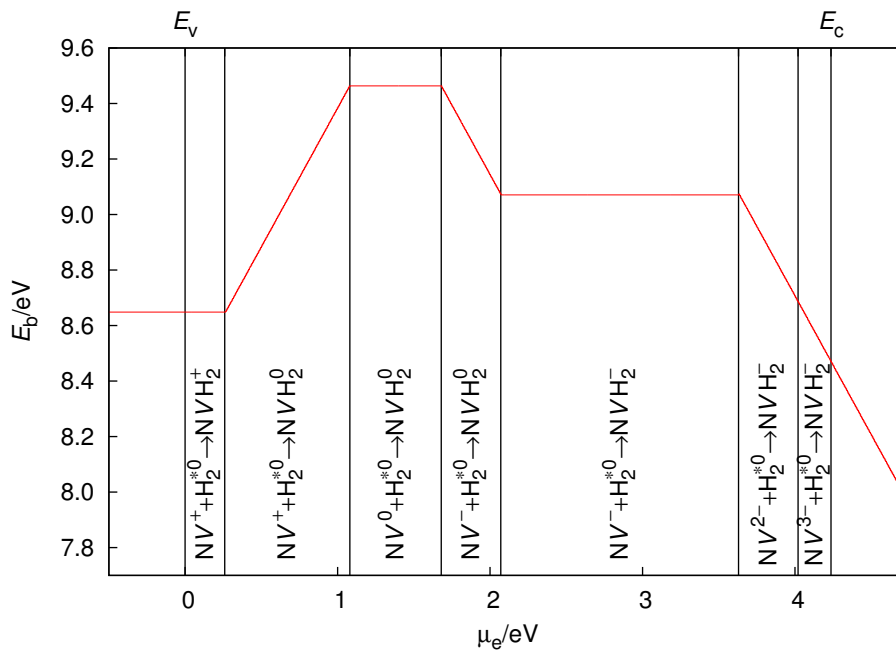


Figure 11.13: The reaction between a  $NV$  and  $H_2^*$  defect to form the  $NVH_2$  centre, further details are listed in Figure 11.4.

The binding energies associated with the reaction between a  $NV$  and  $H_2^*$  defect range from around 8.6 eV to 9.4 eV. This high binding energy is mainly due to the stability of

the  $H_2^*$  defect.

This reaction (Figure 11.13) involves defects that have been previously identified in diamond, whereas the reaction between  $VH_2$  and  $N_s$  defect involves the elusive  $VH_2$  defect. The binding energies associated with this reaction is much lower, ranging from approximately 1.5–4.4 eV.

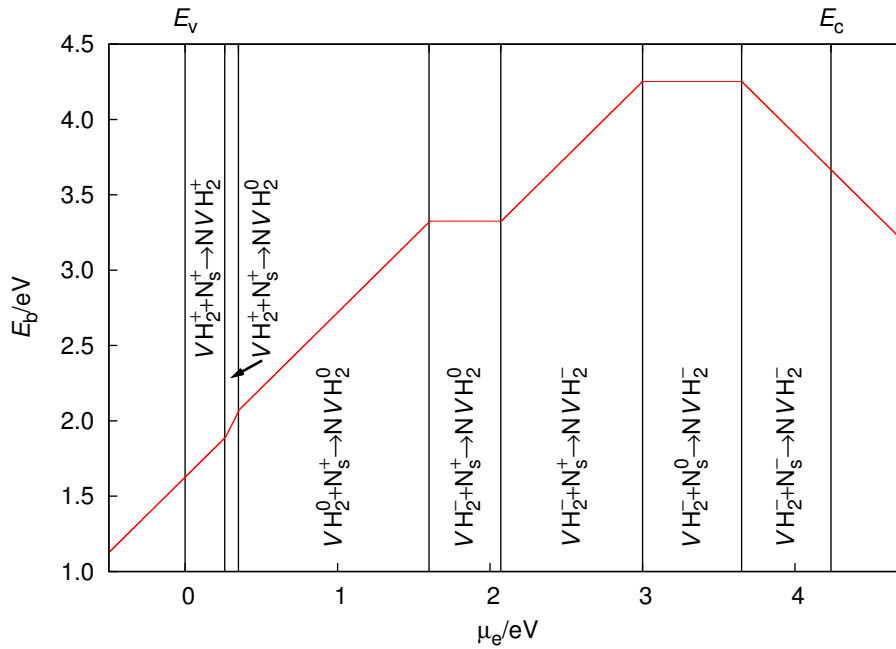


Figure 11.14: The reaction between a  $VH_2$  and  $N_s$  defect to form the  $NVH_2$  centre, further details are listed in Figure 11.4.

### 11.10 $N_2VH$

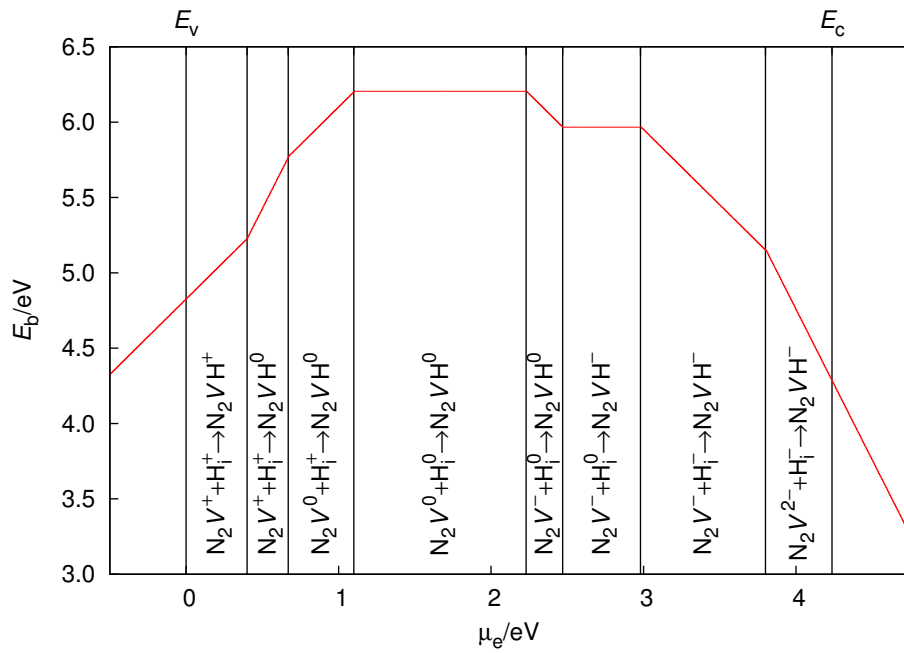
As the  $N_2VH$  defect, which was recently identified via EPR experiments [12] has only one radical it is more thermodynamically stable when compared to the  $NVH$  defect for example, it was deduced however, that the  $NVH$  defect was not directly converted to  $N_2VH$  but that there was an intermediate stage between the conversion.

The  $N_2VH$  defect was produced in multiple CVD samples after annealing at 1800 °C. Three possible routes to formation were considered: ' $N_2V + H_i$ ' (Figure 11.15a),

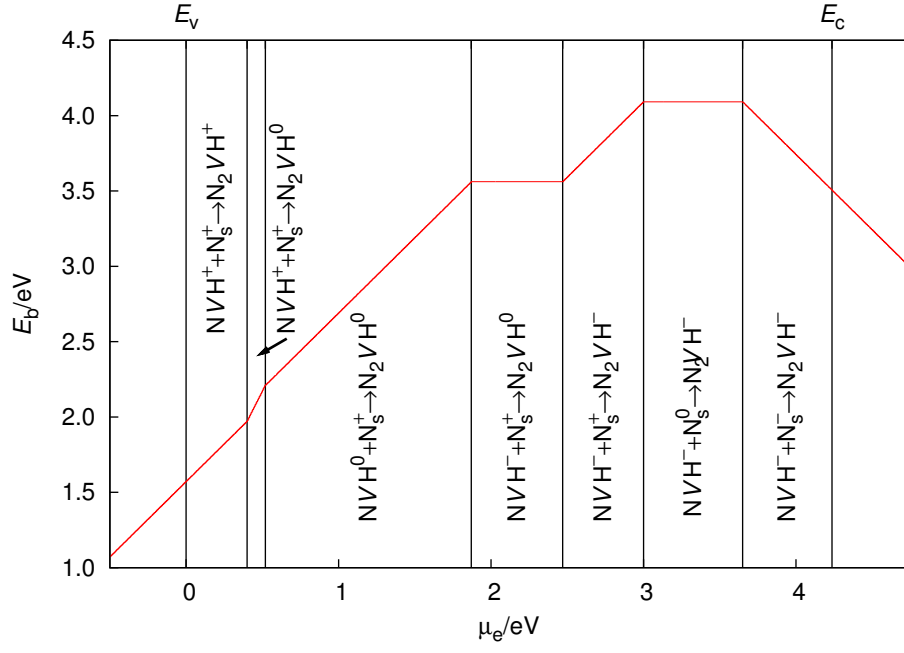
'NVH + N<sub>s</sub>' (Figure 11.15b) and 'VH + N<sub>2</sub>' (Figure 11.16).

In CVD samples A-centres are not formed, so the reaction between the VH and N<sub>2</sub> defect will not be available in the diamond used in the experimental observation. The reaction between the NVH and N<sub>s</sub> was also suggested not to occur directly and that an intermediate state would be involved, perhaps if the migration of the nitrogen is assisted via an interstitial or vacancy the intermediate would be a combination of that and the NVH defect. The binding energy associated with this reaction in Figure 11.15b ranges from 1.5–4.1 eV.

An alternative reaction between the N<sub>2</sub>V and H<sub>i</sub> produces a range of binding energies from 4.1–5.6 eV.



(a)



(b)

Figure 11.15: a) The reaction between a  $N_2V$  and  $H_i$  defect and b) the reaction between a  $NVH$  and  $N_s$  defect, both form the  $N_2VH$  centre, further details are listed in Figure 11.4.

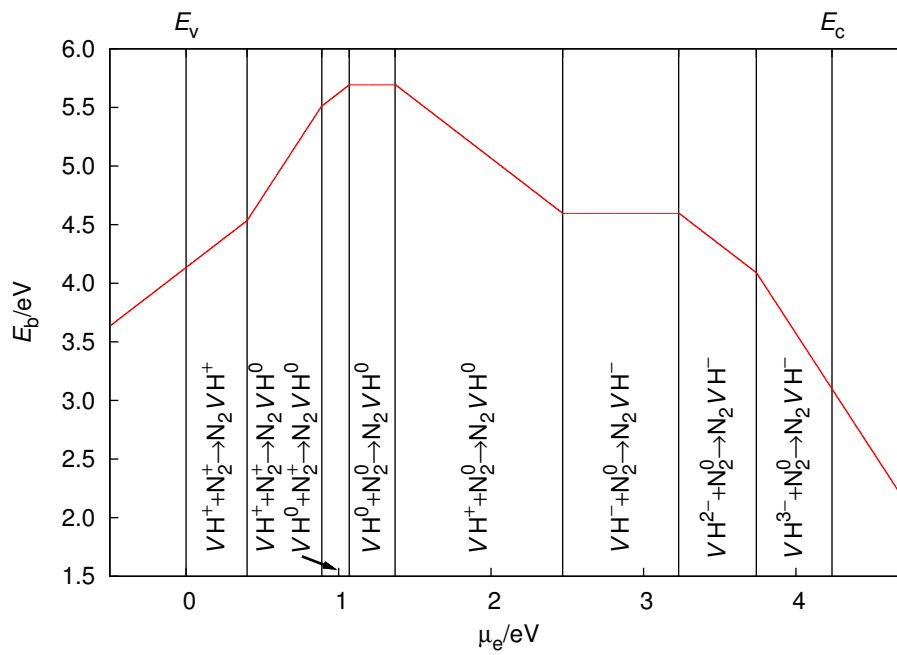


Figure 11.16: The reaction between a VH and  $N_2$  defect to form the  $N_2VH$  centre, further details are listed in Figure 11.4.

11.11  $N_3V$ 

The  $N_3V$  defect is found in diamond in much smaller concentrations than A- and B-centres but at a comparable level to  $N_2V$  defects, although the  $N_3V$  defect is more thermodynamically stable when compared to the  $N_2V$  defect. Due to this it was suggested that the  $N_3V$  defect was not involved directly with the aggregation process to form the B-centres or that the formation of  $N_3V$  is only formed intermittently under annealing conditions [12].

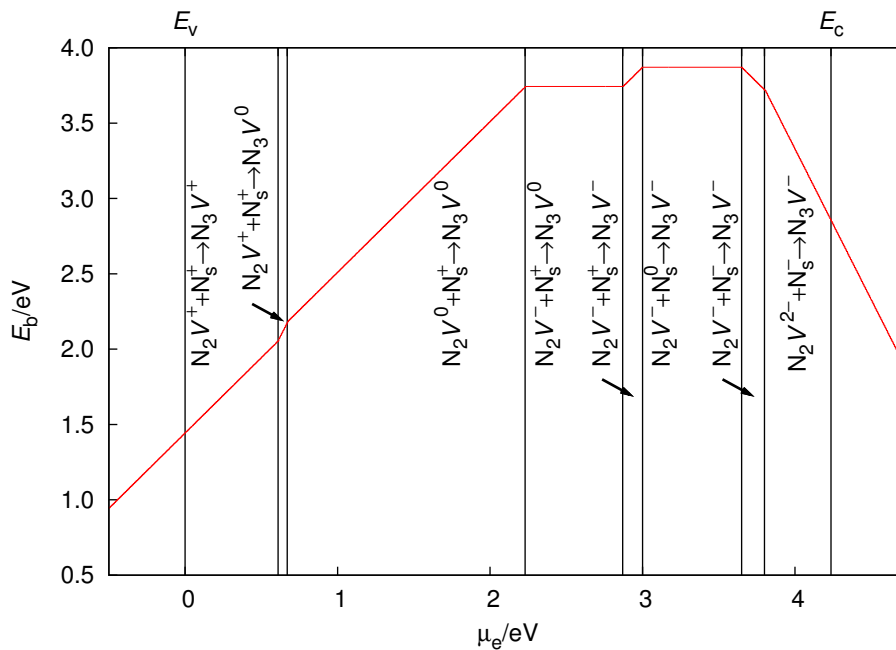


Figure 11.17: The reaction between a  $N_2V$  and  $N_s$  defect to form the  $N_3V$  centre, further details are listed in Figure 11.4.

Potential reactions to form the  $N_3V$  centre include those between the  $N_2V$  and  $N_s$  defect (Figure 11.17) or  $NV$  and  $N_2$  defect (Figure 11.18). As the defect is seen in CVD material the A-centre will not be available to aggregate so therefore the reaction between the  $N_2V$  and  $N_s$  defect will be preferable in this case. The binding energy for this reaction ranges from 1.5 eV to 3.9 eV. The defect is also seen in HPHT diamond after annealing, so in this case  $NV$  may bind with the  $N_2$  defect.

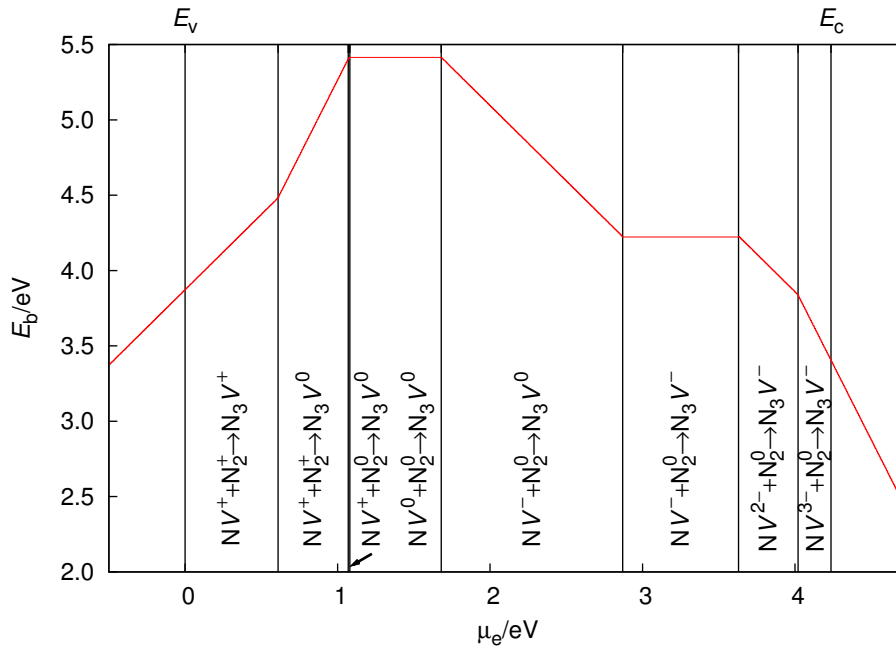
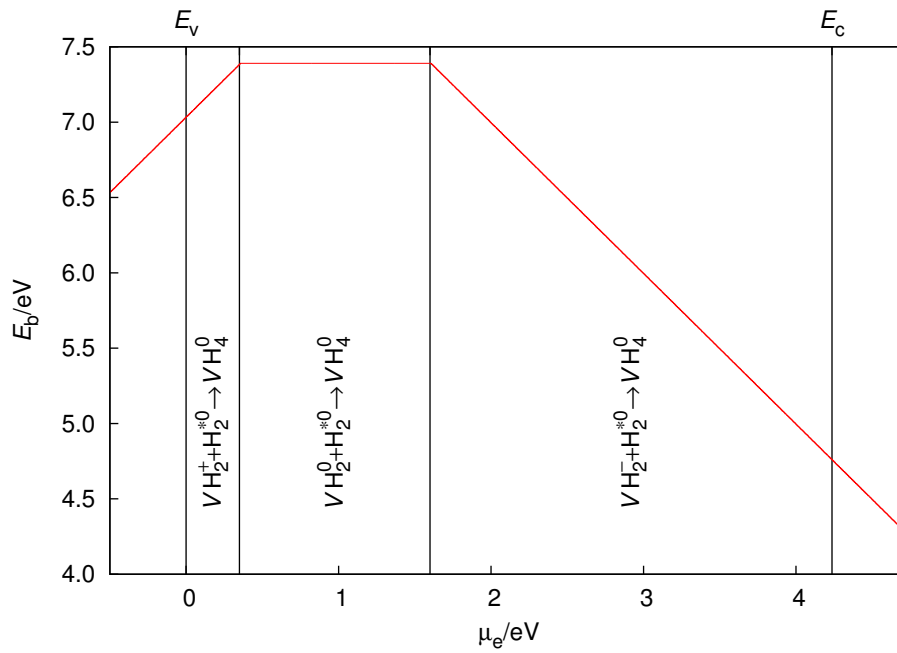


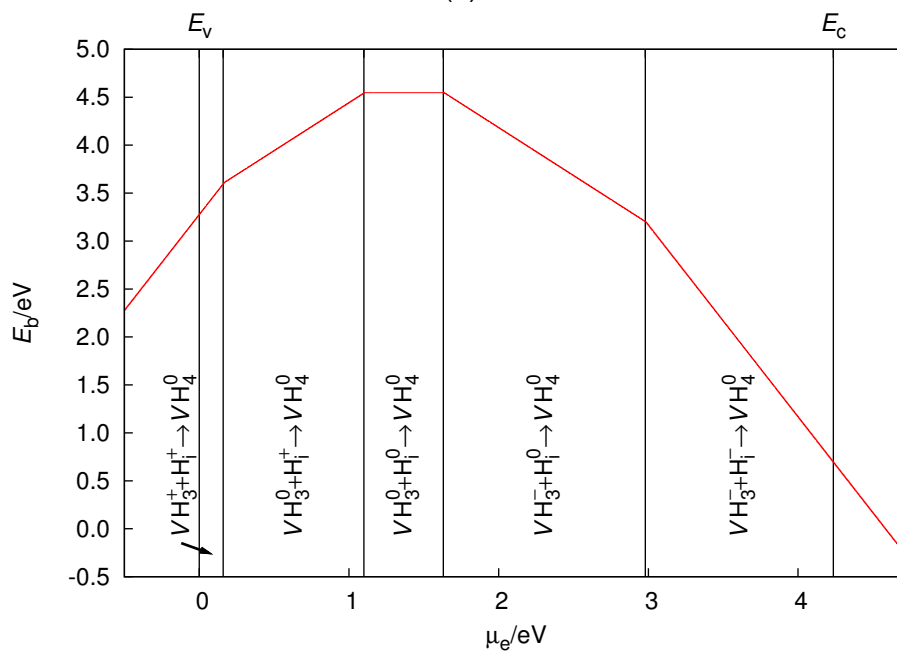
Figure 11.18: The reaction between a NV and N<sub>2</sub> defect to form the N<sub>3</sub> V centre, further details are listed in Figure 11.4.

### 11.12 VH<sub>4</sub>

The 1371 cm<sup>-1</sup> bend mode has been suggested based on symmetry grounds to belong the VH<sub>4</sub> defect [155] and our results are within 9–11 cm<sup>-1</sup> of this suggestion. No stretch mode has been associated with the bend mode as it has been suggested that it would be obscured by a broad band from 2850–3000 cm<sup>-1</sup> but the calculated bend mode is outside this region at by 830 cm<sup>-1</sup> at 3830 cm<sup>-1</sup>. If this assignment is correct, according to reference [162] it is also found to be grown in and persists to 1800 °C. As VH<sub>4</sub> is a fully saturated defect it is not a surprise that this potential confirmation of identification persists at high anneals, it is however surprising that a fully saturated defect is initially grown into CVD diamond as no other fully saturated defects in the set where  $n + m = 4$  are.



(a)



(b)

Figure 11.19: a) The reaction between a  $VH_2$  and  $H_2^*$  defect and b) the reaction between a  $VH_3$  and  $H_i$  defect, both form the  $VH_4$  centre, further details are listed in Figure 11.4.

Potential methods of formation include a reaction between  $VH_2$  and the  $H_2^*$  defect (Figure 11.19a) or between  $VH_3$  and  $H_i$  (Figure 11.19b), both of these however contain defects that have not previously identified in diamond.

The binding energies associated with  $VH_2$  and the  $H_2^*$  defect visualised in Figure 11.19a, range from 4.6–7.4 eV. And the binding energy associated with the reaction ' $VH_3 + H_i$ ' range from 2.4–4.5 eV.

11.13 NVH<sub>3</sub>

The NVH<sub>3</sub> defect has yet to be identified in any type of diamond. Nevertheless, potential reactions that produce NVH<sub>3</sub> have been considered.

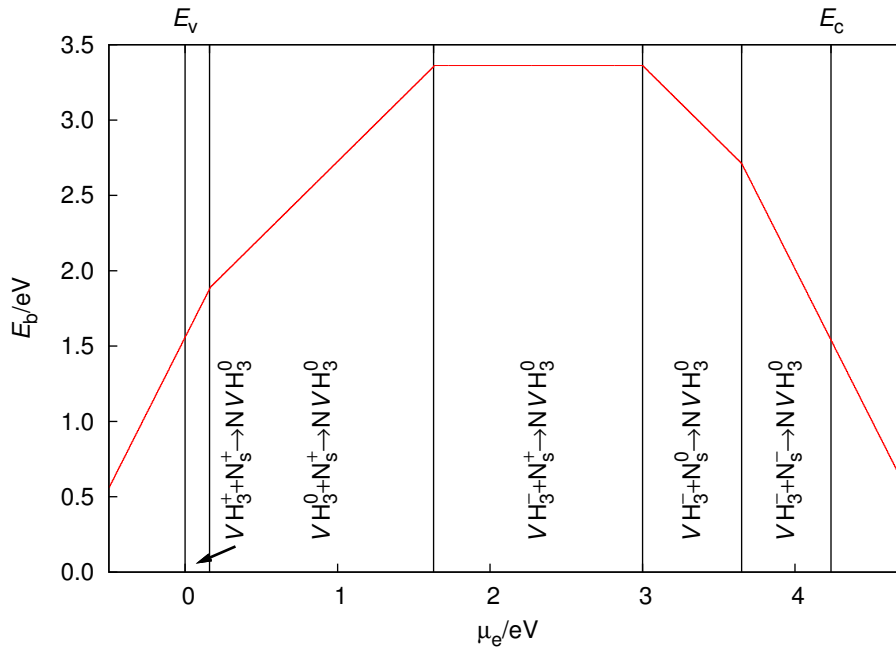
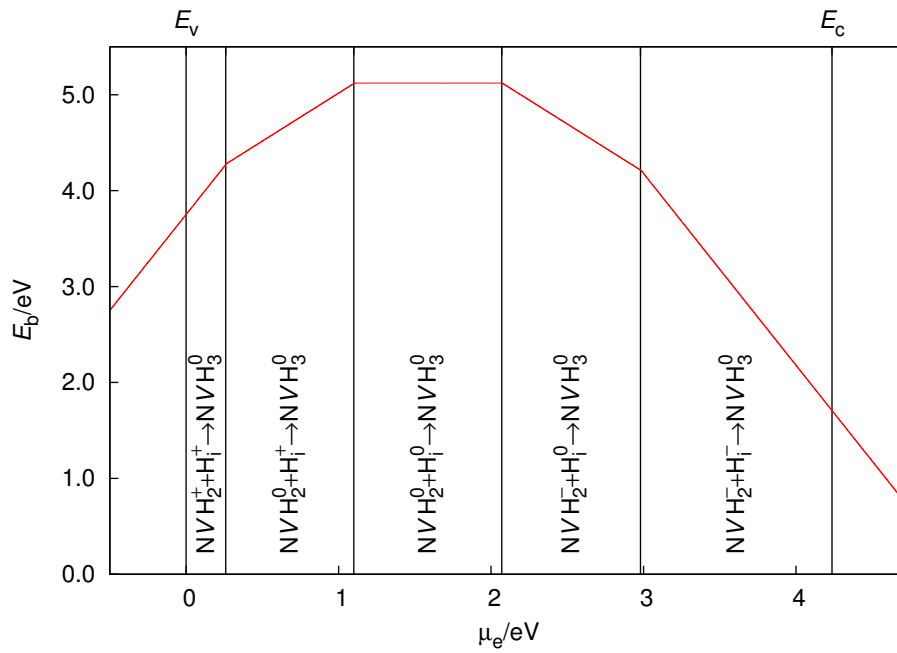
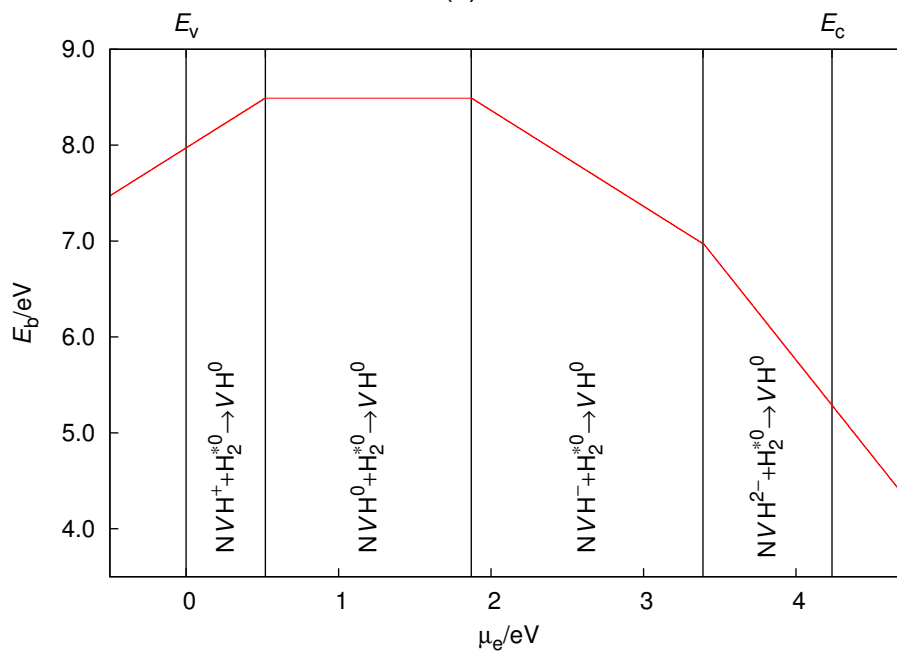


Figure 11.20: The reaction between a  $VH_3$  and  $N_s$  defect to form the  $NVH_3$  centre, further details are listed in Figure 11.4.

The binding energies associated with the reaction between the  $VH_3$  and  $N_s$  defect (Figure 11.20) has a range of binding energies from 1.5–3.4 eV. The binding energies associated with the  $NVH_2$  and  $H_i$  reaction (Figure 11.21a) range from 3.8–5.2 eV. And for the final reaction between  $NVH$  and  $H_2^*$  (Figure 11.21b), the binding energies range from 5.2 eV to 8.5eV.



(a)



(b)

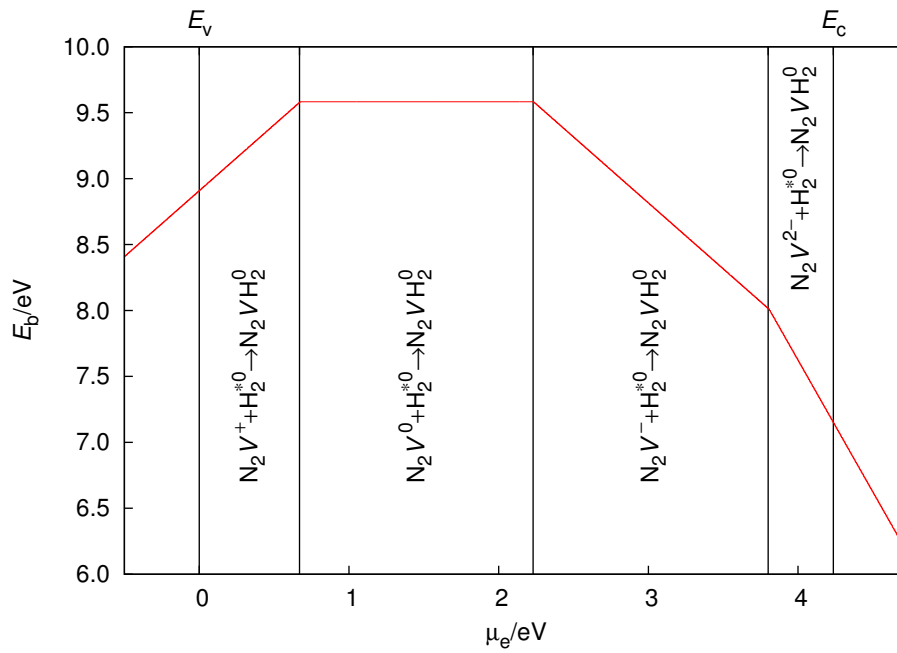
Figure 11.21: a) The reaction between a  $\text{NVH}_2$  and  $\text{H}_i$  defect and b) the reaction between a  $\text{NVH}$  and  $\text{H}_2^*$  defect, both form the  $\text{NVH}_3$  centre, further details are listed in Figure 11.4.

### 11.14 $N_2VH_2$

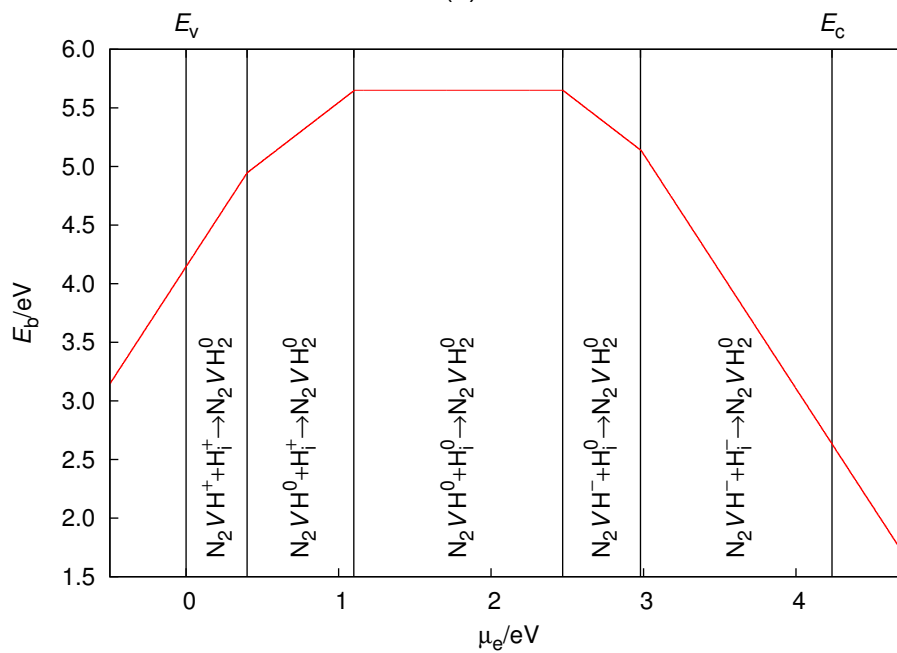
The  $N_2VH_2$  defect has also not been identified in diamond of any form but potential reaction pathways include:  $N_2V$  and  $H_2^*$  defect (Figure 11.22a),  $N_2VH$  and  $H_i$  defect (Figure 11.22b), the  $NVH_2$  and  $N_s$  (Figure 11.23a), and  $VH_2$  and  $N_2$  (Figure 11.23b).

Perhaps now the  $N_2VH$  defect has been identified, if there was a source of hydrogen made available there is potential to form the more thermodynamically stable  $N_3VH$  defect. The binding energy associated with this reaction between  $N_2VH$  and  $H_i$  ranges from 2.5 eV to 5.6 eV (Figure 11.22b).

The reaction between  $N_2V$  and the  $H_2^*$  defect has a corresponding binding energy of 7.2–9.6 eV. The reaction between  $NVH_2$  and  $N_s$  defect has a range of 1.2–3.8 eV. And the reaction between  $VH_2$  and  $N_2$  has a range of 1.6–5.8 eV.

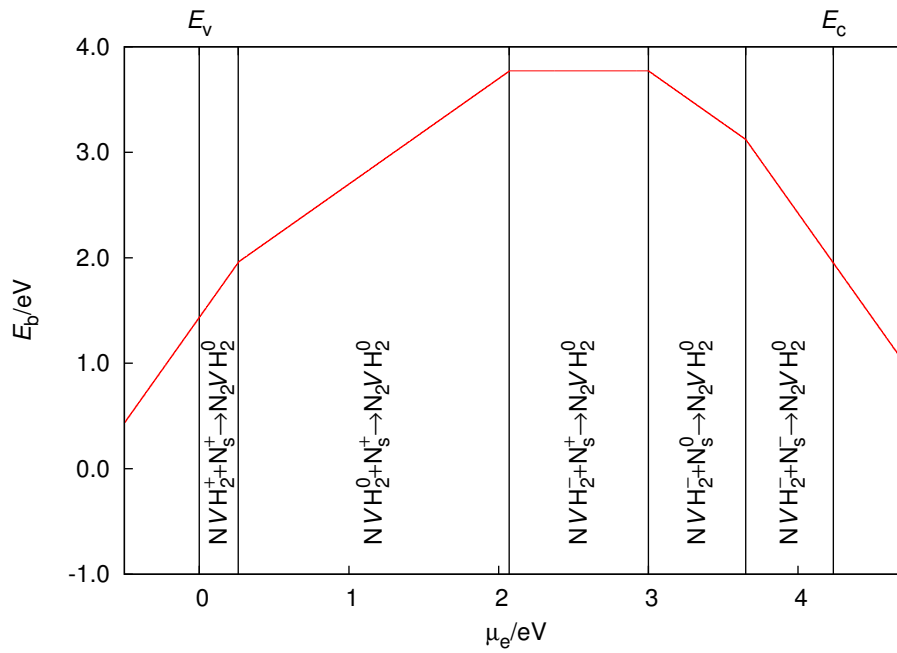


(a)

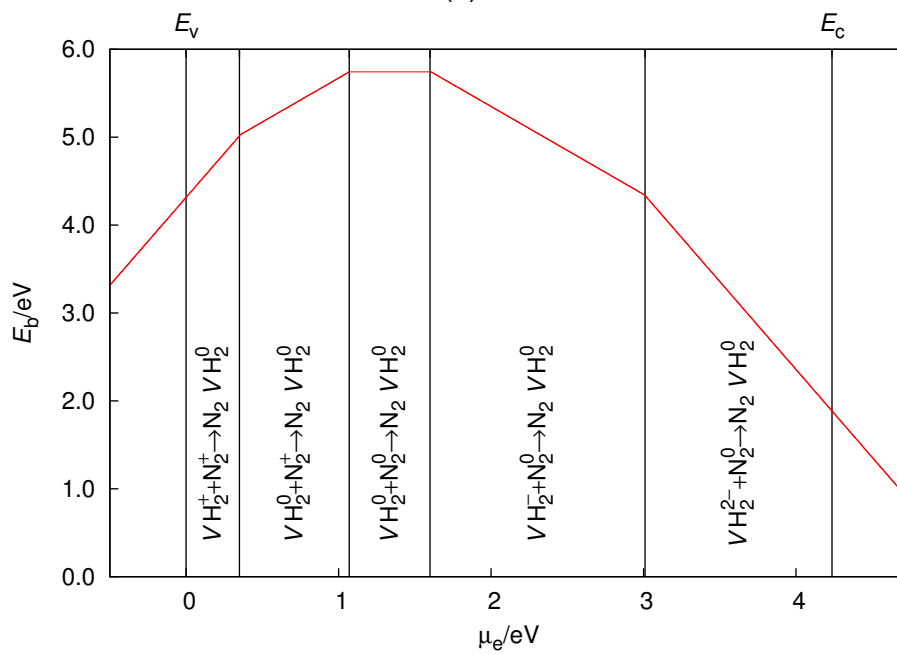


(b)

Figure 11.22: a) The reaction between a  $N_2V$  and  $H_2^*$  defect and b) the reaction between a  $N_2VH$  and  $H_i$  defect, both form the  $N_2VH_2$  centre, further details are listed in Figure 11.4.



(a)



(b)

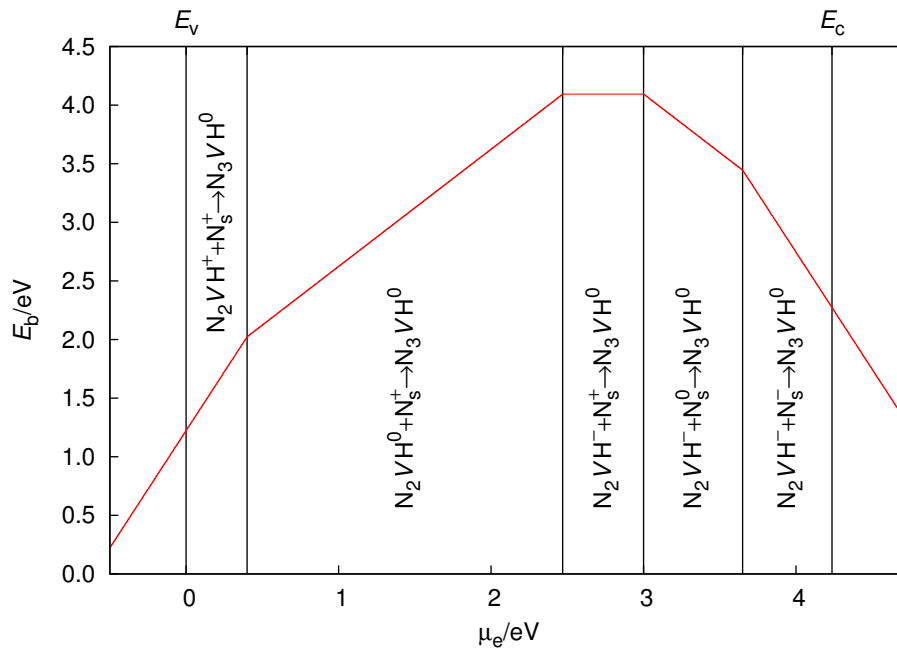
Figure 11.23: a) The reaction between a NVH<sub>2</sub> and N<sub>s</sub> defect and b) the reaction between a VH<sub>2</sub> and N<sub>2</sub> defect, both form the N<sub>2</sub>VH<sub>2</sub> centre, further details are listed in Figure 11.4.

### 11.15 N<sub>3</sub>VH

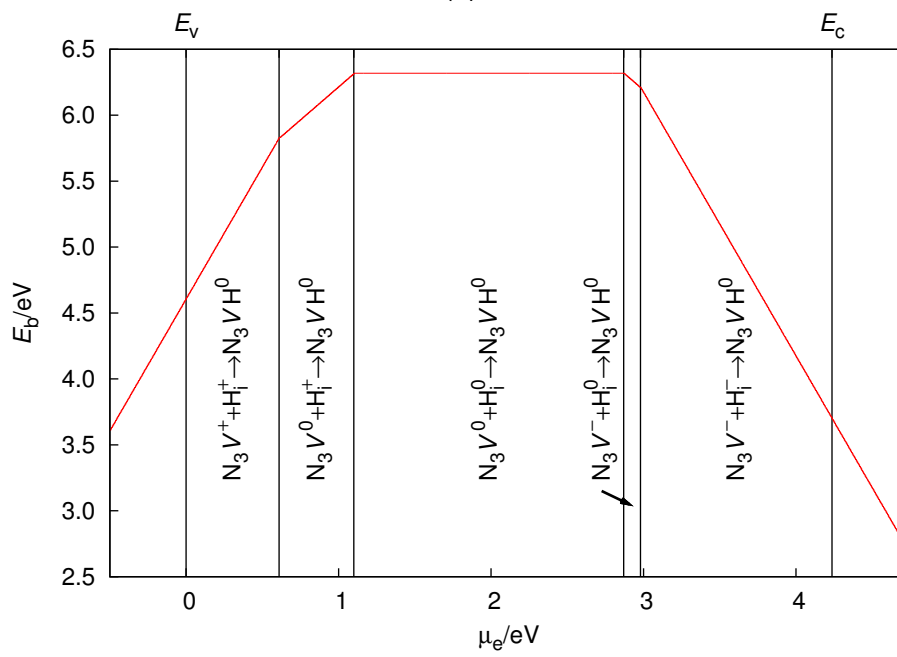
The N<sub>3</sub>VH defect was recently identified as the 3107 cm<sup>-1</sup> optical peak but has been seen in natural diamond samples previously. The defect has also been identified in HPHT and CVD grown diamonds that have then been subsequently annealed. This defect is fully saturated and is seen to persist at high temperature anneals of 2200 °C. It was suggested that the NVH defect is not directly involved in the aggregation to form the N<sub>3</sub>VH defect similar to the formation process associated with the N<sub>2</sub>VH. The reaction considered here that involves NVH also involves the A-centre that is not available in CVD diamond, where multiple hydrogen defects are more likely to be formed.

The reaction processes considered here consist of a reaction between N<sub>2</sub>VH and N<sub>s</sub> (Figure 11.24a), N<sub>3</sub>V and H<sub>i</sub> (Figure 11.21b) or NVH and N<sub>2</sub> defect (Figure 11.20).

The binding energies associated with the N<sub>2</sub>VH and N<sub>s</sub> reaction range from 1.2–4.0 eV. For the reaction between N<sub>3</sub>V and H<sub>i</sub>, the binding energies range from 3.8 eV to 6.3eV. And the final reaction considered here, between NVH and N<sub>2</sub> defect has a range of binding energies from 2.2–5.6 eV.



(a)



(b)

Figure 11.24: a) The reaction between a  $N_2 VH$  and  $N_s$  defect and b) between a  $N_3 V$  and  $H_i$  defect to form the  $N_3 VH$  defect, further details are listed in Figure 11.4.

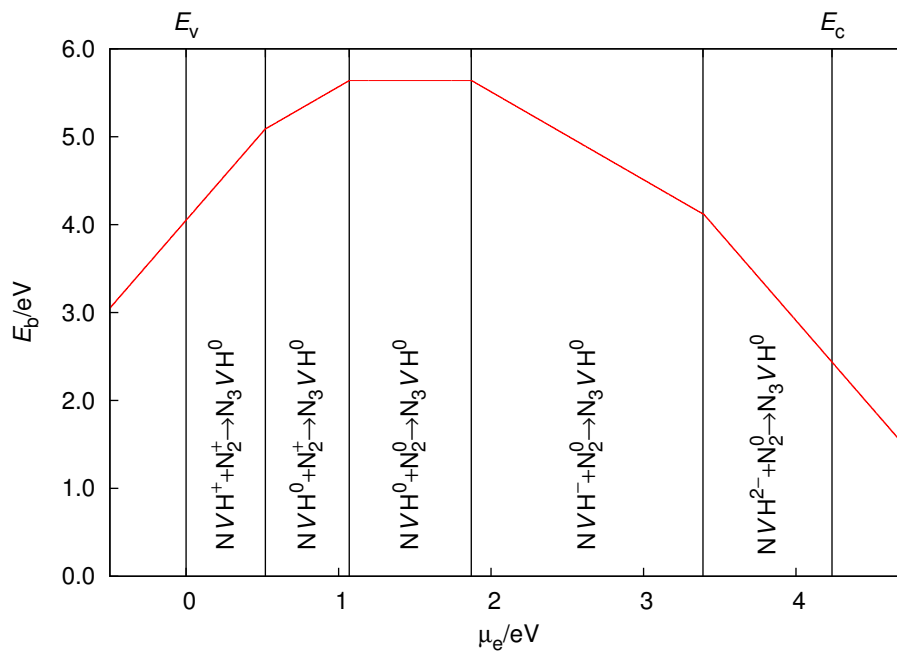


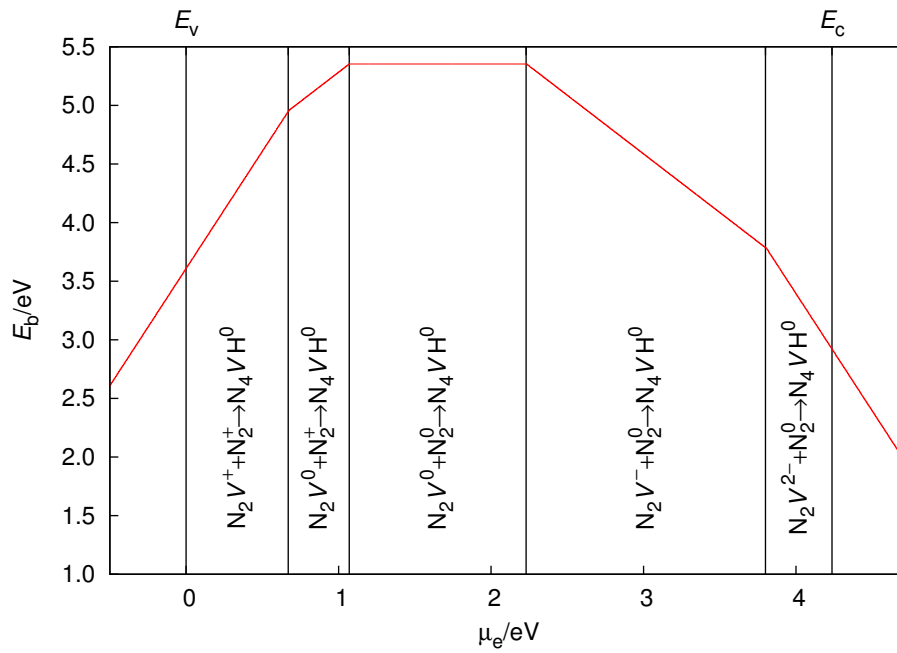
Figure 11.25: The reaction between a NVH and  $N_2$  defect to form the  $N_3VH$  centre, further details are listed in Figure 11.4.

### 11.16 $N_4V$

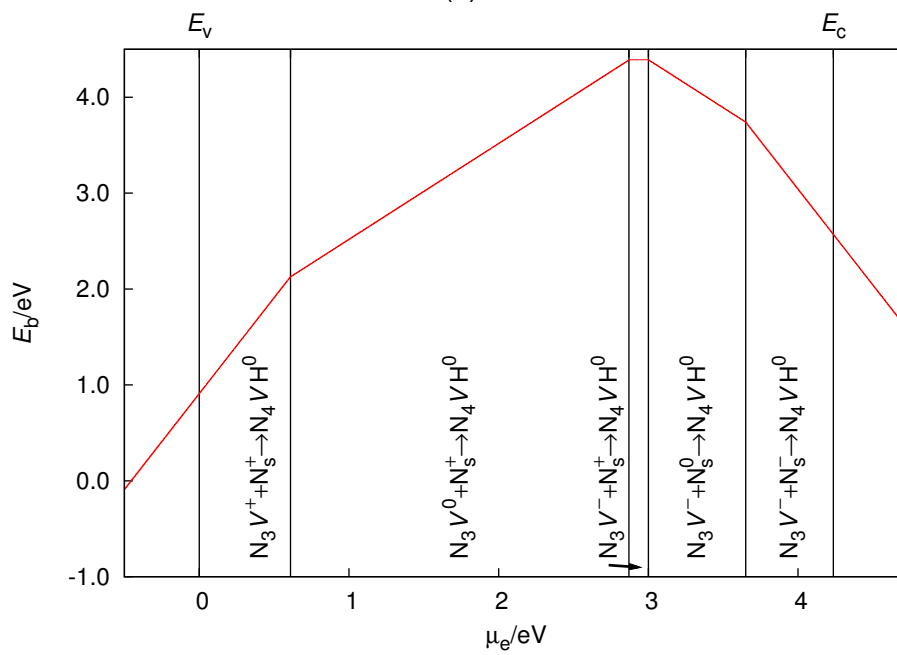
The B-centre has been identified in natural and synthetic diamonds after annealing at 2500 °C. It is considered an end-point of nitrogen aggregation processes as it is a stable, fully saturated defect. In natural diamonds this high temperature is not achieved in growth but over geological timescales the defects aggregate to this thermodynamically stable form.

The details of B-centre formation is unknown but two reactions are considered here. A reaction between the  $N_2V$  and  $N_2$  defect (Figure 11.26a) and a reaction between the  $N_3V$  and  $N_s$  defect (Figure 11.26b). The former, as it involves the A-centre it is not feasible in CVD diamond, the latter involves the  $N_3V$  defect and it has been suggested that this is not involved in B-centre aggregation [12].

The binding energy associated with Figure 11.26a ranges from 2.7–5.4 eV and 0.9 eV to 4.2 eV for the reaction between  $N_3V$  and  $N_s$  in Figure 11.26b.



(a)



(b)

Figure 11.26: a) The reaction between a  $N_2V$  and  $N_2$  defect and b) the reaction between a  $N_3V$  and  $N_s$  defect, both form the  $N_4V$  centre, further details are listed in Figure 11.4.

## **Part III**

### **Summary and conclusions**

## Chapter 12. Summary

*'Don't Believe the Truth'.*

— Studio album by Oasis, 30<sup>th</sup> May 2005.

A reminder to view things critically.

The information presented in this Thesis can be used to aid the identification of point defects in diamond by combining the results with experimental evidence.

The identification of point defects is essential: it can help identify the origin of the diamond and also if treatments have been subsequently applied, this contributes to the value and it is necessary to protect consumer confidence in the gemstone; modelling defects is an important tool that can be used to help identify potential defects that can be exploited in technical applications; it is also important to understand how defects react under different conditions if the diamond is destined for use in an extreme environment.

The results presented are a systematic quantum-chemical study of point defects that incorporate a combination of nitrogen, hydrogen and a single vacancy. All of which are found in varying combinations and concentrations in both natural and synthetic diamond. The results focus on the set  $N_nVH_m$  where  $n + m \leq 4$ , and related defects such as the single substitutional nitrogen.

In regards to the set of defects studied, DFT calculations modelled each plausible charge and spin state of each defect. The structure extracted, donor and acceptor levels analysed where possible and the energetics between defects inspected. The electronic structure, magnetic interactions and infrared vibrational properties were also

calculated. The hyperfine interactions due to the P1 centre have also been investigated further.

## 12.1 Conclusions

Results pertaining to the hyperfine interactions due to the P1 centre confirm the general trend: hyperfine interactions reduce in magnitude as connectivity is reduced rather than direct distance from the centre. The results also revealed that although in the main, assignments from experiment are confirmed some site assignments should be reassigned ( $C_4$  and  $C_5$ ).

With regards to the set investigated, structurally, when a hydrogen is introduced into the set it will preferentially bond to the unstable carbon as it has a radical. When a nitrogen is added in the set it will replace a carbon, due to its stable lone pair it is unfavourable for the hydrogen to bond. Charge and spin does not affect the symmetry of the defects only the bond lengths, particularly the C–H ones where applicable.

The C–H bond length is determined by steric and electronic interactions; when considering each set where  $m + n = 2, 3$  and  $4$  separately, the defects containing nitrogen always have longer bond C–H bond lengths. The C–H bond length generally increases with the addition of charge. There are however exceptions: in the cases where there are spin states of indistinguishable energy, the higher spin of the two has a much larger than expected bond length; a similar change is seen in transition metal octahedral complexes and is attributed to a change in ionic radii of differing spin states. The reduction of C–H bond length is also not as marked with the removal of charge from the defect.

The surrounding immediate bond lengths compress due to the presence of nitrogen compared to carbon radical or a C–H bond which has little effect on the C–C bonds surrounding the centre. There is a preference to alter the C–H bond length as opposed to the rigid structure surrounding the defect, the nitrogen's lone pair does not deform like the C–H bond and instead the structure compensates for the inclusion of nitrogen by relaxing backwards.

Indistinguishable spin states from a theoretical perspective are seen in the  $VH^0$  defect, with  $S = 3/2$  and  $S = 1/2$  spin states. They have a marked difference in optical properties: whereby no internal electronic transitions are feasible in the  $S = 3/2$  spin state but they are possible in the  $S = 1/2$  spin state, there is also a corresponding marked difference in the vibration of the C–H stretch mode, inline with the change in bond length seen between the two defects but unusual due to charge remaining constant.

Indistinct spin states,  $S = 1$  and  $S = 0$  associated with  $VH_2^0$  and  $NVH^0$  defect also have a difference of tenths of angstroms in bond length. In this case the  $S = 0$  defects would have no hyperfine interactions whereas the  $S = 1$  would.

Table 12.1: A summary of the donor and acceptor levels associated with defects studied in the set.

	(+/0)	(0/-)	(-/-2)	(-2/-3)
VH	0.89	1.37	3.23	3.74
NV	1.08	1.68	3.63	4.02
$VH_2$	0.35	1.60	3.01	
NVH	0.52	1.87	3.39	
$N_2V$	0.67	2.23	3.80	
$VH_3$	0.16	1.63		
$NVH_2$	0.26	2.07		
$N_2VH$	0.40	2.47		
$N_3V$	0.61	2.87		

When considering each set individually, defects containing hydrogen have lower donor/acceptor levels than those containing nitrogen. This is a consequence of the nitrogen's lone pair, it is inherently diffuse when compared to a C–H bond and the Coulombic repulsion introduced as electrons are added is more unfavourable. Therefore hydrogen containing defects will preferentially trap electrons. However when all defects are viewed collectively in Table 12.1 there is no longer a distinct order of electrical levels.

Electronic transitions between defect states tend to be sharp as opposed to transitions

Table 12.2: Allowed electronic transitions between highest occupied and lowest unoccupied states. Transitions between states that lie close to the valance band top have not been included. The magnitudes are included in eV and nm for ease of comparison with experimental results. The many body defect states are included.

Defect	Charge	Spin	Many-body transition sym.	Transition magnitude (eV)	Transition magnitude (nm)	Experimental transition magnitude(nm)
VH	0	1/2	${}^2E-^*$	1.41/0.98	879/1265	
	-1	1	${}^3A_2-{}^3E$	1.63	761	
NV	+1	0	${}^1A_1-{}^1E$	0.81	1531	
	0	1/2	${}^2E-{}^2A$	1.48/0.93	838/1333	575 [191]
	-1	1	${}^3A_2-{}^3E$	1.91	649	637 [191]
VH <sub>2</sub>	+1	1/2	${}^2A_1-{}^2B_1$	0.23	5391	
	0	0	${}^1A_1-{}^1B_1$	0.86	1442	
	-1	1/2	${}^2B_1-{}^2A_1$	0.97	1278	
NVH	+1	1/2	${}^2A'-{}^2A'/$ ${}^2A'-{}^2A''$	0.36	3444	
	0	0	${}^1A'-{}^1A''$	0.96	1292	
	0	1	${}^3A'-{}^3A'$	1.76	704	
	-1	1/2	${}^2A'-{}^2A''$	1.16	1069	
N <sub>2</sub> V	+1	1/2	${}^1A_1-{}^2B_1$	0.49	2530	
	0	0	${}^1A_1-{}^1B_1$	1.06	1170	503 [191]
	0	1	${}^3B_2-{}^3A_1$	1.94	639	
N <sub>3</sub> V	-1	1/2	${}^2B_1-{}^2A_1$	1.33	932	982 [192]
	0	1/2	${}^2E-{}^2A_1$	2.47	502	415 [191]

\* ${}^2E$  ground state, but several possible excited states.

between the bulk and the defect, due to the variable energies of the valance band and conduction band. Defect-defect transitions are summarised in Table 12.2, transitions between defect-defect states that involve states that lie close to the valance band top have been omitted due to the dispersion in the states. Assuming that the excited state is described adequately enough using the band structure, the difference in energy of

the states can describe the electronic transitions.

Only  $N_3V$  is included from the set where  $n + m = 3$ , as the  $VH_3$  defect has no allowed electronic transitions between the highest occupied and lowest unoccupied states, and the  $N_2VH$  and  $NVH_2$  only have allowed transitions with defect states that lie atop of the valance band therefore one can not definitively assert their position in the band gap.

In general, when comparing like to like transitions and charge states, the magnitude and position in the band gap increases as hydrogen is removed from the defect. Also when comparing like to like transitions, as charge increases, the magnitude of the transitions and position of the defect states also increase.

The vibrational modes associated with the C–H stretch mode increases as bond length decreases (and therefore the more hydrogen involved in the defect in each set the higher the stretch mode). There is however no clear trend with the bend modes as sterical hindrance/repulsion from surrounding components has a greater influence.

Some potential assignments of vibrational modes have been mentioned in the previous Chapters but further corroboration would be necessary to be confident. However, one assignment stands out: the  $NVH^+$  defect, it has a calculated stretch and bend mode which are within 1% and 5% respectively of experiment [163]. If this is the case, it gives extra rigour to the potential  $NV^+$  identification in similarly grown material.

There is often a large shift in vibrational modes when charge or spin is changed, in the case of the  $N_2VH$  for example when the defect changes charge from neutral to negative there is a predicted shift of  $350\text{cm}^{-1}$  in C–H stretch mode.

Tunnelling rates are undetermined so static and dynamic hyperfine tensors have been included for comparison.

In general, larger spin densities of defects of the same charge have larger hyperfine principal values.

Nitrogen has larger hyperfine interactions compared to hydrogen, the carbons in nitrogen containing defects also have larger principal values when compared to those containing hydrogen.

Carbon bonded to the hydrogen has a small hyperfine interaction when compared to

unsaturated carbon radicals. As the carbon radical is where the majority of unpaired electrons is located the largest hyperfine interactions are seen here. When a motional average is calculated the hyperfine values are reduced.

The experimental hyperfine principal values for the  $VH^-$ ,  $S = 1/2$  defect are close to the calculated values for the static value but are even closer to the motional averaged value for the  $V_2H^-$ ,  $S = 1/2$  defect.

If there are carbon radical(s) available and a hydrogen available in the set tunnelling of the hydrogen between equivalent sites is possible. When more than one hydrogen is involved the problem becomes more difficult as the hydrogens can interact with each other.

The rate of tunnelling is determined by the energy profile and there is little correlation between the defect's contents and the corresponding barrier width and height. The rate will also determine the symmetry seen in experiment. As tunnelling effects are seen in silicon and within other defects in diamond, it is speculated that the  $VH^-$  will tunnel at a rate comparable to the  $NVH^-$ . This is because the  $NVH^-$  centre which is known to tunnel has an averaged symmetry is seen in EPR, and the barrier width is the same to one decimal place. However, previous rate calculations suggests that the  $VH^-$  tunnels at a rate of 50 ps, which is the upper limit of EPR experiment's time resolution.

Thermal stability of defects was found to increase as radicals are removed from the set, either by saturation of dangling bond with a hydrogen or by replacing it with an nitrogen that as an extra electron compared to carbon.

The binding energies associated with the formation of the defects discussed in the full set were presented and where migration data was available potential reaction processes were proposed.

### 12.2 Further work

To definitely assign  $C_6$  and  $C_7$  sites in regards to the P1 centre which is discussed in Chapter 6, further experimental results are necessary to differentiate between the two. Although this will not alter the general observation of the hyperfine interaction closely

related to the connectivity of the sites as opposed to purely distance from the centre, it will add completeness to the results presented.

Furthermore, in regards to the set of defects investigated in Chapters 7 through to 10, in order to get a more detailed picture of the properties presented further calculations may be pursued.

Experiment may also focus on areas where differing spin states are sufficiently close in energy so that changes in spin may be induced by changes in temperature for example and therefore changes in associated properties can be tracked. Changes in charge may also be forced experimentally and associated properties monitored.

To clarify potential vibrational modes associated with the defects, further calculations can be done to reveal the oscillator strengths and the lifetimes of the modes. Stress and strain responses and isotopic changes may also be calculated. Further correlation between experiments can also aid the identification of the defect responsible. For example different isotopes can be grown in, stresses or strains can be manually applied and the temperature at which the experiments are carried out can be lowered.

Although potential electronic transitions may be seen by analysing the band structure, when the electron is excited the positions of the states can change. Excited states are difficult to model using the current method therefore an alternative is necessary.

The energetics of the defects discussed in Chapters 11 can be split into two parts: processes within the defect (like tunnelling) and processes that involve the mobility or dissociation of the whole defect. In both cases further calculations are possible. First, approximations to tunnelling rates for defects where the hydrogen has the potential to tunnel between equivalent carbon radical sites may be pursued. This will give vital information in the perceived symmetry of defects when viewed experimentally. Secondly, mobilities associated with the migration of defects through the diamond crystal lattice may be calculated. This information will provide an added level of detail and may be used to determine the likelihood of reaction processes.

Samples grown with a high hydrogen content and with no added nitrogen may result in illusive multiple hydrogen containing defects, diamonds with boron incorporated within

may form defects in the positive charge state and may create the more mobile  $H^+$  that could aggregate further in multiple hydrogen containing defects.

## Bibliography

- [1] GIA, "Diamond history and lore," November 2017.
- [2] Google, "Google's definition of diamond," November 2017.
- [3] S. Tolansky, *The history and use of diamond*. Methuen, 1962.
- [4] R. W. Hesse, *Jewelrymaking through history: an encyclopedia*. Greenwood Publishing Group, 2007.
- [5] D. Beers, "A diamond is forever," November 2017.
- [6] T. Economist, "The cartel isn't for ever," July 2004. <http://www.economist.com/node/2921462>.
- [7] T. Economist, "Changing facets," February 2007, note=<http://www.economist.com/node/8743058>.
- [8] GIA, "A tradition of science and education," November 2017.
- [9] GIA, "Fancy color diamond history and lore," November 2017.
- [10] J. E. Field, *The properties of natural and synthetic diamond*. Academic Press, 1992.
- [11] C. Kittel, *Introduction to Solid State Physics*. Chichester: John Wiley & Sons, Inc, 8th ed., 2005.
- [12] C. B. Hartland, *A study of point defects in CVD diamond using electron paramagnetic resonance and optical spectroscopy*. PhD thesis, Warwick University, 2004.
- [13] F. P. Bundy, "The p, t phase and reaction diagram for elemental carbon, 1979," *Journal of Geophysical Research: Solid Earth*, vol. 85, no. B12, pp. 6930–6936, 1980.

- [14] J. Y. Tsao, *The world of compound semiconductors*. Sandia National Laboratories, 2004.
- [15] B. Ozpineci and L. M. Tolbert, *Comparison of wide-bandgap semiconductors for power electronics applications*. OAK RIDGE NATIONAL LABORATORY for the U.S. DEPARTMENT OF ENERGY, 2003.
- [16] L. Hounsome, R. Jones, P. Martineau, D. Fisher, M. Shaw, P. Briddon, and S. Öberg, "Role of extended defects in brown colouration of diamond," *physica status solidi (c)*, vol. 4, no. 8, pp. 2950–2957, 2007.
- [17] R. Robertson, J. Fox, and A. Martin, "Two types of diamond," *Philosophical Transactions of the Royal Society of London. Series A, Containing Papers of a Mathematical or Physical Character*, vol. 232, pp. 463–535, 1934.
- [18] A. T. Collins, "Intrinsic and extrinsic absorption and luminescence in diamond," *Physica B: Condensed Matter*, vol. 185, no. 1-4, pp. 284–296, 1993.
- [19] G. Davies, "The a nitrogen aggregate in diamond-its symmetry and possible structure," *Journal of Physics C: Solid State Physics*, vol. 9, no. 19, p. L537, 1976.
- [20] G. S. Woods, "Platelets and the infrared absorption of type Ia diamonds," *Proc. R. Soc. London, Ser. A*, vol. 407, pp. 219–238, 1986.
- [21] C. M. Welbourn, M. Cooper, and P. M. Spear, "De beers natural versus synthetic diamond verification instruments," *Gems and Gemology*, vol. 32, p. 151, 1996.
- [22] G. S. Woods, "The 'type' terminology for diamond," in *Properties and Growth of Diamond* (G. Davies, ed.), no. 9 in EMIS Datareviews Series, ch. 3.1, pp. 83–84, London: INSPEC, Institute of Electrical Engineers, 1994.
- [23] E. C. Lightowers and A. T. Collins, "Determination of boron in natural semiconducting diamond by prompt particle nuclear microanalysis and schottky barrier differential-capacitance measurements," *Journal of Physics D: Applied Physics*, vol. 9, no. 6, p. 951, 1976.
- [24] P. A. Crowther, P. J. Dean, and W. F. Sherman, "Excitation spectrum of aluminum acceptors in diamond under uniaxial stress," *Phys. Rev.*, vol. 154, no. 3, pp. 772–785, 1967.
- [25] E. A. Ekimov, V. A. Sidorov, E. D. Bauer, N. N. Mel'nik, N. J. Curro, J. D. Thompson, and S. M. Stishov, "Superconductivity in diamond," *Nature*, vol. 428, no. 6982, pp. 542–545, 2004.

- [26] M. B. Kirkley, J. J. Gurney, and A. A. Levinson, "Scientific advances in the last decade," *Gems & Gemology*, p. 3, 1991.
- [27] F. Bundy, H. T. Hall, H. Strong, and R. Wentorf, "Man-made diamonds," *nature*, vol. 176, no. 4471, pp. 51–55, 1955.
- [28] H. Liander, "Diamond synthesis," *Allmana Svenska Elektriska Aktiebolaget Journal*, vol. 28, pp. 97–98, 1955.
- [29] E. Walter Hühn, "Company history," 2013. <http://www.e6.com/en/Home/About+us/Company+history/>.
- [30] F. Bundy, W. Bassett, M. Weathers, R. Hemley, H. Mao, and A. Goncharov, "The pressure-temperature phase and transformation diagram for carbon; updated through 1994," *Carbon*, vol. 34, no. 2, pp. 141–153, 1996.
- [31] K. M. Etmimi, *A First Principles Study of Paramagnetic Defects in Diamond*. PhD thesis, Newcastle University, 2010.
- [32] W. G. Eversole and N. Y. Kenmore, 1958.
- [33] W. G. Eversole and N. Y. Kenmore, 1958.
- [34] J. C. Angus, H. A. Will, and W. S. Stanko, "Growth of diamond seed crystals by vapor deposition," *Journal of Applied Physics*, vol. 39, no. 6, pp. 2915–2922, 1968.
- [35] M. Kamo, Y. Sato, S. Matsumoto, and N. Setaka, "Diamond synthesis from gas phase in microwave plasma," *Journal of Crystal Growth*, vol. 62, no. 3, pp. 642–644, 1983.
- [36] D. Goodwin, J. Butler, M. Prelas, G. Popovici, and L. Bigelow, "Handbook of industrial diamonds and diamond films," editor Prelas MA, New York, Dekker, 1998.
- [37] P. W. May, "Cvd diamond: a new technology for the future?," *Endeavour*, vol. 19, no. 3, pp. 101–106, 1995.
- [38] Q. Liang, C. Y. Chin, J. Lai, C.-s. Yan, Y. Meng, H.-k. Mao, and R. J. Hemley, "Enhanced growth of high quality single crystal diamond by microwave plasma assisted chemical vapor deposition at high gas pressures," *Applied physics letters*, vol. 94, no. 2, p. 024103, 2009.
- [39] W. Müller-Sebert, E. Wörner, F. Fuchs, C. Wild, and P. Koidl, "Nitrogen induced increase of growth rate in chemical vapor deposition of diamond," *Applied Physics Letters*, vol. 68, no. 6, pp. 759–760, 1996.

- [40] L. Hounsome, R. Jones, P. Martineau, D. Fisher, M. Shaw, P. Briddon, and S. Öberg, "Origin of brown coloration in diamond," *Physical Review B*, vol. 73, no. 12, p. 125203, 2006.
- [41] C. Clark and C. Dickerson, "The 1.681 ev centre in polycrystalline diamond," *Surface and Coatings Technology*, vol. 47, no. 1-3, pp. 336–343, 1991.
- [42] S. Vagarali, S. Webb, G. Kaplan, W. Jackson, W. Banholzer, and T. Anthony, "High pressure/high temperature production of colorless and fancy colored diamonds," June 27 2002. US Patent App. 08/953,701.
- [43] D. Fisher and R. A. Spits, "Spectroscopic evidence of ge pol hpht-treated natural type iia diamonds," 2000.
- [44] S. Charles, J. Butler, B. Feygelson, M. Newton, D. Carroll, J. Steeds, H. Darwish, C.-S. Yan, H. Mao, and R. Hemley, "Characterization of nitrogen doped chemical vapor deposited single crystal diamond before and after high pressure, high temperature annealing," *physica status solidi (a)*, vol. 201, no. 11, pp. 2473–2485, 2004.
- [45] R. Khan, B. Cann, P. Martineau, J. Samartseva, J. Freeth, S. Sibley, C. Hartland, M. Newton, H. Dhillon, and D. Twitchen, "Colour-causing defects and their related optoelectronic transitions in single crystal cvd diamond," *Journal of Physics: Condensed Matter*, vol. 25, no. 27, p. 275801, 2013.
- [46] T. Hainschwang, D. Simic, E. Fritsch, B. Deljanin, S. Woodring, and N. DelRe, "A gemological study of a collection of chameleon diamonds," *Gems & Gemology*, vol. 41, no. 1, 2005.
- [47] J. P. Goss, C. P. Ewels, P. R. Briddon, and E. Fritsch, "Bistable n<sub>2</sub>-h complexes: The first proposed structure of a h-related colour-causing defect in diamond," *Diamond Relat. Mater.*, vol. 20, no. 7, pp. 896–901, 2011.
- [48] R. Robertson, J. J. Fox, and A. E. Martin, "Two types of diamond," *Phil. Trans. R. Soc. A*, vol. 232, pp. 463–535, 1934.
- [49] H. Dhillon, D. Twitchen, and R. Khan, "Single crystal cvd synthetic diamond material," June 20 2013. WO Patent App. PCT/EP2012/075,237.
- [50] R. Mildren and J. Rabeau, *Optical engineering of diamond*. John Wiley & Sons, 2013.
- [51] T. P. University, "Scientists develop synthetic diamond-based detectors for cern," June 2017.

- [52] D. B. Bucher, D. R. Glenn, J. Lee, M. D. Lukin, H. Park, and R. L. Walsworth, "High resolution magnetic resonance spectroscopy using solid-state spins," *arXiv preprint arXiv:1705.08887*, 2017.
- [53] R. Schirhagl, K. Chang, M. Loretz, and C. L. Degen, "Nitrogen-vacancy centers in diamond: nanoscale sensors for physics and biology," *Annual review of physical chemistry*, vol. 65, pp. 83–105, 2014.
- [54] R. Farrer, "On the substitutional nitrogen donor in diamond," *Solid State Commun.*, vol. 7, p. 685, 1969.
- [55] E. Schrödinger, "An undulatory theory of the mechanics of atoms and molecules," *Physical Review*, vol. 28, no. 6, p. 1049, 1926.
- [56] M. Born and J. R. Oppenheimer, " ," *Ann. Phys.*, vol. 84, p. 457, 1927.
- [57] C. D. Sherrill, "An introduction to hartree-fock molecular orbital theory," *Georgia inst. of technology*, 2000.
- [58] T. J. L. at UCSF, "Hartree-fock introduction," 2017. [http://www.jacobsonlab.org/biophys206/hartree\\_fock.pdf](http://www.jacobsonlab.org/biophys206/hartree_fock.pdf).
- [59] P. Hohenberg and W. Kohn, "Inhomogeneous electron gas," *Phys. Rev.*, vol. 136, no. 3B, pp. 864–871, 1964.
- [60] W. Kohn and L. J. Sham, "Self-consistent equations including exchange and correlation effects," *Phys. Rev.*, vol. 140, no. 4A, pp. A1133–A1138, 1965.
- [61] J. P. Goss, "Theory of hydrogen in diamond," *J. Phys. Cond. Matter*, vol. 15, pp. R551–R580, 2003.
- [62] J. P. Perdew, K. Burke, and M. Ernzerhof, "Generalized gradient approximation made simple," *Phys. Rev. Lett.*, vol. 77, no. 18, pp. 3865–3868, 1996.
- [63] P. R. Briddon and R. Jones, "LDA calculations using a basis of Gaussian orbitals," *Phys. Status Solidi B*, vol. 217, no. 1, pp. 131–171, 2000.
- [64] M. J. Rayson and P. R. Briddon, "Rapid iterative method for electronic-structure eigenproblems using localised basis functions," *Computer Phys. Comm.*, vol. 178, pp. 128–134, JAN 15 2008.
- [65] C. Hartwigsen, S. Goedecker, and J. Hutter, "Relativistic separable dual-space gaussian pseudopotentials from h to rn," *Phys. Rev. B*, vol. 58, no. 7, pp. 3641–3662, 1998.

- [66] R. A. S. AL-Hamadany, *Quantum Mechanical Study of Point and Molecular Defects in Perovskite Nano-systems*. PhD thesis, Newcastle University, 2014.
- [67] H. J. Monkhorst and J. D. Pack, "Special points for Brillouin-zone integrations," *Phys. Rev. B*, vol. 13, no. 12, pp. 5188–5192, 1976.
- [68] J. D. Pack and H. J. Monkhorst, "Special points for brillouin-zone integrations – a reply," *Phys. Rev. B*, vol. 16, pp. 1748–1749, Aug. 1977.
- [69] J. P. Goss, R. Jones, S. J. Breuer, P. R. Briddon, and S. Öberg, "The twelve-line 1.682 eV luminescence center in diamond and the vacancy-silicon complex," *Phys. Rev. Lett.*, vol. 77, no. 14, pp. 3041–3044, 1996.
- [70] P. R. Briddon and R. Jones, "Theory of impurities in diamond," *Physica B*, vol. 185, no. 1–4, pp. 179–189, 1993.
- [71] J. P. Goss, B. J. Coomer, R. Jones, C. J. Fall, C. D. Latham, P. R. Briddon, and S. Öberg, "Small aggregates of interstitials and models for platelets in diamond," *J. Phys. Cond. Matter*, vol. 12, no. 49, pp. 10257–10261, 2000.
- [72] U. Gerstmann, M. Amkreutz, and H. Overhof, "Paramagnetic defects," *Phys. Status Solidi B*, vol. 217, no. 1, pp. 665–684, 2000.
- [73] D. Saada, J. Adler, and R. Kalish, "Sulfur: A potential donor in diamond," *Appl. Phys. Lett.*, vol. 77, pp. 878–879, August 2000.
- [74] L. G. Wang and A. Zunger, "Phosphorus and sulphur doping of diamond," *Phys. Rev. B*, vol. 66, p. 161202(R), Apr. 2002.
- [75] J. P. Goss, B. J. Coomer, R. Jones, T. D. Shaw, P. R. Briddon, M. Rayson, and S. Öberg, "Self-interstitial aggregation in diamond," *Phys. Rev. B*, vol. 63, no. 19, p. 195208, 2001.
- [76] S. J. Breuer and P. R. Briddon, "*Ab initio* investigation of the native defects in diamond and self-diffusion," *Phys. Rev. B*, vol. 51, no. 11, pp. 6984–6994, 1995.
- [77] S. J. Breuer and P. R. Briddon, "Energy barrier to reorientation of the substitutional nitrogen in diamond," *Phys. Rev. B*, vol. 53, no. 12, pp. 7819–7822, 1996.
- [78] T. Hom, W. Kiszewick, and B. Post, "Accurate lattice constants from multiple reflection measurements ii. lattice constants of germanium, silicon and diamond," *J. Appl. Cryst.*, vol. 8, p. 457, 1975.

- [79] M. L. Cohen, "Calculation of bulk moduli of diamond and zinc-blende solids," *Phys. Rev. B*, vol. 32, no. 12, pp. 7988–7991, 1985.
- [80] J. F. Dobson, M. P. Das, and G. Vignale, eds., *Electronic Density Functional Theory: Recent Progress & New Directions*. New York: Kluwer Academic Publishers, April 1998.
- [81] R. M. Dreizler and E. K. U. Gross, *Density Functional Theory*. Berlin: Springer, 1990.
- [82] J. Singh, *Physics of semiconductors and their heterostructures*. New York: McGraw-Hill, 1993.
- [83] A. M. Zaitsev, "Hydrogen related vibrational and electronic transitions in diamond," in *Properties, growth and applications of diamond* (M. H. Nazaré and A. J. Neves, eds.), no. 26 in EMIS Datareviews Series, ch. A5.7, pp. 155–162, London: INSPEC, Institute of Electrical Engineers, 2001.
- [84] J. A. Weil and J. R. Bolton, *Electron paramagnetic resonance: elementary theory and practical applications*. John Wiley & Sons, 2007.
- [85] P. E. Blöchl, "Projector augmented-wave method," *Phys. Rev. B*, vol. 50, pp. 17953–17979, Dec. 1994.
- [86] M. J. Shaw, P. R. Briddon, J. P. Goss, M. J. Rayson, A. Kerridge, A. H. Harker, and A. M. Stoneham, "Importance of quantum tunneling in vacancy-hydrogen complexes in diamond," *Phys. Rev. Lett.*, vol. 95, no. 10, p. 105502, 2005.
- [87] J. Lento, J.-L. Mozos, and R. M. Nieminen, "Charged point defects in semiconductors and the supercell approximation," *J. Phys. Cond. Matter*, vol. 14, no. 10, pp. 2637–2646, 2002.
- [88] G. Henkelman, B. P. Uberuaga, and H. Jónsson, "A climbing image nudged elastic band method for finding saddle points and minimum energy paths," *J. Chem. Phys.*, vol. 113, no. 22, pp. 9901–9904, 2000.
- [89] G. Henkelman and H. Jónsson, "Improved tangent estimate in the nudged elastic band method for finding minimum energy paths and saddle points," *J. Chem. Phys.*, vol. 113, no. 22, pp. 9978–9985, 2000.
- [90] J. P. Goss, P. R. Briddon, M. J. Rayson, S. J. Sque, and R. Jones, "Vacancy-impurity complexes and limitations for implantation doping of diamond," *Phys. Rev. B*, vol. 72, p. 035214, July 2005.

- [91] S. H. Connell, J. P. F. Sellschop, J. E. Butler, R. D. Maclear, B. P. Doyle, and I. Z. Machi, "A study of the mobility and trapping of minor hydrogen concentrations in diamond in three dimensions using quantitative ERDA microscopy," *Diamond Relat. Mater.*, vol. 7, no. 11, pp. 1714–1718, 1998.
- [92] N. H. Nickel, ed., *Hydrogen in semiconductors II*, vol. 61 of *Semiconductors and Semimetals*. San Diego, USA: Academic Press, 1999.
- [93] J. Stiegler, A. Bergmaier, J. Michler, Y. Von Kaenel, G. Dollinger, and E. Blank, "Impurity and defect incorporation in diamond films deposited at low substrate temperatures," *Diamond and related materials*, vol. 7, no. 2, pp. 193–199, 1998.
- [94] C. Glover, M. E. Newton, P. Martineau, D. J. Twitchen, and J. M. Baker, "Hydrogen incorporation in diamond: The nitrogen-vacancy-hydrogen complex," *Phys. Rev. Lett.*, vol. 90, no. 18, p. 185507, 2003.
- [95] J. P. Goss, P. R. Briddon, R. Jones, and S. Sque, "The vacancy nitrogen hydrogen complex in diamond: a potential deep centre in chemical vapour deposited material," *J. Phys. Cond. Matter*, vol. 15, pp. S2903–S2911, 2003.
- [96] U. F. S. DHaenens-Johansson, A. M. Edmonds, M. E. Newton, J. P. Goss, P. R. Briddon, J. M. Baker, R. U. A. Martineau, P. M. amd Khan, D. J. Twitchen, and S. D. Williams, "Epr of a defect in cvd diamond involving both silicon and hydrogen that shows preferential alignment," *Phys. Rev. B*, vol. 82, p. 155205, 2010.
- [97] A. M. Edmonds, M. E. Newton, P. M. Martineau, D. J. Twitchen, and S. D. Williams, "Electron paramagnetic resonance studies of silicon-related defects in diamond (vol 77, 245205, 2008)," *Phys. Rev. B*, vol. 82, no. 24, p. 249901, 2010.
- [98] J. P. Goss, M. J. Shaw, and P. R. Briddon, "Marker-method calculations for electrical levels using gaussian-orbital basis sets," in *Theory of Defects in Semiconductors* (D. A. Drabold and S. K. Estreicher, eds.), vol. 104 of *Topics in Applied Physics*, pp. 69–94, Berlin/Heidelberg: Springer, 2007.
- [99] D. A. Liberman, "Slater transition-state band-structure calculations," *Phys. Rev. B*, vol. 62, no. 11, pp. 6851–6853, 2000.
- [100] C. Peaker, M. Atumi, J. Goss, P. Briddon, A. Horsfall, M. Rayson, and R. Jones, "Assignment of 13 c hyperfine interactions in the p1-center in diamond," *Diamond and Related Materials*, vol. 70, pp. 118–123, 2016.
- [101] W. V. Smith, P. P. Sorokin, I. L. Gelles, and G. J. Lasher, "Electron-spin resonance of nitrogen donors in diamond," *Phys. Rev.*, vol. 115, pp. 1546–1553, September 1959.

- [102] A. Mainwood, "Nitrogen and nitrogen-vacancy complexes and their formation in diamond," *Phys. Rev. B*, vol. 49, no. 12, pp. 7934–7940, 1994.
- [103] E. B. Lombardi, A. Mainwood, K. Osuch, and E. C. Reynhardt, "Computational models of the single substitutional nitrogen atom in diamond," *J. Phys. Cond. Matter*, vol. 15, pp. 3135–3149, 2003.
- [104] K. M. Etmimi, M. E. Ahmed, P. R. Briddon, J. P. Goss, and A. M. Gsiewa, "Nitrogen-pair paramagnetic defects in diamond: A density functional study," *Phys. Rev. B*, vol. 79, no. 20, p. 205207, 2009.
- [105] O. D. Tucker, M. E. Newton, and J. M. Baker, "EPR and  $^{14}\text{N}$  electron-nuclear double-resonance measurements on the ionized nearest-neighbor dinitrogen center in diamond," *Phys. Rev. B*, vol. 50, pp. 15586–15596, December 1994.
- [106] J. Rosa, M. Vaněček, M. Nesládek, K. Meykens, and L. M. Stals, "Photoionization cross-section of dominant defects in CVD diamond," *Diamond Relat. Mater.*, vol. 8, pp. 721–724, 1999.
- [107] J. P. Goss, P. R. Briddon, S. J. Sque, and R. Jones, "Donor and acceptor states in diamond," *Diamond Relat. Mater.*, vol. 13, no. 4–8, pp. 684–690, 2004.
- [108] R. Jones, J. P. Goss, and P. R. Briddon, "Acceptor level of nitrogen in diamond and the 270-nm absorption band," *Phys. Rev. B*, vol. 80, no. 3, p. 033205, 2009.
- [109] R. Ulbricht, S. T. van der Post, J. P. Goss, P. R. Briddon, R. Jones, R. U. A. Khan, and M. Bonn, "Single substitutional nitrogen defects revealed as electron acceptor states in diamond using ultrafast spectroscopy," *Phys. Rev. B*, vol. 84, p. 165202, Oct 2011.
- [110] J. Koppitz, O. F. Schirmer, and M. Seal, "Pseudo-Jahn–Teller optical absorption of isolated nitrogen in diamond," *J. Phys. C*, vol. 19, pp. 1123–1133, 1986.
- [111] R. M. Chrenko, H. M. Strong, and R. E. Tuft, "Dispersed paramagnetic nitrogen content of large laboratory diamonds," *Phil. Mag.*, vol. 23, pp. 313–318, 1971.
- [112] A. T. Collins, M. Stanley, and G. S. Woods, "Nitrogen isotope effects in synthetic diamonds," *J. Phys. D*, vol. 20, pp. 969–974, 1987.
- [113] S. C. Lawson, D. Fisher, D. C. Hunt, and M. E. Newton, "On the existence of positively charged single-substitutional nitrogen in diamond," *J. Phys. Cond. Matter*, vol. 10, pp. 6171–6180, July 1998.
- [114] D. C. Hunt, *D. Phil. Thesis*. PhD thesis, University of Oxford, 1999.

- [115] R. J. Cook and D. H. Whiffen, "Electron nuclear double resonance study of a nitrogen centre in diamond," *Proc. R. Soc. London, Ser. A*, vol. 295, pp. 99–106, November 1966.
- [116] A. Cox, M. E. Newton, and J. M. Baker, "C-13, N-14 And N-15 Endor Measurements On The Single Substitutional Nitrogen Center (P1) In Diamond," *J. Phys. Cond. Matter*, vol. 6, no. 2, pp. 551–563, 1994.
- [117] R. C. Barklie and J. Guven, "<sup>13</sup>C hyperfine structure and relaxation times of the p1 centre in diamond," *J. Phys. C*, vol. 14, pp. 3621–3631, 1981.
- [118] T. Gaebel, M. Domhan, I. Popa, C. Wittmann, P. Neumann, F. Jelezko, J. R. Rabeau, N. Stavrias, A. D. Greentree, S. Praver, J. Meijer, J. Twamley, P. R. Hemmer, and J. Wrachtrup, "Room-temperature coherent coupling of single spins in diamond," *Nature Phys.*, vol. 2, no. 6, pp. 408–413, 2006.
- [119] F. Jelezko, T. Gaebel, I. Popa, M. Domhan, A. Gruber, and J. Wrachtrup, "Observation of coherent oscillation of a single nuclear spin and realization of a two-qubit conditional quantum gate," *Phys. Rev. Lett.*, vol. 93, no. 13, p. 130501, 2004.
- [120] U. Gerstmann and H. Overhof, "The new assignment of hyperfine parameters for deep defects in diamond," *Physica B*, vol. 308–310, pp. 561–564, 2001.
- [121] M. J. Rayson and P. R. Briddon, "Highly efficient method for kohn-sham density functional calculations of 500-10000 atom systems," *Phys. Rev. B*, vol. 80, no. 20, p. 205104, 2009.
- [122] M. J. Rayson, "Lagrange-Lobatto interpolating polynomials in the discrete variable representation," *Phys. Rev. E*, vol. 76, p. 026704, AUG 2007.
- [123] J. M. Baker, J. A. van Wyk, J. P. Goss, and P. R. Briddon, "Electron paramagnetic resonance of sulfur at a split-vacancy site in diamond," *Phys. Rev. B*, vol. 78, no. 2, p. 235203, 2008.
- [124] J. P. Goss, P. R. Briddon, and M. J. Shaw, "Density functional simulations of silicon-containing point defects in diamond," *Phys. Rev. B*, vol. 76, no. 7, p. 075204, 2007.
- [125] U. F. S. D'Haenens-Johansson, A. M. Edmonds, M. E. Newton, J. P. Goss, P. R. Briddon, J. M. Baker, P. M. Martineau, R. U. A. Khan, D. J. Twitchen, and S. D. Williams, "Epr of a defect in cvd diamond involving both silicon and hydrogen that shows preferential alignment," *Phys. Rev. B*, vol. 82, p. 155205, Oct 2010.

- [126] B. Hetényi, F. De Angelis, P. Giannozzi, and R. Car, "Reconstruction of frozen-core all-electron orbitals from pseudo-orbitals," *J. Chem. Phys.*, vol. 115, pp. 5791–5795, Oct. 2001.
- [127] A. Cox, M. E. Newton, and J. M. Baker, "Endor studies on the n1 di-nitrogen center in diamond," *J. Phys. Cond. Matter*, vol. 4, pp. 8119–8130, OCT 12 1992.
- [128] K. Szász, T. Hornos, M. Marsman, and A. Gali, "Hyperfine coupling of point defects in semiconductors by hybrid density functional calculations: The role of core spin polarization," *Phys. Rev. B*, vol. 88, p. 075202, Aug 2013.
- [129] T. Chanier and A. Gali, "Ab initio characterization of a ni-related defect in diamond: The w8 center," *Physical Review B*, vol. 87, no. 24, p. 245206, 2013.
- [130] C. Peaker, J. Goss, P. Briddon, A. Horsfall, and M. Rayson, "The vacancy–hydrogen defect in diamond: A computational study," *physica status solidi (a)*, vol. 212, no. 11, pp. 2431–2436, 2015.
- [131] C. Glover, M. E. Newton, P. M. Martineau, S. Quinn, and D. J. Twitchen, "Hydrogen incorporation in diamond: the vacancy-hydrogen complex," *Phys. Rev. Lett.*, vol. 92, p. 135502, 2004.
- [132] C. Glover, *A study of defects in single crystal CVD diamond*. PhD thesis, Warwick University, 2003.
- [133] P. M. Martineau, S. C. Lawson, A. J. Taylor, S. J. Quinn, D. J. Evans, and M. J. Crowder, "Identification of synthetic diamond grown using chemical vapor deposition (cvd)," *Gems & Gemology*, vol. 40, no. 1, pp. 2–25, 2004.
- [134] M. E. Newton, "Electron paramagnetic resonance of radiation damage centres in diamond," in *Properties and Growth of Diamond* (G. Davies, ed.), no. 9 in EMIS Datareviews Series, ch. 5.2, pp. 153–158, London: INSPEC, Institute of Electrical Engineers, 1994.
- [135] J. P. Goss, R. Jones, S. Öberg, and P. R. Briddon, "(C<sub>As</sub>)<sub>2</sub>-hydrogen defects in GaAs: a first-principles study," *Phys. Rev. B*, vol. 55, no. 23, pp. 15576–15580, 1997.
- [136] A. Collins, "Migration of nitrogen in electron-irradiated type Ib diamond," *Journal of Physics C: Solid State Physics*, vol. 11, no. 10, p. L417, 1978.
- [137] G. Waldherr, J. Beck, M. Steiner, P. Neumann, A. Gali, T. Frauenheim, F. Jelezko, and J. Wrachtrup, "Dark states of single nitrogen-vacancy centers in diamond unraveled by single shot nmr," *Physical review letters*, vol. 106, no. 15, p. 157601, 2011.

- [138] B. Grotz, M. V. Hauf, M. Dankerl, B. Naydenov, S. Pezzagna, J. Meijer, F. Jelezko, J. Wrachtrup, M. Stutzmann, F. Reinhard, *et al.*, “Charge state manipulation of qubits in diamond,” *Nature communications*, vol. 3, p. 729, 2012.
- [139] P. Diggle, “Investigating the nitrogen vacancy charge state in boron/nitrogen co-doped single crystal synthetic diamond,” July 2017.
- [140] A. Kerridge, A. H. Harker, and A. M. Stoneham, “Quantum behaviour of hydrogen and muonium in vacancy-containing complexes in diamond,” *J. Phys. Cond. Matter*, vol. 16, pp. 8743–8751, 2004.
- [141] J. Isoya, H. Kanda, Y. Uchida, S. C. Lawson, S. Yamasaki, H. Itoh, and Y. Morita, “Epr identification of the negatively charged vacancy in diamond,” *Phys. Rev. B*, vol. 45, pp. 1436–1439, January 1992.
- [142] G. D. Watkins and J. W. Corbett, “Defects in irradiated silicon: electron paramagnetic resonance and electron-nuclear double resonance of the Si-*E* center,” *Phys. Rev.*, vol. 134, no. 5A, pp. A1359–A1377, 1964.
- [143] G. Davies, “Dynamic Jahn-Teller distortions at trigonal optical centres in diamond,” *J. Phys. C*, vol. 12, pp. 2551–2566, 1979.
- [144] J. P. Goss, P. R. Briddon, V. Hill, R. Jones, and M. J. Rayson, “Identification of the structure of the  $3107\text{cm}^{-1}$  h-related defect in diamond,” *J. Phys. Cond. Matter*, vol. 26, no. 14, p. 145801, 2014.
- [145] X. Zhou, G. D. Watkins, K. M. McNamara Rutledge, R. P. Messmer, and S. Chawla, “Hydrogen-related defects in polycrystalline CVD diamond,” *Phys. Rev. B*, vol. 54, no. 11, pp. 7881–7890, 1996.
- [146] K. Iakoubovskii, A. Stesmans, K. Suzuki, A. Sawabe, and T. Yamada, “Symmetry of the hydrogen-vacancy-like defect *h1* in diamond,” *Phys. Rev. B*, vol. 66, no. 11, p. 113203, 2002.
- [147] K. Iakoubovskii and A. Stesmans, “Characterization of hydrogen and silicon-related defects in cvd diamond by electron spin resonance,” *Phys. Rev. B*, vol. 66, no. 19, p. 195207, 2002.
- [148] S. Felton, A. Edmonds, M. Newton, P. Martineau, D. Fisher, D. Twitchen, and J. Baker, “Hyperfine interaction in the ground state of the negatively charged nitrogen vacancy center in diamond,” *Physical Review B*, vol. 79, no. 7, p. 075203, 2009.

- [149] X.-F. He, N. B. Manson, and P. T. Fisk, "Paramagnetic resonance of photoexcited n-v defects in diamond. i. level anticrossing in the 3 a ground state," *Physical Review B*, vol. 47, no. 14, p. 8809, 1993.
- [150] J. H. N. Loubser and J. A. van Wyk, "?," *Diamond Res.*, vol. 11, p. 4, 1977.
- [151] J. H. N. Loubser and J. A. van Wyk, "Electron spin resonance in the study of diamond," *Rep. Prog. Phys.*, vol. 41, pp. 1201–1248, August 1978.
- [152] B. Bech Nielsen, L. Hoffmann, M. Budde, R. Jones, J. Goss, and S. Öberg, "H interacting with intrinsic defects in Si," *Mater. Sci. Forum*, vol. 196–201, pp. 933–937, 1995.
- [153] A. M. Edmonds, *Magnetic resonance studies of point defects in single crystal diamond*. PhD thesis, Warwick University, 2008.
- [154] S. Liggins, *Identification of point defects in treated single crystal diamond*. PhD thesis, Warwick University, 2010.
- [155] R. Cruddace, *Magnetic resonance and optical studies of point defects in single crystal CVD diamond*. PhD thesis, Warwick University, 2007.
- [156] G. Davies, M. Nazaré, and M. Hamer, "The h3 (2.463 eV) vibronic band in diamond: uniaxial stress effects and the breakdown of mirror symmetry," in *Proceedings of the Royal Society of London A: Mathematical, Physical and Engineering Sciences*, vol. 351, pp. 245–265, The Royal Society, 1976.
- [157] J. A. van Wyk and G. S. Woods, "Electron spin resonance of excited states of the H3 and H4 centres in irradiated type Ia diamonds," *J. Phys. Cond. Matter*, vol. 7, no. 25, pp. 5901–5911, 1995.
- [158] P. Udvarhelyi, G. Thiering, E. Londero, and A. Gali, "Abinitio theory of n<sub>2</sub>V defect as quantum memory in diamond," *arXiv preprint arXiv:1704.07289*, 2017.
- [159] M. Crossfield, G. Davies, A. Collins, and E. Lightowlers, "The role of defect interactions in reducing the decay time of h3 luminescence in diamond," *Journal of Physics C: Solid State Physics*, vol. 7, no. 10, p. 1909, 1974.
- [160] J. E. Lowther, "?," *J. Phys. Chem. Solids*, vol. 45, p. 127, 1984.
- [161] J. P. Goss, P. R. Briddon, H. Pinto, and R. Jones, "Optically active point defects in high quality single crystal diamond," *Phys. Status Solidi A*, vol. 207, no. 9, pp. 2049–2053, 2010.
- [162] P. Martineau. Private communication, 2015.

- [163] E. Nako. Private communication, 2017.
- [164] B. L. Green, M. W. Dale, M. E. Newton, and D. Fisher, "Electron paramagnetic resonance of the  $n_2 v$ - defect in  $n_{15}$ -doped synthetic diamond," *Physical Review B*, vol. 92, no. 16, p. 165204, 2015.
- [165] C. Peaker, J. Goss, P. Briddon, A. Horsfall, and M. Rayson, "Di-nitrogen–vacancy–hydrogen defects in diamond: a computational study," *physica status solidi (a)*, vol. 212, no. 11, pp. 2616–2620, 2015.
- [166] G. Davies, C. Welbourne, and J. Loubser, "Optical and electron paramagnetic effects in yellow type Ia diamonds," *Diamond Research 1978*, pp. 23–30, 1978.
- [167] C. D. Clark, R. W. Ditchburn, and H. B. Byer, "The absorption spectra of natural and irradiated diamonds," *Proc. R. Soc. London, Ser. A*, vol. 237, pp. 75–89, 1956.
- [168] W. Runciman, "Stress spectra of defects in diamond," *Proceedings of the Physical Society*, vol. 86, no. 3, p. 629, 1965.
- [169] P. Crowther and P. Dean, "Phonon interactions, piezo-optical properties and the inter-relationship of the  $n_3$  and  $n_9$  absorption-emission systems in diamond," *Journal of Physics and Chemistry of Solids*, vol. 28, no. 7, pp. 1115–1136, 1967.
- [170] B. Green, B. Breeze, and M. Newton, "Electron paramagnetic resonance and photochromism of  $n_3 v_0$  in diamond," *Journal of Physics: Condensed Matter*, vol. 29, no. 22, p. 225701, 2017.
- [171] J. A. van Wyk and J. H. N. Loubser, "ENDOR of the P2 centre in type-Ia diamonds," *J. Phys. Cond. Matter*, vol. 5, no. 18, pp. 3019–3026, 1993.
- [172] I. N. De Weerd, F. amd Kupriyanov, "Report on the influence of hthp annealing on the  $3107\text{ cm}^{-1}$  hydrogen related optical absorption in natural type Ia diamonds," *Diamond Relat. Mater.*, vol. 11, pp. 714–715, 2002.
- [173] I. Kiflawi, A. Mainwood, H. Kanda, and D. Fisher, "Nitrogen interstitials in diamond," *Phys. Rev. B*, vol. 54, no. 23, pp. 16719–16726, 1996.
- [174] C. E. Housecroft and A. G. Sharpe, *Inorganic Chemistry*. Pearson Education Limited, 2008.
- [175] G. S. Woods and A. T. Collins, "Infrared absorption spectra of hydrogen complexes in type I diamonds," *J. Phys. Chem. Solids*, vol. 44, no. 5, pp. 471–475, 1983.

- [176] B. Bech Nielsen, P. Johannesen, P. Stallinga, K. Bonde Nielsen, and J. R. Byberg, "Identification of the silicon vacancy containing a single hydrogen atom by EPR," *Phys. Rev. Lett.*, vol. 79, no. 8, pp. 1507–1510, 1997.
- [177] C. A. J. Ammerlaan and E. A. Burgemeister, "Reorientation of nitrogen in type Ib diamond by thermal excitation and tunnelling," *Phys. Rev. Lett.*, vol. 47, no. 13, pp. 954–957, 1981.
- [178] R. Q. Hood, P. R. C. Kent, R. J. Needs, and P. R. Briddon, "Quantum monte carlo study of the optical and diffusive properties of the vacancy defect in diamond," *Phys. Rev. Lett.*, vol. 91, no. 07, p. 076403, 2003.
- [179] G. Davies, S. C. Lawson, A. T. Collins, A. Mainwood, and S. J. Sharp, "Vacancy-related centers in diamond," *Phys. Rev. B*, vol. 46, no. 20, pp. 13157–13170, 1992.
- [180] J. P. Goss, R. Jones, M. I. Heggie, C. P. Ewels, P. R. Briddon, and S. Öberg, "Theory of hydrogen in diamond," *Phys. Rev. B*, vol. 65, no. 11, p. 115207, 2002.
- [181] S. P. Mehandru and A. B. Anderson, "The migration of interstitial h in diamond and its pairing with substitutional B and N: molecular orbital theory," *J. Mater. Res.*, vol. 9, no. 2, pp. 383–395, 1994.
- [182] C.-s. Yan, Y. K. Vohra, H.-k. Mao, and R. J. Hemley, "Very high growth rate chemical vapor deposition of single-crystal diamond," *Proceedings of the National Academy of Sciences*, vol. 99, no. 20, pp. 12523–12525, 2002.
- [183] A. M. Edmonds, U. F. S. D'Haenens-Johansson, R. J. Cruddace, M. E. Newton, K. M. C. Fu, C. Santori, R. G. Beausoleil, D. J. Twitchen, and M. L. Markham, "Production of oriented nitrogen-vacancy color centers in synthetic diamond," *Phys. Rev. B*, vol. 86, no. 3, p. 035201, 2012.
- [184] A. T. Collins, "The fermi level in diamond," *J. Phys. Cond. Matter*, vol. 14, no. 14, pp. 3743–3750, 2002.
- [185] S. Papagiannidis, *Ab Initio Modelling of Defect Complexes in Semiconductors*. PhD thesis, Newcastle University, 2003.
- [186] P. Deák, B. Aradi, M. Kaviani, T. Frauenheim, and A. Gali, "Formation of nv centers in diamond: A theoretical study based on calculated transitions and migration of nitrogen and vacancy related defects," *Phys. Rev. B*, vol. 89, p. 075203, Feb 2014.

## Bibliography

---

- [187] H. Pinto, R. Jones, D. W. Palmer, J. P. Goss, P. R. Briddon, and S. Öberg, "On the diffusion of nv defects in diamond," *Phys. Status Solidi A*, vol. 209, pp. 1765–1768, 2012.
- [188] J. D. Holbeck, B. Bech Nielsen, R. Jones, P. Sitch, and S. Öberg, " $H_2^*$  defect in crystalline silicon," *Phys. Rev. Lett.*, vol. 71, no. 6, pp. 875–878, 1993.
- [189] P. Briddon, R. Jones, and G. M. S. Lister, "Hydrogen in diamond," *J. Phys. C*, vol. 21, no. 30, pp. L1027–L1031, 1988.
- [190] J. P. Goss, R. Jones, M. I. Heggie, C. P. Ewels, P. R. Briddon, and S. Öberg, "First principles study of H in diamond," *Phys. Status Solidi A*, vol. 186, no. 2, pp. 263–268, 2001.
- [191] G. Davies, "Current problems in diamond: towards a quantitative understanding," *Physica B*, vol. 273–274, pp. 15–23, 1999.
- [192] Y. Mita, Y. Nisida, K. Suito, A. Onodera, and S. Yazu, "Photochromism of  $H_2$  and  $H_3$  centres in synthetic type Ib diamonds," *J. Phys. Cond. Matter*, vol. 2, no. 43, pp. 8567–8574, 1990.

## The Hohenberg and Kohn proof

Assume two different systems (1 and 2) have different potentials ( $V$ ), Hamiltonians ( $\hat{H}$ ) and wave functions ( $\Psi$ ). But they have the same charge density ( $n(\mathbf{r})$ ). The energy of the two different systems are therefore:

$$E_1 = \langle \Psi_1 | \hat{H}_1 | \Psi_1 \rangle \quad (1)$$

and

$$E_2 = \langle \Psi_2 | \hat{H}_2 | \Psi_2 \rangle. \quad (2)$$

Applying the variational principle to Equations 1 and 2 yields,

$$E_1 = \langle \Psi_1 | \hat{H}_1 | \Psi_1 \rangle < \langle \Psi_2 | \hat{H}_1 | \Psi_2 \rangle. \quad (3)$$

Rearranging the above leads to:

$$E_1 < \langle \Psi_2 | \hat{H}_2 | \Psi_2 \rangle + \langle \Psi_2 | \hat{H}_1 - \hat{H}_2 | \Psi_2 \rangle, \quad (4)$$

$$E_1 < E_2 + \langle \Psi_2 | V_1 - V_2 | \Psi_2 \rangle, \quad (5)$$

$$E_1 < E_2 + \int (V_1 - V_2) n(\mathbf{r}) d^3\mathbf{r}. \quad (6)$$

The same can process can be applied again to the other system, resulting in,

$$E_2 < E_1 + \int (V_2 - V_1) n(\mathbf{r}) d^3\mathbf{r}. \quad (7)$$

Adding the Equations 6 and 7 gives a contradictory result,

$$E_2 + E_1 < E_1 + E_2. \quad (8)$$

Therefore proving the first Hohenberg-Kohn theorem via *reductio ad absurdum*: two systems that have the same ground state charge density will have the same external potential.